Technische Universität München
TUM School of Engineering and Design

Enhancement and Optimization of a Turbulence Model for Vortex Dominated Flows based on Experimental Data

Matteo Moioli

Vollständiger Abdruck der von der TUM School of Engineering and Design der Technischen Universität München zur Erlangung eines

Doktors der Ingenieurwissenschaften (Dr. -Ing.)

genehmigten Dissertation.

Vorsitz: Prof. Dr.-Ing. Chiara Manfletti

Prüfer*innen der Dissertation:

1. apl. Prof. Dr.-Ing. Christian W. M. Breitsamter
2. Prof. Dr.-Ing. Rolf Radespiel

Die Dissertation wurde am 18.05.2022 bei der Technischen Universität München eingereicht und durch die TUM School of Engineering and Design am 18.09.2022 angenommen.

Acknowledgments

This dissertation stands as the outcome of the work performed during my time at the Chair of Aerodynamics and Fluid Mechanics at the Technical University of Munich, which I gratefully acknowledge as the greatest framework which could I have hoped for. As a research associate, I have been able to learn, try and improve many aspects both from a technical and a personal point of view. Therefore, I am surely a better engineer but also a better person. For these reasons, I would like to thank all the people that have been at my side and contributed to the accomplishment of this never-trivial, always motivating path.

I wish to thank Prof. Breitsamter for his supervision. His ability to provide the best support and consequential technical suggestions has inspired me. He has always listened to my questions and replied with the evident objective to make my work successful. I would like to thank Dr. Kaare A. Sørensen for its amazing support throughout the whole time and its capability to always spark in me the motivation to reach for more. He is always ready for a technical exchange as well as the best moral support, printed with a smile.

I had the luck to share my time at the Chair with different great colleagues. Constructive discussions, help and friendful interactions were always part of my days. Starting from the colleagues I shared the office for the most part of the time, Stefan Pfnür and Andrei Buzica and moving on to Dr. Maximilian Winter, Dr. Vladislav Rosov, Dr. Marco Stuhlpfarrer, Christopher Reinbold, Dr. Florian Knoth, Patrick Pöelzlbauer, Florian Heckmeier, Andreas Kümmel, Jonathan Pflüger, Johannes Ruhland and all the other colleagues. Similarly, I would like to thank the department of aerodynamic design at Airbus where I have been able to properly collaborate in a very constructive way and feel part of a working group.

I would like to thank my wonderful family for their support. Although I never had to reach out for help, to know that they would have been there for anything is the best foundation to focus on the daily tasks. The experience of visit and spend time with them at the best occasions gives always special emotions. Similar can be said for my friends Mirko, Mauro, Fabio, Riccardo, Michele and Cristiano thanks to their ability to lighten the tough days with a pair of jokes. In particular and with special honours, I would like to thank my brother Roberto as he has inspired me throughout my whole life and it is for me almost impossible to find a single aspect where no exchange or talk with him was of major importance.

Abstract

The numerical simulation of large-scale leading-edge vortex flow is fundamental for the investigation of the aerodynamic characteristics of high-agility aircraft based on low-aspect-ratio wings. With the state-of-the-art numerical methodologies, the computational cost and the accuracy level compared to experimental data remain a limitation to the generation of numerical aerodynamic datasets. A major contribution to the discrepancies between numerical results and the real flow physics is given by the modeling of turbulence. This is inherent in turbulence models based on the Boussinesq assumption in the context of the Reynolds-Averaged Navier-Stokes equations. Whereas the employment of scale resoling or more complex turbulence models enhance the accuracy level, the computational cost increases prohibitively for the generation of a large dataset. In fact, in the context of the design and development phases of an highly agile aircraft, a large amount of points are computed at every design loop. Therefore, the generation of a dataset has strict requirements which relate to efficiency, accuracy and reliability. A methodology to achieve a higher grade of accuracy is formulated, tested and applied. It consists of a series of steps. A baseline one-equation eddy-viscosity model which is commonly used for external aerodynamic applications is selected. The model complexity is enhanced by means of additional eddy-viscosity production terms. The terms are formulated with physical characteristics of vortex flows as targets and they are exclusively active in the vortex flow field by means of the definition of an identifier quantity which is coupled with every additional term. A series of calibration coefficients of the additional terms is optimized by means of a gradient-descent algorithm. The minimization function is the mean absolute error between the numerical results and the experimental data. The optimized model is able to increase substantially the accuracy for a cluster of cases around the calibration target. A series of dependencies are analyzed with respect to the correlation between the required set of coefficients on different vortex types and development stages. Extensions of the model have been added in order to further improve its accuracy enhancement and the predictive capability. For the first goal, a zonal methodology is formulated which permits to define different sets of coefficients for the respective zones of the flow domain. For the second one, an artificial neural network is trained on the data available from all the investigated test cases and the respective optimization procedures. The neural network is employed to predict a new set of coefficients when a new test case is analyzed and no experimental data or past information on similar conditions are available. The methods are applied on a series of relevant test cases covering a large spectrum of flow/geometrical conditions. The results are significant and the method is ready for the application on a large dataset of cases.

Zusammenfassung

Die numerische Simulation großräumiger Wirbelströmungen an der Vorderkante ist von grundlegender Bedeutung für die Untersuchung der aerodynamischen Eigenschaften von hochagilen Flugzeugen auf der Grundlage von Flügeln mit geringem Streckung. Bei den modernen numerischen Methoden stellen die Rechenkosten und die Genauigkeit im Vergleich zu experimentellen Daten eine Einschränkung bei der Erstellung numerischer aerodynamischer Datensätze dar. Ein wesentlicher Beitrag zu den Diskrepanzen zwischen den numerischen Ergebnissen und der realen Strömungsphysik liegt in der Modellierung der Turbulenz. Dies liegt an den Turbulenzmodellen, die auf der Boussinesq-Annahme im Zusammenhang mit den Reynolds-gemittelten Navier-Stokes-Gleichungen basieren. Während die Verwendung von skalenauflösenden oder komplexeren Turbulenzmodellen die Genauigkeit erhöht, steigen die Rechenkosten für die Erzeugung eines großen Datensatzes prohibitiv an. Im Zusammenhang mit den Entwurfs- und Entwicklungsphasen eines hochagilen Flugzeugs wird bei jeder Entwurfsschleife eine große Anzahl von Punkten berechnet. Daher werden an die Erzeugung eines Datensatzes strenge Anforderungen in Bezug auf Effizienz, Genauigkeit und Zuverlässigkeit gestellt. Es wird eine Methode zur Verbesserung der Genauigkeit entwickelt, getestet und angewendet. Sie besteht aus einer Reihe von Schritten. Es wird ein Ein-Gleichungs-Wirbelviskositätsmodell gewählt, das oft für externe aerodynamische Anwendungen verwendet wird. Die Komplexität des Modells wird durch zusätzliche Wirbelviskositäts-Erzeugungsterme erhöht. Die Terme werden mit physikalischen Eigenschaften von Wirbelströmungen als Zielvorgaben formuliert und sind ausschließlich im Wirbelströmungsfeld durch die Definition einer Identifikationsgröße aktiv, die mit jedem zusätzlichen Term gekoppelt ist. Eine Reihe von Kalibrierkoeffizienten der Zusatzterme wird mit Hilfe eines Gradientenabstiegsalgorithmus optimiert. Die Minimierungsfunktion ist der mittlere absolute Fehler zwischen den numerischen Ergebnissen und den experimentellen Daten. Das optimierte Modell ist in der Lage, die Genauigkeit für eine Gruppe von Fällen um das Kalibrierungsziel herum erheblich zu erhöhen. Eine Reihe von Abhängigkeiten werden im Hinblick auf die Korrelation zwischen dem erforderlichen Koeffizientensatz und verschiedenen Wirbeltypen und Entwicklungsstadien analysiert. Es wurden Erweiterungen des Modells vorgenommen, um seine Genauigkeit und Vorhersagefähigkeit weiter zu verbessern. Für das erste Ziel wird eine zonale Methodik formuliert, die es erlaubt, verschiedene Koeffizientensätze für die jeweiligen Zonen des Strömungsbereichs zu definieren. Für das zweite Ziel wird ein künstliches neuronales Netz auf der Grundlage der Daten aller untersuchten Testfälle und der jeweiligen Optimierungsverfahren trainiert. Das neuronale Netz wird zur Vorhersage eines neuen Satzes von Koeffizienten eingesetzt, wenn ein neuer Testfall analysiert wird und keine experimentellen Daten oder frühere Informationen über ähnliche Bedingungen verfügbar sind. Die Methoden werden auf eine Reihe relevanter Testfälle angewandt, die ein breites Spektrum an strömungsgeometrischen Bedingungen abdecken. Die Ergebnisse sind signifikant und die Methode ist bereit für die Anwendung auf einen großen Datensatz von Fällen.

Contents

List of Figures

List of Tables

Nomenclature

Symbols

Symbol	**Unit**	**Description**
α	$-$	Regularization factor of the gradient descent algorithm
α, AoA	°	Angle of attack
β, AoS	°	Angle of sideslip
δ_{ij}	$-$	Kronecker delta function
λ	$-$	Taper ratio
Λ, AR	$-$	Aspect ratio
$\mathbf{c}$	$-$	Turbulence model coefficients
$\mathbf{u}$	m/s	Velocity vector
$\mathcal{E}(\boldsymbol{c})$	$-$	Weighted mean absolute error of the optimization routine
$\mathcal{H}$	$\mathrm{m/s^2}$	Helicity
μ	Pa s	Dynamic viscosity
ν	$\mathrm{m^2/s}$	Kinematic viscosity
$\nu_t, \tilde{\nu}$	$\mathrm{m^2/s}$	Eddy viscosity
ω	/s	Vorticity
ρ	$\mathrm{kg/m^3}$	Density
τ	Pa	Shear stresses
τ_{ij}^{t}	Pa	Turbulent stresses
φ	°	Sweep angle
ξ	$-$	Vortex identifier quantity
C_L	$-$	Lift Coefficient
c_p	J/(K kg)	Specific heat at constant pressure
c_r	m	Root chord
c_t	m	Tip chord
c_v	J/(K kg)	Specific heat at constant volume
C_{Mx}	$-$	Rolling Moment Coefficient

C_{My}	$-$	Pitching Moment Coefficient
C_P	$-$	Pressure coefficient
d	m	Distance
h	m	Height
k	m^2/s^2	Turbulent kinetic energy
l_μ	m	Mean aerodynamic chord
M	$-$	Mach number
P	Pa	Pressure
r	m	Radius
Pr	$-$	Prandtl number
R_a	µm	Arithmetical mean deviation of profile height
R_z	µ	Average peak to valley of profile height
Re	$-$	Reynolds number
s	m	Wing semi span
$S, \tilde{S}$	/s	Strain rate
S_{ref}	m^2	Reference area
T	° K	Temperature
t	s	Time
u, v, w	m/s	Velocity components
U_∞	m/s	Free stream velocity

Subscripts

Symbol	**Description**
vl	Vortex limit
dir	Unit vector (direction)
bv	Vortex source terms
bvh	Vortex helicity-based source terms
bvb	Vortex breakdown source term
sw	Switch
N	Normal

Abbreviations

Acronym	**Description**
ADS	Airbus Defence and Space GmbH
AER	Chair of Aerodynamics and Fluid Mechanics
ANN	Artificial Neural Network
AUSM	Advection Upstream Splitting Method
AVT	Applied Vehicle Technology
CAD	Computer-Aided Design
CAWAPI	Cranked Arrow Wing Aerodynamic Project International
CFD	Computational Fluid Dynamics
CNC	Computerized Numerical Control
DDES	Delayed Detached Eddy Simulation
DES	Detached Eddy Simulation
DLR	German Aerospace Center
DNS	Direct Numerical Simulation
EARSM	Explicit Algebraic Reynolds Stress Model
EVM	Eddy Viscosity Model
FDM	Fused Deposition Modeling
FVM	Finite Volume Method
GCS	Gauss Centre for Supercomputing
GEKO	GEneralized k-ω
HPC	High Performance Computing
LE	Leading Edge
LES	Large eddy simulation
LRZ	Leibniz Supercomputing Centre
LUSGS	Lower-Upper Symmetric Gauss-Seidel algorithm
MAE	Mean Absolute Error
NACA	National Advisory Committee for Aeronautics
NASA	National Advisory Committee for Aeronautics
NATO	North Atlantic Treaty Organization
OPT	Optimized turbulence model
PG	Pressure Gradient

PIV	Particle Image Velocimetry
PLA	Polylactic Acid
PSP	Pressure Sensitive Paint
RANS	Reynolds-averaged Navier-Stokes equations
RSM	Reynolds Stress Model
RTO	Research and Technology Organisation
SA	Spalart-Allmaras model
SA-RC	Spalart-Allmaras with the Rotation Correction
SACCON	Stability and Control Configuration
SAE	Spalart-Allmaras model with Edwards modifcation
SAO	Spalart-Allmaras model Original formulation
SAS	Scale Adaptive Simulation
SGD	Stochastic Gradient Descent
SLA	Stereolithography
SST	Shear Stress Transport
STO	Science and Technology Organization
TE	Trailing Edge
TNT	Turbulent/Non-Turbulent
TUBS	Technical University of Braunschweig
TUM	Technical University of Munich
VFE-2	Second Vortex Flow Experiment
VitAM	Advanced Aircraft Understanding via the Virtual Aircraft Model
W/T	Wind Tunnel
WTT	Wind Tunnel Test
ZDES	Zonal Detached Eddy Simulation

1 Introduction

1.1 Motivation

The development and design of an aircraft is a procedure where academic and industrial research efforts intersect with the time/cost constraints, the scientific validity and the market competition in order to achieve the foreplanned requirements and targets. This is as far as possible from being a trivial task. As the technology, worldwide competition and requirements levels arise with time, the academic and industrial worlds need to collaborate more and more to ask and answer the relevant scientific questions and progress further. This is a factor that plays a major role for the establishment of research projects which combine the two points of view under the same target. This is the case of the Advanced Aircraft Understanding via the Virtual Aircraft Model (VitAM) project which is gratefully acknowledged as the funding project of the current work [2, 3].

Different typologies of aircraft frames and missions require different types of characteristics. In the context of this research, the focus is concentrated on high agility and performance aircraft. Here, the challenges are usually set even higher as the required aerodynamic characteristics target an enhancement of the flight envelope to the very limit with respect to control power, manueverability and performance as well as maintaining affordable stability characteristics, structural and lifetime capabilities. To achieve such requirements, the process of design and development needs to be performed with a prodigeuos accuracy along all the multiple and correlated disciplines involved. In this sense, the aerodynamic compartment lies at the very fundament of this process and, therefore, a deep understanding of the underlying physical properties of the flow affecting the aerodynamics are of extreme importance. The designers and developers have the necessity of exploiting the best tools for analyzing the different steps of the design procedure with a proper accuracy level.

In this context, the accuracy quality is the grade of error which is achieved between the investigation tool and the physical reality. For decades the tools that have been used in this procedure have been wind tunnel tests, flight tests and numerical simulations. Besides their respective advantages and drawbacks, the evaluation criteria for these different development tools can be reduced to accuracy and cost. Where the cost is both referred to the temporal and the economical one. While flight tests provide the best accuracy level with regard to evaluating the device in the actual environment of application, it can only be performed after a prototype is evaluated, constructed and ready to fly under safety constraints. The costs are therefore the highest both economically and in turning time. Wind tunnel tests follows as the accuracy with reality is reduced compared to a free flight test because of the boundary conditions which limitate and affect it. However, the costs are reduced as well, and it can be performed with preliminary design geometries. Eventually, numerical simulation nowadays consists of the tool that permit to have the best turning time at the price of a reduced level of quality in accordance with a suitable numerical methodology. However, at the state of the art at the beginning of the project, the advantages of cost with respect to the numerical methodologies is not always valid for the economical aspects. This depends on the chosen methodology and the size of the generated dataset of flight conditions to be analyzed.

With regard to the aerodynamic data generation, a major importance is maintained by the experimental side comprehending wind tunnel experiments and flight test data. These data furnish a high level of fidelity and therefore play a major role in the certification phase. Moreover, for complex flow fields like the one of full high performance aircraft configurations, the experimental data are the reference data for the validation and verification of the best practice approaches with regard to the numerical simulation. In this sense, the cross-comparison of the different data sources is routinely performed, enhanced by means of extrapolation or statistical corrections and synergized in a final aerodynamic dataset. Different weight is provided to different sources of data on the undergoing design phase. Previously projects or prototypes also provide relevant information concerning the state of the art of the different data sources. At the present state, the tools are used in order to synergize their advantages along the development procedure at the best compromise.

In this context, the VitAM project has set the goal to increase the amount of numerical simulations compared to other sources of data for the generation of datasets, their analysis and eventually also the certification of products. In this sense, the project refers to the development of a virtual aircraft model. At the beginning of the project, in fact, numerical simulations had not only the disadvantage of being less accurate with respect to wind tunnel experiments but also occasionally more expensive. This is particularly true if low speed conditions are addressed where wind tunnel measurements are relatively less expensive and if high level of phyisical modeling and computational discretization are adopted for the simulations. If all the costs related to the numerical simulations are included, as performed at the state of the art of 2016, i.e. the beginning of VitAM project, numerical simulations would actually be more expensive than wind tunnel measurements at a high fidelity level.

The main reason why the target of improvement has been set to the numerical simulation is their potential. Wind tunnel measurements and flight tests are also target of improvement in the scientific community and continously enhanced through the technical and research process, but it is expected that their potential corrrelated with the acquired level of technology is more limited compared to numerical methodologies. The main direction of improvement of such methodologies relates to increasing the complexity of the investigation tools to provide higher precision and/or resolution in the experimental data provided, for example the progress in the employment of Particle Image Velocimetry with regards to full 3D, time dependent and highly resolved images. The VitAM project has therefore identified the two main directions of improvement related to numerical simulations in the aerodynamic design and development process: higher efficiency and higher accuracy.

The task of improving the efficiency has been achieved by the integration of a series of available, new or readapted numerical strategies and methods in order to accelerate the production of numerical datasets in the context of the extended amount of simulations necessary for high maneuverable aircraft where a large amount of parameters are evaluated. Therefore, the envelope of geometrical and flow conditions to be investigated is composed of a multi-dimensional space of the parameters which identify the aerodynamic conditions. In this sense, the integration of different methods into a single highly automatized routine for the generation of numerical datasets is synergistic and it permits a significant improvement of the efficiency level. The original target is achieved with success along the VitAM project. At the end of the project numerical simulations of the considered typology acquires a significant advantage related to economical costs compared to wind tunnel measurements of the same state-of-the-art level.

In the framework of highly agile aircraft, the numerical simulation of the external flow field is acquiring progressively more relevance for the furnishment of aerodynamic data during both the design and development phase. In the last decades, the ratio between computational cost of the numerical simulations and computational power availability has been reducing progressively, thanks to the growth of the second one. This trend has followed for many years the Moore's law which extrapolates as a qualitative law the progress of biennial reduction of the number of transistors per microchip in order to predict the future enhancement of computational efficiency [4]. However, a physical limit has been encountered as the diminishing of the chip size has started to introduce additional limitations or production difficulties which have rapidly slown down the progress of the computational power efficiency. Year after year, the community has started to encounter the problem of whether invest resources in the expansion of the computational resources or into the research of methodologies to increase the efficiency of the numerical simulations preserving the accuracy level. Whereas numerical simulations are becoming less expensive than wind tunnel experiments, the increase of its efficiency permit to increase the number of simulations for an equal amount of computational resources and economical budget. On the other hand, the computational costs of a numerical simulation increase progressively as more complex methodologies are introduced which enclose the modeling of the physical phenomena and/or the discretization methods of the describing equations. Therefore, the academic community has continued with the pursue of increasing the accuracy and physical insight of the numerical methodologies by employing progressively larger computational power. The two points of view have the same objective to maximize the ratio between accuracy and computational cost. For the already illustrated reasons the common trend is the transaction of larger and larger portions of the aerodynamic dataset generation towards the employment of numerical simulations. The turning time required from a design/variation idea which can regard both flow condition or geometric/aerodynamic design is much lower than preparing an additional wind tunnel campaign and model variation. Additionally, a numerical simulation furnishes complete insight into the flow field with no external disturbance, which is more complicated to achieve in the framework of an experimental setup.

However, in the short-term future the complete removal of the experimental component of data is not foreseeable. On the one hand, the accuracy that is required for the full development and certification of an aircraft is not achieved by means of stand-alone numerical simulations at the current state of the art. On the other hand, experimental data are and will remain necessary for the validation of the numerical setup or the verification of new numerical methodologies. It is also necessary to consider that the redundancy of information plays also an important role in the decision of what portions of resources are given to different methodologies of investigations. Hence, a common practice is to compare the different sources of data to gather more confidence in the actual results if they correlate under a reasonable level of accuracy. Otherwise, if discrepancies are encountered between different sources, it gives a clear input for double-checking the results and solve the issue by improving the know-how about which discrepancy may occurr.

The modeling of turbulence for the state-of-the-art numerical simulations of high performance aircraft is addressed as the cause of the dominant discrepancies with data coming from experimental investigations which traditionally are able to accurately capture the aerodynamic characteristics of such flying configurations. The research community has followed the direction of improving the modeling part of a turbulent flow by means of introducing additional equations and/or extending the range of resolved scales of turbulence which correlates with additional complexity, sometimes associated with numerical instabilities, and more importantly computational costs. In this study, a different approach is considered where instead of extending the model complexity while being calibrated for general or global classes of flows, the model is calibrated on a granular basis for clusters of similar flow types and conditions to the ones of interest. A commonly used baseline turbulence model which employs proper qualities of numerical stability and robustness as well as accuracy for attached flows is selected as starting point for the proposed modeling extension. This modeling enhancement is related to the most challenging flow conditions in order to improve the accuracy level by means of the information deriving from experimental data on a portion of the dataset, which is the optimization target. Such information is inferred through an automatic calibration with a gradient descent algorithm which targets the minimization of the error between the numerical simulation and experimental data. The optimized model is applied to a certain cluster of flow cases around the calibration target in order to have the best compromise between accuracy improvement and predictive capability (Fig. 1.1).

In the context of high agility aircraft, the most common wing planforms employed in the recent past and the next future belong to the family of low aspect ratio wings. Therefore, the aerodynamics and the flow physics of highly swept, low aspect ratio wings have been the target of experimental, theoretical and numerical investigations for several decades. Their characteristics for high transonic and supersonic speeds as well as their high agility at high angles of attack fit properly to the demanding performance requirements of highly maneuverable aircraft. Except for some unswept planforms, e.g. the Lockheed F-104 Starfighter employs a supersonic aerodynamic profile instead, the majority of such class of aircraft employs wings with sweepback and, in particular, delta wings. This typology of wing is commonly referred to as delta wing because its shape recalls the greek letter Δ. The swept leading edge permits to increase the critical mach number and, consequently, the occurrence of wave drag, enhancing the

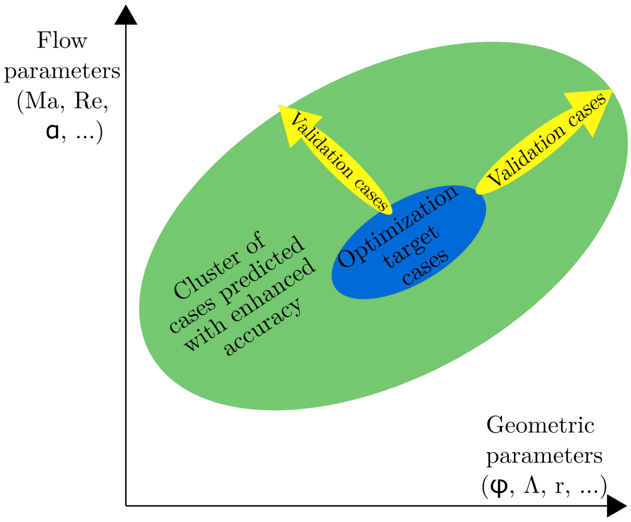

Figure 1.1: Qualitative representation of the fields of cases relevant for the steps of the application of the proposed methodology, mapped along the relevant parameters which defines a test case according to the geometrical and flow parameters. A first optimization target, the following extension by means of validation variations and the cluster of the flow cases for which the accuracy level is enhanced.

efficiency of such wing configurations at transonic speeds [5]. From another point of view, the sweepback permits to increase the relative wing thickness by maintaining the same critical Mach number, hence enhancing structural and storage capabilities with respect to both under carriage stores and wing internal fuel [6]. In particular, due to the short span and large tapering of the wing, the wing is provided with a higher torsional stiffness and bending resistance. The transonic drag increases less abruptly whereas the supersonic drag peak is reduced. The lift coefficient increase with Mach number up to sonic conditions, afterwards it has no abrupt reduction but it smoothly reduces. Moreover, it permits an extension of the buffet-free region of the flight envelope thanks to the vortex flow which also provides a more gradual lift loss at post-stall angles of attack. In the supersonic regime, the occurrence of a supersonic leading edge is delayed by the same effect. Moreover, a delta wing permits to have a low relative thickness of the wing which also results in a reduction in the wave drag component. Another more practical aspect is that the aircraft is provided with more compact dimensions which offer advantages with respect to the its naval-carrier application. As regards the subsonic regime, a delta wing manifests a lower lift coefficient compared to a high aspect-ratio wing which results to the need of flying at high angles of attack at very low speed [6]. Aircraft wing planforms are usually more complex than a single delta wing, the synergy of the aerodynamic effects of multiple delta wings, high-lift devices, leading edge extensions and similar introduce advantages from the aerodynamic and flight dynamic point of view. However, this leads to an increase of the complexity of the physical behavior of the flow which corresponds to additional challenges for the available numerical tools to achieve proper levels of accuracy.

The most important flow field features which characterize the aerodynamic of a delta wing are the large-scale vortices which separate at the leading-edges and their interaction with the aerodynamic surfaces. For this reason, the progress of the application of delta wings in the aerospace industry is intensively connected with the the physical understanding of leading-edge vortices.

1.2 Leading-edge Vortices

Vortical flow fields are present in several fluid dynamic applications either as a secondary/side effect or as designed flow to be employed and controlled. A vortical motion of fluid inherently corresponds to 3-dimensional and complex flows [7] such as tornadoes, vortices developing shear flows, vortical structures inside fully turbulent mixing layers or the rolling of vortices due to a Klevin-Helmoltz instability. A vortex can be encountered also in a laminar regime as for the shedding of laminar vortices downstream cylinders at low Reynolds number, however the focus of the current research is dedicated to vortices at high Reynolds numbers, at a fully turbulent regime.

Vortices play a major role in the development of the mixing, diffusion and transport of the fluid quantities of the associated flow domain as well as the generation of fluid instabilities or modification of the boundary layer behavior, i.e. increasing the frictional drag. Commonly multiple vortical structures are present in the same flow domain and their physical understanding becomes progressively more complex as their number and the level of cross-interaction grows.

1.2.1 Vortex Generation on Delta Wings

With regard to aerodynamic applications of the present research, i.e. delta wings, the highly swept leading edge is the geometrical feature that provokes the separation of the wall-bounded vorticity. This flow feature is a large-scale vortex, the characteristic dimension of which is of the same order of magnitude as the resolved geometry. It developes itself above the wing planform at positive angles of flow incidence, following a series of stages related to the geometry and the flow regime until it break downs into a more chaotic structure that eventually is dissipated into smaller and smaller scales along the turbulent cascade. Its interaction with the aerodynamic surface drastically dominates the aerodynamic characteristics of such geometries commonly applied for high performance aircraft. The sudden appearance and the displacement of the vortex breakdown instability above the wing surface has a drastic impact on the aircraft stability, control and limitations in the flight envelope for aerodynamic and/or structure interactions reasons [8].

During decades of research and application of delta wings, several aspects have been investigated from both an aerodynamic and vortex physics point of view by means of the study of different geometrical variations, the test of new solutions and additional geometrical complexities. These investigations can follow different directions. Firstly, it is possible to follow an iterative process to develop a basic or state-of-the-art delta wing planform into a more complex geometry with enhanced aerodynamic performance. Secondly, the objective can be the investigation of the details of the vortex flow field and its dependencies on the geometrical aspects. Both ways are naturally connected and often cross-dependent. The first can provide deeper insight into the flow field variation by means of a certain geometrical change and the second can return the outcome of the investigation into an increased efficiency in the selection of the different steps or variations which compose an iterative design process.

Already at small angles of attack and velocities, as the flow encounters the leading edge, it is uncapable to stay attached while following the highly curved and swept leading-edge profile and it separates into a vortex sheet (Fig. 1.2). The vortex sheet eventually rolls into a vortical structure above the wing upper surface [9, 1]. The structure of the vortex viewed in a cross-flow plane (Fig. 1.3), is composed by 3 parts which are the vortex-sheet, the rotational core and inner viscous sub-core. The vortex sheet embeds the transport mechanism of the circulation into the rotational core where a spiral form is developed. The rotational core has a diameter around 1/3 of the local wing span [1] and it is characterized by strong tangential velocities. The viscous sub-core is dominated by dissipation effects and consists of around 5% of the local span.

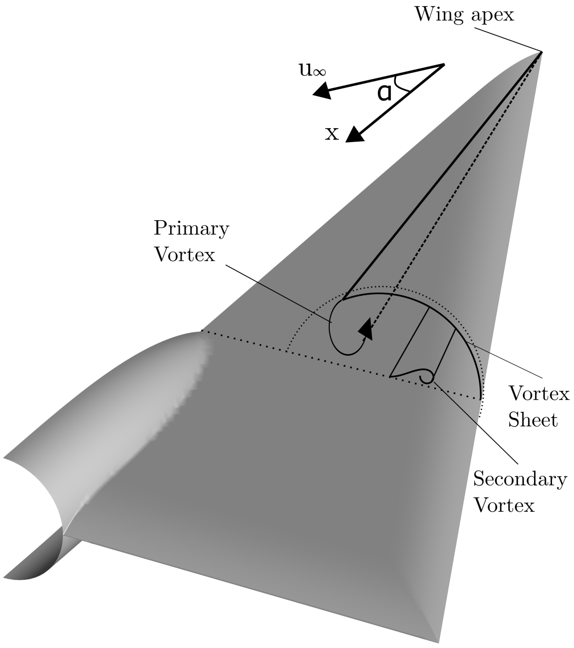

Figure 1.2: Schematic representation of the separation of the primary and the secondary vortices around the leading edge of a delta wing.

The rotational core is characterized by high axial and azimuthal velocities. The axial component in the inner core reaches values up to three times the freestream velocity. High rotational velocities propagate out of the core and interact with the surface wing producing a suction footprint. A maximum of the additional velocity is reached below the vortex axis [9] and corresponds to the minimum of the pressure distribution. A streamline visualization would show wall streamlines directed outwards with an inflection below the vortex axis [9, 10]. The high rotational velocities also induce the flow to circumvent the vortex and reattach on the surface while moving outwards at a reattachment line of the primary vortex. The flow moves from the reattachment line outwards where it experiences a second separation due to the high adverse gradient of pressure present between the reattachment line and the leading-edge high pressure values [1]. This phenomenon is a consequence of the viscous nature of the flow. In fact, in a Euler type numerical solution, no secondary vortex is appreciable [11]. For an analogue effect, especially for laminar boundary layers, a tertiary vortex structure, having the same rotation direction of the main vortex, is induced by the secondary counterrotating vortex and the adverse pressure gradient between the secondary suction peak and the attached flow between the two vortical structures.

The secondary vortical structures interact with the wing surface with the same mechanism and they impress on the aerodynamic surface suction footprints, usually relatively narrower and with a weaker suction peak compared to the main vortical structures. The secondary structure also influence the primary vortex by moving it upwards and inwards [11, 9] and it is dependent on the presence of a laminar or turbulent regime [12]. Hence, it depends on the Reynolds number and this acquires further sensitivity as the leading-edge curvature decreases. The additional high suction areas of primary and secondary vortices result in an additional lifting force acting on the wing providing a non-linear dependence of the lift force on the angle of attack inside the condition of a fully developed vortex. This dependence is linear for traditional high aspect ratio and low swept wing planforms. Theoretical approximations have been formulated in order to predict the additional vortex lift on top of the classical linear dependence on the angle of attack. A notorious example is the Polhamus formula (Eq. 1.1) which has shown agreements with the tendencies of the experimental results [13].

$$C_L = K_p sin\alpha cos^2\alpha + K_v cos\alpha sin^2\alpha \tag{1.1}$$

Where the total lift is decomposed into a potential-lift and a vortex-lift term, scaled by the K_p and K_v coefficients respectively and calculated by means of potential and lifting-surface theories.

1.2.2 Vortex Stages and Development

A leading-edge vortex is dependent on several aspects, ranging from the flow condition to the aerodynamic geometry. The vortex flow can be characterized by means of its swirl number, typology (jet vs wake) and stability. The swirl number is defined as the ratio between the axial fluxes of angular and axial momentum. Therefore, it determines how strong a vortex is swirling. Moreover, a vortex flow related to a delta wing can be identified by means of the geometrical characteristics of the aerodynamic geometry. In this sense, the leading geometry plays an important role as well as the leading-edge sweep, the angles of attack and the sideslip angle. These are the main parameters which influence the vortex flow development above a delta wing. The influence of compressibility effects is quantified by the Mach number. The Reynolds number refers to the turbulence state of the flow and hence the vortex separation position, the cross-section of the secondary vortex as well as the wake region. The other flow and geometrical variables may also have an influence which is usually of secondary importance but due to the non-linearity and complexity of the phenomenon may acquire significance.

Firstly, the leading-edge shape plays an important role in the definition of the first separation onset of the vortex [14]. Commonly, the leading-edge shape can be classified with regard to its roundness, starting from the inferior extreme of having a sharp edge, i.e. zero radius. A sharp or relatively small leading-edge radius results in a fixed separation position of the vortical structure at the apex of the wing, which makes the dependence of the separation onset on the flow condition negligible. Therefore, a fixed separation onset removes a degree of complexity from the vortex system. As the leading-edge radius increases, the sensitivity of the separation onset on the flow condition increases. In this sense, the angle of attack and sweep angle play also a major role in influencing the separation onset: by increasing the angle of attack or decreasing the sweep angle the separation onset moves upstream. The onset of the boundary layer transition of the separating flow is sensitive to the Reynolds number[12]. With this regard, as Re increases the transition onset of the boundary layer from laminar to turbulent regime moves upwards. The state of the boundary layer is visible with an oil flow visualization thechnique applied on the vortex dominated surface. The transition position is indicated by the presence of an offset of the secondary attachment line which moves closer to the leading edge as soon as the boundary layer regime turns into turbulent. This is due to the fluid dynamic property of a turbulent boundary layer which employs an enhanced separation resistance towards adverse pressure gradient. The dependence of the transition onset is linearly dependent on the Re number, in this sense a Re defined with a length scale equal to the transition onset x_t is constant, as Hummel experimental investigation reports [9].

Normally, the leading-edge shape does not influence the breakdown of the vortex. However, as reported by Huang [15], if its shape has a large size relative to the wing size, it may affect the resulting flow by modifing the effective angle of attack.

After having isolated the effect of the leading-edge shape and curvature, it is reasonable to proceed by considering the parameters with the most direct influence on the vortex development. These are the planform sweep angle and the angle of attack of the flow relative to the planform. The vortex structure can be identified under different forms or stages along an envelope of cases which include the leading-edge curvature, sweep angle and angle of attack. Through this analysis, it is important to remind that the influence of an increase in angle of attack is usually comparable to a decrease in sweep angle [9], at a first order of comparison. Hence, this is especially valid for small variations.

Starting from very low angles of attack, a vortex develops already along the entire leading-edge extension if this is sharp or the curvature is relatively high whereas for more

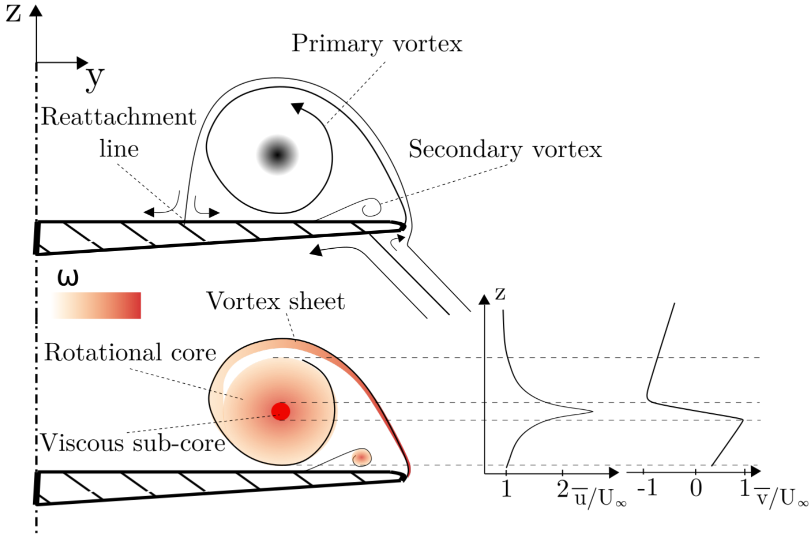

Figure 1.3: Schematic representation of the separation of a vortex in a cross-flow plane including the qualitative distribution of the vorticity, the axial and the tangential velocities.

rounded leading edges the flow is able to follow the edge contour and remains attached (I) (Fig. 1.4). At this condition of incipient separation [14] along the whole leading edge, the cross-flow C_P distribution has a minimum in proximity of the leading edge. A narrow separation is present which does not include a rotational structure. The streamtraces are divided due to the unbalance between flow inertia and the pressure gradient in the span direction. The C_P level decreases following the leading-edge length, without reaching a critical and unstable condition. However, by increasing the angle of attack the flow is not able to remain attached and it separates at an outboard position along the leading edge, resulting in a partially developed vortex stage (II). The C_P level at the leading-edge reaches a minimum just slightly ahead of the vortex separation. In this location, the streamtraces that diverge from the incipient separation location upstream reconverge at the leading edge [14]. After the initial separation, the onset progressively moves upstream with an increase of the incidence angle until it reaches the wing apex and a fully developed vortex is achieved (III). In other words, the critical C_P level along the leading edge, which permits the vortex separation, moves upstream with an increase of the angle of attack [1]. The same effect is experienced by the change to a larger sweep angle. For sharp leading edges, a fully developed stage is present from the angle of initial vortex separation. After the vortex has reached a fully developed condition, the axis of the vortex moves further inboard as the angle of attack is increased until it stops reaching a fixed position (IV). Meanwhile, the vortex axis also moves further away from the wing surface [1]. Hence, the cross-section of the vortical structure progressively increases. For this reason, in case of particularly slender wings, the vortices of the two sides can start to interact with each other and generate an asymmetry in their evolution [16, 17]. What happens next is of extraordinary importance for the aerodynamic characteristics of delta wings since it abruptly changes the vortex flow. A further increase in the angle of attack causes an instability or critical condition, referred to as vortex breakdown [18, 19, 20]. This phenomenon starts to take place at the wing's trailing edge which is commonly referred to as the angle of attack of initial breakdown. This stage is called a fully developed vortex with breakdown (V) (Fig. 1.4). Afterwards, the breakdown location moves progressively upstream with the angle of attack [16, 19, 21, 22]. Eventually the breakdown location reaches the wing apex and a condition of periodic vortex shedding [17] and stall is encountered (VI). The stall behavior and the flow shedding changes further with the angle of attack.

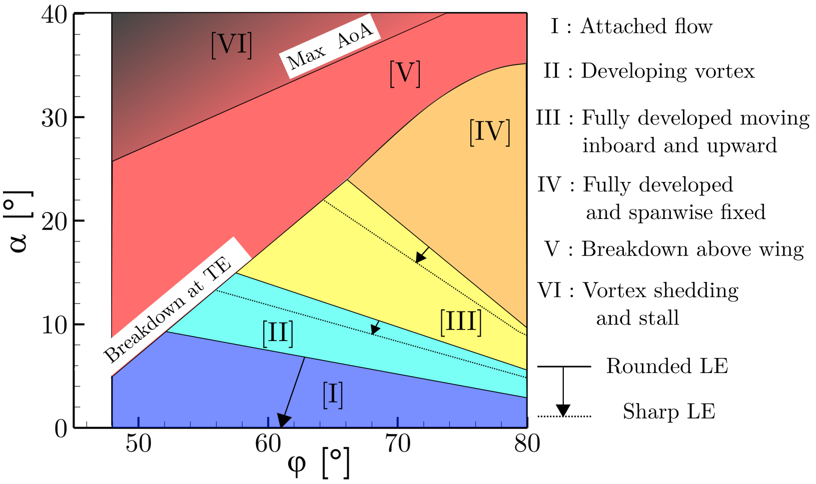

Figure 1.4: Description of the development stages of a leading-edge vortex flow in the parametric space of the angle of attack and the sweep angle [1].

1.2.2.1 Vortex Breakdown

The vortex breakdown phenomenon is crucial for the aircraft stability as it can rapidly occurr and move chordwise as a consequence of even small angle-of-attack and sideslip-angle variations. Moreover, the vortex breakdown depends on the wing sweep angle [22, 17] which, other than variable-sweep aircraft, is usually a fixed geometrical feature of a wing planform. With similar flow and geometrical parameters, the variation of the sweep angle corresponds to a modification of the dimension and stability of the vortical structure: a higher sweep angle causes a more stable vortex and a downstream movement of the vortex breakdown location. The dependence of the vortex breakdown on the sweep angle is comparable with a sideslip-angle variation because the apparent sweep angle that the two wings experience correspond to an offset from the geometrical sweep angle equal to the sideslip angle [20]. In fact, the windward side encounters the flow at a lower sweep angle and the opposite for the leeward side. This results correspondingly in a downstream and an upstream breakdown position displacement. The suction footprints change, resulting in a visible variation of the rolling moment. The $C_{Mx_{\beta}}$ is usually difficult to predict and usually leads to large deviations between numerical simulations and experimental data.

The angle of attack of initial breakdown (Fig. 1.5), i.e. the angle at which breakdown takes place over the trailing edge, changes significantly between different sweep angles of the wing planform [16]. For this reason, moderate to high sweep angles are favourable to delay breakdown and to reduce supersonic wave drag. When a low sweep angle is employed, generally a high sweep strake is applied in order to generate a more stable vortex. A non slender delta wing is not commonly utilized stand alone. Ol and Gharib [22] compared the vortex structure of a 50° swept delta wing with one of 65° sweep angle. The experimental analysis confirmed the presence of the offset of the vortex development stages to lower angles of attack for a lower sweep angle. Additionally, the unburst portion of the vortex changes with high angles of attack. The slender wing maintains the classic jet type vortex with a definite peak of the vorticity and axial velocity in the vortex core whereas the non-slender wing fails to maintain such characteristics. This confirms that the sweep angle variation has additional influence over the vortex type and flow evolution and it is only qualitatively comparable to the angle of attack variation with respect to the vortex stage.

The breakdown position and type can be influenced by different factors. As reported by Lambourne and Bryer [18], the total pressure in the core and the adverse gradient of pressure in the direction of the vortex axis are relevant for the position of the breakdown [1]. Moreover, they have identified the breakdown phenomenon with three characteristics: the abrupt axial deceleration, the sudden switch of the flow to a spiral movement and the generation of a large-scale turbulence in a wake-like flow. Many theories have tried to explain such phenomenon either as an instability or a critical state of the balance between the external axial adverse pressure gradient, the swirl value of the rotational core and the flow divergence amount [23]. The Reynolds number instead has a low influence with regard to the breakdown position whereas the deflection of a trailing-edge flap moves the breakdown position as consequence of the adverse pressure gradient variation. Therefore, a deflection upwards results in a movement upstream of the vortex breakdown and the other way around for a downwards deflection [18]. Vortex breakdown can behave in two different manners, e.g. with a spiral or bubble form, in accordance with the geometrical and flow conditions (Fig. 1.6, 1.7). The two forms of breakdown are considered the two extremes of a continouos series of conditions which depend on the Reynolds number [20]. Whereas a spiral breakdown shape corresponds to a high Reynolds number, a bubble type relates to a low Reynolds number flow [1]. The delta wing reported by Visbal [8] in his work generates a spiral type breakdown with a region of axial reversal flow. It employs a sweep angle of 75° at a Reynolds number of $9.2 \cdot 10^3$ based on the wing chord. At such low Reynolds number, the employment of a turbulence model loses significance, therefore the simulations can be performed as laminar reducing at minimum the discrepancies that are only related to the numerical discretization. This serves as an additional proof of how the major contribution to the large discrepancies of such vortex dominated flows in the framework of RANS simulations is the modeling of turbulence. During the study of Visbal, it was found that

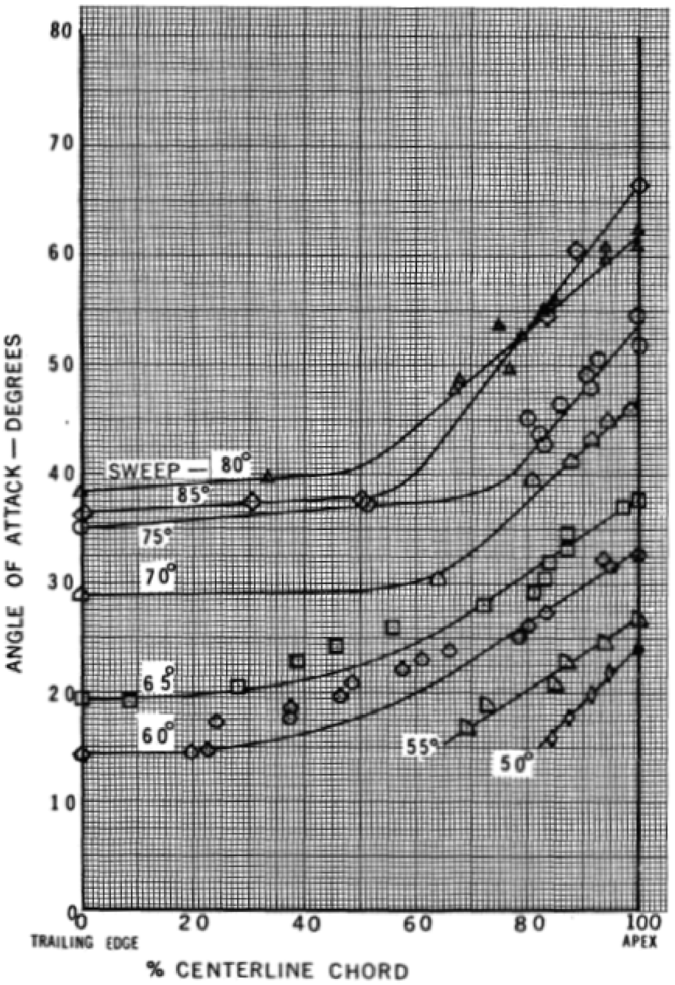

Figure 1.5: Vortex breakdown position relative to the wing chord for different angles of attack and sweep angles of a flat delta wing [16].

the interaction of the spiral structure with the wing promoted surface pressure fluctuations. It has also been shown how the vorticity contour along cross-flow planes changes drastically across the breakdown as the rotational structure is dissipated and the highly rotating core disappears (Fig. 1.8). A bubble-like breakdown is characterized by an oval recirculation zone after a stagnation point along the vortex axis. The bubble type is also referred to as an axisymmetric mode breakdown [20]. The vortex breakdown is an unsteady phenomenon [20]. Its position oscillates around a mean position at relatively high frequencies (Fig. 1.9). Therefore, even if the Reynolds number has low influence on the vortex stage and breakdown, it does influence the unsteadiness of the flow and its time-dependent behavior, e.g. the frequency and size of breakdown location oscillation or the typology of the wake type flow downstream of bursting. Harvey [24] investigated

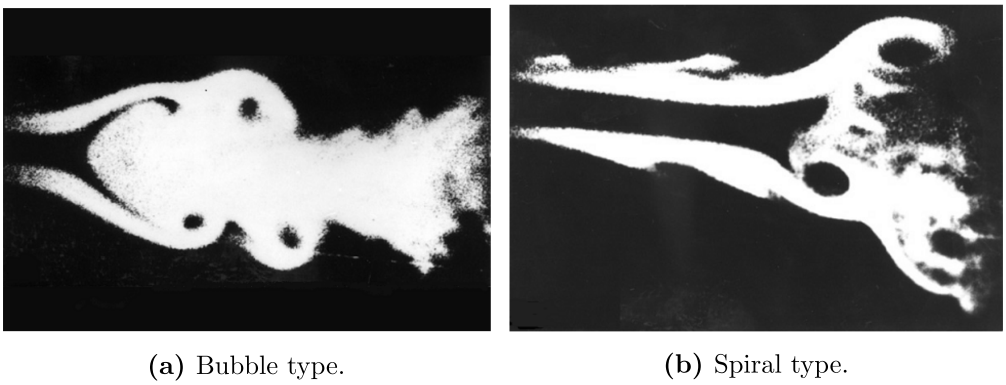

(a) Bubble type. **(b)** Spiral type.

Figure 1.6: Smoke visualization of a the vortex breakdown for a delta wing with $\varphi = 76°$ at $AoA = 40°$ [20].

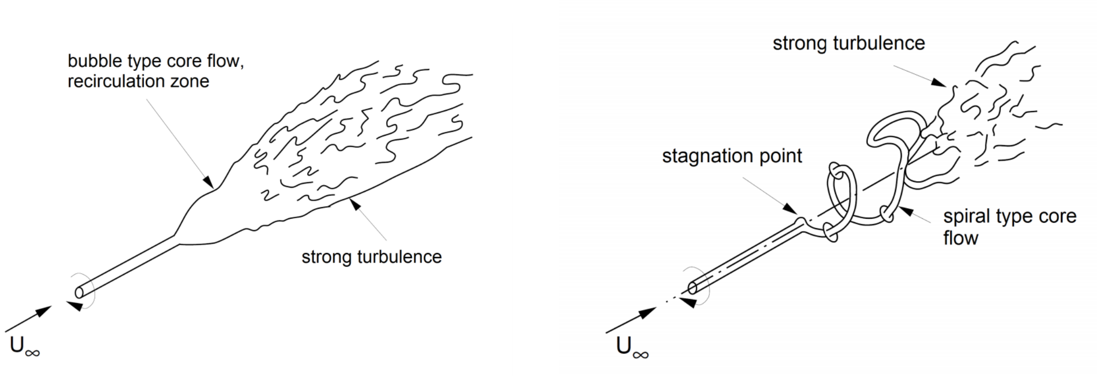

Figure 1.7: Representation of a bubble (left) and a spyral (right) type of vortex breakdown [1].

the dependence of the vortex breakdown in a tunnel on its swirl angle. He pointed out how in this experiment the breakdown appeared to be the critical flow condition intermediate between a jet type vortex and a wake type vortex. Same conclusions where derived from other wind tunnel measurements [20]. It was visualized as a bubble of reversed flow. A jet type vortex corresponds to the condition of having an axial core velocity larger than the free-stream speed whereas the opposite is valid for a wake-type vortex. An increase in the swirl of the flow acts similarly to a larger adverse pressure gradient, displacing breakdown upstream [20, 23]. The vorticity generated at the leading edge is transported by convection and diffusion through the vortex sheet into the core region where it is a dominating flow variable. The two transport mechanisms are defined by means of scales whose ratio is of the order of $1/Re^{0.5}$. From experimental data it is visualized that the rate of expansion of the leading-edge vortex is much larger than the ratio value. For this reason, between the two transport mechanisms, the large-scale vortex is dominated by the convection which is largely independent of the Reynolds number [23]. However, diffusion of vorticity becomes important with regards to phenomena at

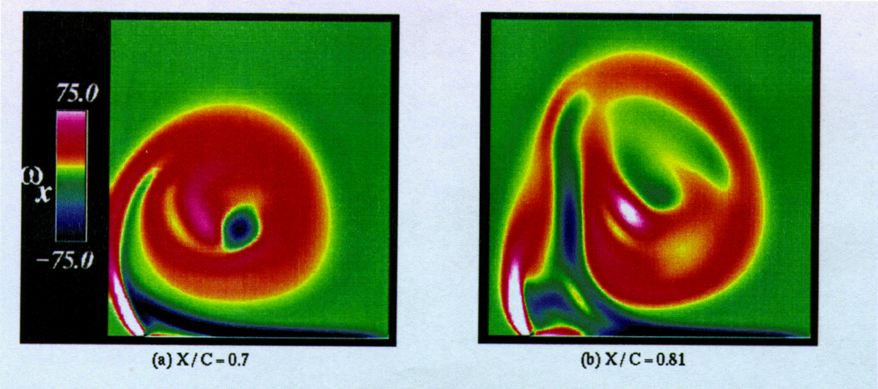

Figure 1.8: Contour of the axial vorticity on two crossflow planes downstream of breakdown at the coordinates of $x/c_r = [0.7, 0.81]$ of the vortex flow around a delta wing with $\varphi = 75°$ at $M = 0.2$ and $AoA = 34°$ [8].

a smaller scale such as the inner spiral structure of the vortex, the viscous sub-core or the post-breakdown chaotic wake. Therefore, the Reynolds number is relatable to the typology of breakdown and the flow characteristics downstream of it, but only in relation with small scale structures. The viscous sub-core is usually very small, around 3-5% of the vortex diameter and, inside of it, very high axial velocities can appear. Erickson also reports how the effect of turbulence or a simulation with a high constant eddy viscosity have the effect to reduce the radius of the central core due to the higher diffusivity [23].

The vorticity quantity relates proportionally to the increasing strength of the vortex and in relation to the breakdown the quantity increases along the development axis until it reaches a maximum before breakdown (Fig. 1.9). Corresponding to the breakdown position, an abrupt decrease of the vorticity takes place [25]. Even more abrupt is the change of the integrated helicity distribution through the breakdown. The helicity quantity, which is the dot product between the vorticity and velocity axis, relates properly with a structured vortex region.

1.2.2.2 Vortex Interactions

High performance aircraft regularly experience the presence of multiple vortical structures which may also interact and merge. Planforms employ compositions of different portions of the main wing, divided into a strake and an aft wing portion where the two different leading-edge sweep angles cause the separation of two vortices of different development stages. Moreover, the presence of the control surfaces, i.e. horizontal stabilizers or canard wings, provoke the generation of additional vortices. Additional vortices separate with the presence of deployed leading-edge slats or flaps which generate a geometrical discontinuity and a local angle of attack difference which invokes vortices of different types above the main wing. Whereas horizontal surfaces downstream of the main wing have no interaction on other vortical structures or flow features, vortices separating on canard wings or at a deployed slat influence, interact and/or merge with

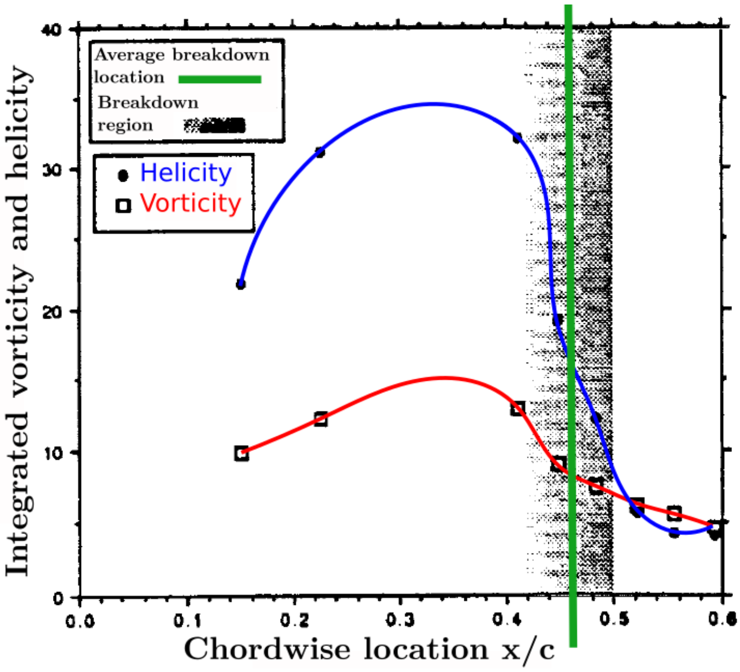

Figure 1.9: Chordiwse distribution of the integrated vorticty and helicity in relation to the breakdown position from the data gathered by Ivanski [11, 25].

the main wing vortex depending on the flow condition. Moreover, vortices are regularly present above the fuselage and may interact with the wing flow. In the case of particularly rounded leading-edge geometries, the separation of multiple vortices might take place at different positions along the leading edge. Complexity is added when different vortices separate around the wing planform and their separation onsets are not fixed. In this scenario, further dependence on β is introduced as the separation position may be dependent on it as well. For all of the mentioned cases one concept is clear, the complexity of the multi-vortical flow increases drastically as they interact and merge, hence introducing cross-dependencies in their evolution.

In the case of a double-delta- or multi-delta-configuration a corresponding number of primary vortices and secondary structures separate at the different leading-edge sweeps. With the wing having several sweep angles, the generated vortical structures represent different evolution stages. With respect to a straked double-delta wing, depending on the size of the strake wing compared to the main wing it is expected that the evolution of the vortex-vortex interaction changes progressively with the angle of attack [1]. Starting at low angles of incidence the vortices show almost no interaction. The first vortex is, however, inherently influenced by the geometrical presence of the aft wing because downstream of the kink the rotational sheet separating at the leading edge transports momentum exclusively to the second vortex. The inboard vortex then reduces its rotational strength as consequence of viscous effects and it is pushed outward by the outer vortex which is developing due to the vorticity fed into its structure. The vortices rotate in the same direction, therefore they tend to rotate around each other. The interaction strength increases as the angle of attack rises as consequence of the cross-sectional increase of the vortices [26] and eventually the inner vortex merges into the outboard vortex. By further increasing the angle of attack, the merging position moves upstream until it reaches the kink position between the two portions of the wing. The position of the kink influences the development of the multiple vortex system. When the kink is shifted upstream, the phenomena of interaction and merging move to larger angles of attack. The dependencies for such phenomena correlate also to the presence of different sweep angles which change the strength of the rollling sheet feeding the vortical flow. A parameter that is easily associated with these phenomena is the kink angle $\Delta\varphi$, i.e. the difference between the strake and the aft wing sweep angles (Fig. 1.10). Whereas for a null kink angle, which corresponds to a single strake wing, there is only one vortex, with increasing aft wing sweep the interaction starts to take place from the highest angles of attack. The angle of attack at which the breakdown of the merged vortices takes place reduces with $\Delta\varphi$, as the sweep angle of the outer vortex provokes a less stable vortex. For very large kink angles, the breakdown of the outer vortex starts to take place at angles of attack smaller than the angle at which the vortices merge. On the contrary, for very large $\Delta\varphi$, the vortices stay far apart until the breakdown phenomenon takes place for both structures and, therefore, they do not experience close interaction or merging. In a middle region, however, the breakdown of the outer vortex may take place while the merge position is moving upstream. In this region, the highest complexity of the flow is experienced because different cross dependencies may occurr depending on the angle of attack, kink angle and the sweep angles. Whereas at small angles of attack the behavior is similar to the high angles of kink, where the breakdown occurs before any other phenomenon happens, as the incidence angle increases, the breakdown of the outer vortex may be delayed by the stabilizing effect of the inner vortex. In general, the employment of multiple vortical flows on the same case increases the complexity of the physical understanding and therefore the prediction of the aerodynamic behavior s. This effect lines up in concordance with the difficulties of numerical methodologies or physical modeling, such as turbulence models, to solve the enhanced complexity maintaining a constant grade of accuracy.

1.2.3 Compressibility Effects

An additional fluid dynamics characteristic which interacts with the evolution and development of vortex flows is the compressibility of the flow. Until this section, for the sake of clarity and a step-wise explanation, such effects have not been introduced in the phenomenology description. However, compressibility is relevant for high performance aircraft whose flight envelope includes for large portions high subsonic, transonic and supersonic regimes. In these conditions, compressibility has a first effect on how the vortex stability and structure is. The vortex manifests a more flattened structure closer to the wing surface [27]. A flatter suction distribution follows as the wing area interacting with the vortex is more extended. Moreover, in the case of a transonic or supersonic regime shock waves may occurr above the wing and drastically influence the vortex flow.

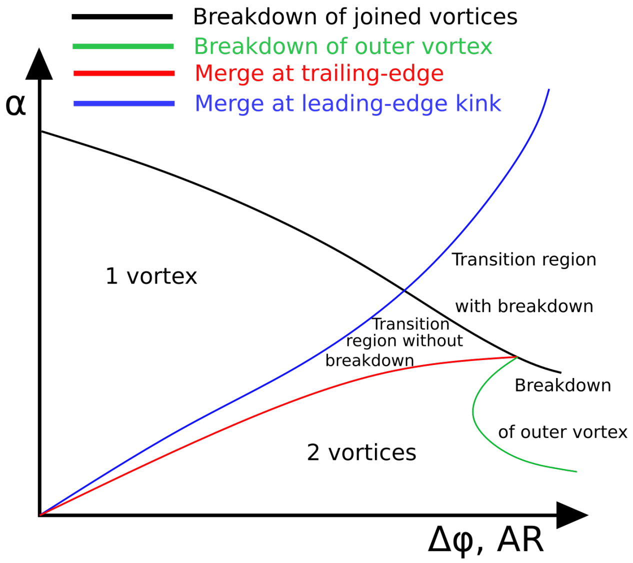

Figure 1.10: Qualitative sketch of the development of vortices over double-delta wings depending on the features: leading-edge kink angle $\Delta\varphi$ and angle of attack α [26].

Concentrating at first on a supersonic flow regime, if we define the normal angle of attack α_N and the normal Mach number M_N as their values normal to the leading-edge shape, it is possible to draft a sketch of the different vortex-shock interacting stages along a reasonable envelope [28] (Fig. 1.11). A clear distinction feature is the vertical line at $M_N = 1$ which identifies the transition from a subsonic to a supersonic leading edge. For supersonic leading edges a shock wave is always present. For a low normal angle of attack a vortex separation (B) is present above the wing with no secondary structure or shock. By increasing α_N at constant compressibility condition, the flow turns into a classical vortex with no schock (A) [28]. When the angle of attack increases even further a shock wave takes place above the vortex region (C). Since it lays above the vortex, it has no direct aerodynamic interaction with the wing upper surface.

For supersonic leading edges, the actual vortex separation takes place more inboard compared to subsonic cases. Starting back from the lower left corner of the graph and now following a variation along the M_N axis, the bubble eventually disappear leaving space to a shock above the wing surface with no separation (D). The flow follows a supersonic expansion around the leading edge and, moving inboard, it encounters the shock. At this point, if the angle of attack is relatively small, no separation is induced or encountered by the weak shock which is just responsible for deflecting the flow. As α_N rises, the shock increases its strength until it induces a bubble-like separation (E). This separation appear as a small bubble inboard of the shock. Consequently, for a further increase of the incidence angle, the bubble increases in size and the shock wave moves above the separated flow (F). However, the influence of the shock on the wing surface is now significant and evident from experimental investigations.

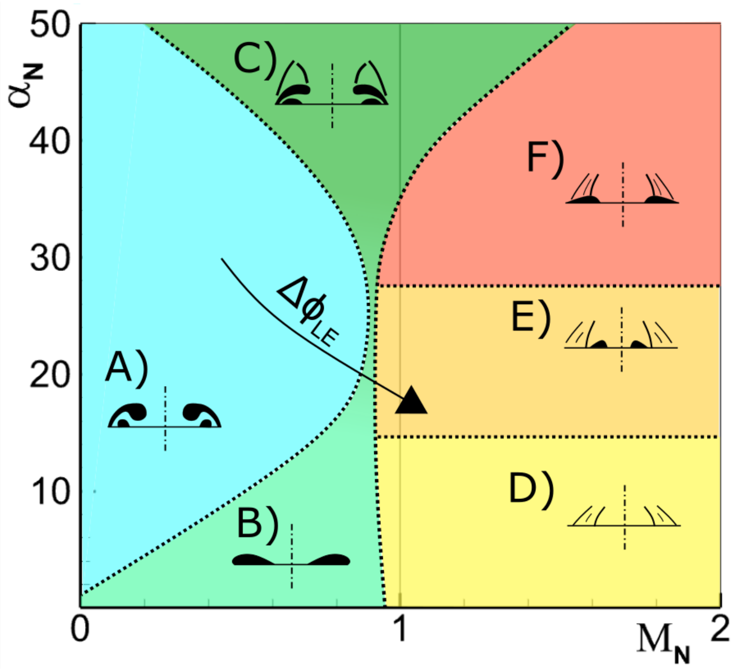

Figure 1.11: Map of the vortex-shock interaction stages along the parametric variations of the normal angle of attack α_N, the normal mach number M_N and the leading-edge sweep angle φ_{LE} [28].

The leading-edge sweep is also important for the classification of the shock-vortex interaction stages. Furthermore, its value directly influences the formulation of the normal components of α_N and M_N. As illustrated qualitatively in Figure 1.11, a variation of the leading-edge sweep value corresponds approximately to a linear curve with negative slope. Hence, an increase of the φ_{LE} corresponds to a delay of a supersonic condition to take place at the leading edge and it provides a variation similar to a reduction of α_N and M_N.

The flow phenomenology for a supersonic regime is however less complex than a transonic one. In such cases, multiple shock-waves and vortex-shock interactions develop in the high angle-of-attack region of the envelope [27]. At high angles of attack a shock wave takes place above the vortex sheet and this shock wave causes abrupt changes of the cross-flow velocities. Moreover, at a transonic regime the turning of the flow above the highly swept wing causes the occurrence of compression waves which eventually collapse into a shock wave. This phenomnenon may happen in concurrence with the leading-edge vortex and they can intersect. The interaction between vortex and shock wave causes a degeneration of the organized vortical structure into a breakdown condition. However, a fundamental question may be posed about the causality of these two phenomena with regard to their position above the wing. Hence, is the vortex breakdown and instability setting the position of the shock or is the shock wave high gradient of pressure and discontinuity which triggers the vortex breakdown? Although the question initiates interesting investigations about the phenomenon, the proposed research is equally valid and it is sufficient to identify a co-existence of shock and breakdown onset. An increase of the angle of attack causes the displacement of the shock wave / vortex burst occurrence to move upstream. The effect is consistent with the movement of the breakdown position at subsonic conditions. If the angle of attack is fixed, instead, the breakdown position changes with Mach number in different ways according to different wind tunnel measurements. With respect to the experiments performed by Erickson [27] the breakdown position moves downstream. However, Wendt [29] refers that an opposite effect is evident from his experimental data. This suggests that the dependence of such flow features to the compressibility level may include cross-dependences from other characteristics of the geometry or flow conditions. In general, the interaction between schock waves and vortex flows offers additional complexity and non-linearities of the dominating parameters.

1.2.4 Additional Geometrical Variation and Effects

Geometrical variations span within a large range of cases starting from the parameters discussed above, like sweep angle or leading-edge radius, down to the introduction of control surfaces or additional aerodynamic devices. With respect to control surfaces, the highest relevance for the current research is dedicated to the ones that more directly or abruptly interact with the development of the dominant vortical structures over the wing. In this respect, the evaluation of the downstream interference of aerodynamic devices is of high interest. Whereas a trailing-edge flap or a vertical tail may have an effect on the vortex development above the wing by means of the rear pressure variation, hence causing a difference of the adverse pressure gradient, the most significant influences are evident for control surfaces acting on the flow upstream of the main wing, e.g. canard fore-planes, leading-edge slats, strakes or leading-edge extensions. The presence of underwing stores, such as external fuel tanks or landing gear enclosures, may influence the vortex flow field as their type, size and mounting position may introduce important disturbances in the flow upstream of the wing leading edge. In particular, if the nose of the element is positioned upstream of the wing's leading edge, the downstream effect is more drastic. This effect clearly increases furthermore with the aircraft angle of attack. Therefore, they can influence the separation onset, type and development of the main wing vortices. Moreover, the number of vortex separations may increase if the flow separating from the store reattaches the flow at the leading edge, suppressing the vortex coming from inboard. Several combinations of stores of different type and size form a relevant portion of an aerodynamic database of a high manueavrable aircraft. It is of high importance to correctly understand the flow physics and the aerodynamic effects of such variations and to develop numerical tools, which are able to predict with the highest possible accuracy such complex flow cases.

1.2.4.1 Leading-edge Slat Deployment

A leading-edge slat is a control surface device which is deployed at the wing's leading edge in order to increase the incidence of the incipient flow separation and augmenting the maximal C_L and angle of attack. By reducing the intensity of the high suction peak on the wing, it is able to postpone the angle of attack of first separation [6]. The leading-edge slat is part of the category of high-lift devices which are applied to an aircraft in order to enhance the maximum lift available for particular flight conditions such as landing and take off. Similarly, TE devices increase the lift with the additional effect that stall occurrs at lower angles of attack than LE devices, which is particularly relevant for highly swept wings at high speed [5]. With respect to a highly swept wing, the deployed leading-edge flap clearly directly influences the development of the vortical structure above the main wing since the leading edge is the origin of the vortex sheet separation [30]. As a primary effect it is possible to correlate a leading-edge surface deflection or deployment with a change of the local angle of attack which, as mentioned previously in this section, has a major impact on the stability, strength and evolution of the vortex. As a main effect, the lower angle of attack locally causes a delay of the vortex flow stages, hence it postpones the separation and improves the wing efficiency [31]. At slat deflection for low and moderate angles of attack, the vortex development stage is anticipated and it appears to be stronger and less stable [30]. The vortex generated on the leading-edge slat or flap generates a suction on its surface which has a thrust component due to its deflection relative to the main wing. Therefore, the efficiency of the platform is improved [31, 32]. The increase of the angle of attack causes the vortex to move inboard. This results in the vortical structure to overcome the hinge-line and expand above the main wing. The chord of the control surface cannot be increased indefinetly since it is limited by structural and aerodynamic considerations. Occasionally, the leading-edge slat is not encaved from the complete leading-edge extension but it can start instead at a certain spanwise position. This results in having a main vortex which separates at the fixed wing apex and, downstream, a second vortex which originates from the leading-edge device deployment. Hence, multiple vortices are generated. Cross-dependencies between the two vortices are introduced which increase the complexity of predicting the physical flow development. The influence of a leading-edge flap on the vortex flow field at transonic regimes for a generic 55° swept delta wing has been target of the experimental investigation performed by Erickson [27]. In the transonic regime, the leading-edge upwash generated by the flap causes a reduction of the vortex size and its strength above the control surface (Fig. 1.12). This means that the increased thrust component is reduced progressively with the Mach number. Moreover, a smaller vortex on the flap surface promotes a separation of the wing vortex at the hingeline further downstream. A similar mechanism has been described previously as dependent on the angle of attack and the strength of the vortex. Therefore, it is possible to correlate the influences and to state that an increase in Mach number or an increase in angle of attack promote a movement upstream of the hingeline separation.

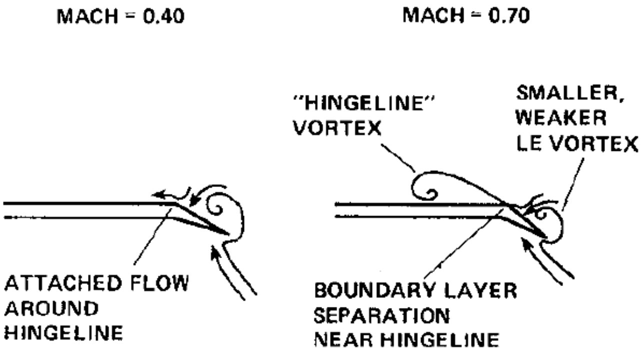

Figure 1.12: Schematic representation of a vortex flow structure in a cross-plane section of a delta wing with a deployed leading-edge device for low and high-subsonic speeds [27].

1.2.4.2 Control Surfaces

Whereas tailplanes have lower impact on the vortex flow field on the main wing, foreplanes, e.g. canard surfaces, have a certain grade of downwash effect on the main wing which depends on their relative positions, shapes and areas [33, 6]. Therefore, with respect to the target of this research, foreplanes are representative of a higher interest due to the possibile flow variation introduced by their deployment. However, with the same mechanism, the quality of the flow which encounters tail planes and, therefore, their effectivity, is influenced drastically by the main wing downwash. Hence, the lack of accuracy in predicting the main wing flow results in a detrimental accuracy of the tail plane effectivity downstream which is of high relevance during the design of aircraft. This is also valid for vertical planes.

A canard has a large influence on the wing for low vertical positions and high canard deflections [33]. The vortex breakdown above the canard surface is delayed due to the acceleration and stabylizing effect provided by the wing flow. However, in the case the canard vortex flow reaches breakdown, its effectivity is reduced. The effect of the canard downwash flow on the main wing consists of a delay of the vortex development stage due to the local reduction of the effective angle of attack. Hence the maximum C_L is increased by a delta-canard configuration.

It is evident how the complexity of the vortex flow is consistently increased by the presence of such interferences between different vortex flows and downwashes. Hence the difficulty for numerical tools to provide a proper prediction is likewise increased.

1.3 Outline of the Thesis

In conclusion, the investigation of vortex dominated flows demonstrates a series of dependencies to the flow condition and geometrical features which suggest that such flow cases may be classified in accordance to a series of parameters that describe their structure and development stage. From this aspect, a good practice is therefore to find a parametric space where the state-of-the-art knowledge of the phenomenon can provide the research with a clear view of which dependency is obvious and more trivial, which introduces complexities and which is eventually less significant or comparable to another parameter variation. For this reason, the evaluation of the available state-of-the-art knowledge about leading-edge vortices has been reported in this section to evaluate, justify and found the basis for the formulation and construction of the methodologies present in this research work.

The thesis is structured in the following way. It permits to follow the research progress along its timeline and grasp the knowledge accumulated along the process. The introduction of this first chapter (Chap. 1) works as fundament of the resarch as the main motivations are expressed along with the state-of-the-art knowledge of the target fluid dynamic flow features which are large-scale leading-edge vortices. Their phyisical nature is described from the basics to the most challenging applications. In the second chapter (Chap. 2), the governing equations of the numerical methodologies employed for the computational fluid dynamics simulations are described. Therefore, the problem of closure of the Navier-Stokes equations is introduced which is the fundamental issue set as target of the current research work. The closure is substituted with a series of different turbulence models and the most commonly used in the context of aerodynamic devices is described at the beginning of the third chapter (Chap. 3). This is selected as the baseline turbulence model which constitutes the starting point of the methodologies developed along this work. In order to set up the starting point and the direction to follow for the research, the state of the art of the numerical simulations of the target aerodynamic cases (Sec 3.2) and of the turbulence modeling improvement (Sec 3.3) are successively reported. From there, the formulation of the model extension and the automatic calibration procedure are described along the physical motivations behind them (Sec 3.4). In order to extend the predictive capability and modeling potential some extensions of the methodology are also described (Sec. 3.5). The results are reported in the fourth chapter (Chap. 4) for a number of test cases. They are reported in aggregations to highlight their vicinity in clusters in the parametric space which describe their geometry and flow conditions. The lesson learned, results summary and outlook are reported in the conclusive chapter (Chap. 5).

2 Governing Equations in Fluid Dynamics

2.1 Navier-Stokes Equations

The scientific representation of a physical problem is modeled by means of mathematical equations which are formulated with the underlying physics of the targeted phenomenon as fundament. In the context of fluid dynamics, the Navier-Stokes equations are used to describe the evolution of a continuum viscous fluid over time and space. The fluid is assumed to be a continuum as the interactions at a molecular level are considered insignificant at a fluid dynamic macroscopic level. The equations describe the conservation of mass, momentum and energy and they consist of a set of non-linear Partial Differential Equations (PDE). The variables employed in the equations eventually necessitate of a thermodynamic state correlation to close the system and represent the pressure in relation with other quantities. Under the assumption of an ideal gas, which is regularly accurate for external aerodynamic problems, the $p = \rho RT$ relation is valid, with R being the gas constant.

2.2 Conservation Equations

A PDE which describes the conservation of a scalar field β can be generalized in its integral conservative form as follows.

$$\frac{d}{dt}\int_{\Omega} \beta d\Omega + \int_{\partial\Omega} \beta \mathbf{V} \cdot \mathbf{n} dS = \int_{\partial\Omega} \chi \nabla\beta \cdot \mathbf{n} dS + \int_{\Omega} Q d\Omega \tag{2.1}$$

This integral form is composed by a series of terms that reflect the physical behavior which they describe. The first term describes the rate of change of the conserved quantity β inside the considered control volume. This change is balanced by the remainig part of the terms which corresponds to three different phenomena. The second term on the LHS represents the convection of the conserved quantity by means of the velocity $\mathbf{V}$ through the boundary $\partial\Omega$ of the control volume Ω. On the RHS, the first term is the surface integral of the diffusion of β by means of the correspondent transport coefficient χ. The last term corresponds to the source or sink terms of β inside the control volume. The integral form can be consequently applied for the three physical quantities to be conserved in a fluid dynamic system and from them derive their differential form combining them into a system of PDE 2.2, written with the tensorial Einstein's notation.

$$
\begin{aligned}
\frac{\partial \rho}{\partial t} + \frac{\partial}{\partial x_j}\left[\rho u_j\right] &= 0 \\
\frac{\partial(\rho u_i)}{\partial t} + \frac{\partial}{\partial x_j}\left[\rho u_i u_j\right] &= \frac{\partial}{\partial x_j}\left[-p\delta_{ij} + \tau_{ji}\right] \\
\frac{\partial(\rho e_0)}{\partial t} + \frac{\partial}{\partial x_j}\left[\rho u_j e_0\right] &= \frac{\partial}{\partial x_j}\left[u_j p + q_j - u_i \tau_{ij}\right]
\end{aligned}
\tag{2.2}
$$

The fluid used in the present work is exclusively air, treated as an ideal gas, for which the heat capacity ratio quantity $\kappa = c_p/c_v$ is equal to 1.4 and the gas constant is $R = 287.058\frac{J}{KgK}$. It is a Newtonian fluid, therefore the shear stress τ is linearly proportional to the deformation of the fluid element, which is the velocity gradient corresponding to the shear stress direction. Such proportionality is described by the coefficient of molecular viscosity or laminar viscosity. The Newton's concept is extended to a 3-dimensional fluid domain by means of the Stokes relation which states that:

$$
\tau_{ij} = \mu_l \left(\frac{\partial u_i}{\partial x_j} + \frac{\partial u_j}{\partial x_i} - \frac{2}{3}\delta_{ij}\frac{\partial u_k}{\partial x_k} \right) \tag{2.3}
$$

The laminar viscosity, due to the variations in temperature for the flow fields of interest, is assumed to change with the fluid temperature according to the Sutherland's law:

$$
\mu_l = \mu_{lref}\left(\frac{T}{T_{ref}}\right)^{3/2} \frac{T_{ref} + T_S}{T + T_S} \tag{2.4}
$$

Where T_{ref} is an arbitrary reference temperature, in the present work is set to 273 K while μ_l to $1.716e-05$ m^2/s. The Sutherland temperature T_S equals 110.4 K. The heat-flux q is defined by the Fourier's law:

$$
q_j = -c_p \frac{\mu}{Pr}\frac{\partial T}{\partial x_j} \tag{2.5}
$$

With the Prandtl number describing the rate between the kinematical diffusivity and the thermical diffusivity, defined as:

$$
Pr = \frac{c_p \mu_l}{k} \tag{2.6}
$$

Where k is the thermical conductivity and the internal energy is $e = c_v T$, whereas the total energy is defined as $e_0 = e + \frac{u_k u_k}{2}$. The Navier-Stokes equations with the listed assumptions form a set of partial differential equations which are finalized by the setup of proper boundary conditions and solvable by means of numerical methods.

2.3 Reynolds and Favre Averaged Navier-Stokes Equations

The Navier-Stokes equations are formally able to solve the instantaneous state of a fluid dynamic system. However, the non-linearity of the equations associated with a high

Reynolds number promote the generation of a very chaotic solution, which is referred to as turbulent flow. In such situation, the chaotic scales from the largest to the smallest influence the state of chaos and turbulence. For this reason, a model that solve down to the smallest scale of case would be necessary to solve the instantaneous solution. To avoid such an extremely computationally expensive numerical procedure, most common turbulence models base their formulation on an average over time of the equations and the fluid dynamic state. In such a way, the chaotic fluctuations are modeled while the average flow is directly solved.

There are two common procedures to average the equations: the Reynolds averaging and the Favre averaging. The Reynolds Averaged Navier-Stokes (RANS) equations base their formulation on a time averaging method:

$$\overline{\Phi} = \frac{1}{t_f} \int_{t_f} \Phi(t) dt \tag{2.7}$$

Where $\bar{\Phi}$ is the averaged quantity, which is also defined as the difference between the instantaneous Φ and the fluctuation Φ'.

$$\overline{\Phi} = \Phi - \Phi' \tag{2.8}$$

The RANS formulation is accurate with respect to fluid at incompressible conditions due to its assumption that the density does not oscillate. However, when a relatively high Mach number is achieved, the compressibility effects are significant. Therefore, the Favre averaging is employed which consists of a density weighted time averaging:

$$\widetilde{\Phi} = \frac{\overline{\rho \Phi}}{\overline{\rho}} \tag{2.9}$$

$$\widetilde{\Phi} = \Phi - \Phi'' \tag{2.10}$$

It is important to notice that the average of the Reynolds fluctuations equals zero, this does not apply to the Favre fluctuations. With regard of the CFD applications, it is common to use a Reynolds-average for the density and pressure variables, while employing the Favre-averaging for the other quantities. Therefore, the following equations are obtained:

$$\begin{aligned}
\frac{\partial \overline{\rho}}{\partial t} + \frac{\partial}{\partial x_j} \left[\overline{\rho} \widetilde{u_j} \right] &= 0 \\
\frac{\partial (\overline{\rho} \widetilde{u_i})}{\partial t} + \frac{\partial}{\partial x_j} \left[\overline{\rho} \widetilde{u_i} \widetilde{u_j} \right] &= \frac{\partial}{\partial x_j} \left[-\overline{p} \delta_{ij} + \overline{\rho u_i'' u_j''} - \overline{\tau_{ji}} \right] \\
\frac{\partial (\overline{\rho} \widetilde{e_0})}{\partial t} + \frac{\partial}{\partial x_j} \left[\overline{\rho} \widetilde{u_j} \widetilde{e_0} \right] &= \frac{\partial}{\partial x_j} \left[\widetilde{u_j} \overline{p} + \overline{u_j'' p} + \overline{\rho u_j'' e_0''} + \overline{q_j} - \overline{u_i \tau_{ij}} \right]
\end{aligned} \tag{2.11}$$

Where $\widetilde{e_0}$ is the density averaged total energy:

$$\widetilde{e_0} = \widetilde{e} + \frac{\widetilde{u_k} \widetilde{u_k}}{2} + k \tag{2.12}$$

And k the turbulent kinetic energy:

$$k = \frac{\widetilde{u''_k u''_k}}{2} \tag{2.13}$$

The equations are solvable for the variables $\overline{\rho}$, $\widetilde{u_i}$ and $\widetilde{e_0}$. In such a way, an open set of PDE is obtained and some terms remain open and necessitate for further correlations to close the system.

Boussinesq Assumption The set of equations (Eq. 2.3) which describe the fluid dynamic behavior of a flow can be closed with a complicated process, but a fundamental assumption is introduced in the context of eddy-viscosity turbulence models which is the Boussinesq assumption. Such assumption states that the Reynolds stresses $\overline{\rho u''_i u''_j}$ are linearly proportional to the velocity gradient, similarly to the Stokes' relation for the shear stress.

However, differently from the molecular viscosity, which is a propriety of the fluid defined by a constitutive relation, the turbulent stresses are proportional by means of a turbulent viscosity μ_t, also called eddy viscosity which is a variable of the flow. It follows that:

$$\tau^t_{ij} = -\overline{\rho u''_i u''_j} \approx 2\mu_t \widetilde{S_{ij}} - \frac{2}{3}\overline{\rho} k \delta_{ij} \tag{2.14}$$

The turbulent stresses τ^t_{ij} can now be summed to laminar stresses τ^l_{ij} resulting in the total stress τ^{tot}_{ij}. By means of the Boussinesq assumption and other reasonable neglections valid for most industrially relevant flows, the equations are rewritten as follows:

$$\begin{aligned}
\frac{\partial \overline{\rho}}{\partial t} + \frac{\partial}{\partial x_j}\left[\overline{\rho}\widetilde{u_j}\right] &= 0 \\
\frac{\partial (\overline{\rho}\widetilde{u_i})}{\partial t} + \frac{\partial}{\partial x_j}\left[\overline{\rho}\widetilde{u_i}\widetilde{u_j}\right] &= \frac{\partial}{\partial x_j}\left[-\overline{p}\delta_{ij} - \widetilde{\tau^{tot}_{ij}}\right] \\
\frac{\partial (\overline{\rho}\widetilde{e_0})}{\partial t} + \frac{\partial}{\partial x_j}\left[\overline{\rho}\widetilde{u_j}\widetilde{e_0}\right] &= \frac{\partial}{\partial x_j}\left[\widetilde{u_j}\overline{p} + \widetilde{q^{tot}_j} - \widetilde{u_i}\widetilde{\tau^{tot}_{ij}}\right]
\end{aligned} \tag{2.15}$$

The equations can now be closed by means of a model which provides the value of μ_t as a variable of the flow. This is the task of the turbulence model.

2.4 The Modeling of Turbulent Flows

A turbulent flow employs a high content of fluctuations and a chaotic behavior where a constant transfer of energy between the mean flow to the fluctuating flow is present. The difference to a laminar flow is the capability of dissipating any disturbance. This distinction is related to the value of the Reynolds number which, in fact, quantifies the ratio between the advection and the diffusion mommentum fluxes, i.e. the ratio between the inertia effects and the viscous effects. The occurrence of a disturbance can be described as the variation of one or more quantities of the flow due to a discontinuity in the geometry or the fluid variables. When the Reynolds number is low, relatively to the class of flow, the high viscous diffusive behavior which dominates the inertial transfer of momentum rapidly diffuse the disturbance and it does not spread or grow. Otherwise, in the case of a turbulent flow, the Reynolds number is high, therefore the inertia dominates the propagation of the disturbance.

To identify how a disturbance grows from an imperturbated flow, we need to start from the equations that describe a laminar flow. The instantaneous equations are decomposed into a turbulent fluctuating portion and a mean portion which now corresponds to a laminar condition, where the Reynolds stresses vanish. Under this assumption the equation of the fluctuations respond linearly to a newly introduced disturbance. This is called the Linear Fluid Dynamic Stability Theory. Such theory is only valid at the very first stage of the disturbance propagation. As soon as the disturbance effect is not infinitesimal anymore, the non-linear terms acquire significance and they are not negligible. From that point on, the propagation of the fluctuations spread rapidly with a non-linear behavior and cross-interacting with each other leading to a highly complex system where time-dependent turbulent structures and diffusive mixing phenomena intersecate along a broad range of length and time scales.

2.4.1 Kolmogorov Hypothesis and Energy Cascade

The following hypothesis and ideas which are commonly referred to for idealizing turbulent flows are well established if a turbulent flow with a high Reynolds number is considered. The flow is determined by a flow length scale $\mathcal{L}$ and velocity $\mathcal{U}$. Richardson (1922) describes a turbulent flow as decomposed in a series of eddies with varying size l_e and speed u_e which interact between each other. From such quantities, a third eddy time-scale can also be defined dimensionally with $\tau_e \approx \frac{l_e}{u_e}$. Kolmogorov starts from this description and formulate a series of hypothesis which determines the behavior of turbulence. Eddies are defined as a turbulent motion which is moderately coherent in a region of scale l_e.

According to the energy cascade, turbulent eddies follow an inviscid cascade process from the largest scales where they are generated by the energy injected from the mean flow and where the viscous effect is insignificant. The large eddies are unstable and break up into smaller ones. This phenomenon is repeated progressively until the cascade process reaches the smallest scales where the turbulence energy is disssipated into heat. Here, the eddies are stable and the viscosity becomes predominant over the inertial transfer of momentum.

The energy cascade idea of Richardson describes the process but the Kolmogorov hypotheses (1941) answer to some important questions related to the quantification of the length scales values, proportion or dependencies between each other or the flow characteristics.

The first hypotheses describes the local isotropy of turbulence. It states that that for "sufficiently high Reynolds number, the small-scale turbulent motions are statistically isotropic". The idea is that the anisotropy present at the largest scale is lost during the energy cascade towards the smallest scales.

By losing the complete information of the large scale flow at the smallest scales, it follows that the statistical characteristics of the small-scale flow is universal. Hence, it does not depend on the large scale flow it is originated from.

The energy which is injected at the largest scale is conserved along the different scales and Kolmogorov assume, with the first similarity hypothesis, that the turbulent eddies depend exclusively on the viscosity ν and the dissipation rate of the turbulent kinetic energy ε. The Reynolds number at the smallest scale is approximately 1 which confirms the appearance of the dissipation significance. The smallest eddy's speed u_η depend, hence, on these two quantities as it can be determined by a dimensional analysis:

$$u_\eta \sim (\nu\varepsilon)^{1/4} \tag{2.16}$$

Therefore, smaller eddies have lower speed and turbulence intensity. The time scale is also derived by a dimensional analysis:

$$\tau_\eta \sim (\nu/\varepsilon)^{1/2} \tag{2.17}$$

And for the length scale η:

$$\eta \sim (\nu^3/\varepsilon)^{1/4} \tag{2.18}$$

Considering now a flow domain experiencing turbulence, the largest scale of the domain can be defined as proportional to the flow length scale $\mathcal{L}$ while the minimum length scale is the scale at which the viscosity corresponds to the diffusion of turbulent momentum. Hence:

$$\nu \sim \varepsilon^{1/3}\eta^{4/3} \tag{2.19}$$

Therefore the length scale ratio between maximal and minimal scales is:

$$\frac{\mathcal{L}}{\eta} \sim \left(\frac{\mathcal{U}^3\mathcal{L}^3}{\nu^3}\right)^{1/4} = Re^{3/4} \tag{2.20}$$

Where $\varepsilon \sim \mathcal{U}^3/\mathcal{L}$ and $\nu \sim \mathcal{U}^2/\mathcal{L}$. With a similar analysis it can be found the ratio between the maximal and minimal speed:

$$\frac{\mathcal{U}}{u_\eta} \sim Re^{1/4} \tag{2.21}$$

And time scale:

$$\frac{\tau_\mathcal{L}}{\tau_\eta} \sim Re^{1/2} \tag{2.22}$$

The second similarity hypothesis states that the middle scales along the cascade between the flow scale and the Kolmgorov scales are uniquely determined by ε while being independent of ν. Here the Reynolds number is large enough to avoid high influence of the viscid dissipation effect.

2.4.1.1 Energy Spectrum

The spectrum analysis is performed to evaluate the energy density $E(k)$ based on a wavenumber k space. The $E(k)$ is the turbulent kinetic energy per unit of mass of the eddies which lies in the wavenumber interval between k and $k + dk$.

The energy function depends on the eddy length scale which can be evaluated dimensionally with the wave number k and the energy dissipation rate ε [34, 35].

$$E(k) \sim \varepsilon^{2/3} k^{-5/3} \tag{2.23}$$

Therefore the function follows a dependence of a $-5/3$ exponentiation along the wavenumber (Fig. 2.1).

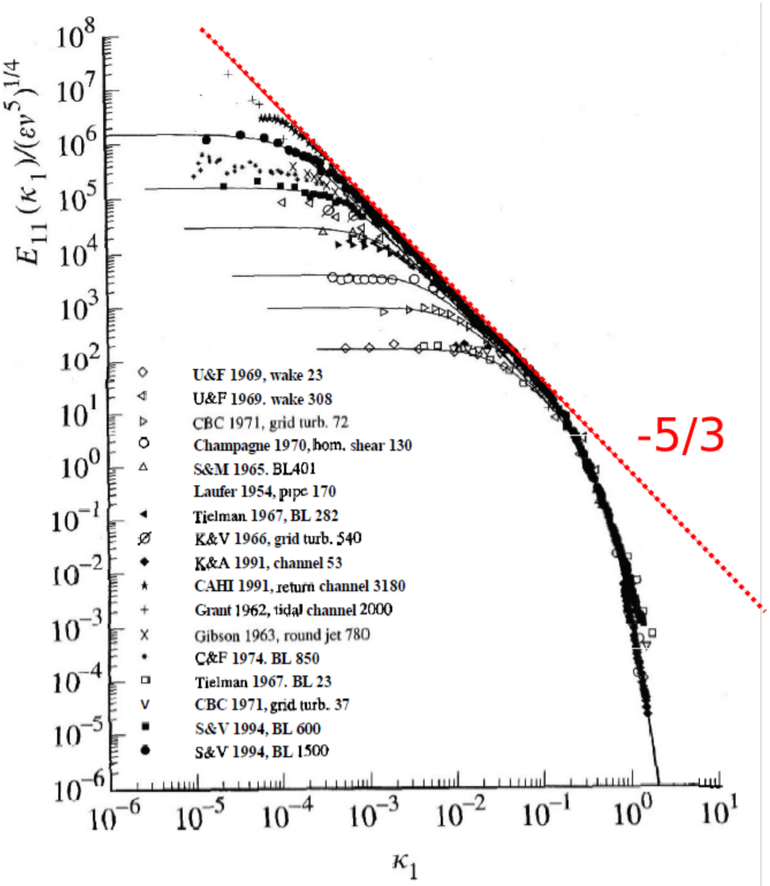

Figure 2.1: Measurements of one-dimensional velocity sprectra (symbols) and model spectra for different Reynolds numbers [34]. The experimental data are taken from Saddoughi and Veeravalli [35].

2.4.1.2 Considerations about the Computational Cost

The Richardson energy cascade idea and the Kolmogorov hypothesis establish the important relations that lie between the largest and the smallest scales for a turbulent flow as well as the dependencies of the difference quantities that dominate such phenomena. The ratio between maximal and minimal scales provide also an estimation of the computational power that is necessary to simulate deterministically a turbulent flow. As seen in Eq. 2.20, 2.21 and 2.22, the scale ratios are dependent on the Reynolds number.

With regard to a turbulent flow simulation, the equations are solved for the 3-dimensional and time-dependent velocities $\mathbf{u}(\mathbf{x}, t)$ describing the full range of turbulence scales. This is the case of a Direct Numerical Simulation (DNS). Taking into account the dependences of the length-scale and time-scale to the Reynolds number we can evaluate the computational cost. The spatial discretization along 3 dimension has to be fine enough to include the smallest turbulent scale. Therefore, the number of grid points for every direction scales with $Re^{3/4}$ (Eq. 2.20). For three dimensions, hence, the number of spatial discretization points $N_{\Delta x}$ scales with $Re^{9/4}$. The time discretization has to be performed with an explicit method due to the extremely large memory requirement. Therefore, the time step Δt is limited by a Courant number smaller than one:

$$C = \frac{u' \Delta t}{\Delta x} < 1 \tag{2.24}$$

and the number of time steps of the considered simulation time T:

$$N_{\Delta t} \sim \frac{T}{\Delta t} \sim \frac{T}{\Delta x / u'} \sim \frac{T}{L/u'} Re^{3/4} \tag{2.25}$$

By combining the spatial and time discretization, the computational cost of a DNS simulation is proportional to Re^3 which makes such methodology applicable only for a small set of cases at low Reynolds number with simple geometries and small domains.

Moving gradually to less computationally expensive methodologies, the Large Eddy Simulation (LES) method is the successive step where only the filtered component of the velocity $\overline{\mathbf{u}}(\mathbf{x}, t)$ at the larger scales is solved directly while a model is introduced for the smaller scales. The idea is to avoid the majority of the DNS computational effort which lies at the smallest dissipative motions which are isotropic and universal. Therefore, the direct solution is constrained to the larger scales which are anisotropic and dependent on the geometry and flow conditions. The advantage with regard to the computational cost is significant compared to DNS. However, it remains prohibitve for the application to large numbers of industrially relevant applications, especially for wall-bounded flows such as aerodynamic applications, and its costs are around 2 orders of magnitude more than the application of a Reynolds-Stress Model (RSM).

With regard to the approaches related to the solution of RANS equations, the turbulence modeling methods are subdivided into two categories. The first are the turbulent-viscosity models which consist of models that provide the eddy viscosity quantity related to the flow field quantities. It can be either in an algebraic manner or by employing one or more transport equations. The second family consists of the modeling of the Reynolds stresses by means of dedicated transport equations, in such a way, that there is no need of an eddy viscosity quantity but they introduce additional complexity, computational costs and often related to additional numerical instabilities. In the context of this research, the objective is to improve RANS eddy viscosity models with the integration of additional flow related terms and the employment of information derived from experimental data.

3 Methodology Description

In the following chapter, the enhancement of the turbulence model for vortex dominated flows is described starting from the baseline turbulence model, addressing the state of the art of turbulence modeling modifications and finally illustrating the proposed methodology along with its possible extensions. The motivations and objectives of the research are reported in parallel to the description in order to justify the steps and choices in the modeling approach as well as for the calibration procedure.

3.1 Baseline Turbulence Model: Spalart-Allmaras

As mentioned in Section 2.4.1.2, the major part of the numerical simulations of aerodynamic and fluid dynamic problems are performed with RANS models due to the good balance between accuracy, computational cost and numerical stability [36]. In this context, different RANS models have been formulated and developed along the years, acquiring different communities of users and favourable applications [37]. The complexity of turbulence, its highly chaotic nature and nonlinear physical behavior are inherent of industrial and academic relevant flow types. Different types of turbulence models have been formulated with an empiric content by targeting a class of flows, starting from fundamental ones [38]. It is often complicated to completely agree about which turbulence model is the most suitable because this choice is highly dependent on the target flow case. External aerodynamic problems are routinely solved by employing eddy viscosity models, where the Spalart-Allmaras (SA) model [39] has shown proper accuracy and predictive capabilities with regard to attached flows. The SA model is also applied to separated and rotational flows, such as the vortices that dominate delta wings. However, as the separation or vortical flows create complex flow scenarios, the model may lose its predictive capability whereas it maintains proper grades of accuracy for the regions of attached flow. For the reason of high efficient computations, the SA model is chosen as baseline for the development of the methodology.

3.1.1 Baseline Model

The Spalart-Allmaras eddy viscosity turbulence model [39] consists of a single transport equation of the eddy viscosity quantity ν_t. The model has been introduced with aerodynamic flows as specific targets and by formulating a transport equation composed of different blocks which represent the physical phenomena that balance out inside a wall-bounded turbulent flow. The objective was to have a numerically stable, locally valid, Galilean invariant model. The locality of the model permits to evaluate ν_t in a point without depending on the solution at other points of the domain. This provides a great advantage for the application of the model to unstructured grids. The SA model has shown robust behavior with regard to the definition of wall and free-stream boundary conditions. The convergence rate, stability and accuracy for attached or mild separated flows has been confirmed along the several applications and the model is still extensively used for modern numerical investigations.

3.1.1.1 Free Shear Flows

The eddy viscosity ν_t expresses the linear relationship $-\overline{u_i u_j} = \nu_t S_{ij}$ between the Reynolds stresses and the strain-rate tensor $S_{ij} = (\partial u_i/\partial x_j + \partial u_j/\partial x_i)/2$ as stated by the Boussinesq assumption (Sec. 2.3). The k term is neglected differently from some two-equations models. The material derivate of ν_t on the LHS of the equation is balanced with the RHS terms, which are added progressively to a preliminar formulation for free-shear flows introducing single additional phenomena. Starting from a free-shear flow, the RHS is composed of a production and a diffusion term. The scalar ν_t needs to be coupled with a scalar norm S that provides a suitable evaluation of the deformation tensor $\partial u_i/\partial x_j$. Meanwhile, the norm has to be an invariant value. The vorticity norm ω has been used in the original formulation because, in the target applications, turbulence is mostly present where vorticity is dominant. Strain rate or the norm of the whole tensor could also be used with no difference. The ω will be indicated as S for consistence with the original formulation. Therefore, the production term of the baseline formulation is $c_{b1} S \nu_t$.

The diffusion term is based on the spatial derivative of ν_t and formulated with the operator $\nabla \cdot ((\nu_t/\sigma)\nabla \nu_t)$ where σ is the Prandtl number. It is important to notice that this term is not conservative which is a characteristic that is traditionally admitted in turbulence modeling even if not favourable. The diffusion term is hence completed with the form $\frac{1}{\sigma}\left[\nabla \cdot ((\nu + \tilde{\nu})\nabla \tilde{\nu}) + c_{b2}(\nabla \tilde{\nu})^2\right]$ in order to provide a conservative property to the quantity $\nu_t^{1+c_{b2}}$. This first version of the model is therefore valid for free shear flows.

$$\frac{D\nu_t}{Dt} = c_{b1} S \nu_t + \frac{1}{\sigma}\left[\nabla \cdot (\nu_t \nabla \nu_t) + c_{b2}(\nabla \nu_t)^2\right]. \tag{3.1}$$

3.1.1.2 Wall Destruction

With the introduction of a wall, its effect is felt through the boundary layer by means of a term which has a destruction effect on the Reynolds shear stress. This effect relates to the distance from the wall d and a wall destruction term $-c_{w1}(\nu_t/d)^2$ is introduced. The term has no influence in free-shear flows where the distance tends to infinite. Consequently, the destruction term tends to zero. In such a way, the wall-destruction term does not alter the calibration of the model at the previous formulation step which is valid for free-shear flows. Applications of the model have returned an accurate reproduction of the log-layer region of a boundary layer, while returning too low skin-friction coefficients over a flat-plate flow. In order to overcome this limitation, a non-dimensional smoothing function f_ω is multiplied to the destruction factor. The function is based on a dimensionless mixing length definition.

$$r = \frac{\nu_t}{S\kappa^2 d^2} \tag{3.2}$$

The function f_ω is formulated in order to have a value of 1 in the log layer.

$$f_\omega(r) = g\left[\frac{1 + c_{\omega 3}^6}{g^6 + c_{\omega 3}^6}\right]^{\frac{1}{6}}, \qquad g = r + c_{\omega 2}(r^6 - r) \tag{3.3}$$

In addition, Spalart and Allmaras [39] addressed the modeling of the buffer and viscous sublayer. The modified eddy viscosity $\tilde{\nu}$ is introduced which is equal to ν_t except in the viscous region. Therefore, a smoothing function f_{v1} is introduced in order to have an eddy viscosity equal to $\kappa y u_\tau$ both in log and buffer layer.

$$\nu_t = \tilde{\nu} f_{v1}, \qquad f_{v1} = \frac{\chi^3}{\chi^3 + c_{v1}^3} \tag{3.4}$$

Where

$$\chi = \tilde{\nu}/\nu. \tag{3.5}$$

The production term needs a smoothing function f_{v2} in order to maintain a proper behavior through the different stages of the boundary layer. In this sense, S is substituted with $\tilde{S}$ with the objective to maintain its log-layer dependence as $\tilde{S} = u_\tau/(\kappa y)$.

$$\tilde{S} = S + \frac{\tilde{\nu}}{\kappa^2 d^2} f_{v2}, \qquad f_{v2} = 1 - \frac{\chi}{1 + \chi f_{v1}} \tag{3.6}$$

The final step in the turbulence model formulation addresses the treatment of laminar and transition regions. However, the tripping term responsible for transition is not reported here because the research concentrates on fully turbulent cases and the model is more often used for such applications [40]. The addition which takes into account laminar regions is formulated to make $\tilde{\nu} = 0$ a stable solution of the model equation. It is assumed that in a laminar region $\tilde{\nu}$ shall be of order of ν at most. Therefore, the production term is multiplied with $1 - f_{t2}$ and the destruction term is balanced consequently, with:

$$f_{t2} = c_{t3} exp(-c_{t4}\chi^2) \tag{3.7}$$

In the end, all the reported steps result in the following turbulence model formulation.

$$\frac{D\tilde{\nu}}{Dt} = c_{b1}\tilde{S}(1 - f_{t2})\tilde{\nu} + \frac{1}{\sigma}\left[\nabla \cdot ((\nu + \tilde{\nu})\nabla\tilde{\nu}) + c_{b2}(\nabla\tilde{\nu})^2\right] - (c_{w1} f_w - \frac{c_{b1}}{\kappa^2} f_{t2})\left[\frac{\tilde{\nu}}{d}\right]^2. \tag{3.8}$$

With

$$\begin{aligned} &c_{b1} = 0.1355 \qquad \sigma = \frac{2}{3} \qquad c_{b2} = 0.622 \qquad \kappa = 0.41 \\ &c_{w1} = \frac{c_{b1}}{\kappa^2} + \frac{1 + c_{b2}}{\sigma} \qquad c_{w2} = 0.3 \qquad c_{w3} = 2.0 \qquad c_{v1} = 7.1 \\ &c_{t3} = 1.1 \qquad c_{t4} = 0.5 \end{aligned} \tag{3.9}$$

The model has been extensively used in the community of external aerodynamic flows, in particular, with regard to attached flow conditions where the model expresses its best performance in terms of accuracy due to its formulation and calibration procedure. The model also manifests suitable numerical stability and robustness. Moreover, the model shows low dependence or critical outcomes with respect to the initial and freestream conditions. The ideal value at the freestream would be zero, but routinely a value largely smaller than μ is used to overcome possible problems in the solver where round-off errors or dividing by $\tilde{\nu}$ is employed along the model implementation in the solver code.

3.1.2 Edwards modification

The modification by Edwards and Chandra [41] consists of a variation of the model formulation and calibration procedure for the viscous sublayer. The main differences are related to the modeling of the strain-rate norm in the near-wall region, where it acquires the form of:

$$\tilde{S} = \overline{S}^{\frac{1}{2}} \left[(1/\chi) + f_{v1} \right] \tag{3.10}$$

Here S is not the vorticity norm but the strain rate. Moreover, the argument that takes into account the wall-blockage effect is differently defined.

$$r = \frac{\tilde{\nu}}{\kappa^2 d^2 \overline{S}} \tag{3.11}$$

The modified formulation permits to improve the convergence behavior of the solver which presents an oscillatory trend in the residuals after an initial rapid decrease with the baseline formulation. The Edwards-Chandra modification returns a smooth and more rapid convergence whereas the accuracy is conserved in the near-wall region.

3.2 State of the Art: the Numerical Simulation of Vortex Dominated Flows

The numerical simulation of vortex dominated flows is routinely performed by means of RANS simulations employing an eddy-viscosity linear turbulence model [42]. The advantages provided by such a class of turbulence models are the numerical stability, the proper grade of accuracy for flows close to the calibration targets and the affordable computational effort [36]. These qualities make it a common choice for the generation of large datasets where a sustainable computational cost is an important requirement. Moreover, the numerical stability offers the possibility to implement automatic toolchains for the handling of the simulation without the need of expedients for monitoring the stability into detail. The focus of this research is the accuracy with respect to complicated classes of flows such as vortex dominated flows. For the solution of such flow cases, traditional eddy-viscosity models exhibit the largest deficiencies due to the physical assumption underneath. It is important to notice and mention that, at the state of the art, there are other classes of turbulence models which need to be compared in order to identify the advantages or disadvantages of this research. More complicated turbulence models such as scale hybrid LES-RANS models have the advantage to provide an higher grade of accuracy. However, the computational cost increases significantly as the spectrum of resolved scales increases. The employment of Large Eddy Simulations (LES) or Detached Eddy Simulations (DES) are, at the state of the art, confined to the investigation of details of a class of flow for a relatively small number of cases and, mostly, at an academic level of investigation. In an industrial framework or when a large dataset needs to be produced, the RANS models are still employed for the major part of the cases.

With respect to vortex dominated flows, the lack of accuracy of its numerical solution can be evaluated as an error with the experimental data, which can be the aerodynamic coefficients, the flow field velocities and/or the surface pressure distribution. As the vortex increases its intensity with respect to rotational level and instability, hence when the angle of attack of the considered wing increases, the discrepancies grows. This is particularly true with respect to the position and type of the breakdown instability as it consists of a complex and highly turbulent flow.

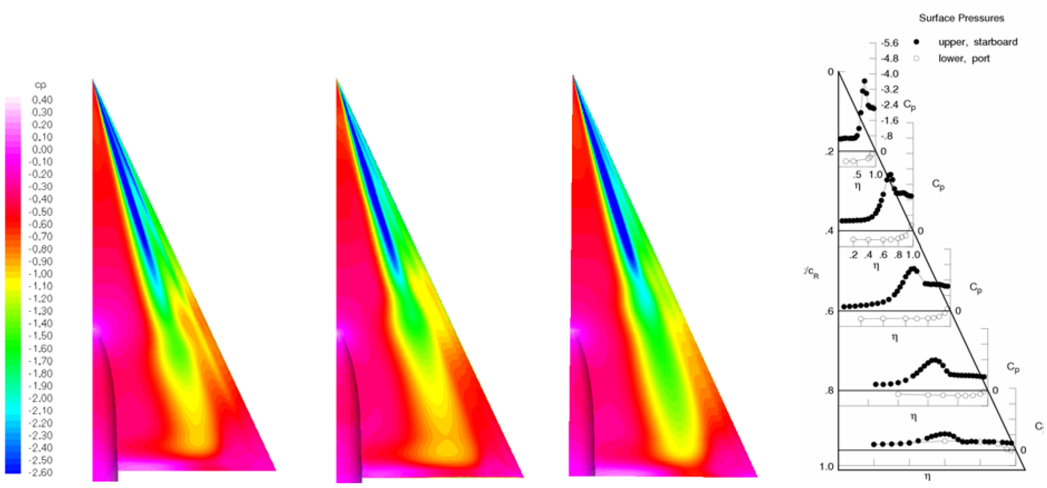

EADS (Structured) **KTH (Unstructured)** **NLR (Structured)** **NASA (Experiment)**

Figure 3.1: Pressure distribution on the upper surface of the VFE-2 configuration with a sharp leading edge at $M = 0.40$, $AoA = 18°$ and $Re = 6x10^6$. Comparison between different partner contributions and the experimental data. Simulation comparisons reported by Fritz and Cummings [43].

3.2.1 Second Vortex Flow Experiment

An important source of information about the state of the art of numerical simulations of vortex flows is the Second Vortex Flow Experiment (VFE-2) where the best common practices of academies, research establishments and industries of international relevance have been applied to the same wing geometry [43]. Different aspects of the vortex development phases have been included in this research: from the separation onset along a rounded leading edge at low angles of attack, covering the range of fully developed and bursting vortices to post-stall conditions. With regard to the separation onset, discrepancies were found from the experimental data and the results appear to be sensitive mostly to the turbulence model as well as the computational grid refinement when a drastically coarse level is employed. The effect of the Reynolds number acquires importance when it is low enough to require turbulence transition models and this has a relevant impact on the correct prediction of the separation onset. However, the focus of the current research is dedicated to fully turbulent cases where the Reynolds number effects are small [43]. Differences from the experimental data were even more evident with respect to the breakdown position and vortex development by increasing the angle of attack for different numerical grids, turbulence model definitions and also solver implementations. This suggests how the main source of error is related to the Boussinesq assumption which is at the fundament of all the turbulence models employed. The breakdown onset is located upstream compared to the available experimental data which relates to the turbulence models providing a wider vorex core and a more unstable condition (Fig. 3.1). At transonic conditions [43, 44], the main discrepancies are again located at the breakdown strength and position which is strictly related to the shock position above the wing upper surface. The shock wave coincides with the vortex transition into a chaotic wake flow. The application of DES and Delayed DES (DDES) models provides the possibility to investigate with more details the effect of the small scales of turbulence to the vortex flow [45]. It is accompanied by a significant increase of the computational costs, complexity of the numerical simulation setup to achieve stable solutions, with a properly refined mesh and suitable settings. Moreover, this does not guarantee that the numerical solution is in a better agreement with the experimental data [45].

3.2.2 Cranked Arrow Wing Aerodynamic Project International

A community of experts collaborated in the context of the Cranked Arrow Wing Aerodynamic Project International (CAWAPI) where the flight test data provided for the F-16XL experimental aircraft are employed as validation data for the numerical investigations [46, 47]. In the CAWAPI project, the performance of different turbulence models has been evaluated. The sensitivity to the turbulence modeling appears to be important for capturing details of the vortex development, in particular, with respect to the breakdown position and type at high angles of attack. Another lack of accuracy is evident at transonic conditions where a proper prediction of the vortex-shock interaction is not achieved. The mesh refinement is also important but its effect reduces after a certain grade of refinement is reached [48], similarly to the findings of the VFE-2 project. Grid adaptation employing different refinement algorithms exhibits advantages for improving the solution's accuracy with regard to the average level of error with the surface pressure distribution. However, the features with larger discrepancies, e.g. vortex-shock-breakdown interactions, show low sensitivity to the numerical grid type or further refinement. These features are also not significantly improved by using RSM or hybrid RANS-LES turbulence models [49, 50]. In the proximity of such flow features, which are highly unsteady, the employment of Unsteady RANS (URANS), i.e. time resolved, computations produce noticeable differences of the numerical solution compared to steady RANS simulations. Reynolds Stress Models (RSM) are also employed and show that additional details can be derived from their numerical solution. However, in some occasions, no improvement is noticeable compared to eddy viscosity models. Furthermore, it is reported that, at low angles of attack, no improvement is brought by the employment of DES models as well as the activation of the available rotation corrections for the eddy viscosity models. It is shown how the deflection of control surfaces may introduce discrepancies with the experimental data whereas the reference zero-control configuration has an higher grade of accuracy. This is related to the introduction of separations or stronger adverse gradients of pressure which have a destabilizing effect on the vortex flow. In the end, a best practice approach is found with respect to the assessment of a proper numerical grid convergence whereas for turbulence modeling it appears that no turbulence model is the best for all the flow conditions and control surfaces variations [46]. Hitzel [51, 52, 53] investigated the performance of the available numerical tools for the subsonic and transonic cases at high angles of attack showing how the mesh sensitivity after a certain grade of refinement is “negligible” [54] compared to the turbulence modeling issues. The application of different turbulence models, included a Scale-Adaptive Simulation (SAS) approach, exhibits here only small variations. The pressure distribution is overall in reasonable agreement with the flight test data and the main discrepancies are located in the proximity of vortex breakdown. However, the SAS model introduces complexity in the numerical setup but it shows higher capability to capture the unsteady behavior as well as the breakdown locations. Park and al. [55] and Hitzel [56] reported results where the application of a DES or DDES model improve the accuracy level obtained for regions like breakdown and the precision in capturing the right suction level and size of the vortex. Lofthouse and Cummings [57], during a similar investigation, describe a similar improvement with DES models but also the application of a rotation correction to the eddy viscosity SA model provides a comparable improvement, at least with regards to the average surface pressure distribution. In general, an important input for the application of computational fluid dynamics to this kind of aerodynamic applications remains the user’s experience and a certain preliminar phase for assessing the sensitivity of the solution on the turbulence model by testing different formulations and associated modifications.

3.2.3 AVT-161 and AVT-201 Task Groups: SACCON and X-31

In the context of the NATO RTO Task Group AVT-161 [59], the goal has been to assess the level of fidelity achievable by the state-of-the-art numerical methods with regards to the prediction of the stability and control characteristics of an aeronautical vehicle. Two aircraft configurations are included in the study, the SACCON and the X-31 configuration. The first is a 53° swept lambda wing with a rounded leading edge whereas the second is a generic aircraft with a canard control surface and a cranked delta wing planform with 56.6° and 45° sweep angles. Both configurations employ a relatively rounded leading-edge geometry which introduces an additional element of complexity

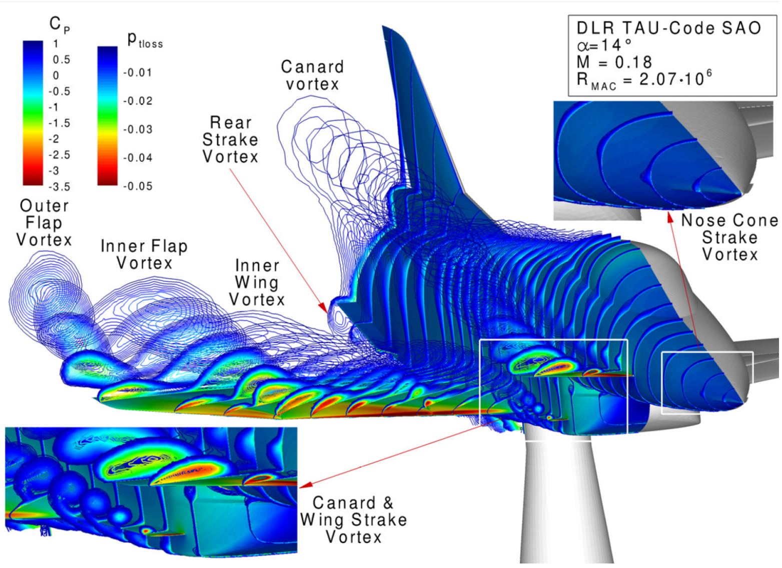

Figure 3.2: Vortex topology represented by means of consecutive volume cuts over the X-31 configuration. Simulation performed with the DLR TAU-Code by Schütte et al. [58].

to the vortex flow field due to the separation onset which is not fixed at leading-edge apex. Hence, the numerical simulation has to predict a proper vortex onset along the leading-edge extension. The X-31 configuration generates a complex system of vortices (Fig. 3.2) where they all influence each other starting from the fuselage nose vortex, passing through the canard and wing strake vortices and downstream to the main wing vortices. The application of the most traditional turbulence models for aerodynamic applications (Fig. 3.3), SA and k-ω, shows that the turbulence model sensitivity is high already at moderate AoAs ($AoA = 14°$) because large differences are evident from the surface pressure distribution [58]. The breakdown position is predicted to take place farther upstream for k-ω compared to the experimental data. At higher AoAs, the turbulence model manifests its lack of capability to capture more physical details of the complex flow field. Boelens [60] compares the TNT k-ω model with and without rotation correction and the EARSM model. The only model that manifests a consistent difference from the others is the TNT k-ω with rotation correction which is able to improve the accuracy overall. However, some discrepancies remain for all turbulence models: all the numerical simulations manifest the merging of the strake and wing vortices whereas experimental data show none. The sensitivity of the rotation correction appears to be concentrated on the breakdown location as expected from the experience of other applications.

The numerical simulations performed for the SACCON configuration [61] exhibit similar characteristics with regard to the sensitivity to the numerical grid, solver and turbulence model. In this case, it is important to notice that, since the vortex separation onset is a sensitive region, the discretization resolution close to the leading edge acquires

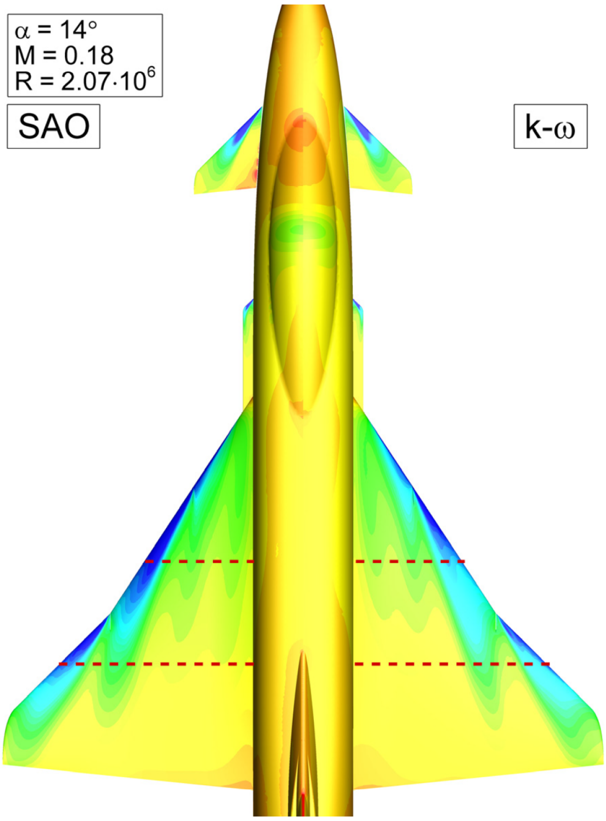

Figure 3.3: Pressure distribution on the upper surface of the X-31 configuration. Comparison between the k-ω and the SA models. Simulations performed with the DLR TAU-Code by Schütte et al. [58].

even more importance. Between the different tested turbulence models, the one which provides a better agreement with the experiment is the SA model. This suggests again how still at the current state of the art it is not clear which turbulence model is "better" to use for a new configuration and a first phase of numerical setup validation is necessary. The discrepancies with the experimental data are evident also from the pitching moment curve where its flattening is not predicted. This is not related to the separation onset prediction but instead to the breakdown location and strength (Fig. 3.4). The application of the RSM model improves the breakdown proximity but it loses accuracy in the separation onset prediction. The SA model is able to predict the separation onset with higher fidelity [62]. The EARSM model instead shows a better accuracy in the region dominated by the separation onset but the accuracy decreases with a stronger vortex flow at higher angles of attack, whereas the k-ω SST model [63] predicts a flow field which is comparable to the one resulting from the SA model application. The application of the rotation correction to the k-ω model [64] returns a worse accuracy with respect to the pitching moment curve compared to the uncorrected model. This is more significant for the region at higher angles of attack where a sudden pitch-up appears due to vortex breakdown. Paul and Martin [65] concentrated their investigation on the transonic conditions at $M = 0.7$ which shows a similar accuracy grade of the RANS turbulence model. They state that RANS models remain the best compromise of accuracy, stability and cost for the generation of a large amount of points. They see the necessity of moving to more complex turbulence models at a later design step where the detailed flow description may be of interest or relevant. The SACCON geometry has been further investigated in the context of the following AVT-201 STO task group [66]. Discrepancies which are similar to the results of the previous project are experienced for different turbulence models, solvers and numerical grids [67]. It is again important to notice that more complex models, such as RSM or hybrid models, do not improve the accuracy grade for all the cases even though their computational cost is significantly higher. Moreover, the participating partners have also investigated different sideslip configurations. This is not a mild variation because the introduction of a sideslip angle to the free stream flow means that the windward side experiences a smaller effective sweep angle and the leeward side a larger sweep angle. Therefore, the aerodynamic configuration will experience an asymmetrical vortex flow development because the vortex stage and development are directly dependent on the sweep angle. This introduces complexities and higher probability of a lack of accuracy from the modeling of turbulence. Whereas at low angles of attack the dependency of the aerodynamic coefficients on the sideslip is approximately linear, the increase of the angle of attack introduces non-linear dependencies due to the different breakdown nature above the windward and leeward sides. Therefore, the turbulence model uncertainty increases.

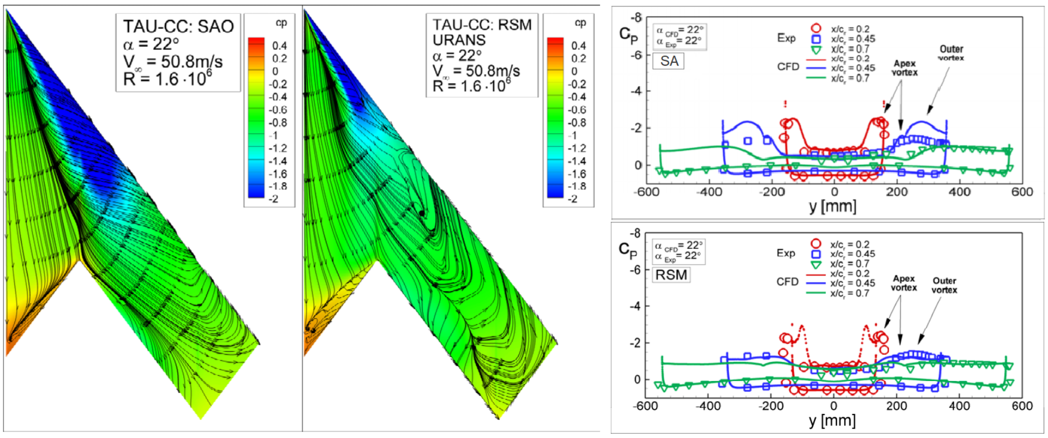

Figure 3.4: Pressure distribution on the upper surface of the SACCON configuration. Comparison between the RSM and the SA models. Simulations performed with the DLR TAU-Code by Schütte et al. [61].

3.2.4 AVT-183 Diamond Wing and SAGITTA Blended Wing Body

The STO AVT-183 Task group performed experimental and numerical investigations of a 53° swept diamond wing with a rounded leading edge. Therefore, the main target of the research was the understanding of the separation onset of vortical flows. For this reason the range of moderate angles of attack is the focus of the cross-comparison of the numerical results [68, 69]. However, experimental data are available also for high angles of attack up to 32° where a post-stall condition of the vortex flow is achieved [70]. The comparison of the numerical results of different contributors show that both an EARSM model and the SA model lack accuracy with respect to the first vortex separation as well as its development in the region downstream [71]. The separation onset is predicted too far downstream by the numerical solution. The employment of the SA model with the rotation correction provides a worse accuracy level because it displaces the vortex separation even farther [72]. The ZDES model employed by ONERA provides a better prediction instead [72]. A similar configuration which has also involved different studies and investigations is the blended wing body geometry, based on a diamond wing shape, called SAGITTA [73]. The planform is comparable to the AVT-183 diamond wing except for the leading-edge roundness, the body thickness and a small variation in the sweep angle which is 55°. The complexity of this flow is due to the large body thickness and the roundd leading edge which provokes an offset of the vortex separation onset. The accuracy of the numerical solution is achieved with proper application of RANS simulations with the SA model except for the separation onset at the angle of attack of 20° which is located farther downstream compared to the experimental data [73, 74].

3.2.5 AVT-316 Multiple Swept Delta Wing

In the context of the STO task group AVT-316, a generic multi-swept delta flat wing configuration [75, 76] is investigated both experimentally and numerically including several geometrical and flow condition variations. Here, the presence of different wing sweep angles contributes to enhance the flow complexity. In fact, the geometrical discontinuity of the leading-edge geometry corresponds to the separation of a new vortex. The vortices are also of different strength, stability and nature being generated from different leading-edge sweep angles. Moreover, they eventually interact/merge in different fashions according to the angles of attack and sideslip. The combination of multiple vortices, high angle of attack and sideslip conditions extremize the complexity of the flow. Moreover, in the case of the transonic flow condition the vortex-shock-breakdown interaction adds up to the flow intricacy. Hence, large discrepancies are to be expected as it can be seen in the comparison in Figure 3.5. Whereas at low and medium angles of attack the vortex flow typology is predicted with a reasonable grade of accuracy from RANS, the stall condition on the windward wing is completely missed by the RANS computation at $AoA = 24°$. This is important to notice because this result indicates that for some cases the state-of-the-art CFD tools can still predict a wrong flow characteristic which would result in large uncertainties about the stability and control characteristic of such a planform in a preliminary development phase. The application of a different turbulence model manifests a clear sensitivity of the flow phenomenon to it and a RSM model provides the best accuracy with respect to the high angles of attack except for a certain delay in the angle of attack of the sudden increase of the pitching moment[77].

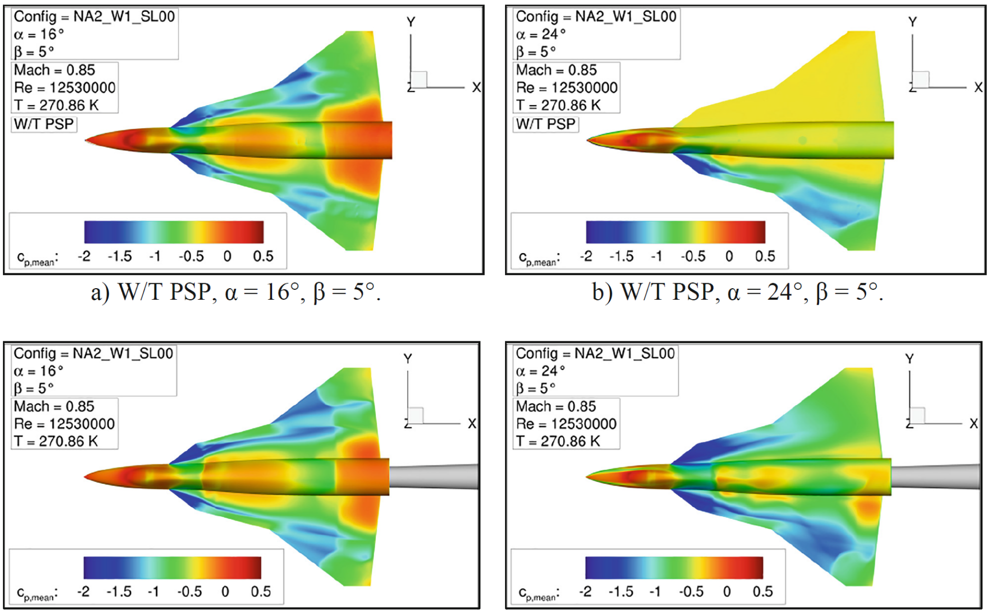

a) W/T PSP, α = 16°, β = 5°. b) W/T PSP, α = 24°, β = 5°.

c) CFD, α = 16°, β = 5°. d) CFD, α = 24°, β = 5°.

Figure 3.5: Pressure distribution on the upper surface of the AVT-316 triple delta wing generic configuration. Comparison between the PSP experimental data and the CFD computations with SA-neg model and rotation correction. Simulations performed with the DLR TAU-Code by Hövelmann et al. [75].

3.2.6 General assessment

In conclusion, at the state of the art, RANS simulations are the main contributor in the production of datasets of aerodynamic configurations which employ vortex dominated flows. They are considered the best compromise of accuracy, stability and computational costs for both academic and industrial applications. Their advantages dominate when the number of simulations to be performed increase. When the required level of physical description of the vortex field is set to higher standards, Reynolds Stress Models or LES-RANS hybrid methodologies are employed in order to acquire a better insight into the detailed description and analysis of the vortex flow. The lack of accuracy caused by the modeling of turbulence is related to the limitations introduced by the Boussinesq assumption with regards to highly separated or rotational flows as well as by their formulation and calibration procedure being based on fundamental test cases in order to generalize the model as much as possible. In the following section, the state of the art and the research trends with respect to the improvement of turbulence modeling is reported to set the starting point for the formulation of the proposed methodology.

3.3 State of the Art: Turbulence Modeling Variations and Corrections

The research in the context of turbulence modeling have followed different directions along the last two/three decades. On the one hand, the necessity of deeper knowledge about the details in many complex flows has contributed to develop further scale resolving models by reducing assumptions and modeling restrictions. Full LES simulations remain dedicated to a small spectrum of fundamental cases due to their computational costs and the application to a full complex geometry is not expected to be routinely integrated in the recent future. Therefore, the development of a series of RSM models and then LES-RANS hybrid methodologies including the different variants of DES models [78] have been the target of this branch of research. In this direction, the research has addressed the improvement of the modeling itself but also the stability problems as well as improving the experience with their employment in order to extend its usability in different contexts. Nevertherless, the employment of hybrid RANS-LES models is mostly applied where details of the flow are of high relevance. However, the research performed on these methods manifests potential for the future, especially, if the computational resources will increase drastically, contrarily to what the trend is showing at the moment.

On the other hand, for the majority of the cases, mostly when a larger number of flow conditions and geometries need to be calculated, the RANS methodology thrives. Inside the RANS methodology, Eddy Viscosity Models (EVM) form the largest portion of applications whereas RSM and second moment closure models progressively increased their utilization along the years. Due to the extensive usage of EVM for the numerical solution of aerodynamic cases, the research community has dedicated a considerable amount of resources for the improvement of the main drawbacks of RANS methodologies, which are their lack of accuracy with respect to certain classes of flows. This is the case for flows where the frequency of unsteady phenomena present in the flow is much lower than the frequency of turbulence itself. Hence, the averaging process of the RANS equations remains valid [78]. Furthermore, the Boussinesq assumption employed for EVMs limits the model's accuracy for cases where highly separated or rotational flows are dominant. Moreover, for both the first or the second order closures of the Reynolds stresses in the NS equations, the terms of the formulated equations are always weighted by means of coefficients. These coefficients undergo a calibration procedure which is performed by comparison with theory or high fidelity data such as DNS solutions or experimental data. Theoretical and DNS solutions are available for fundamental cases. With respect to DNS, the computational costs limit their feasibility at low Reynolds numbers. If experimental data are included, they are chosen from general flow cases in order to provide high globality to the model and hence maximize their predictive capability (Fig. 3.6). This provides a penalty in terms of accuracy with respect to flow cases and conditions which differ from the fundamental cases.

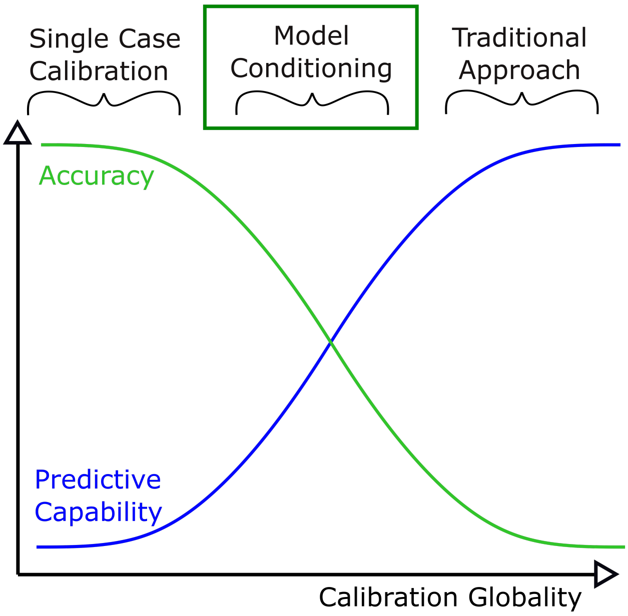

Figure 3.6: Sketch of the calibration target of physical models. Qualitative expectations of the predictive capability versus the accuracy level.

3.3.1 Rotation and Curvature Corrections

Along the years, several modifications of existing turbulence models or new approaches for improving the fidelity of RANS models have been formulated, investigated and also applied. At first, the modifications are often applied to one of the traditional turbulence models, the most common are SA, k-ϵ or k-ω, and, secondly, they are usually reformulated and adapted to the others. Several corrections and modifications have been tested in order to overcome the accuracy problem encountered for highly curved, rotating or recirculating flows [79]. However, they are specific for a single or a restricted number of cases and flow conditions and usually not Galilean invariant. Howard et al. [80] investigated different possible modifications to the available k-ϵ model based on the Coriolis force in order to address the presence of curvature and rotation in a duct flow. Launder et al. [81] similarly have added a term in the ϵ transport equation in order to correct the solution for a boundary layer developing along a curved geometry. Degani and Schiff [82] identified an over-prediction of eddy viscosity at vortex suction peaks for the one-equation Baldwin-Lomax turbulence model. This effect is common with other turbulence models, SA as well. They corrected the original model coefficients in combination with a solver modification by introducing a function to locate the suction peaks and trim the eddy viscosity level. The work of Park and Chung [83] similarly addresses the lack of accuracy by introducing a correlation between the third-order diffusive transport of the k-ϵ model with a function of a velocity and curvature time scale. Moreover, they modified the coefficient of the destruction term of ϵ in order to better fit the decay of turbulent kinetic energy for flows with high curvature effects. A series of other modifications were formulated to address the same curvature/rotation problems with different approaches. The main problem of the direct introduction of the streamlines curvature in the model equation is the failure of the Galilean invariance. In order to solve the problem of having many solutions for the same problem but with some lack of generality, Spalart and Shur formulated their rotation and curvature correction [84] with a more generalized and accurate form. Moreover, the correction is Galilean invariant. To achieve this, a function based on velocity derivatives of a higher order is formulated and introduced into the model. For this reason, the succcessive application tests performed by Shur et al. [79] has shown an increase of around 20% of the computational costs. They claim that the modification introduces no degradation of the convergence behavior. However, the application on vortical flows has introduced higher oscillations in the expressed aerodynamic forces which occasionally requires a larger number of iterations for proper convergence compared to the original SA form. The SA model is modified by means of the rotation correction function f_{r1}.

$$f_{r1}(r^*, \tilde{r}) = (1 + c_{r1})\frac{2r^*}{1 + r^*}\left[1 - c_{r3}tan^{-1}(c_{r2}\tilde{r}\right] - c_{r1} \tag{3.12}$$

Where the coefficients read:

$$c_{r1} = 12 \qquad c_{r2} = 1.0 \qquad c_{r3} = 1.0 \tag{3.13}$$

And the variables:

$$r^* = \frac{S}{\omega} \tag{3.14}$$

$$\tilde{r} = 2\omega_{ik}\S_{jk}\left[\frac{DS_{ij}}{Dt} + (\epsilon_{jmn}S_{jn} + \epsilon_{jmn}S_{in})\Omega^{'}_{m}\right] \tag{3.15}$$

Where $\Omega^{'}$ is the reference frame's rotation. This rotation correction behaves often well as reported also by the authors [79] with the application to fundamental cases for assessment and testing. However, with respect to leading-edge vortices it is not able to consistently provide improvements compared to the baseline turbulence model. In fact, the modification target basic flows like a U-duct and a C-duct geometry. With respect to their high rotational characteristics these basic flows employ turbulence model deficiencies which are sassociated with those obtained for larger-scale leading-edge vortices above delta wings. Therefore, it has been shown in the previous paragraph 3.2 that the solution of vortical flows can acquire better accuracy by the application of the SA-RC model [85]. In particular, for highly separated vortices or shedded ones at high angles of attack and/or low sweep angles. However, since leading-edge vortices can develop in a series of different evolution stages and types, there are cases where no significant improvement is appreciable [86] and other cases where adjustments of the eddy viscosity which are mild or concentrated in regions of the flow field are detrimental to the flow stability. As the sweep angle increases or the angle of attack decreases, more stable vortices are present and the effect of the variation is too abrupt. Hence, there are cases where its application decreases the accuracy grade [87]. The correction improvement is not flexible and consistent enough in order to be applied without preliminar testing and providing a comparison with the original turbulence model form. The correction can be applied theoretically to every eddy viscosity model. Menter and Smirnov [88] have adapted it to the two-equation k-ω model and attention has been dedicated to adjust the effectivity of the correction with a limiter function $f_{r1,lim}$ (Eq. 3.16). The lower limit of 0.0 is introduced for stability purposes. This is important to notice because the introduction of corrections may deteriorate the stability and it is common practice to test this quality of the numerical solver when a modification is introduced. The upper value of 1.25 is based on the consideration that the production term of a turbulence model is higher if based on the strain rate S compared to the vorticity tensor ω. In fact, the SA model relates the production of eddy viscosity to the vorticity tensor ω, the k-ω model uses the strain rate S instead. This difference is limited with an empirical ratio.

$$f_{r1,lim} = max\{min(f_{r1}, 1.25), 0.0\} \tag{3.16}$$

Another direction of research for the improvement of turbulence models accuracy has been the employment of nonlinear terms and formulations. The turbulence modeling of swirling flows has been the target of a research study of Shih et al. [89] which has shown accuracy advantages for the numerical simulation of swirling flows that characterize the internal flow of aircraft engines. The model is based on the employment of a cubic Reynolds stress-strain term within the baseline k-ϵ model. The modification introduces additional computational costs of around +15%. Craft et al. [90] formulated a cubic eddy-viscosity model based on a similar concept by means of a cubic term which follows the physical correlation between strain-rate and vorticity in order to provide a general formulation of it. The equation coefficients are afterwards calibrated on fundamental test cases. Hamid [91] has formulated a k-kL two-equation turbulence model and introduced a non-linear variant which improves the accuracy for some test cases. Parmar et al. [92] have introduced a generalized formulation for non-linear EVMs which also employs a modification for addressing other flow variables such as the mean pressure gradient. The model maintains the Galilean invariance and its application exhibits potential to improve the accuracy level.

Subbian et al. [87] apply a rotation correction to the k-ω SST model for the numerical simulation of fundamental cases, i.e. a flat plate, a backward facing step, and a more complex case which consists of the VFE-2 delta wing at transonic conditions. This application has the objective to evaluate the solution sensitivity to the corrections and develop additional terms to be calibrated by means of a Bayesian update methodology. Nevertherless, it is interesting to notice that the correction is not detrimental to the solution of the basic cases and it shows a low sensitivity of the result. However, the application of it to the VFE-2 delta wing (Fig. 3.7a) with the original calibration returns a decrease of the accuracy. The vortex footprint is in fact larger and characterized by a lower suction peak if compared to the original model and the experimental data. It appears that the location of the breakdown instability is moved too much upstream by the correction. Therefore, Subbian et al. gathered significant information from these sensitivity analysis both to motivate the development of additional terms and to justify the research of their innovative calibration technique. Ali et al. [86] applied the rotation correction of the k-ω SST model to a centrifugal compressor geometry where curvature and rotational flow are dominant features of the flow. However, no large separation is visible. The correction introduces only minor differences in the flow velocity profiles (Fig. 3.7b).

3.3.1.1 Additional Corrections

The application of modifications based on both empirical and physical assumptions has shown potential to improve the target class of flows. This has been the focus of different research works and progressively more complex flows have been addressed analyzing their main discrepancies with experimental data by employing the baseline models. Zhang [93] applied a rotation correction based on the Hellsten formulation [94]. Hellsten formulated a different kind of rotation correction compared to SA-RC claiming that its formulation could be simplified. In fact, the SA-RC model necessitates the computation of higher-order velocity derivatives which raise the computational cost of the numerical simulations. The correction formulated by Zhang is based on a general definition of the Richardson number for common three-dimensional flows and it is a function of the first-order velocity derivatives only.

The approach of extending a turbulence model by targeting a type of flow has shown potential in many cases with regards to accuracy. However, the predictive capability is not usually a main focus of these models extensions. They focus instead on the physical content that the target case manifests as a flow typology and then calibrate the available coefficients, usually manually, until the solution is as close as possible to some fundamental examples or experimental data. The research has progressed with the focus on improving the accuracy on more and more complex flows. Arolla and Durbin [95] provide another example of a correction. In this case, it modifies the production term of ω based on the streamline curvature following the original idea of Pettersson [96]. Stabnikov et al. [97] formulated a correction based on a function which multiplies the transport equation of the turbulent kinetic energy instead of both equations of the model. This variation brought improvements to different test cases, vortex flows included.

In order to better summarize the state of the art, Asnaghi et al. [98] compared a series of available curvature corrections available at their state of the art with respect to the separation of a Rankine tip vortex. More than ten rotation corrections were tested on the same test case as well as the baseline turbulence model and a laminar solver. What is important to notice is that the results showed that:

- The noticeable differences between the different simulations illustrate how sensitive a vortex separation is to turbulence modeling. In this case the k-ω SST model is not capable to predict a correct tip vortex structure. Euler simulations predict the vortex but fail to capture reasonably accurate levels of velocities due to the influence on the vortex of the boundary layer separation. This result is similar to

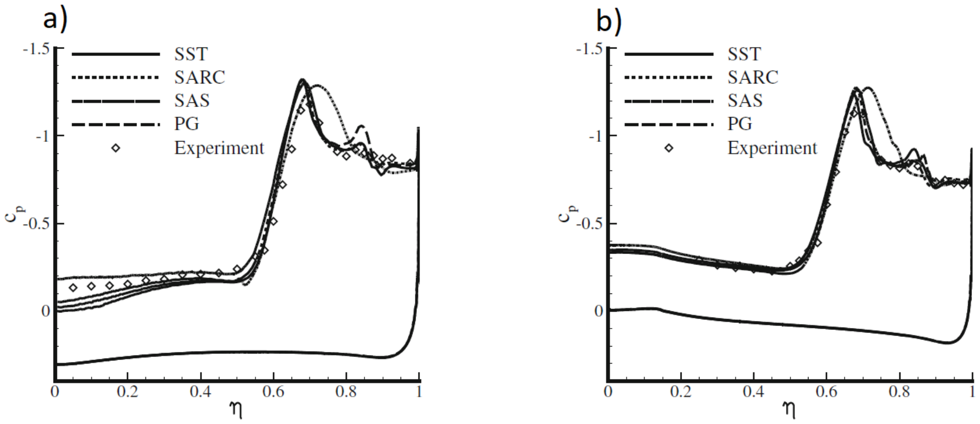

(a) Spanwise distribution of C_P on the upper surface of the VFE-2 delta wing at $M = 0.8$ and $AoA = 13.3°$ at the positions of a) $x/c_r = 0.6$ and b) 0.8. Numerical simulation performed by Subbian et al. [87].

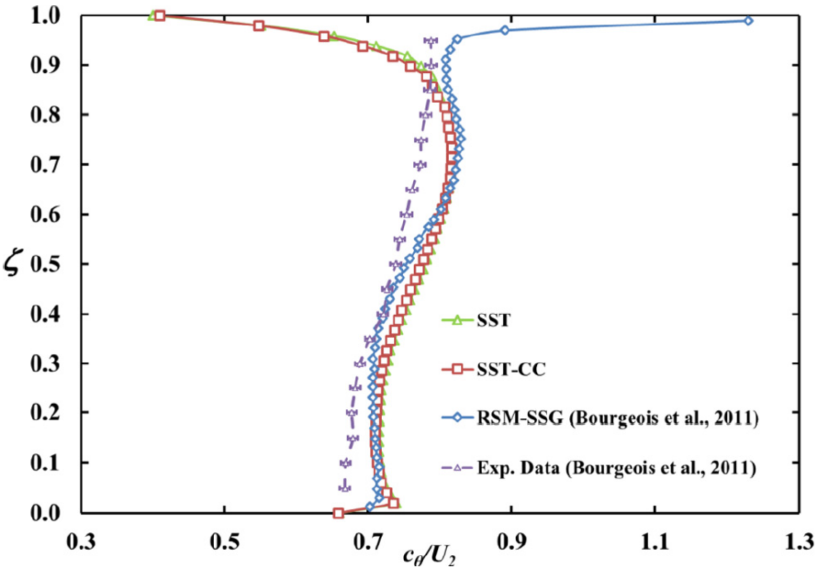

(b) Normalized circumferential velocity at the mixing plane. Numerical simulation performed by Ali et al. [86].

Figure 3.7: Comparison of the numerical results with experimental data and different turbulence models of different test cases. Assessment of the generality and flexibility of the traditional rotation and curvature correction from Spalart and Shur [84].

what expected for Euler simulations above delta wings with respect to the absence of the secondary vortex because it is generated from the boundary layer separation.

- The applied variants of rotation corrections provide different effects with regard to the eddy viscosity distribution variation itself. Pettersson [96] and [95] modifications, for example, work similarly since they are based on the same starting idea. Most of the models eventually provide a reduction of ν_t in the core and an increase outisde. The strength of the effect changes between the models. The "effect radius" which splits the core and outer vortex influence regions manifests differences as well. Some of them reduce the eddy viscosity field in the complete vortex. Consequently the accuracies of results differ from model to model. The authors of the work relate this to the formulation, the clipping/limiting of terms and the calibration process. Clipping and limiting a certain function on a pair of fundamental calibration cases may introduce hard limitations on predicting other flows.

- A distinction is highlighted between the corrections which work on the production terms of the equation variables and others which act directly on the eddy viscosity distribution itself.

- The authors mention that the numerical grid refinement has an effect on the correction functions and the terms.

- It is indicated that the corrections which behave better in terms of accuracy are the one that have influence also in the boundary layer region. Presumably these corrections may lack of predictive capability instead.

Zhang and Agarwal [99] have formulated a correction based on the Richardson model for the Wray-Agarwal model which is a more recent one-equation eddy-viscosity model. The equation is a transport equation of the variable R which is the ratio k/ω. The model's coefficients have been optimized by means of a calibration process. The correction has shown mild advantages to the Spalart-Shur correction in terms of accuracy improvement for common fundamental cases with rotation and curvature flow features. Moreover, it does not introduce additional computational costs.

Bush et al. [100] have gathered the points of view of the main experts of turbulence modeling at their state of the art and have indicated the best recommendations for the recent future research in RANS turbulence modeling. An upper limit of accuracy for RANS simulations will be reached for some applications in the future but the authors find points of disagreement how to overcome this barrier. Some see the possibility to increase this barrier by using improvements of the modeling approaches as well as new methodologies. Hence, they highlight how further research into RANS modeling is important and they feel that a larger than necessary effort has been dedicated to more complex or scale resolving models which still have the main problem of their high computational costs. In fact, the authors explain how RANS simulations form the major part of simulations for industrial applications in most of the development phases as well for academic investigations. They also highlight that free vortices in particular associated to delta wings are one of the flows which suffer for lack of accuracy at the state of the art. As an outlook, the authors suggest a series of important directions along which the research should be developed. Between these, there are the extension of models to complex physical flows and by addressing particular cases with a certain grade of globality.

Menter et al. [101] have taken into consideration the need for a more generalized 2-equation turbulence model which is able to be adapted for the considered target class of flow without losing the well behavior for the original calibration for the flow on flat plates. The adaptation is at first thought to be based on the freedom of the user to modify free parameters and select regions of the flow where different sets of parameters are applied. The k-ω model is used as baseline model and the final formulation is referred to as "GEneralized k-ω" or GEKO model. The authors also specify the importance of assessing the minimization of the other sources of error before the application of the GEKO methodology. The comparison to experimental data is reccomended to guide the GEKO modeling adaptation. There are points in common with the methodology formulated throughout this research project. The differences are related to the class of turbulence models, the target flow features and the manual calibration procedure. Here, different coefficients are available in order to address different discrepancy sources such as flow separation, mixing of fress shear flows, free jet flows as well curvature/rotation corrections. As instance of an application, the variation of different values of the coefficient for the separated flow term provides high sensitivity to the numerical solution and the possibility to improve the prediction of the separated flow over airfoils at and beyong stall conditions (Fig. 3.8).

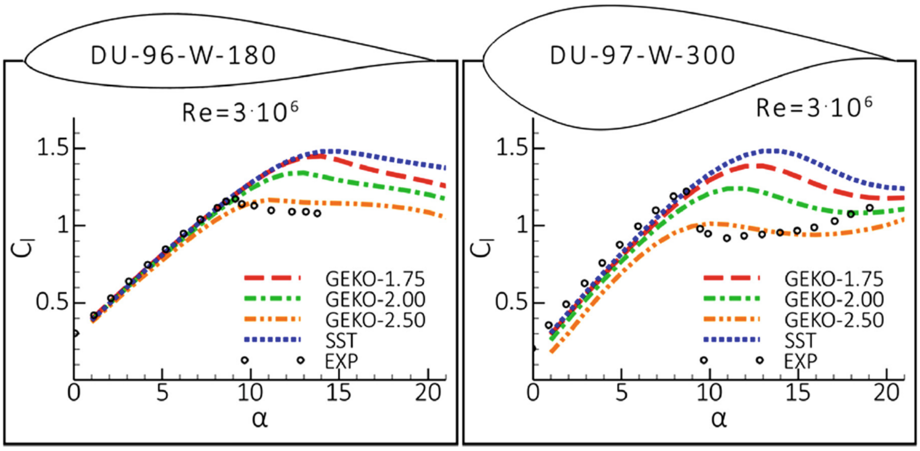

Figure 3.8: Pressure coefficient distribution predicted by different values of the free parameter dedicated to the flow separation. Numerical simualtions performed by Menter et al. [101].

3.3.1.2 Data-Driven Enhancements

An important branch which has been developing in the last few years is the employment of data-augmentation techniques for turbulence models [102]. Hence, the progressively increasing availability of data from experimental data and high fidelity simulations has permitted the exploitation of these sources of information for augmenting the set-up of RANS models by means of inferring and prediction methods. The Bayesian update method [87] has provided the possibility to include in the model a stochastic quality and to utilize the information about the reference data uncertainty in order to improve the predictive capability of such models. The development of efficient statistical inference algorithms has provided tools for using large amounts of data. Furthermore, the recent development of more and more performing and complex deep neural networks and machine learning tools provides a potential synergy with the need of an improvement in the physical modeling in terms of accuracy and computational feasability. Likewise, this applies to the modeling of turbulence in fluid dynamics. Therefore, the application of deep neural networks to large amounts of data from high fidelity simulations or experimental data may improve traditional RANS turbulence models to their maximum barrier. This is seen as a promising direction to follow for the years to come.

Singh et al. [103] has coupled an inferring tool with a neural network in order to modify the SA turbulence model by means of a correction factor which multiplies the production term in the flow domain (Fig. 3.9). Hence, firstly an inversion problem is solved in order to find the pointwise correction factor which provides the most accurate solution possible relative to the experimental data. Afterwards, the inversed field is set as target for the neural network training step. The model is enhanced with the trained neural network in order to predict the correct factor in an unknown test case and flow field. The results are promising with regards to the flow around an airfoil and other simple 2-dimensional cases. Hence, the approach shows its potential for further improvement and extensions to more complex flows by challenging its prediction capability. Zhu et al. [104] and Wu et al. [105] offer similar methodologies in order to infer high fidelity data into an additional term of the turbulence model. They pose the discrepancies between the true Reynolds stresses coming from DNS simulations and the RANS modeled stresses as the target of the neural network to learn the correlation based on the input flow. Afterwards, the regression function is used to improve the prediction of the turbulence models. Zhao et al. [106] have followed a different approach where the machine learning methodology is applied to an algorithm for finding the most promising extension of a baseline model. Parmar et al. [92] have employed a feed-forward deep neural network in order to include information coming from DNS data and associate it as a surrogate model to the turbulence model formulation.

The proposed research, although it does not include machine learning technique at the core of the methodology and the calibration procedure, shares most of the objectives and motivations with this branch of research. Moreover, it fits properly as a starting point for further developments in this direction due to the significant information coming from its application, formulation and results. A method based on an Artificial Neural Network is developped in order to extend the predictive capability of the methodology for cases

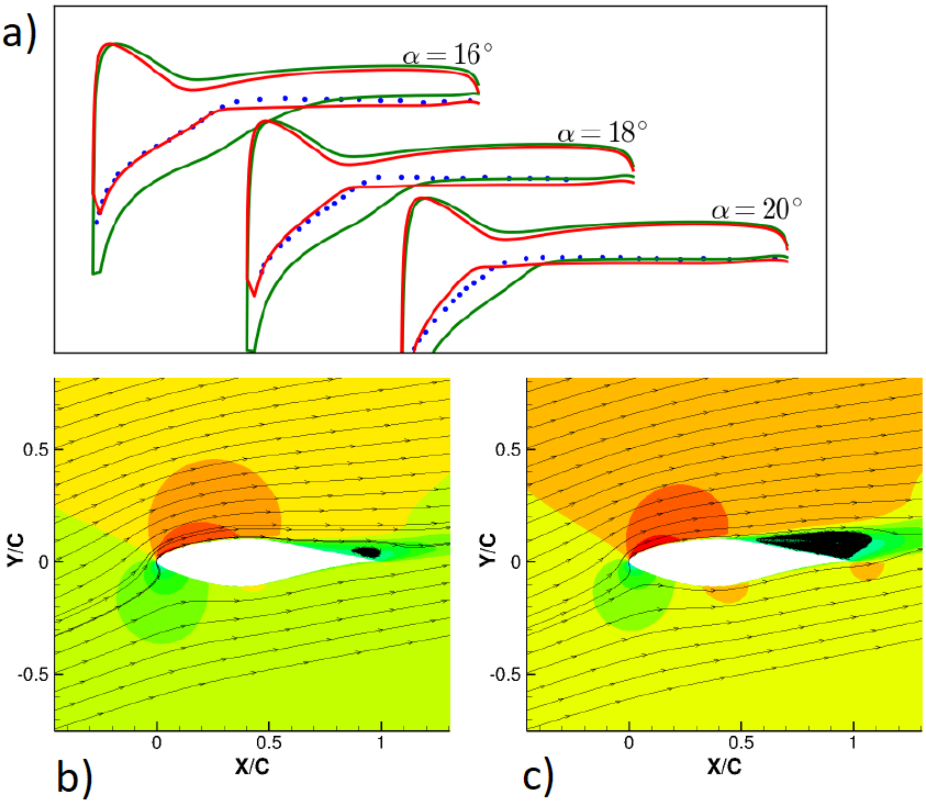

Figure 3.9: Example of the method by Singh et al. where a) the pressure distribution over an airfoil is reported for the baseline model (green line) and the neural network augmented model (red line) compared to the experimental data (blue dots) [102, 103]. The pressure contour and the flow streamlines are represented for b) the baseline model and c) the neural network augmented model.

where no experimental data are available and based on the optimizations performed on previous test cases as dataset (Sec. 3.5.2).

3.3.2 Summary and Methodology Justification

The lack of accuracy of RANS simulations remains an important issue at the current state of the art. Whereas the research into more complex and scale resolving turbulence models — RSM, scale adaptive or RANS-LES hybrid models — has been and remains an important direction of research, RANS turbulence modeling is the most common tool employed for the numerical simulation of different classes of flows. They employ a proper accuracy for basic flows, an affordable computational cost and a good stability behavior. The modifications and improvements available at the state of the art interact at different levels with these qualities. The proposed methodology is formulated in order to maintain unaltered the good behavior of the baseline model and enhance it exclusively in the flow features where it lacks accuracy. Along the different paths of research in this context, there are several ways of gathering information from higher fidelity data and exploit them within the modeling approach. In this case, the data which have been used are exclusively experimental data and they are inferred to the modeling of turbulence by means of an automatic calibration. To avoid a point-wise calibration the methodology balances a partial sacrifice of globality in order to gain a significant amount of accuracy for a relatively broad cluster of cases around the calibration point. This quality is relevant in the production of an aerodynamic and numerical dataset. As mentioned by different authors in their research works, it is also very important to address the other sources of error before applying modifications to the turbulence model. Therefore, attention has been paid for assessing the sensitivity of the numerical grid as well as the convergence rate, geometric simplification and numerical setup.

3.4 Turbulence Model Enhancement

In the following section, the description of the turbulence model modification is reported. The formulation of the different terms is described starting from their original physical idea to their application to verify the region of activity. The Spalart-Allmaras turbulence model with the Edwards modification is used as starting point and baseline. The SA model has been originally formulated for attached and mild separating external aerodynamic flows as target and it employs a proper grade of accuracy for flows of that typology. Therefore, being the main focus of this research the improvement of the solution of large-scale leading-edge vortices, the influence of the modification is isolated within the vortical structures. Any influence that might deteriorate the baseline calibration of the boundary and near-wall region of the model is avoided. In order to accomplish this, a flow quantity which identifies the vortex structure needs to be selected and its formulation is described as a first step in Section 3.4.2. No higher grade of the velocity derivatives is computed and, therefore, no significant additional computational costs are introduced. With regards to the maintenance of stability, it is addressed during the application of the methodology for the reported test cases. The coefficients of the different turbulence model terms are calibrated by means of an automatic toolchain which utilizes experimental data as minimization target.

3.4.1 VitAM Research Project

The methodology has been developed in the context of the research project called Advanced Aircraft Understanding via the Virtual Aircraft Model (VitAM) where different partners have addressed the fields where a step forward with respect to the fidelity and efficiency of numerical simulations of an aircraft model is necessary. A close collaboration has been established between the Technical University of Braunschweig (TUBS), Airbus Defence & Space (ADS) and the Technical University of Munich (TUM). The focus of the group has been the improvement of accuracy and efficiency of vortex dominated flows. The efficiency has been improved by ADS where a series of known and new numerical methods have been synergized inside a single routine for the production of an aerodynamic dataset. TUBS and TUM together with ADS have, afterwards, concentrated their efforts on solving the accuracy issues encountered with the RANS simulations of leading-edge vortices. Two directions have been followed. The one presented in this work is the one developed by TUM and ADS [107, 108]. Whereas the other developed by TUBS employs some differences [109]. The model enhancement proposed by TUBS is based on the Menter-SST two-equation turbulence model and is composed by three additional terms which target vortex flows, wake flows and pressure gradient dominated flows respectively. The calibration methodology is different, being statistical instead of deterministic. It is performed by means of a Bayesian Update method and it is capable of including the uncertainty of the calibration data. The establishment of a surrogate model permits to fullfil a sensitivity analysis at a fraction of the computational cost. A close and constructive collaboration has been established in this group and this has permitted to both sides to reciprocally acquire experience and insight.

3.4.2 Vortex Identifier Quantity

As described in section 3.3.1, the Spalart-Shur correction for rotation and curvature employs the ratio r^* between the strain-rate tensor norm S and the vorticity norm ω and it is used to select a region of the flow dominated by rotation. This follows the definition of a vortex region by Hunt [110] which states that a vortex is identified when and where the second invariant of the velocity gradient $\nabla \mathbf{u}$ is positive. It follows that ω, i.e. the anti-symmetric components of $\nabla \mathbf{u}$, is larger than S, i.e. the symmetric components. Moreover, Hunt states that the pressure inside a vortex region is lower than the ambient pressure and, hence, a gradient of pressure is formed in the radial-wise direction. The pressure reaches a minimum at the rotation axis of the vortical flow.

The same relation is also used in the definition of the Q-criterion [110, 111] which has a positive value where a vortical region is present. It can be easily seen how the two definitions are coincident; Q is positive only if ω is larger than S.

$$Q = \frac{1}{2}\left(\omega^2 - S^2\right) > 0 \tag{3.17}$$

This is consistent with what Truesdell has defined [112] with the kinematic vorticity number N_k. This number indicates the rotational quality of an element regardless of its vorticity magnitude. Jeong and Hussain [113] define a vortex as a region where $N_k > 1$. This is again equivalent to state that $Q > 0$. However, N_k has the difference that it does not discriminate between vortices with different vorticity levels but only the quality of the rotation, i.e. if it is closer to a solid-body rotation ($N_k = \infty$) or to a irrotational motion ($N_k = 0$).

$$N_k = \frac{\omega}{S} > 1 \tag{3.18}$$

The formulation of an vortex identifier quantity ξ for the proposed methodology is necessary in order to influence the vortex flow field. It is based on the quantities summarized above, where the main physical feature is described by the ratio ω/S. Moreover, a small number ϵ is added in the implementation for numerical reasons, i.e. to avoid overflow where S has a value equal to zero. Moreover, the maximum value between the quantity and zero is selected in order to avoid negative values in the field.

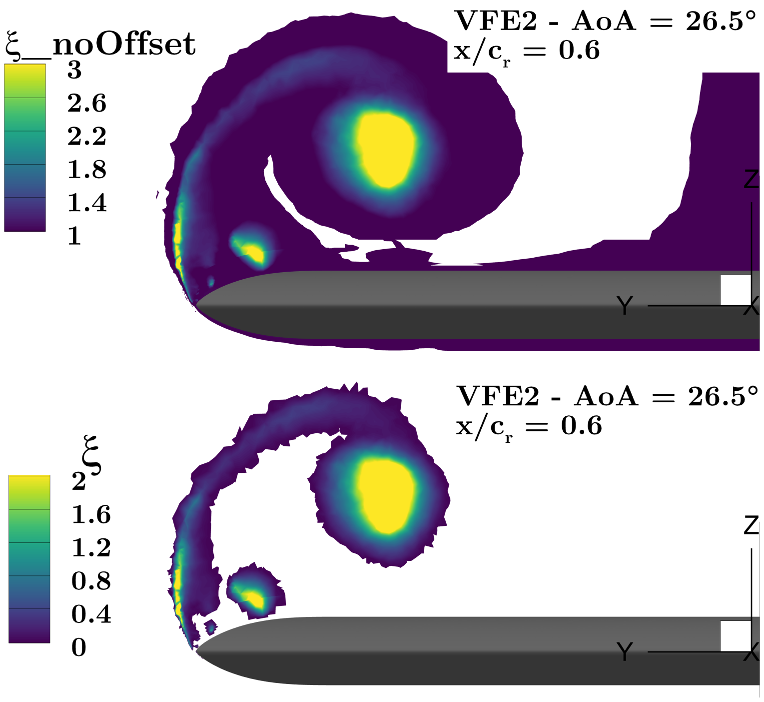

Figure 3.10: Visualization of a the cross-flow distribution of the ξ quantity before and after the application of the offset c_{vl} to avoid interaction with the boundary layer.

$$\xi = max\left[\left(\left(\frac{\omega}{S+\epsilon}\right) - c_{vl}\right), 0.0\right]; \qquad c_{vl} = 1.05 \tag{3.19}$$

Where the coefficient c_{vl} is introduced to switch off the activity of ξ inside the boundary layer region where no influence is desired. Its value is set to the value of 1.05 after evaluating the values interval of the ratio ω/S in a boundary layer region (Fig. 3.10). In fact, starting from the norms of ω and S (Eqs. 3.20, 3.21) and assuming that inside a boundary layer the only relevant component of $\nabla\mathbf{u}$ is $\frac{\partial u}{\partial z}$, the value of the ratio has a maximum equal to 1. This value is confirmed in the Jeong and Hussian definition [113]. The quantity ξ does not simply work as a switch function or qualitative like N_k but it returns a distribution along the vortex field and different behavior for different vortex typologies.

$$\omega = \left[\left(\frac{\partial u}{\partial y} - \frac{\partial v}{\partial x} \right)^2 + \left(\frac{\partial u}{\partial z} - \frac{\partial w}{\partial x} \right)^2 + \left(\frac{\partial v}{\partial z} - \frac{\partial w}{\partial y} \right)^2 \right]^{1/2} \tag{3.20}$$

$$\begin{aligned} S = \Bigg[& \left(2 \left(\frac{\partial u}{\partial x} \right)^2 + 2 \left(\frac{\partial v}{\partial y} \right)^2 + 2 \left(\frac{\partial w}{\partial z} \right)^2 \right) + \\ & + \left(\frac{\partial u}{\partial y} + \frac{\partial v}{\partial x} \right)^2 + \left(\frac{\partial u}{\partial z} + \frac{\partial w}{\partial x} \right)^2 + \left(\frac{\partial v}{\partial z} + \frac{\partial w}{\partial y} \right)^2 \Bigg]^{1/2} \end{aligned} \tag{3.21}$$

The effect of the application of the offset to avoid the effect on the boundary layer is visible in Figure 3.10, where the contour scale is adapted to have the same range of values with the offset applied. Without the application of the offset, the vortex identifier quantity would also be active in the complete boundary layer region for both the upper and lower surface of the wing where the original model — in particular on the lower surface which is the pressure side where the flow is well attached — provides a proper grade of accuracy. In this figure, it is also easy to notice in detail how a tertiary vortex structure separates between the secondary vortex and vortex sheet separating at the leading edge.

Therefore, it is a useful tool that permits to distinguish influences over different flow fields. Moreover, it does not introduce any numerical stability problem when coupled with any of the turbulence model modifications. The ξ quantity is visualized by means of volume cuts (Fig. 3.11) for two different configurations which will be target of application for the proposed methodology. First of all, it is visible for both configurations that the identifier quantity does not influence the boundary layer except where the vortex is separating which is properly selected as part of the vortex structure. Moreover, the shear-layer separating from the leading edge is identified by the quantity ξ which is important as well. The vortex developing above the wing with higher sweep angle, e.g. the VFE-2 wing, manifests stronger values of ξ inside the core due to its stable jet-type flow. This is different from a moderate sweep angle, e.g. the Model53, where the vortex shows lower values of ξ in the core and its value dissipates within a shorter radial distance. It is also noticeable how the radial-wise distribution is different from the VFE-2 case. Whereas the 65° case causes the ξ variable to drop fast from the core to the outer region, this happens more gradually for the Model53. The ξ quantity also identifies a vortex separation above the fuselage geometry and below the wing on the Model53. Moreover, the tip vortex at the end of the slat control surface is captured. It is also noticeable for the VFE-2 that the secondary vortex is identified and it shows a distribution of ξ that is comparable to the one of the first part of the primary vortex. With a moderate sweep angle, the secondary vortex is less visible also due to the presence of two vortices and the deployed slat. The ξ quantity is also capable of capturing the vortex structure after breakdown as it can be seen from the sections from $x/c_r = 0.7$ and downstream on the VFE-2. The identifier quantity is maintained high in the center structure which is a spurious continuation of the core and in the outer region where high tangential velocities are conserved for a longer distance. The two vortical flow structures on the moderate

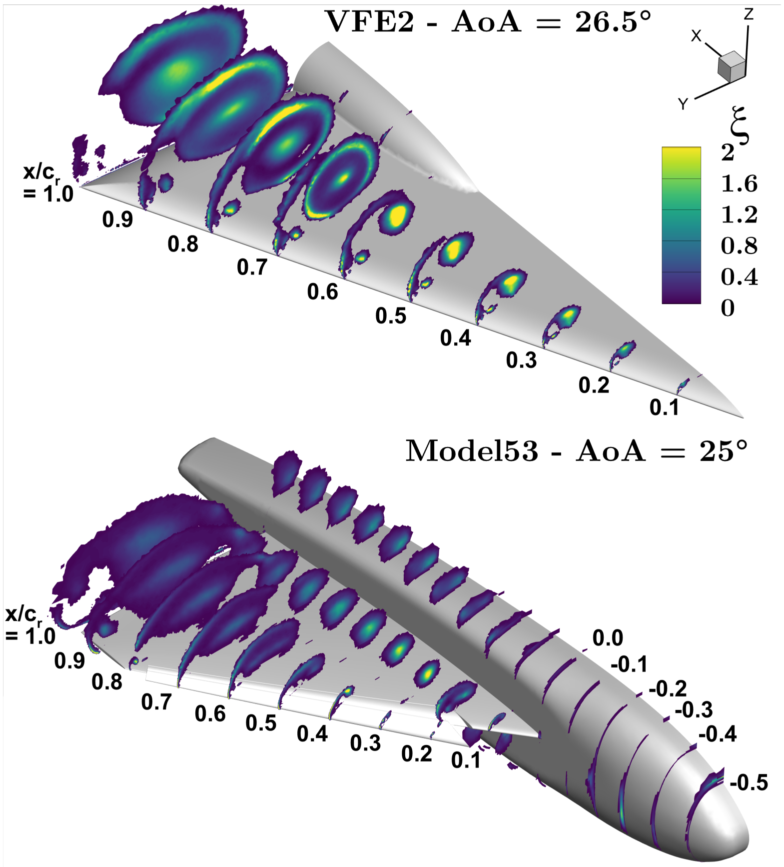

Figure 3.11: Visualization of consecutive volume cuts representing contours of the vortex identifier quantity ξ for two different delta wing configurations with high and moderate sweep angle, i.e. the VFE-2 wing with $\varphi = 65°$ and the Model53 with $\varphi = 53°$.

sweep angle exhibit the difference caused by the different local angles of attack. In fact, the vortex separated at the deployed slat is originated from a relative lower angle of attack. For this reason, its values of ξ are lower. Another important quality is that the identifier selects also the regions where the two vortex structures interact and mildly merge in the outer region.

3.4.3 Formulation of Additional Vortex Source Terms

In the following section, the formulation of the turbulence modification, composed of a series of source terms active in the vortex flow field, is reported and described. Firstly, their characteristics are summarized. The terms are:

- Coupled with one possible form of the ξ quantity in order to influence the vortex region exclusively and avoid any direction interaction with the boundary layer.

- Formulated as a source term. In a preliminary phase of the research, also diffusion terms have been tested without advantages or additional flexibility when compared to source terms.
- Formulated with the physical dynamics of leading-edge vortices derived from numerical simulations, theory and state-of-the-art wind-tunnel experiments as fundament and reference. In this sense, their formulations are set to target different characteristics or cover a range of distributions which can be consequently combined through the calibration procedure into a model that can be both accurate for complex vortex structures and flexible in predicting a relatively wide range of cases.
- Properly non-dimensional and Galilean invariant.
- Avoid to substantially increase the computational costs and to introduce non-physical convergence/stability issues.

The final turbulence model formulation is composed as follows:

$$
\begin{aligned}
\frac{D\tilde{\nu}}{Dt} = c_{b1}\tilde{S}(1-f_{t2})\tilde{\nu} - \Bigg[& \overbrace{c_{bv1}\xi S\tilde{\nu}}^{(a)} + \overbrace{c_{bv2}\xi^{\frac{1}{2}} S\tilde{\nu}}^{(b)} + \overbrace{c_{bv3}\xi^{2} S\tilde{\nu}}^{(c)} + \\
& + \overbrace{c_{bv4}\left(min\left(\frac{1}{\xi}, c_{vr,lim}\right)\right)\xi_{sw} S\tilde{\nu}}^{(d)} + \overbrace{c_{bvh1}\xi\widetilde{\mathcal{H}}\tilde{\nu}}^{(e)} + \\
& + \overbrace{c_{bvh2}\left[max\left(min\left(\frac{1}{\widetilde{\mathcal{H}}}, 1.0\right), 0.0\right)\right]\xi\omega\tilde{\nu}}^{(f)} + \overbrace{c_{bvb}\xi|\nabla\mathbf{u}\omega_{dir}|\tilde{\nu}}^{(g)}\Bigg] \\
& + \frac{1}{\sigma}\left[\nabla\cdot((\nu+\tilde{\nu})\nabla\tilde{\nu}) + c_{b2}(\nabla\tilde{\nu})^{2}\right] - (c_{w1}f_{w} - \frac{c_{b1}}{\kappa^{2}}f_{t2})\left[\frac{\tilde{\nu}}{d}\right]^{2}
\end{aligned}
\tag{3.22}
$$

With

$$\mathcal{H} = \mathbf{u}\cdot\omega \tag{3.23}$$

$$\widetilde{\mathcal{H}} = \frac{|\mathcal{H}|}{U_{\infty}} \tag{3.24}$$

And with ω_{dir} being the vorticity direction vector.

$$\omega_{dir} = \frac{\omega}{|\omega|} \tag{3.25}$$

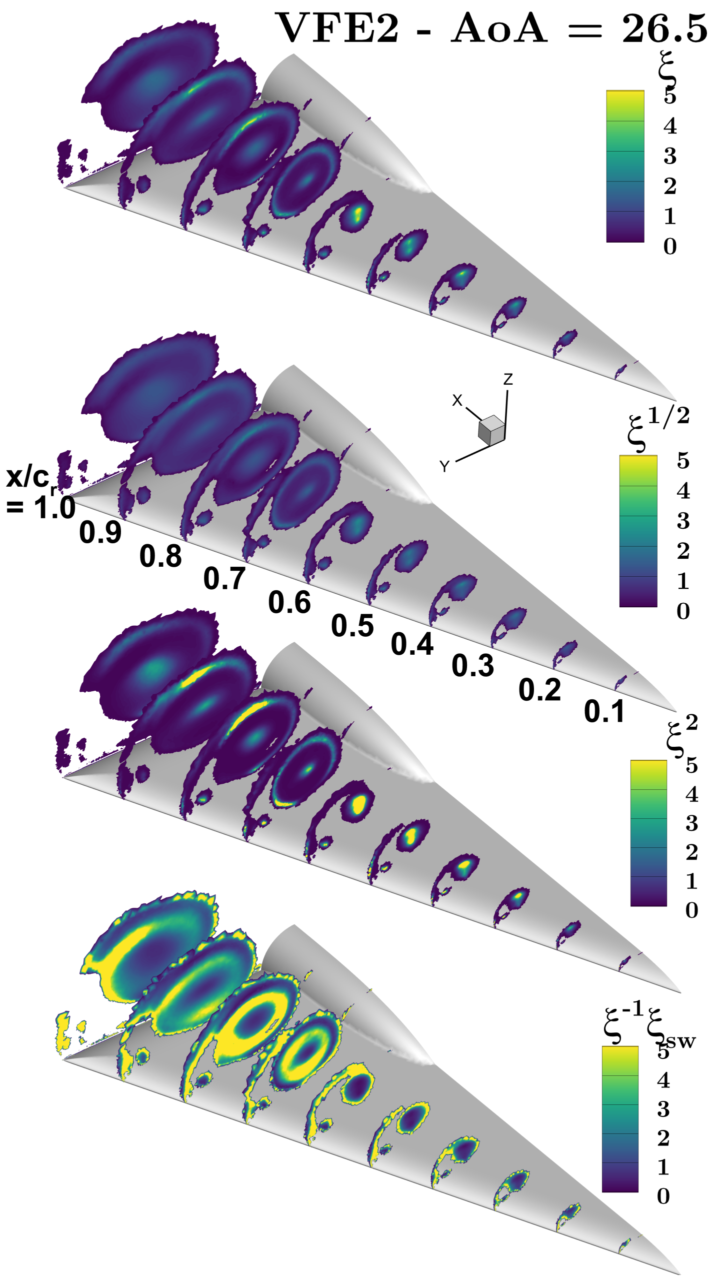

Figure 3.12: Visualization of consecutive volume cuts representing contours of the vortex identifier quantity ξ and its variations which correspond to different turbulence model vortex destruction terms. On the upper left corner the original ξ is represented whereas on the right, starting from above, the respective variations of $\xi^{1/2}$, ξ^2 and $\xi^{-1} \cdot \xi_{sw}$ are reported.

Starting from the baseline source term $c_{b1}\tilde{S}\tilde{\nu}$, a first term (a) is formulated by maintaining the same form but with a linear dependency on ξ, limiting the effect to the vortex

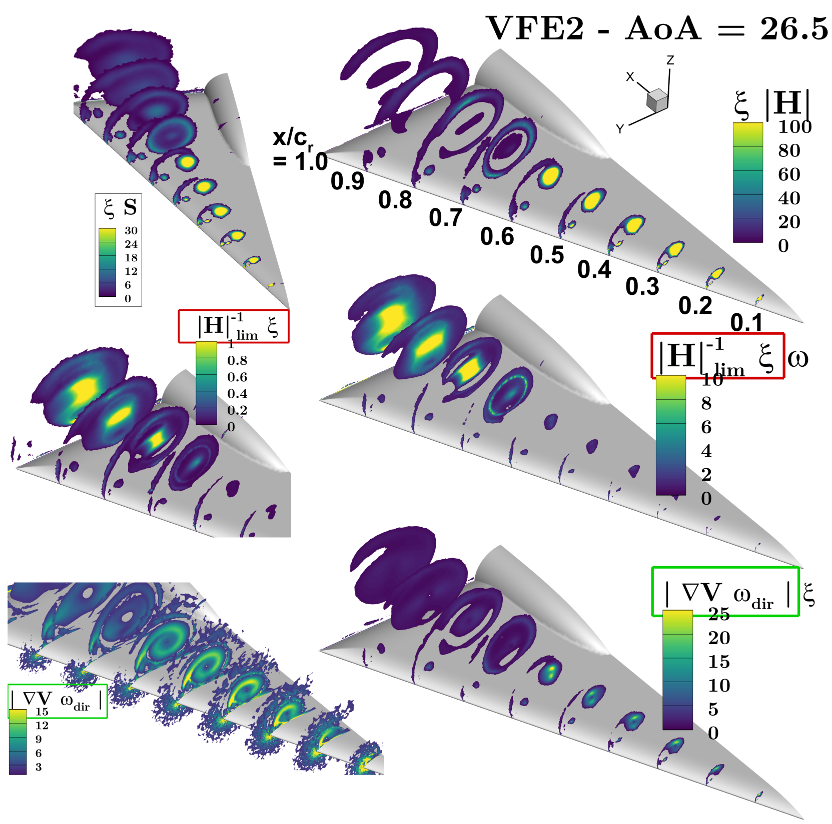

Figure 3.13: Visualization of consecutive volume cuts representing the contours of vortex identifier quantity ξ and its variations which correspond to different turbulence model vortex destruction terms related to the breakdown position. On the upper-left corner the original ξ is represented as reference. Then the different quantities expressing the terms follow, respectively: $\xi\mathcal{H}$, $\left[max\left(min\left(\frac{1}{\mathcal{H}},1.0\right),0.0\right)\right]\xi$, $\left[max\left(min\left(\frac{1}{\mathcal{H}},1.0\right),0.0\right)\right]\xi\omega$,$|\nabla\mathbf{u}\omega_{dir}|$ and $|\nabla\mathbf{u}\omega_{dir}|\xi$.

region but with the same influence distribution as of the original term (Figs. 3.10, 3.11). It has been illustrated that ξ has a certain distribution for different zones and types of the leading-edge vortex evolution. Therefore, if the ξ distribution is combined with different exponentiation laws of it, it is possible to formulate a series of terms with different distributions with the objective to create more flexibility for the model. The terms which have been mainly employed in this research are reported. The term (b) is based on a sublinear dependence, with an exponentiation of 1/2 of ξ. Its influence drops in regions where peaks of ξ are present, i.e. the vortex core, whereas it gains weight in the region after breakdown (Fig. 3.12). The $\xi^{1/2}$ quantity presents a flatter distribution along the different zones of the vortex. In order to dispose a term capable to concentrate its influence in the core region (Fig. 3.12), a term which has a superlinear dependency on ξ, i.e. with an exponentiation of 2, is formulated (c). The superlinear term has more influence on the secondary structure and in the spurious rotational zones in the region downstream of vortex breakdown (Fig. 3.12). In order to extend the flexibility of the model, an inverse distribution of ξ is provided to a term (d) which is based on the combination of a switch function of ξ, which is 1 only where $\xi > 0.0$, and an inverse exponentiation of ξ. The ξ^{-1} is also limited with a $c_{vr,lim}$ value of 10 in order to avoid local overshooting values. The inversion of the distribution furnishes a strong influence on the region downstream of vortex breakdown except for its spurious core and outer high rotational zone (Fig. 3.12). Moreover, the vortex sheet is highly influenced and this term is expected to have higher influence on the separation onset of the vortex compared to the others. The term manifests a low influence on the core region, in particular, on the unburst vortex. With the formulation of these first four terms a substantial flexibility with regard to the radial-wise distribution of influence is achieved. Along the preliminar testing of terms also other formulation were tested, but in the end they showed no additional flexibility or significant difference to the employment of these four terms and their combinations.

As second step, additional terms are formulated in order to better address the vortex development direction with respect to the breakdown position and the distinction between the structured unburst vortex, the breakdown proximity and the wake region downstream of breakdown. The region upstream of the breakdown instability is characterized by a coherent vortical structure where high values of rotational and axial velocities are present. Moreover, the vorticity increases along the vortex development path until it reaches a certain quantity which, in combination with the adverse pressure gradient from the trailing edge, determines the occurrence and position of the breakdown instability. The helicity quantity $\mathcal{H}$ is the dot product of the vorticity and the velocity vector and expresses the alignment of the two vectors. Hence, $\mathcal{H}$ is dominant in the structured and unburst portion of a vortex. In fact, the vorticity vector inside a vortex has a dominant component parallel to the vortex axis, with the larger component is the x-component. This component is also the dominant one of the velocity vector. It is intuitive that $\mathcal{H}$ is high inside an unburst vortex where the alignment of the velocity and vorticity is significant. This can also be correlated with the stability of a vortex. Moreover, a modification of the Spalart-Allmaras model is available in the literature [114] and it includes a correction term of the definition of the strain rate used in the production term. Liu et al. [114] have addressed this modification for improving the sensibilization of the SA model to the solution of 3-dimensional corner vortices. Their modification is, however, costrained to a certain range of cases of compressors and is not Galilean invariant. The helicity $\mathcal{H}$ is formulated with the velocity vector which does not maintain the variance and it is dependent on the reference. The proposed methodology could survive a dependency on the reference frame because its application could be exclusively suggested for leading-edge vortices developing around delta wings in a fixed domain, but this would be detrimental to the range of applications or future extensions. Hence, the problem is solved by employing the absolute value of the $\mathcal{H}$ components. This is also useful to avoid the inclusion of the chirality quality, which is detected by the $\mathcal{H}$ quantity. Hence, its value is positive or negative in relation to the vortex's rotation direction. The right wing of a full aircraft would experience an opposite value compared to the left wing, where the vortex rotates counterwise. This would also be valid between the primary vortex and its secondary structure which counter rotates. Therefore, the absolute value $|\mathcal{H}|$ expresses the magnitude of the helicity without referring to the chirality quality or reference frame. The second issue coming from the use of an helicity-based term is that it is a dimensional quantity, again because of the presence of the velocity vector. To overcome this problem, the term is made dimensionless by means of a velocity quantity of reference and the quantity $\tilde{\mathcal{H}}$ is defined (Eq.3.23). For this and many of the relevant flow cases, the free-stream velocity is taken but any other reference velocity could be used. A term (e) which focuses on the structured vortex portion is formulated by coupling the $\tilde{\mathcal{H}}$ quantity, which substitutes the velocity-gradient related factor, and the vortiex identifier ξ. The region of influence is visualized in the upper-right corner of Figure 3.13 and it shows, if compared to the first additional term (a), that the major influence is concentrated on the region upstream of breakdown, i.e. until $x/c_r = 0.6$ in the case of the VFE-2 wing. From $x/c_r = 0.7$ and downstream, the influence drops significantly.

To balance the flexibility of the model, a term which concentrates its influence on the region downstream of breakdown is necessary. Thus, the inverse of the $\tilde{\mathcal{H}}$ variable is used and coupled with a min/max limitation to transform it into a switch function which selects the region which is not dominated by helicity. In order to confine this effect to the vortex flow region, it is multiplied again with the vortex identifier ξ. Its zone of influence is visible in the Figure 3.13, in the middle-left picture. Whereas the influence is significantly reduced in the structured helicity-dominated part of the vortex, a substantial influence is present downstream of breakdown. Larger values are visible in the center of the wake-like vortex and the distribution of the selection quantity reduces in the radial-wise outward direction. The term (f) formulation is concluded with the multiplication of the vorticity quantity as expression of the velocity gradient content in order to preserve the same dimensional form of the original production term. The zone of influence does not change except for some details and the values being larger (Fig. 3.13).

Due to the importance of an accurate prediction of the vortex breakdown type and position, additional flexibiltiy is provided to the model by means of a term (g) which concentrates its influence on the breakdown proximity. The breakdown instability consists of an abrupt disruption of the high tangential and axial velocities of the structured vortex into a chaotic wake flow with lower velocities and only a mild spurious rotational structure. Hence, the region in the proximity of breakdown is dominated by high gradients of velocity due to its sudden change. Moreover, the alignment described from the helicity quantity in the healthy vortex now ceases to exist. The velocity change in the direction of the vorticity is identified as the product between the velocity gradient tensor and the vorticity direction vector. The absolute value of the resulting vector is employed to formulate the term. The quantity can be visualized and it returns high values in the proximity of breakdown but it also maintains significant influence in the structured vortex (Fig. 3.13). The quantity has also influence in the proximity of the leading edge. The coupling with the vortex identifier quantity ξ confines the effect in the vortex and highlights that its effect is negligible in the vortex sheet, the secondary vortex or in the region downstream of breakdown. The higher values are, in fact, in the core of the vortex upstream of breakdown and mostly in the proximity of it. The formulated terms constitute the turbulence model enhancement upon the baseline model. Other terms were tested during the formulation phase of the model, however, the reported ones are the selected ones which provide the better behavior and combination with regards to their possible accuracy improvement and flexibility.

3.4.4 Optimization Procedure

At the end of the turbulence model modification, a set of parameters are available for the model tuning and calibration. A calibration procedure for a generic mathematical model is inherent of the modeling procedure itself, however, several possibilities are available for the developer based on the necessities and objectives. In the context of turbulence models, the target is traditionally set to achieve a global calibration in order to have a single tuning valid for the majority of the flows and, hence, maximizing its predictive capability and minimizing the user effort. For this reason, the calibration targets are in general really fundamental test cases which express the general characteristics of turbulent flows on simple geometries and flow conditions. However, when a globally calibrated model encounters a complex flow whose characteristics are far away from the calibration test cases, with respect to the flow typology, the model's accuracy decreases. Contrarily, a model can be calibrated on a single flow case achieving its maximum possible accuracy but compromising its predictive capability (Fig. 3.6). Model complexity — the number and diversity of parameters and terms — plays an important role in this context, permitting to represent additional features and, as consequence, to increase the possible accuracy and predictive capability consequently. However, a compromise between the two objectives remains a matter of decision for the modeler. The selection of the level of globality is based on different factors:

- The accuracy level required for the numerical simulations to be performed, according to the different steps of design/development/investigation.
- The quality of the available high fidelity data employed as target of the calibration. Their nature (DNS and/or experimental data), their coverage and resolution of the parametric envelope of cases, their amount and their fidelity level.
- The generality and flexibility potential of the turbulence model terms that are available for calibration. In the case of a model enhancement, the effectivity of the additional terms to physically target the flow regions which lack accuracy is fundamental. Hence, they have to be formulated after having acknowledged the sources of inaccuracy at the state of the art and having definded terms that influence these regions and phenomena accordingly.
- The size and variability of the cases envelope for which the simulations have to be performed with the final optimized model. Hence, how broad the spectrum of cases is with regard to flow conditions and geometrical variations.

- The computational and man-hour costs for the model calibration and application relative to the amount of numerical computations to be performed.

In the context of this research, this modeling framework has been followed and focused on two main aspects. The first one is increasing the physical complexity of a baseline model with additional terms which address the sources of the lack of accuracy. This has been described in details in the previous Section 3.4.3. In such a way, the model has the potential to represent the complex target flows with higher accuracy and flexibility without being detrimental for the baseline model on basic cases. The second focus is the calibration procedure which can be defined as a regional calibration. The objective here is to find the best possible compromise between the accuracy improvement possible with the employed model and the predictive capability (Fig. 3.6). Therefore, the target of the calibration is not set to a specific single test case or globally valid for fundamental flows but for a class of flow features of interest, which in this research consist of leading-edge vortices. Nothing excludes the application of the methodology for other types of flows, following the formulation of appropriate terms if required. Vortex dominated flows has such high physical complexity which causes a globally calibrated model to have an inherent lack of accuracy and low probability to properly predict all the regions of the flow. These focuses are considered as the most important factors with regard to the application of a turbulence model enhancement in the context of highly agile aircraft. In fact, in this field, large envelopes of cases are routinelly considered and the main part of the variations are not or only partially related to a drastic variation of the vortex flow. Hence, this gives an advantage to the application of an optimized model on a cluster of flows. Moreover, the accuracy requirements are very high in most cases and increases further as the development phases progresses.

Therefore, along the current research, when a test case is selected to address a certain class of flows, two steps are generally performed: firstly, the calibration phase is performed either on a portion of the data points available or on a certain geometry baseline and, secondly, the derived set of coefficients is applied to a validation spectrum of cases which can be mildly or significantly different from the calibration target in either or both the geometrical and the flow characteristic parameters (Fig. 1.1). In the first phase, the achievable accuracy is evaluated as well as the influence on the flow field or if there is any solver performance variation. In the following validation phase, the flexibility or potential of the method to be applied for a larger dataset is investigated. In this sense, a question is posed: how much accuracy improvement is maintained after a certain amount of geometrical and/or flow condition variations from the baseline calibration target. Therefore, the cluster of target test cases which benefit from the calibration is identified (Fig. 1.1).

The optimization procedure is implemented as a Python toolchain which manages different tasks and it is provided with user defined inputs. The optimization algorithm is formulated from the fundamental level starting with basic Python libraries in order to integrate the routine with the numerical solver and to monitor the corresponding numerical simulations. It consists of a first-order, i.e. a gradient descent optimization, formulation with the target to minimize the objective function which is the weighted

L-1 error $\mathcal{E}(\boldsymbol{c})$ between the numerical results and the experimental data as reference (3.26) and where the variables are the turbulence model coefficients $\boldsymbol{c}$ associated to the additional terms.

$$\mathcal{E}(\boldsymbol{c}) = \frac{\sum_{i=1}^{m} \sum_{j=1}^{n} \left[\varepsilon^{(i,j)} \;\; w_{dp}^{(i)} \right]}{m\; n\; \left(\sum_{i=1}^{m} w_{dp}^{(i)} \right)} \tag{3.26}$$

Where m stands for the number of design points, i.e. configurations in terms of geometry and flow condition, n the number of experimental data points per design point, w_{dp} is a weighting factor that can be set if different sensitivities are necessary for the single design point. $\varepsilon^{(i,j)}$ is the error between experimental and numerical data of the single j-data point of the i-design point. In fact, the user may choose the number of design points to be included in the process.

The optimization algorithm is inherently local, hence, it may return different optima from different starting points. Hence, the optimizer gives the user the possibiltiy to start from any possible starting point $\boldsymbol{c_0}$. In practice, the user tries different starting points to investigate the presence of different local optima and analyzes how much they differ in terms of accuracy improvement and coefficients values. Although, the locality of the algorithm is an important drawback, the algorithm provides fast convergence. Moreover, the understanding of the flow typology and location of discrepancies at a initial phase gives an important insight to the experienced user about which direction is considered physically valid. In this sense, the experience from previous applications of the methodology is important. If a moderate variation in terms of flow condition or geometry is present, an optimal set of coefficients for a previously analized test case may be used as starting point. In such a way, the optimization is faster and is based on a physical common basis between different but comparable cases. Hence, the combination of previous experience along with the investigation of the flow typology change and the testing of a reasonable amount of starting points gives the user a best practice approach to address a new application target. In any case, different optimization techniques are possible to be applied for the methodology and this can be a future task for extending the current methodology.

The optimizer (Fig. 3.14) handles both the starting and monitoring of the numerical simulations, the optimization algorithm and the Input/Output communication between the simulations and the algorithm. At the start, it reads the necessary information of the numerical simulations which act as starting points $\boldsymbol{c_0}$, hence the numerical grid files, the solution files and the numerical parameters and setup to be used. The starting point coefficients $\boldsymbol{c_0}$ are equal to 0 if the baseline SA model is selected. The optimizer progresses iteratively and at every iteration several numerical simulations are started. A base simulation is the one employing the coefficient values furnished from the previous iteration. At the first step, the base simulation is a simple re-start of the starting coefficients $\boldsymbol{c_0}$. At the same time, incremental simulations are started after a certain amount of iterations from the base simulation to speed up their convergences. Every incremental simulation corresponds to the application of a value increment $\boldsymbol{c} + \boldsymbol{\Delta c}$ of one of the active coefficients q. At the end of the iteration, the optimizer receives the outputs of the numerical solutions. For every incremental solution, the error with the experimental data $\mathcal{E}^{(i)}(\boldsymbol{c} + \boldsymbol{\Delta c})$ is evaluated. By means of the sensitivities of the incremental errors compared to the baseline error and the values of the increments, the gradients are evaluated. The algorithm is applied for determining the new set of coefficients for the base simulation of the next iteration. If the error has reached the target level and the variation along the last few iterations is under a certain range, the optimization is finished and the final set of coefficients is selected as the optimum.

There are different settings of the optimization toolchain; some of them are obligatory and need attention from the user and others have default settings and can be altered if issues are encountered along the optimization. The setup of the optimization procedure requires the following inputs:

- The numerical simulation used as starting point as well as the initial turbulence model coefficients.
- The experimental data information regarding their values as well as their typology. For example, if the surface steady pressure measurements are used, the optimizer needs the geometrical position of every probe in order to extract the value from the numerical solution and the weighting factors of every design point and experiment point.
- The algorithm relaxation factor α to regularize the convergence of the optimization in order to avoid the overshoot of local minima. The default value is 0.5.
- The number of numerical iterations of the simulations for both the base and incremental ones. The first optimization iteration employs more solver iterations if the starting model is not the baseline SA model.
- The information about the active turbulence model coefficients. The most important parameters are the increments of the different coefficients which can be set independently. The values need to be suitable for achieving a proper grade of convergence of the numerical simulations with the user defined number of iterations. At the same time, the increments have to be high enough to provide a proper sensitivity level to the numerical solution. The minimum and maximum values can be selected in order to avoid a divergence due to non-physical values.

The optimization is terminated by monitoring the convergence of the minimization function. Whereas most of the settings have been fixed as default values from the application experience, some remain of particular importance for a successful optimization procedure. This is true in particular for the compromise between the computational costs of the optimization and the sensitivities of the turbulence model parameters. Hence, a good compromise between the number of the solver iterations for each optimization step and the incremental values of the coefficients needs to be established in a first phase of testing when a new test case is selected.

An important input from the user is also to determine which design points need to be included in the optimization procedure. In fact, when the calibration test case is

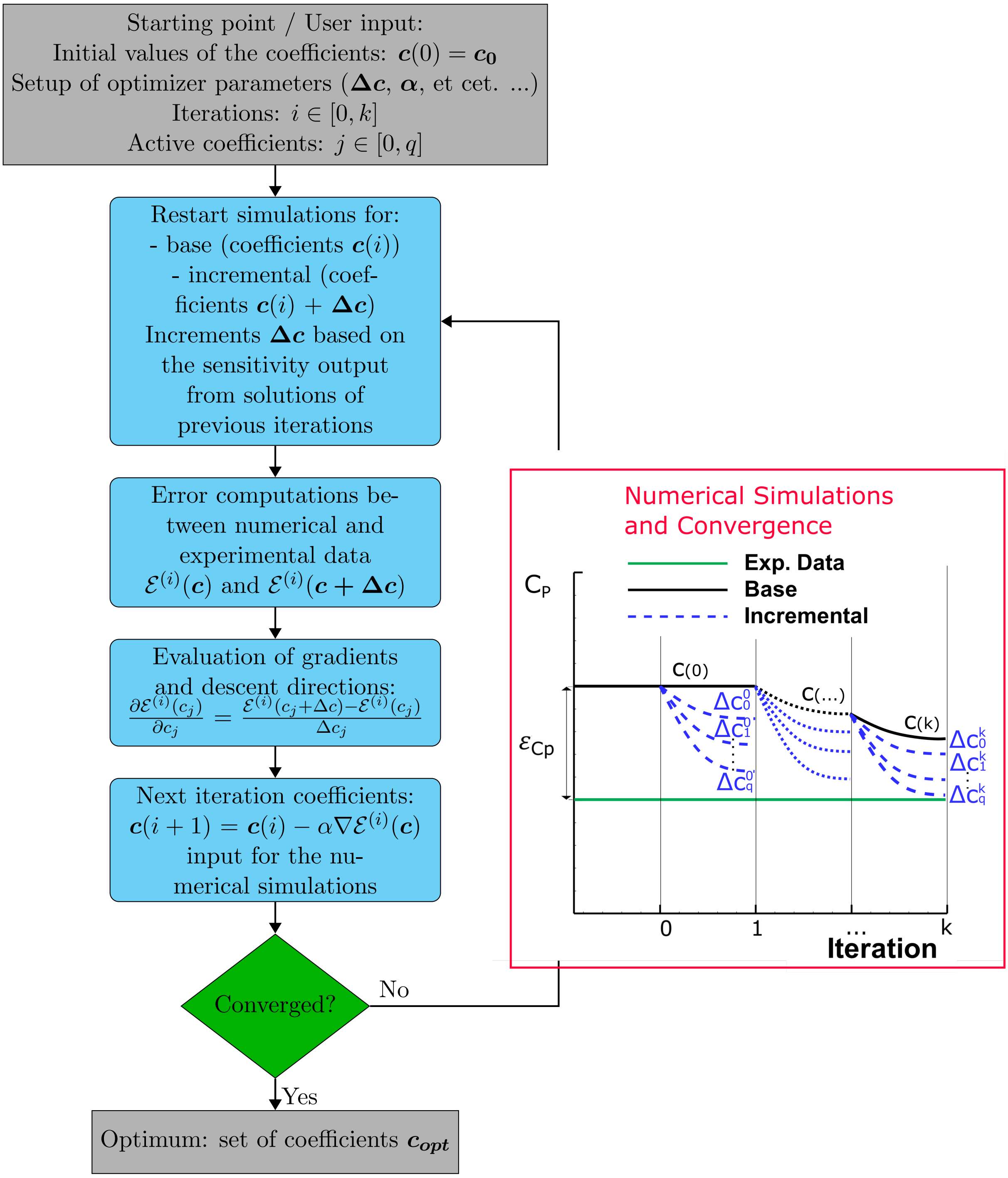

Figure 3.14: Flow chart of the optimization procedure including the gradient descent algorithm and the handling of the intercommunication with the numerical simulations. Also shown, a qualitative convergence of the solver for C_P of the base and incremental simulations along the optimization iterations.

chosen there are different possibilities with regard to which angles of attack, geometric variations or flow condition combinations to be included in the optimization procedure. In this context, once again the experience from past applications is important along with the understaing of the considered flow cases. A series of best practice guidelines are established and updated throughout the application of the methodology on different classes of flow.

The common direction of application is associated with the following points:

- The most baseline geometrical configuration is chosen. Hence, the less complex and without control surface deployments or variations.
- The flow condition which manifests the highest and extensive discrepancies to the experimental data is selected. Often this is performed for a single angle of attack which presents the flow features with the most severe lack of accuracy.
- The sensitivity of the turbulence model terms are tested with single manual runs of reasonable increments to underselect the terms which have more efficiency in influencing the flow features.
- The optimization is performed from the SAE baseline model. Meanwhile, additional optimizations are launched from different starting points to address the algorithm's locality.
- The optimal set of coefficients is tested on the complete angle-of-attack polar. If the accuracy drops, the optimization is restarted from this set of coefficients by inlcuding more angles of attack. The same guideline is followed with regard to other important geometrical or flow condition variations.
- If the optimized model still lack consistent improvements, additional more "exotic" starting points may be tested and more turbulence model parameters may be included. At this point, the gain of accuracy at the cost of additional complexity in the optimization procdedure is evaluated in order to decide whether the level of accuracy achieved as well as its predictive capability on the needed variations are fulfilling the requirements.

After the final set of optimal coefficients is defined, the validation phase usually extends to a different test case or geometry with more consistent variations in the parametric space (Fig. 1.1). A natural decrease of the predictive capability of the model is usually visible except where the vortex flow characteristics remain similar. However, the variation in the accuracy improvement is expected to be low and its gain high enough to justify the extension of the model calibration to a prediction phase. When a new test case is available with new experimental data, a good practice is to test already available optimal sets of coefficients from previous applications to find common directions.

3.5 Methodology Extensions

3.5.1 Zonal Approach

It has been reported how complicated a vortex dominated flow is when multiple vortex structures are present. They generate from different portions of wings with different sweep angles as well as from different aerodynamic devices, e.g. deflected fore- and aft-planes. The presence of different portions of leading-edge devices such as slat surfaces generates different vortical structures in relation to their relative angle of attack with the free-stream flow. Since the model enhancement avoids interactions with the boundary layer and regions not dominated by a vortical structure, it is possible to introduce a zonal formulation in order to provide different sets of coefficients for different confined geometrical regions of the flow domain (Fig. 3.15). The idea of having different zones with different turbulence models is also indicated in the formulation of the GEKO model of Menter et al. [101].

The implementation consists of the geometrical definition of the zones and the introduction of additional coefficients which relate to a zone exclusively. The zones are geometrically defined by means of six planes which determine the outer borders of the parallelepiped. Each plane is defined by a point and a normal vector. In such a way, the zones can be a parallelepiped of any shape in order to easily fit a region dominated by a complex flow feature. The coefficients are now multiple and correlated to an index number. The first values are related to the whole domain except the additional defined subzones. Thus, in the case that no zone is defined, only these first values are active and they will be valid for the whole domain. The successive coefficients relate in an ordered manner to the geometrical zones. When the numerical simulation starts, every point of the domain inside the boxes is flagged with the relative zone number and at the turbulence model computation step the turbulence model coefficients are selected pointwise according to the zone flag. In Figure 3.15, an example of a zonal preparation is represented. Here a double delta wing (Sec. 4.1.6) which employs two vortical structures, respectively at the strake and at the aft wing, is furnished with two zones covering the first separation of the strake vortex (red parallelepiped) and the main wing vortex (blue parallelepiped). Alternatively, it is also possible to just define a single zone and outside of it, i.e. also on the other vortex structure, let the global coefficients be active. This extension of the methodology is expected to increase the capability of the turbulence model to acquire further accuracy enhancement where different vortical structures are present. In particular where it is evident that the cross-interaction and the merging of the two vortices is difficult to be matched from a full-domain calibration. However, as consequence, the predictive capability is possibly reduced as the target flow of the calibration is more specific. The reduction of the predictive capability is expected to be less and less severe the more the flow features are separated from eachother. Another feasible application of the zonal approach is the case where two already available optimal set of coefficients are combined into the same numerical simulation where two delta wings are included in the same configuration. For example, in the case of a fore or rear horizontal control plane with a different geometry compared to the main wing.

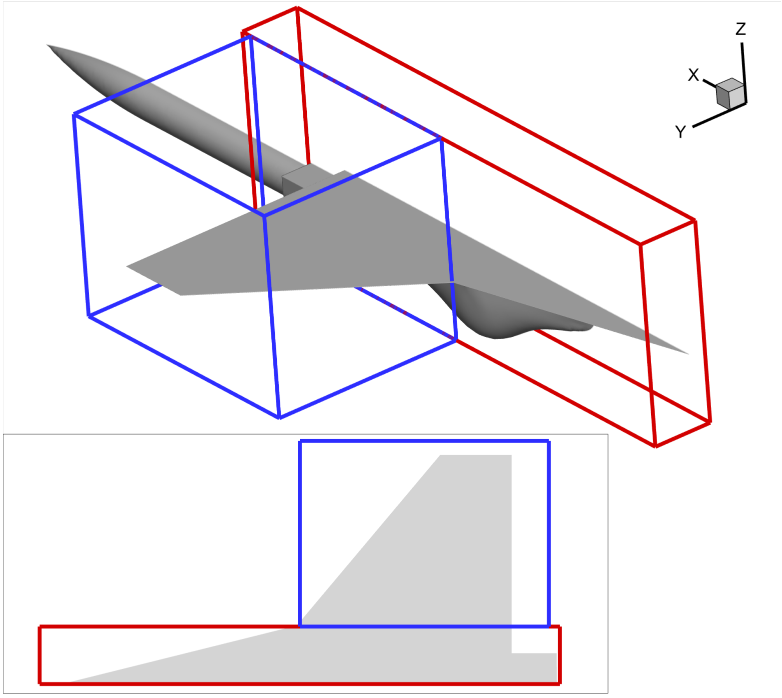

Figure 3.15: Example of the geometrical definition of two distinct zones for two distincts set of turbulence model coefficients on a double delta configuration.

3.5.2 Optimal Turbulence Model Prediction by means of an Artificial Neural Network

In Section 4.4, the primary application of the methodology is reported where the calibration phase for a test case is followed by the validation of the optimized model on progressively different test cases. This is performed to evaluate the potential of improvement for a dataset of cases extended from a common baseline case. The methodology has shown a significant and consistent grade of accuracy improvement. Moreover, this has been confirmed with a statistical evaluation of the accuracy enhancement provided on a large dataset with a common baseline full aircraft geometry performed at ADS. However, a limitation of the methodology remains related to the prediction of the optimal set of coefficients for cases which employ significant differences from the available experimental data or previously optimized test cases. In this section, the possibilities regarding the extension of the predictive capability are reported with respect of their development, application and the outlook on possible future extensions.

3.5.2.1 Application based on the Vortex Development Stage

The first possible expansion of the methodology is the result of the establishment of experiences of the user or the community through consecutive applications of the methodology. As information is gathered about how the optimizer captures the most significant sensitivities of the flow features through the turbulence model optimization, a better insight of the dependencies of the vortex flow stage to the necessary set of the turbulence model coefficients is acquired. By means of the analysis of the optimum application, it is possible to qualitatively correlate the main influences and variation of the resulting solution with the characteristics of the vortex flow and its development. The characteristics of which are also correlated to the wing geometry and flow conditions. As consequence, when a new case is investigated with the baseline turbulence model, it is possible to recognize a similar vortex flow stage and condition. Assuming the baseline SAE model is providing the same discrepancies to the numerical solution, thanks to the previous experience and the identification of the vortex flow condition, an optimum available from previous test cases which employs analogous conditions can be applied in order to improve the accuracy without the need of further experimental data. For this reason a parametric identification of a new test case with respect to its geometrical features and flow conditions is important to position it in the envelope of vortex flow stages as reported in Figure 4.12. An example of this approach is reported in Section 4.4.2, where different test cases are associated to a previously optimum based on the similarities of their geometrical and flow condition features and the SAE baseline discrepancies from the experimental results.

3.5.2.2 Neural Network for the Regression of the Set of Coefficients

The results reported in the Chapter 4 suggest that a reasonable correlation can be identified by the user through experience and analysis. In this way, the predictive capability of the method is enhanced with the application of previous optima for new test cases where the same feature is recognized. However, the extension is limited by a pure transposition of the optimum for clearly identified features at a macroscopic level. For example, when two cases share the same sweep angle, range of angles of attack and vortex flow stage. The user has to face the uncertainties when a new test cases lie outside of the available analyzed test cases. The modification of the optima by interpolating or averaging is not suggested when no additional validation data is present due to the highly non-linear nature of the underlying physics. For this reason, the user has often to set back to the most safe settings. The idea proposed in this section is to apply a machine learning methodology to all the data gathered from the optimizations performed during the research in order to regress a model which returns the optimal set of coefficients of a new case based on its geometrical and flow condition features. It is expected that the accuracy improvement obtained with this extension is lower of what achievable with an optimization process with experimental data but higher than interpolating or adapting manually the set of coefficients from other cases. Moreover, the performance of this model increases as the dataset expands.

3.5.2.3 Data Selection, Description and Preparation

The acquisition, selection and preprocesing of a favourably large amount of unbiased data is essential for the succesful application of a machine learning application. In our case, the data availability with the regard to the pure optimal set of coefficients in relation to the features describing the aerodynamic case is limited. It is also not expected to gather enough data in the recent future in order to have a number of data in the order of thousands. As a common step for such a condition, the data scientist wants to find additional sources of data and/or to extend it by means of data-augmentation techniques. In this case, the possibility to augment data is not straightforward like it is with the state-of-the-art techniques for classification or auto-encoding of image like data [115] where methodologies have been applied and have shown consistent good results in order to avoid overfitting issues. In the framework of the data available, no clear definition of data-augmentation is applicable. Because of the high level of physical and numerical content included in the single data point, a high risk of diminishing the underlying physical information is expected. The proposed solution consists of gathering additional data which are already available and can be extracted from the archive of all the gradient descent algorithms performed along the current research [116]. In fact, the monitoring system of the optimization toolchain saves, throughout the calibration procedure, all the information about the coefficient values, the accuracy level, the single error per comparison point and the sensitivity to the turbulence model variation at every iteration. These are data which represent a correlation between the turbulence model coefficients and the flow case with the achieved accuracy level. However, this source of data is not of the most favourable type. It is highly biased by the action of the gradient descent algorithm which follows a certain direction in the parameter space and it is local. A more favourable option would be, instead, to establish a statistically unbiased distribution of data points by means of a sampling procedure or the set-up of a dataset of simulation to cover the parameters space. This is a possible outlook for the future in order to extend the validity of this approach and to construct a fully unbiased and statistical surrogate model. This is the direction taken by TUBS for the establishment of a surrogate model for their Bayesian Update methodology [109].

At the current state, however, it is considered attractive to investigate if the information already available from the optimization procedures, recovered as feedback into a machine learning approach, returns a valid regression model of the turbulence model coefficients related to a certain geometrical and flow case. Data are available for the different test cases reported in Section 4.4. The data available are gathered by means of a first manual selection of the folders containing the optimization monitor files of the performed iterations. From this set of folders the optimization with mistakes or performed as part of a developing or testing version of the methodology are removed. The remaining folders contain a so called history file where the information of the optimization convergence are reported.

Therefore, the set of features $\mathbf{x}$ is composed of geometrical and flow condition parameters. The geometrical parameters include the most relevant ones for the description of the development of a vortex flow. They are the angle of attack AoA, the sweep angles φ_i (if a single delta wing is present, they share the same value), the taper ratio λ, the aspect ratio Λ, the leading-edge radius as ratio of the root chord r_{LE}/c_r. The flow condition is described with the Mach and Reynolds numbers. The target data $\mathbf{y}$ to be predicted are the turbulence model coefficients (Fig. 3.16). In addition to these features, the minimiza-

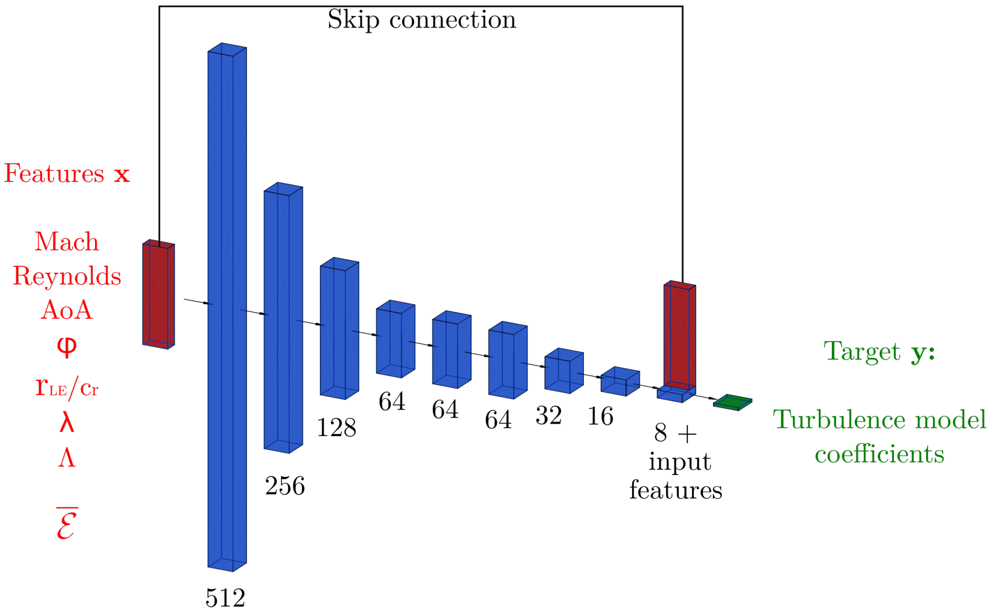

Figure 3.16: Schematic representation of the artifial neural network structure and the information of the layers size.

tion function is introduced by the augmentation procedure, therefore, when a prediction is performed with the neural network, also the level of accuracy improvement needs to be provided as feature. This additional feature is formulated as the relative variation of the mean absolute error with the experimental data:

$$\overline{\mathcal{E}} = \frac{\mathcal{E}(\boldsymbol{c}^i) - \mathcal{E}(0)}{\mathcal{E}(0)} \tag{3.27}$$

Where $\mathcal{E}(\boldsymbol{c})$ is the minimization function of the optimization procedure defined in the Equation 3.26, $\mathcal{E}(0)$ is the error of the baseline model and $\boldsymbol{c}^i$ are the turbulence model coefficients at the i-th iteration. In this section, $\boldsymbol{c}^i$ are also referred to as $\mathbf{y}$ since they are the target data of the regression. In order to be realistic and not to overshoot the range of the learning feature values, the mean of the accuracy improvement levels achieved within the optimization procedures performed during this research is provided as $\overline{\mathcal{E}}$ input for the prediction step. With the described data augmentation procedure, the number of data points including all the available test cases and optimizations histories is around 2400. It is a suitable amount for the development of a proof-of-concept of the method. Additional data may be added as more optimization procedures are performed when new experimental data are available.

3.5.2.4 Structure and Hyperparameters of the Artificial Neural Network

The Artificial Neural Network used for the prediction of new set of coefficients is formulated in the Tensorflow 2 framework [117]. The hyperparameters are selected by means of a grid search of the isolated settings. The best performance is provided by the settings reported in the following table: The Artificial Neural Network predicter (ANN-Pred) model is composed of an input layer for the features described in the previous section. It envelopes a depth network of nine hidden fully connected neuron layers (Fig. 3.16). Every layer is provided with the LeakyReLU activation function [118] with a standard 0.3 slope of the negative values and a batch normalization method is employed for regularization. A significant improvement in the training and validation performances has been provided with the application of a skip connection from the input features to the last hidden layer where they are finally concatenated (Fig. 3.16). A small value of dropout $p = 0.9$ has improved the validation showing how it reduces the overfitting behavior of the training step (Table 3.1). The output of the tensorflow compilation of the ANN-Pred model is reported in the following lines:

Table 3.1: Hyperparameters selected as results of a grid search of their influence on the training and validation performances.

Parameter	Value
Optimizer	Stochastic Gradient Descent (SGD)
Learning rate	0.005
Alpha regulation	0.005
Loss function	MAE
Batch size	32
Number of Epochs	300
Dropout	0.1 every hidden layer

```
_________________________________________________________________
Layer (type)                 Output Shape              Param #
=================================================================
dense (Dense)                multiple                  4096
_________________________________________________________________
dense_1 (Dense)              multiple                  131328
_________________________________________________________________
dense_2 (Dense)              multiple                  32896
_________________________________________________________________
dense_3 (Dense)              multiple                  8256
_________________________________________________________________
dense_4 (Dense)              multiple                  4160
_________________________________________________________________
dense_5 (Dense)              multiple                  4160
_________________________________________________________________
dense_6 (Dense)              multiple                  2080
_________________________________________________________________
```

```
dense_7 (Dense)              multiple                  528
_________________________________________________________________
dense_8 (Dense)              multiple                  136
_________________________________________________________________
leaky_re_lu (LeakyReLU)      multiple                  0
_________________________________________________________________
leaky_re_lu_1 (LeakyReLU)    multiple                  0
_________________________________________________________________
leaky_re_lu_2 (LeakyReLU)    multiple                  0
_________________________________________________________________
leaky_re_lu_3 (LeakyReLU)    multiple                  0
_________________________________________________________________
leaky_re_lu_4 (LeakyReLU)    multiple                  0
_________________________________________________________________
leaky_re_lu_5 (LeakyReLU)    multiple                  0
_________________________________________________________________
leaky_re_lu_6 (LeakyReLU)    multiple                  0
_________________________________________________________________
leaky_re_lu_7 (LeakyReLU)    multiple                  0
_________________________________________________________________
leaky_re_lu_8 (LeakyReLU)    multiple                  0
_________________________________________________________________
batch_normalization (BatchNo multiple                  2048
_________________________________________________________________
batch_normalization_1 (Batch multiple                  1024
_________________________________________________________________
batch_normalization_2 (Batch multiple                  512
_________________________________________________________________
batch_normalization_3 (Batch multiple                  256
_________________________________________________________________
batch_normalization_4 (Batch multiple                  256
_________________________________________________________________
batch_normalization_5 (Batch multiple                  256
_________________________________________________________________
batch_normalization_6 (Batch multiple                  128
_________________________________________________________________
batch_normalization_7 (Batch multiple                  64
_________________________________________________________________
batch_normalization_8 (Batch multiple                  32
_________________________________________________________________
dropout (Dropout)            multiple                  0
_________________________________________________________________
dense_9 (Dense)              multiple                  48
_________________________________________________________________
concatenate (Concatenate)    multiple                  0
=================================================================
Total params: 192,264
Trainable params: 189,976
Non-trainable params: 2,288
_________________________________________________________________
```

3.5.2.5 Training, Validation and Prediction

The dataset is split into a training and a validation set. The validation set consists of 20% of the dataset. The data of the test cases for which the ANN-Pred is applied are not included. The dataset is scaled with a min-max scaler function, i.e. the values of every feature and target are scaled relative to the minimum and maximum:

$$MinMax(x_i) = \frac{x_i - min(x)}{max(x) - min(x)} \tag{3.28}$$

Where x_i is the i-th element of the column x of the dataset and $0.0 \leq MinMax(x_i) \leq 1.0$. The training process is performed with SGD optimizer for 300 epochs and the loss function MAE drops significantly (Fig 3.17). In the last 50 epochs the training loss oscillates between 0.052 and 0.05, therefore, the convergence is reached and the training process is interrupted. The validation loss function exhibits a similar value and the convergence manifests a proper behavior of the learning process. The shape and the distance between the two curves exhibits no overfitting of the model to the data. The resulting MAE is of the order of 0.05 which means a 5% error between the actual turbulence model coefficients and the predicted ones. It is a proper level of accuracy not only for a proof-of-concept phase of the methodology but also for a first phase of application. For this reason, the methodology has been applied to a series of different test cases reported in Chapter 4.

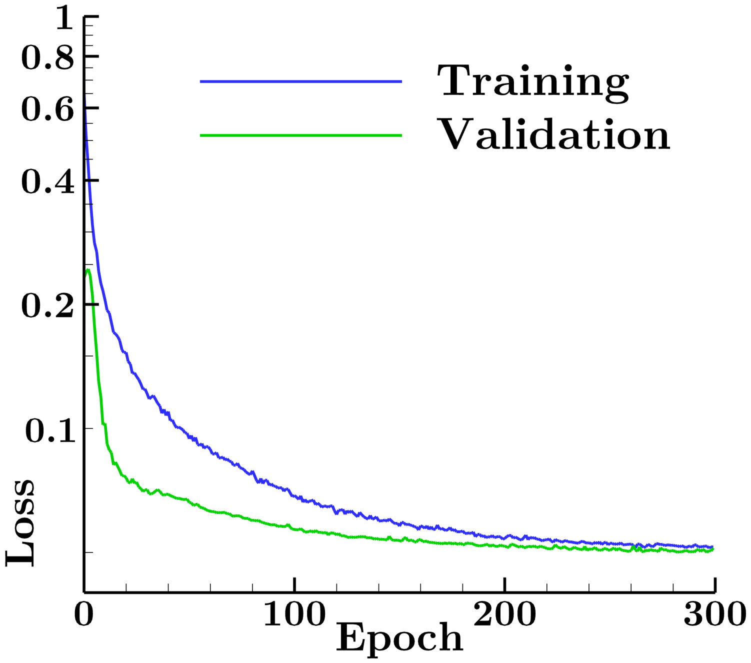

Figure 3.17: MAE loss function vs the epoch number for the training and validation steps.

4 Results and Discussion

4.1 Test Cases Description

The test cases used for the application of the methodology are reported in this section. Some of the test cases have already been described in the state-of-the-art section (Sec. 3.2). In such a case, they are referred to the according subsection and completed for the necessary information of the description of results. The test cases are grouped according to their overall geometrical and vortex flow characteristics.

4.1.1 AVT-183: Diamond Wing

The 53° swept diamond wing has been designed and studied in the framework of the NATO-STO AVT-183 task group and its description is introduced in Section 3.2.4. The objective was to investigate the separation onset and the vortex topology around a rounded leading edge which is considered attractive for the application to blended wing bodies. The sweep angle is associable to the SACCON geometry [61] which was used as reference for the establisment of the diamond wing test case. The separation onset is highly sensitive to the boundary layer regime developing at the leading edge. Experimental campaigns and numerical investigations have been performed to understand the dependency of the separation position [68, 69]. For this reasion, the angles of attack in the range between 10° and 20° have been the main target of research. By moving to higher angles of attack, a fully developed vortex flow with breakdown (25°) and a stall condition is achieved ($\geq 30°$) [70]. The wind tunnel experiments have been performed at the W/T-A at TUM-AER. The model is a half-span model mounted above a peniche (Fig. 4.1). The peniche is an ortogonal extrusion of the root profile with 90mm height. The experimental data with the application of 150 μm trip dots are considered to be compared with the fully turbulent numerical simulations [119]. Steady surface pressure measurements are used to evaluate the accuracy of the turbulence model modification and its numerical results.

The geometrical parameters are reported in Table 4.1 whereas the selected flow condition is shown in Table 4.2. The 53° sweep angle is the lowest encountered for a single wing in the current research. The diamond shape is delineated by the relatively larger φ_{TE} of -26.5°. The aerodynamic profile is a NACA 64A006 with a r/c_r of 0.23% which means that a relatively round profile is encountered by the flow and a partially developed vortex takes place at moderate angles of attack. As mentioned, the target of research is the development of the incipient separation of a vortex. However, the fully developed and stalled cases at the largest angles of attack are employed as validation cases for the application of the optimization performed on the Model53 data, described in the following section.

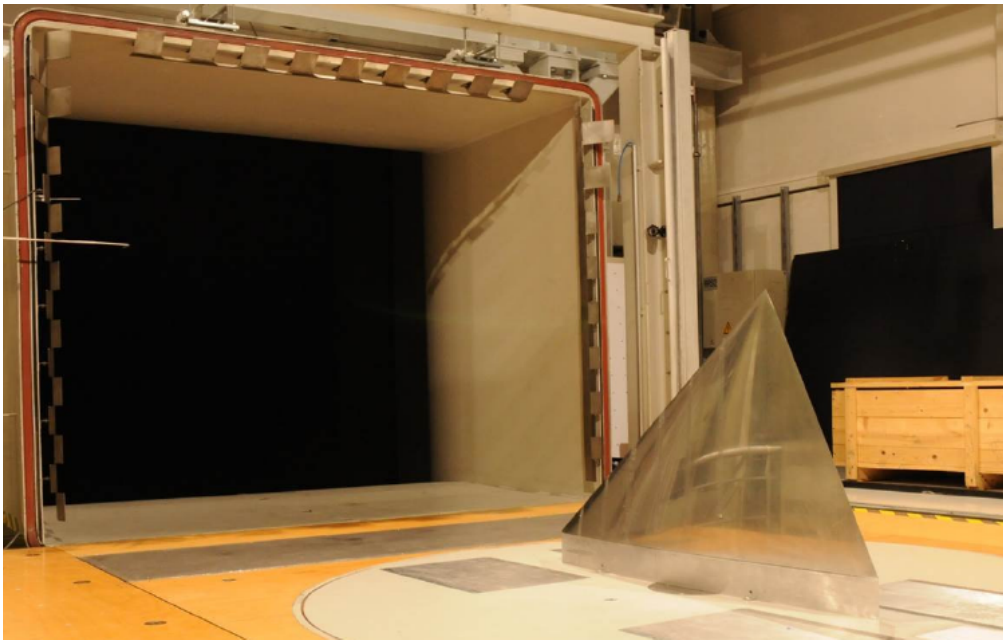

Figure 4.1: The diamond wing half-span model (AVT-183) mounted in the open test section of the W/T-A facility at TUM-AER [119].

4.1.2 Model53 & Model56

The Model53 and Model56 delta wings fabrication is extensively described in the appendix (Section A) due to its peculiar production which employs an additive manufacturing technique [120]. The development of this novel production procedure has been a parallel target of research in the context of this work. The Model53 geometry (Table 4.1) consists of a 53° swept cropped delta wing, with a 4° tip twist and a 20° deployed slat surface (Fig. 4.2). Hence, the sweep angle coincides with the one of the AVT-183 diamond wing and is the lowest available for the main wing in this research. The Model56, instead, consists of a variation of the Model53 with a 3° increase in the sweep angle, namely $\varphi = 56°$ and is designed to be a valuable validation case for the Model53 optimization. Due to the presence of a slat deployment, a first vortex separates at the apex of the wing while a second separation takes place at the deployed slat (Sec. 1.2.2.2). The different local angle of attack influences the second vortex flow field which has different characteristics compared to the first one. The two vortices interact at larger angles of attack.

In fact, the most challenging vortex flow stages take place at large angles of attack for which aircraft with a similar wing shape fly with a comparable slat deployment. A second but not less important reason, is the higher complexity introduced by the presence

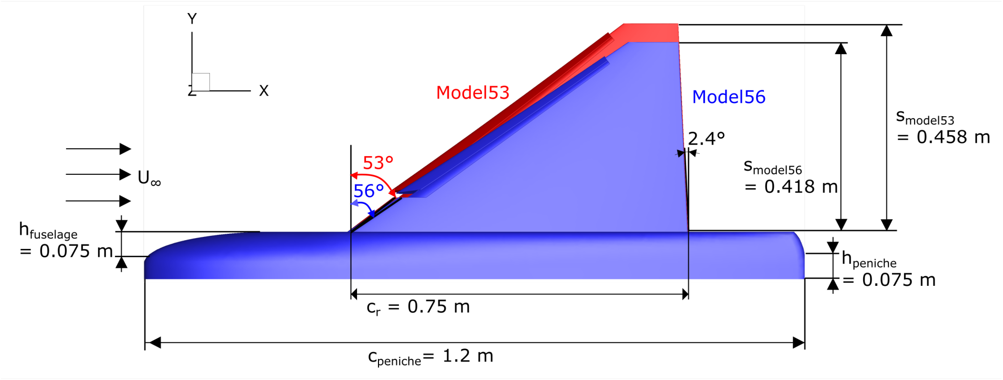

Figure 4.2: Top view of the xy-plane representing the Model53 and Model56 construction sketch and indication of the main geometrical distances.

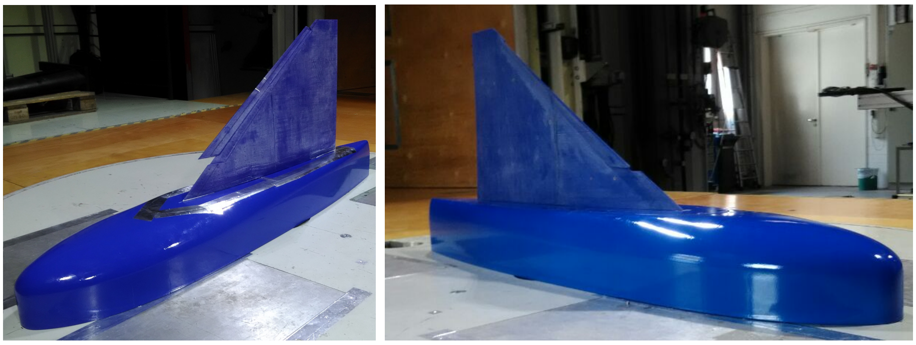

(a) Model53 **(b)** Model56

Figure 4.3: Wind tunnel models mounted on a common generic fuselage part and péniche system at the open section of the W/T-A facility at TUM-AER.

of two vortical structures and their developing interactions. Hence, this enhances the challenge of the methodology application and it gives further insight how complex flow cases are handled by the turbulence modeling extension. Another design feature has been the selection of a relatively small leading-edge radius of 1.2 mm, i.e. $r/c_r = 0.16\%$. Therefore, the vortex flow separation is extended to the geometrical apexes. This permits to concentrate the investigation on the main source of discrepancies for similar configurations which is the vortex development and breakdown strength and position at large angles of attack (Sec. 3.2).

The wind tunnel measurements have been performed at the W/T-A facility (Fig. 4.3) at TUM-AER [120] and steady surface pressure measurement data have been used as target quuantites of the calibration procedure [108]. The half model is mounted on a system of generic fuselage and peniche to avoid interaction with the wind tunnel floor boundary layer. The low subsonic flow conditions are reported in Table 4.2. The Model56 shares the same mountage, flow condition and experimental procedure.

4.1.3 SAGITTA - 55° Swept Blended Wing Body

The SAGITTA test case refers to the 1:10 full W/T model of a blended wing body configuration developed ina joint research program of TUM, THI, DLR and Airbus Defence and Space [119, 73]. It has a leading-edge sweep of 55° (Table 4.1) and the possibility to interchange the leading-edge geometry [119, 74]. Hence, the leading-edge sweep provides a mild variation from the Model53 and AVT-183 diamond wing sweep angles. Moreover, it employs a diamond shape similarly to the AVT-183 wing. The model employs 7 different sections for static pressure measurements and it is connected to the mounting system through a rear sting and a six-component balance in order to measure forces and moments (Fig. 4.4). The mounting system permits 3-axis independent movements, therefore, it offers the possibility to measure different sideslip and roll angles for different angle-of-attack polars. The surface pressure data are employed for the evaluation of the numerical results in the current work. The wind tunnel measurements are performed with a Reynolds number of $Re = 2.3 \cdot 10^6$ based on the mean aerodynamic chord l_μ of 0.801m and at a Mach number of $M = 0.13$ which correspond to a free stream velocity between 44 and 46 m/s (Table 4.2). The wind tunnel measurements are performed in a range between -4° and 20° and the reference experimental data taken for this research are the ones were the transition is fixed by means of the application of trip strips similarly to what studied on the AVT-183 diamond wing [119]. In a second phase of the study of the SAGITTA configuration, additional wind tunnel measurements have been performed for the extension of the flight envelope and the evaluation of the overal aerodynamic characteristics. In this second phase, the maximum angle of attack has been increased up to 40° while the free stream velocity has been slightly decreased to $M = 0.1$ and $Re = 1.77 \cdot 10^6$ based on the mean aerodynamic chord of 0.801m (Table 4.2). The focus of the first phase of experiments at low/middle angles of attack was the investigation of partially developed vortices around blended wing body geometries. A good cross comparison can be performed between this geometry and the AVT-183 diamond wing which employs a similar configuration with variations in terms of sweep angle, body thickness and leading-edge radius. The relative thickness is of 12% and it is twice the value of the AVT-183 wing. Therefore, an attached flow is maintained up to larger angles of attack compared to the AVT-183 case. This difference is significant with respect to the development stages of the vortices and it introduces additional challenges for the turbulence model extension. Moreover, it provides insight for the validation of a previously optimized version of the model. During the research of Hövelmann [73], the leading edge was splitted in four sectors with interchangeable radii. For the current application, the baseline geometry is chosen which consists of a first sector with a sharp leading edge and a rounded edge (0.99% of c_r) for the remaining leading-edge extension. The range of high angles of attack manifest a vortex stage from a fully developed status to a completely stalled and shedded one. For this reason, this portion of angles of attack

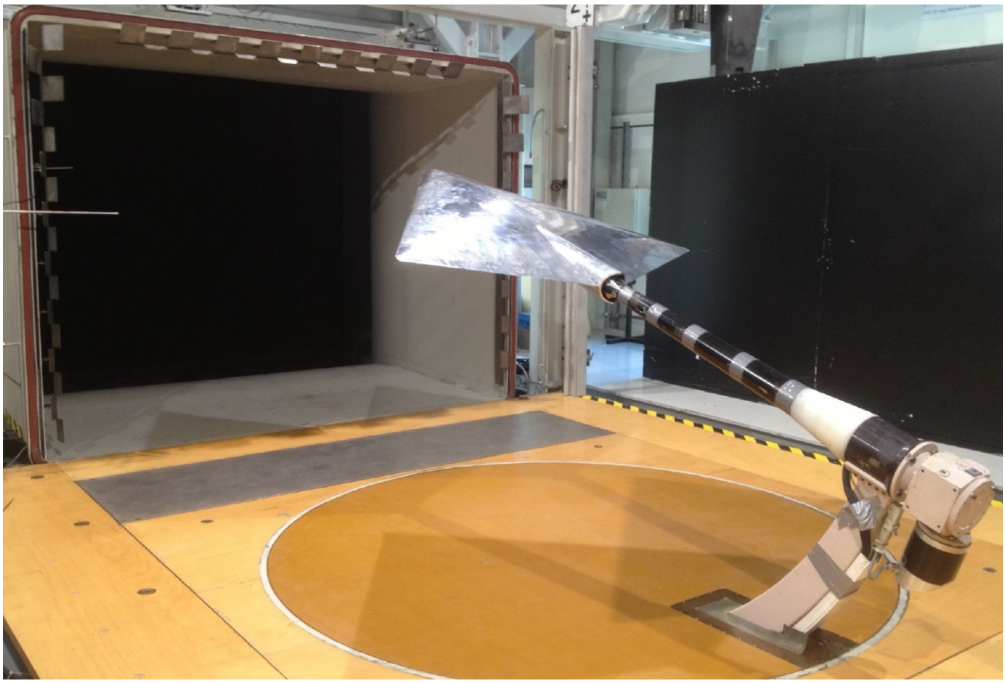

Figure 4.4: The SAGITTA blended wing body full-span model mounted in the open test section of the W/T-A facility at TUM-AER [119].

provides an additional validation case for similar vortex flow topologies at comparable sweep angles.

4.1.4 60° Delta Wing - DW60

As mentioned in the previous section 4.1.2, parallel to the current research work, a methodology has been developed for the production of semi-span wind tunnel models by means of additive manufacturing techniques (App. A). The possibility to produce full models has been successively investigated with the production of a full-span 60° cropped delta wing — called DW60 for abbreviation — without a fuselage and a straight trailing edge. Like the Model53 and Model56, it is produced in PLA material by means of a FDM procedure and it includes surface pressure probes. Differently from the Model53, where the pressure taps and tubes are integrated in the wing, here hollow portions are designed in order to accomodate the sylicon tubes for the pressure measurements, which are directly connected underneath the suction surface in correspondence to orifices already produced in the 3d-printing process (Fig. 4.5).

The pressure probes are integrated in only one of the wing halves. No sideslip has been measured as the objective was to validate the reliability and fidelity of such typology of wind tunnel model. No balance system has been integrated to measure aerodynamic forces because the objective of the model is to provide data about the surface pressures which has a higher grade of importance in the application of the turbulence modeling

Figure 4.5: DW60 wind tunnel model seen from below, showing the hollow portions for the tubes accomodation and the interconnections for the final assembly.

calibration method and provides better insight in evaluating the measurement of the vortex structure above the upper wing surface. The base airfoil is a NACA 65A006 airfoil with a chord length of 515 mm (Table 4.1) and a radius equal to 0.3% of the c_r. The wind tunnel measurements have been performed at W/T-B at TUM-AER (Fig. 4.6) and it has been mounted on a support connected at the neutral point of the wing to its lower surface. This test case offers the possibility to investigate the predictive capability of optima derived from similar or different planforms. Moreover, it offers a difference with respect to Reynolds and Mach number compared to the low subsonic condition for the previously reported cases. The geometry is also relatively simple and it permits to concentrate the analysis on the single vortex flow per side. The range of angles of attack is constrained by the support system and the maximum angle of attack achieved is 25°.

4.1.5 65° Delta Wing - VFE-2

A highly swept delta wing test case is investigated and it employs a 65° sweep angle. The geometry (Table 4.1) corresponds to the delta wing investigated by NASA in a series of experimental and numerical analysis [121, 122, 123] covering a wide range of angles of attack, Mach numbers, Reynolds number and also geometric modifications, i.e. interchangeable leading edges (Sec. 3.2.1). The sharp, small and medium leading-edge radii are considered in the present work for either calibration or validation. Following the NASA investigations, a down-selection of cases were performed in the context of the Second International Vortex Flow Experiment (VFE-2) [124] for which additional experimental data are available such as PIV and PSP data for selected angles of attack. The main part of the investigation concentrates on the subsonic regime at $M = 0.4$ while the Reynolds number varies between $Re = 2.0 \cdot 10^6$ and $Re = 6.0 \cdot 10^6$ (Table 4.2). The

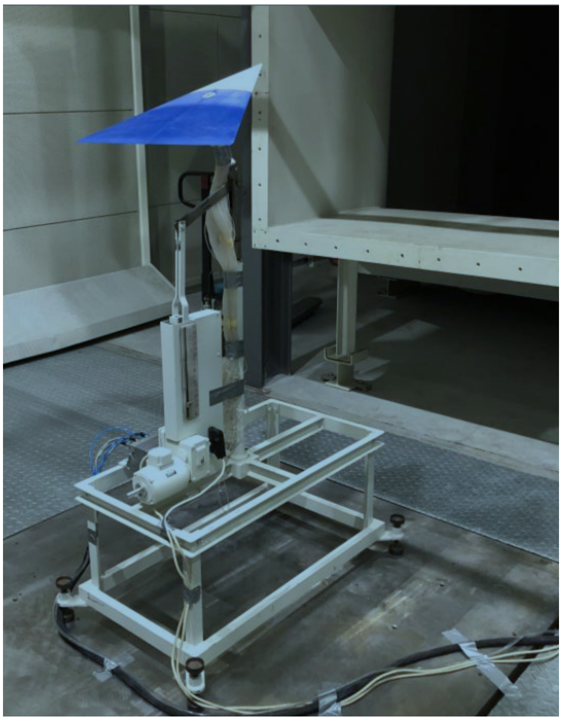

Figure 4.6: DW60 wind tunnel model installed in the open section of the W/T-B facility at TUM-AER.

geometry is the same used for the figures in the description of the model formulation (Sec. 3.4) and for indicating the physical features of a vortex flow with the Figures 3.12 and 3.13. The calibration case is performed with the small leading-edge radius whereas the validation is on different Reynolds numbers and leading-edge shapes. The main focus for the experimental data is on the steady surface pressure measurements for the range of angles of attack where the main discrepancies are found in the course of previous intensive research works [124, 125, 126] (Sec. 3.2.1) as well as with the application of the baseline SAE model during the present methodology application. The main numerical issues are found in the prediction of the breakdown type and position as well as the vortex structure, development stage and suction levels. The most relevant angles of attack are reported for discussing the results.

4.1.6 Erickson Double Delta Wing - DD76/40

In order to widen the range of investigated flows, a planform of multiple portions with different sweep angles is selected. A solution of this kind has high relevance as the application of such class of planforms is frequently applied in modern highly maneuverable aircraft. Moreover, the vortex flow complexity increases extensively as the separation of multiple vortices takes place in correspondence with the different leading-edge sections. Therefore, the presence of multiple vortices and their mutual-interactions introduce additional challenges for the investigated numerical methodologies. For this reason, it is considered a complex test case but fundamental for improving the method potential. The NASA double delta wing [127] is selected because it has been subject of a wide range of experimental investigations, including the measurements of integral forces, surface steady pressures and PSP measurements. The leading-edge shape is completely sharp and no partially developing vortex is therefore experienced. The main focus of the calibration is posed on the aerodynamic coefficients data due to the low number and resolution of the suction side pressure probes. Hence, the optimization on this test case provides a good test case for verifying the behavior of the calibration procedure by exclusively including integral forces. The pressure measurements are used as additional verification of the accuracy variation. The planform is available in three variations with regard to the juncture shape between the inboard and outboard leading edges. The junction influences drastically the structure of the outboard vortex as well as its downstream cross-interaction with the inboard vortex. Along the NASA experiments, three different junctions are investigated: a baseline with no fillet, a parabolic fillet and a diamond shaped fillet. The first two have been used along this research and the baseline one at subsonic conditions is reported in the results şection (Sec. 4.4.5.1). The baseline planform is composed by a 76° swept strake inboard section and an outboard wing with $\varphi = 40°$. The leading-edges junction is situated at 53% of c_r (Table 4.1). The strake, by employing a higher sweep angle, has the objective to generate a highly structured vortex in order to stabilize the outbard vortex which is more sensitive to the occurence of a breakdown instability. With regard to the flow conditions, different Mach numbers are reported from subsonic to supersonic conditions at a Reynolds number of 2 million and in a range of angles of attack between 10° and 20° (Table 4.2). The test case is used for a calibration process of a multiple vortex configuration and to investigate the capability of a zonal approach as an extension of the proposed methodology (Sec. 3.5.1). The optimum derived from this configuration is then tested to similar configurations which employ different wing portions with significant junction angles.

4.1.7 AVT-316 Generic Triple-Delta Wing Configuration

In the context of the NATO-STO AVT-316 task group [75, 76], a series of generic planforms, which consist of multiple wing portions with different sweep angles, are subject of both experimental and numerical investigations [77, 128]. The relevance of multiple delta-wing planforms have acquired more and more relevance throughout the last decades due to their potential of further improving the aerodynamic characteristics of highly agile aircraft. The test case is selected as target of the proposed methodology due to the presence of high fidelity experimental data and because it is a reference to the present state of the art for the best practices of numerical simulations from different international contributors (Fig. 3.5). The test case manifests an increased level of complexity with respect to the vortex flow characteristics since it is dominated by multiple vortex structures which interact. The experimental data employed in the reported results are related to the ADS-NA2-W1 triple delta wing which employs respectively a 52.5° for the "negative" strake, a 75° sweep for the mid wing section and a 52.5° sweep for the rear wing section (Table 4.1). The planform of the related wind tunnel model is 8 *mm* thick and employs a sharp leading edge. Different flow conditions have been investigated and set as target of the methodology application. However, the results reported comprehend the flow conditions (Table 4.2) at M = 0.5 and 0.85 with different angles of attack and also non-symmetric flow, i.e. a non-null sideslip angle. The angle-of-attack range covers angles up to 40°. Therefore, the optimization has been employed for the angles of attack and sideslip where the highest discrepancies relative too experimental data for standard turbulence model are present. The available experimental data comprehend forces and moments as well as digital plots of postprocessed steady PSP measurements. PSP data furnish a high resolution distribution of the surface pressures and a suitable source of experimental information to be inferred in the optimization procedure. The test case works also as a validation case of the optimum derived from the DD76/40 case (Sec. 4.1.6)

4.1.8 Summary of Test Cases

During the development, testing and application of the proposed methodology different test cases for a series of flow and geometrical variations have been analyzed. A subportion of them is reported for the sake of a better explanation of the most relevant steps which have brought the research work to its completeness at this dissertation state. The reported test cases are summarized by means of the following tables (Tables. 4.1, 4.2), offering an overview of the covered parametric space with respect to geometrical and flow conditions.

Table 4.1: Wing planform parameters of the reported test cases. If a half model is considered, the surface area of the full geometry is reported

Name	φ_{LE}	φ_{TE}	Λ	λ	$c_r[m]$	$c_t[m]$	$l_\mu[m]$	$b/2[m]$	$S_{ref}[m^2]$	$r/c_r\%$
AVT-183	53°	-26.5°	2.191	–	1.2	0.0	0.8	0.657	0.788	0.23
SAGITTA	55°	-25°	2.001	0.025	1.2	0.03	0.801	0.6175	0.759	var
Model53	53°	-2.7°	2.06	0.16	0.75	0.12	0.51	0.458	0.408	0.16
Model56	56°	-2.7°	1.92	0.146	0.75	0.11	0.505	0.418	0.364	0.16
DW60	60°	0.0°	2.15	0.0194	0.515	0.01	0.344	0.2872	0.1535	0.3
VFE-2	65°	0.0°	1.865	0.0	0.654	0.0	0.436	0.3048	0.1993	0.0-0.1
DD76/40	76°/40°	0.0°	2.323	0.16	0.406	0.065	0.277	0.4147	0.0717	0.0
AVT-316 ADS-NA2-W1	52.5°/75°/52.5°	-6.25°	2.11	0.125	0.802	0.1003	0.468	0.4166	0.3289	0.0

Table 4.2: The flow conditions of the reported test cases.

Name	M_∞	Re_{l_μ}
AVT-183	0.15	$2.7 \cdot 10^6$
SAGITTA ($AoA \leq 20°$)	0.13	$2.3 \cdot 10^6$
SAGITTA ($AoA \geq 20°$)	0.1	$1.77 \cdot 10^6$
Model53	0.15	$1.7 \cdot 10^6$
Model56	0.15	$1.7 \cdot 10^6$
DW60	0.09	$0.7 \cdot 10^6$
VFE-2	0.4	$2.0 - 60.0 \cdot 10^6$
DD76/40	0.5	$2 \cdot 10^6$
AVT-316 ADS-NA2-W1	0.5 - 0.85	$8.93 - 12.53 \cdot 10^6$

4.2 Numerical Setup

In the following section, the numerical setup of the different CFD simulations is reported by indicating which methodologies are in common or exclusive for the different test cases.

4.2.1 Numerical Settings

All the numerical simulations in the present work, including the simulations inside the optimization procedure and the preliminary testing for the model formulation, are performed by means of the TAU-Code [129] solver. It is a highly-parallelizible solver of the Navier-Stokes equations suitable for the computation of large domains on high performance computer systems. The software is developed by the German Aerospace Center (DLR) with a cell-vertex formulation and the capability to run with hybrid-unstructured grids. With respect to the numerical discretization and grid preparation, further details are described in Sec. 4.2.2. The simulations consist of 3-dimensional aerodynamic cases in a compressible fully-turbulent flow regime. The TAU-Code reads in the primary grid by means of its preprocessing module in order to generate the different levels of refinement of the multigrid scheme and the dual grid. Due to the cell-vertex formulation, a dual grid is necessary in order to prepare the control volumes correlated with the grid points and be valid for the application of a finite volume formulation. In order to employ a FVM method, different discretization schemes are available which the users can select according to the flow case to be solved. During this research, a “steady” solution is the target of the performed numerical simulations. However, an implicit dual-time stepping method is used to increase the solver stability. The time steps are large because the objective is to improve numerical stability and not to capture unsteady phenomena. Unsteady phenomena (e.g. the helical mode instability leading to breakdown) are expected to experience a reduction in accuracy with the numerical setup but this reduction is considered lower than the mismatch due to turbulence modeling. Therefore, the computation of the unsteady solution is not set as a requirement of the research due to the significance of the additional computational costs. Moreover, for the generation of large data-sets, usually steady solutions are considered enough for similar configurations. With respect to numerical relaxation, a multigrid method is employed to accelerate and stabilize the convergence by means of the generation of different grid levels at progressively coarser levels of refinement. This provides the capability to employ larger time steps and to switch grid refinement to coarser levels, following a certain switching cycle, in order to diffuse faster the oscillations with large amplitudes which are otherwise conserved for longer at the finer levels of discretization. With respect to the resolution in time, a Backward-Euler implicit method is used along with a LUSGS algorithm. The fluxes are discretized by means of the AUSMDV methodology which combines two variations of the original formulation of the Advection Upstream Splitting Method (AUSM) which are the flux Difference (AUSMD) and the Vector splitting (AUSMV) methods. With respect to turbulence modeling, all the reported numerical simulations are performed with the original or one of the variations/extensions of the SAE turbulence model, either available or formulated and programmed during the research work. The numerical simulations are run on the HPC system SuperMUC at the Leibniz Supercomputing Centre (LRZ), which contributes to the Gauss Centre for Supercomputing (GCS). The computational budget has been granted by LRZ with the project *pr27ce*[1]. It has permitted to run the numerical simulations in a highly-parallized and efficient manner. The high performance of the HPC and the support of LRZ to the current research is gratefully acknowledged[2].

4.2.2 Numerical Grids

With regard to the numerical grids used in the present work, two different pieces of software have been employed. The in-house Mesher from Airbus Defence and Space and the commercial software CENTAUR from CentaurSoft [3]. The two utilities are comparable in terms of typology and overall characteristics of the achievable numerical grid. Both are used in order to follow the same meshing procedure and quality targets. The numerical grids consist of hybrid-unstructured discretizations where a structured portion of the mesh is dedicated for the resolution of the boundary layer regions in concordance with the viscous wall treatment of the geometrical outer surfaces. On the one hand, the structured prism layers permit to avoid high grid dissipation in the boundary layer region where the solution is highly sensitive and the main component of the velocity gradient is in the wall-normal direction. On the other hand, the unstructured mesh offers the best flexibility to follow complex geometries. Pyramidal elements are employed by the mesher to connect the prism layers and the outer tetreahedrons. Moreover, particular attention is dedicated to increase the resolution with regard to highly curved geometrical features such as wing and fuselage edges (Fig. 4.8) as well as the intersection of geometrical features. The regions of the flow field which are dominated by the vortex flow — influenced by strong velocity gradients — are refined in order to include the vor-

---

[1] `https://doku.lrz.de/download/attachments/43320893/2020_SuperMUC-Results-Reports.pdf`, retrieved January 2022

[2] `www.lrz.de`, retrieved January 2022

[3] `www.centaursoft.com`, retrieved January 2022

tex flow development along the computed flow conditions, in particular, with respect to the envelope of angles of attack (Fig. 4.8). Additional levels of fineness are also applied in order to address the mesh sensitivity level of the methodology and for evaluating the level of convergence of the grid fineness level with regard to the numerical result. For the major part of the computations, a reasonable grid fineness is chosen in order to hedge the computational cost to a reasonable level. Hence, a refinement level is chosen which provides resolution errors which are insignificant in comparison with the ones related to turbulence modeling. As shown in Figure 4.7, whereas the additional levels of mesh refinement introduce a small variation of the numerical results for the baseline model, it is important to notice that a similar sensitivity is present with respect to the application of the optimized model. This sensitivity is the effect which is relevant for the successful employment of the optimization procedure. Therefore, a moderate level of refinement (such as level 0 in Figure 4.7) is chosen for the optimization procedures. The numerical grid generation starts from the description of the surfaces, it continues with the generation of the prism layers and concludes with the volumetric tetrahedral grid (Fig. 4.8).

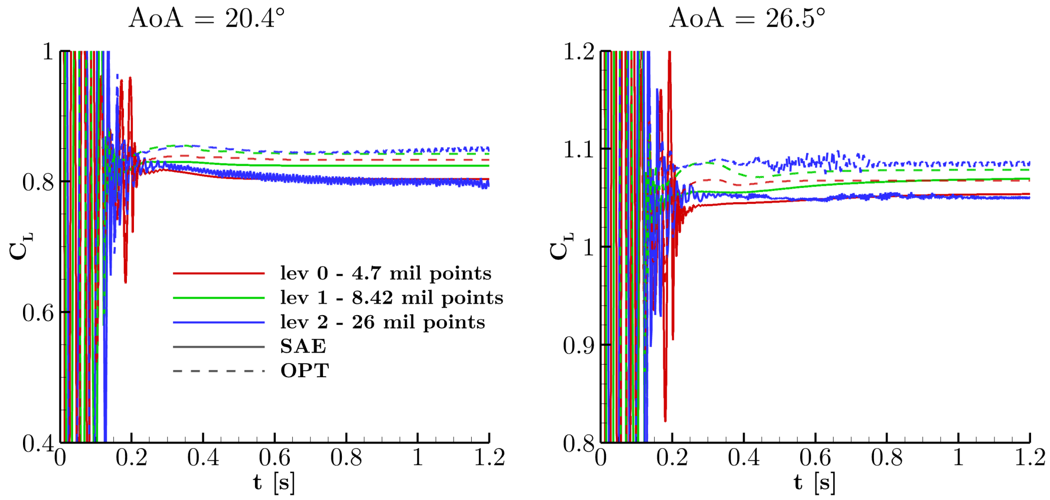

Figure 4.7: The mesh convergence results are reported for the 65° swept delta wing with $r/c_r = 0.033\%$, $M = 0.4$ and $Re = 6 \cdot 10^6$. The C_L convergence is reported for the angles of attack of 20.4 and 26.5 for three levels of mesh refinement. The baseline SAE and the optimized turbulence model are compared.

The number of points of the numerical grids are listed in Table 4.3 and they are represented in Figures 4.8, 4.9, 4.10 and 4.11. With regard to half-span models, where no sideslip condition is investigated, the numerical domain is included in a hemisphere composed of the symmetry plane and the farfield surface (Fig. 4.8). The symmetry plane corresponds to the height which is reached by the boundary layer developing above the wind tunnel floor of the correlated experimental investigation. If the half configuration is derived from a full wind tunnel model, the symmetry plane simply corresponds to the geometrical symmetry of the model. The farfield employs the definition of the free

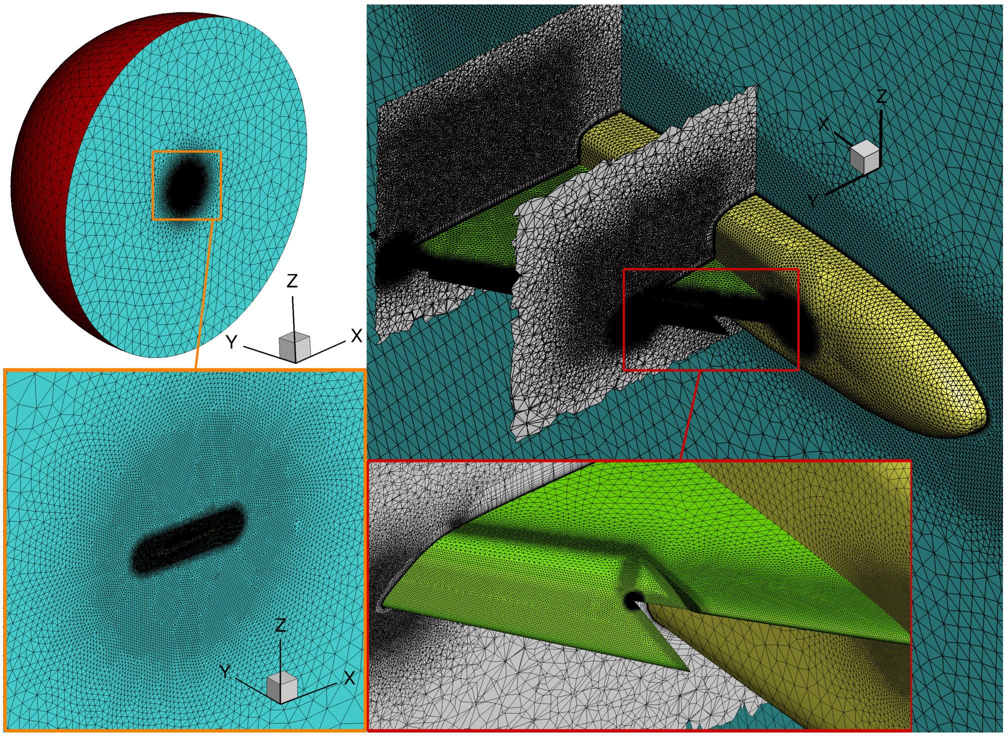

Figure 4.8: Visualization of the numerical grid for the Model53 case.

stream conditions and it is created in order to have a sufficient distance between the geometry and the freestream. In this way, a proper flow relaxation is achieved during the numerical simulation along the domain volume. In case of a full model, a symmetry boundary condition is not present and a full sphere is employed as a farfield condition. Geometrical components present in the wind tunnel models which presumably influence the flow around the aerodynamic surfaces are also included in the computational domain with a simplified geometry. With regard to a full model, the more common example is the support sting which connect the model to the support and the moving system. The connection sting can influence the experimental measurements of vortex dominated flows [119]. With regard to half models instead, a peniche is usually applied to avoid the interaction of the wing to floor boundary layer which may significantly interact with the separation onset of the vortex structure at the delta wing's leading edge [120]. However, the peniche geometry needs to be included in the numerical domain as it also influences the vortical flow development over the wing surface.

4.3 Classification of Test Cases

Due to the presence of a broad spectrum of test cases to which the turbulence model adaptation methodology has been applied, a closer classification is useful for further discussing the results without unnecessary repetitions. The classification can follow dif-

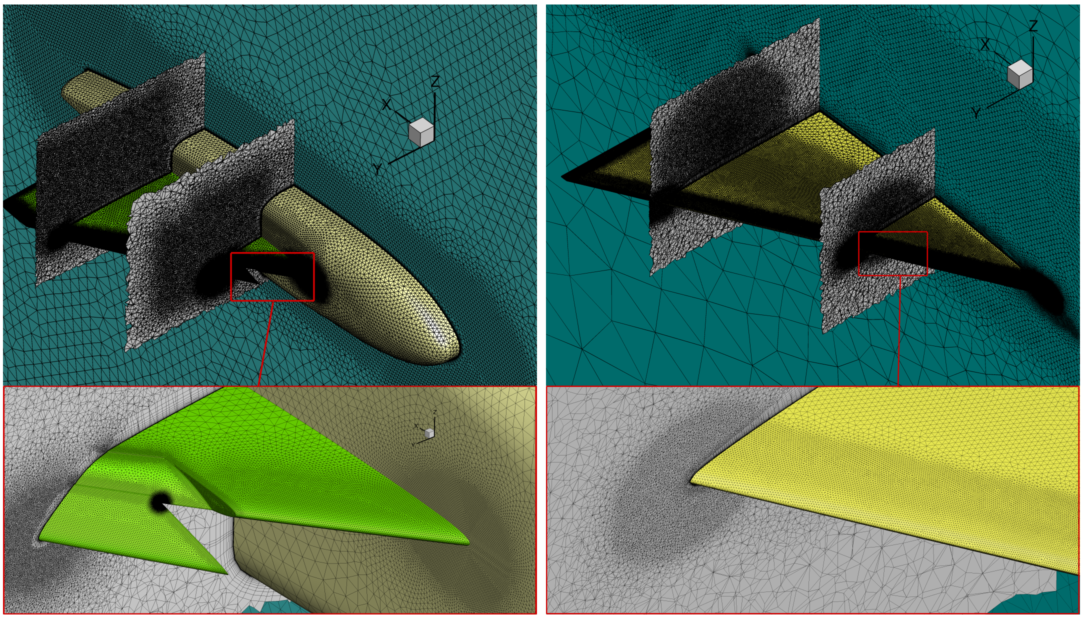

(a) Model56. **(b)** DW60.

Figure 4.9: Visualization of the numerical grid of additional test cases (pt.1).

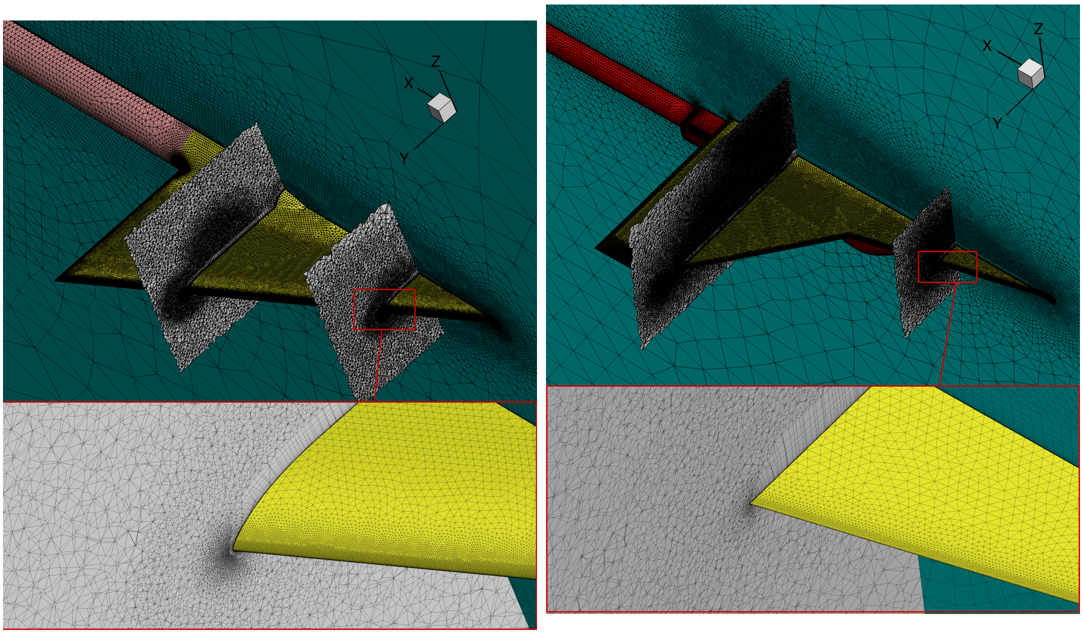

(a) VFE2 with small leading-edge radius. **(b)** Erickson's Double Delta wing with the baseline fillet.

Figure 4.10: Visualization of the numerical grid of additional test cases (pt.2).

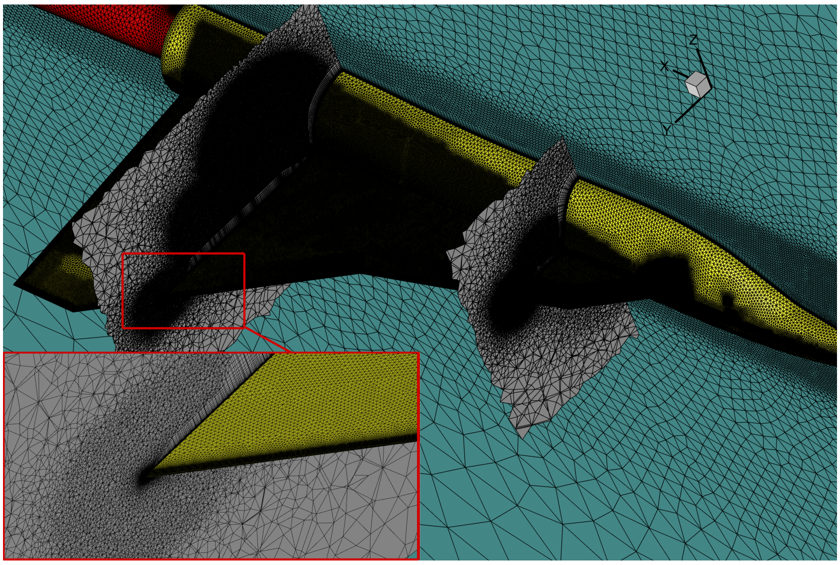

(a) Triple delta wing configuration.

Figure 4.11: Visualization of the numerical grid of additional test cases (pt.3).

ferent directions and it is not always trivial to classify a case in a straightforward manner. Therefore, the different classification possibilities are reported as follows, starting from the ones mainly used and followed by the secondary points of view. Such classifcations are based on a physical fundament and they are particularly described in Section 1.2.

4.3.1 Vortex stage classification

The test cases are subdivided into groups that describes different stages or kinds of vortex topologies. As introduced, such a classification is mainly qualitative as the development itself is not something that is physically split into definite portions but follows a progressive process along some fluid dynamics quantities. In the case of delta wings the stage of a vortex is most commonly influenced by its leading-edge sweep angle and angle of attack. The other geometric parameters reported in the description tables (Tables 4.1, 4.2) have normally of secondary influence. However, they are not negligible for a quantitave analysis. Further complexity is introduced in the flow field and in a clear classification when a double- or multi-delta wing configuration is employed (Sec. 4.1.6, 4.1.7) as well as when multiple vortices develop along aerodynamic devices such as a slat (Sec. 4.1.2).

The classification is reported in a schematic view with Figure 4.12. It is noticeable that the range of low angles of attack is poorly covered except for the AVT-183 and the SAGITTA cases which have in common a rounded leading edge. In this sense, the leading-edge curvature is of higher importance when a vortex experience a partially developed stage at low angles of attack. With respect to this region of the vortex flow stages, results are reported for the AVT-183 diamond wing at low angles of attack (Sec. 4.4.3).

Table 4.3: Numerical grids used for the optimization/application of the proposed methodology for the half-span geometries of the reported test cases (Figs. 4.8, 4.9, 4.10, 4.11).

Name	Total n. of points 10^6
AVT-183	15.4
SAGITTA	13.8
Model53	8.9
Model56	10.2
DW60	10.9
DD76/40	4.4
AVT-316 ADS-NA2-W1	18.8

It is relevant to notice that the requirements in terms of the model coefficients may be significantly different between the separation onset and the flow characteristics at higher angles of attack. Therefore, it is expected that a different optimal set of coefficients may be required between low and high angles of attack for a rounded-leading-edge geometry. Whereas it is not preferable that a distinction between the two regions of the angle of attack range may need to be established for such configurations. Hence, they employ different calibrations for the partially developed stage and for the fully developed vortex with breakdown and stall.

With regard to the mapping of the test cases (Fig. 4.12), they are positioned in a graph where the two cartesian dimensions correspond to the angle of attack and the sweep angle. Low sweep angles correspond to low-aspect ratio delta wings which experience unstable vortical structures with strong suction footprints, low super-linearity trends of the lift force over the angle of attack and the appearance of dead water flow stages downstream of vortex breakdown. The stall condition in this portion is more important to be investigated as it correlates with angles of attack larger than 28° which are incidences of the envelope requirements of corresponding high performance aircraft. Therefore, the good prediction of such ranges of angles of attack is relevant. However, in the same cluster of cases also the middle range of angles of attack are commonly included because good practice suggests to provide an optimal set of coefficients which does not decrease the accuracy for already well predicted cases by the baseline turbulence model. Clearly, this is valid only for such test cases where a relatively high curvature of the leading-edge contour is present and, hence, no high sensitivity of the turbulence modeling is related to the separation onset/type. This portion of the classification includes the high angles of attack regions of the Model53, Model56, AVT-183 diamond wing and the SAGITTA blended wing body.

Moving to larger sweep angles and lower aspect ratios, delta wings which are related to strake geometries are encountered. In this cluster, therefore, also the combination of such a strake with aft wings are also reported in the configuration of double- or multi-delta wings. Whereas it is not expected that an optimum of a strake like geometry improves the accuracy for the aft wing or the cross-influence of the two or more vortices, the optimum of a high sweep angle geometry is possible to be applied in a zonal method

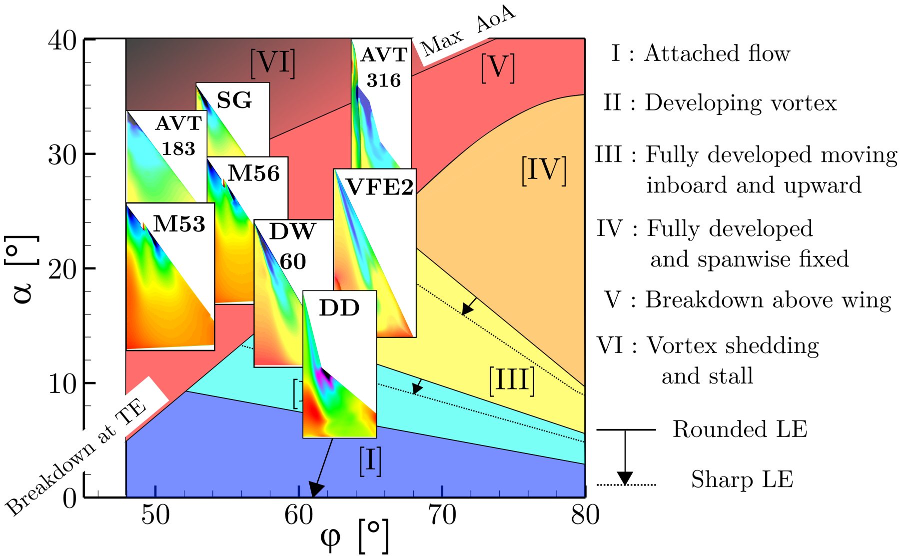

Figure 4.12: Description of the development stages of a leading-edge vortex flow in the parametric space of the angle of attack and the sweep angle and identification of the main test cases; cf. [1].

(Sec. 3.5.1) with the target to improve the strake vortex development while further refining a second optimal set of coefficients for the outboard vortex. With respect to geometries like the VFE-2 and the DW60 wings, the angle of attack range is limited to middle-high values without encountering the stall regime which happens at very high angles of attack for such sweep angles.

It is not expected that a single optimum results in a constant improvement for the different test cases in this cluster where the geometrical differences are significant and drastically influencing the vortex flow field. However, whereas the application of a single optimum to different test cases maintains its level of interest and it provides significant insight into the methodology potential, a good practice is to follow reasonable directions when applying an optimum to new test cases based on experience and physics motivations.

4.3.2 Reynolds and Mach number

A second direction of subdivision can be performed by splitting the test cases according to the Reynolds number and Mach number of the freestream conditions. This is more of a transversal classification along the test cases and thought to be a possibility to distinguish the trend of the turbulence model calibration between different compressibility and turbulent states of the flow. In this way, extrapolate possible guidelines for the application of an optimum from a certain freestream condition to another. The majority of the investigations and applications have been performed for the low and middle subsonic regime. Therefore, up to a Mach number of 0.5. A consistent number of applications have been also performed for a transonic regime at around $M = 0.8$ which is traditionally complicated to predict for baseline turbulence models.

It is important to notice that at a transonic regime the appearance of shock waves determines the triggering of the vortex breakdown at a certain position which is usually less sensitive to turbulence modeling. Therefore, it is expected to find less discrepancies with regard to the position of vortex breakdown. On the other hand, the interaction of the shock wave with the vortex flow provides a complex flow feature. No significant sensitivity of the turbulence model calibration to such phenomena could be experienced and included in an optimization performed at a low subsonic regime. It is therefore expected to find a reduction of the accuracy improvement if a single optimum is applied for both regimes. However, a portion of the improvement is possible to maintain with flow curvature effects that are related to the geometry and with less influence from compressibility effects.

With respect to the Reynolds number influence (Sec. 1.2), the direct effect on the vortex development may also be significant. However, if a transition from a laminar to turbulent boundary layer is present, it is influenced by the Reynolds number [12]. Moreover, the breakdown type can change according to the Reynolds number as well as the swirl number. Additional influence of the Reynolds number to the vortex flow is related to the separation onset [12].

4.4 Evaluation and Analysis

4.4.1 Slender delta wing - 65° Swept Delta Wing with Interchangeable Leading-Edge Geometries

As summarized in Section 4.1.5, the VFE2 test case consists of different subcases. However, one of those is selected as calibration target and starting point for the investigation and optimization procedure, while the others are dedicated to the following validation step as well as a means to evaluate the flexibility of the methodology for significant geometrical variations.

4.4.1.1 Small Leading-Edge Radius

Baseline Turbulence Model Results and Vortex Flow Characteristics. The small leading-edge radius case, i.e. $r/c_r = 0.033\%$, is selected as a good compromise in the range of the leading-edge shapes available for the first calibration phase of the methodology application [107]. After a first analysis of the accuracy achieved by the baseline SAE turbulence model, the selection of the relevant angle-of-attack polars as targets of the optimization procedure is performed. The objective is to include all the important features that need to be improved and, consequently, to enhance the prediction of the vortex characteristics included in the target flows at a physical level. It is observable, in fact, that the baseline turbulence model is not able to properly predict the suction peak of the first and secondary vortices as well as the breakdown position (Fig. 4.13). In fact, already at 16.3°, the SAE model anticipates the breakdown somewhere between

0.8 and 0.95 of the c_r (Fig. 4.15a) whereas the experimental data maintains a narrow peak which indicates a structured stage of the vortex with high levels of helicity. The same is evident for the highest angle of attack where the position moves upstream as expected with an increase of the angle of attack (Sec. 1.2). As indicated in the report from Wentz and Kohlman [16], for a 65° swept flat delta wing, the breakdown position takes place above the traling edge at around 20° whereas, at 26°, the breakdown should be located at around 70% of c_r (Fig. 1.5). According to the same experimental data, the breakdown instability reaches the wing apex at an angle of attack of around 37°. It is however important to remember that such wind tunnel measurements were performed with a flat delta wing. Therefore, whereas a qualitative comparison is reasonable, quantitatively it is expected that deviations are present due to the different vortex generation caused by the leading-edge roundness with consequent differences in the vorticity injection through the vortex sheet. The leading-edge shape is sharp enough to fix the vortex separation onset at the wing apex already at small angles of attack. This is evident from the surface C_P distributions already at the angle of attack of 16.3° (Fig. 4.15a) where a suction peak starts to influence the wing surface at the very apex region of the wing. The fixed separation onset is also confirmed by the experimental data available from the NASA report [122]. Moving downstream, the vortex moves more inboard while a secondary vortex starts to be evident between 20% and 40% of c_r (Fig. 4.13). As the angle of attack increases, the vortex separation remains fixed at the apex while the appearance of the secondary vortex takes place at a location further upstream. Moreover, as physical consequence of the increased strength of the vortex flow with the higher angles of attack, the vortex axis moves further inboard. The vortex structure acquires more strength from the vortex sheet which feeds its vortical structure with momentum and generates a larger vortex which influences a larger area above the wing. At the same time, the vorticity in the core region, upstream of the eventual breakdown, manifests larger values. This shows that its predisposition to reach an instability status increases. Consequently, the suction peak levels of both main and secondary vortices increases. The onset of the separation in correspondence to the leading edge indicates how the vortex generation is dominated by the sharpness of the leading-edge shape. A high value of vorticity is, in fact, in correspondence to the leading-edge proximity and not slightly inboard as it happens for an increased roundness. The vortex sheet rolls up above the wing and its evolution into a vortical structure is physically reasonable, as described in section 1.2. The breakdown for the SAE model is located slightly upstream of the 80% of c_r cut with respect to the angle of attack of 20.4° (Fig. 4.16a) whereas it takes place just downstream of the cut at 0.6 of c_r for the angle of attack of 26.5° (Fig. 4.17a). With respect to AoA = 16.3° (Fig. 4.15a), the SAE model predicts the presence of the vortex breakdown in the proximity of the trailing edge, i.e. at around 90% of c_r, as indicated by the presence of a reverse flow which correlates with the drop of the vorticity value between the cross-flow planes of 80% and 95% of c_r. This is not in agreement with the findings reported by Wentz and Kohlman as the angle of attack is much lower than the angle of trailing-edge breakdown experienced in the wind tunnel measurements. This consideration is furthermore confirmed by the comparison of the surface pressure distribution from the experimental data (Fig. 4.13) of the NASA report [122]. The evolution of the vortex is appreciable in the sequence of cross-flow cuts showing the vorticity contour along the x direction. The positions of vortex breakdown are confirmed by the sudden drop in the core vorticity down to almost values of zero and an expansion of the vorticity outer contour (Figs. 4.15b, 4.16b, 4.17b). Moreover, the iso-surfaces correspondent to the values of 0.25 and 0.0 of the ratio between the axial velocity and the freestream velocity u/U_∞ highlight relevant features of the flow downstream of breakdown. The first value indicates a region dominated by a really weak wake flow as plausible under the condition of a burst vortex and the second value permits to distinguish a region of reversed flow which indicates the proximity downstream of the breakdown instability. The SAE model accurately solves the regions which are not or only partially and indirectly influenced by the vortex. The pressure distribution on the lower surface provides a high grade of accuracy with the experimental data and this confirms the good capability of the baseline model to properly solve attached flows (Fig. 4.13). A similar observation is made for the region inboard of the upper surface where the vortex flow has a negligible influence which is mostly true for the region where a structured and narrow vortex is present, hence, nearer to the apex and/or low angles of attack. As indication of the appropriate grade of mesh fineness with respect to the regions of the vortex flow, where minor turbulence model sensitivities are expected, the surface C_P accuracy to experimental data manifests a proper grade of agreement in the region of the vortex with a jet type flow (Fig. 4.13). Discrepancies with the experimental data increase as the vortex flow region develops and/or acquires more strength and grade of instability. For this reason, it is evident how the region of highest sensitivity to the turbulence model is expected to be the vortex breakdown proximity and its wake. However, whereas the turbulence model already provides accurate results for the structured region, it does not necessarily demonstrate that no eddy viscosity production rate is necessary in this reason. This statement is physically motivated by the fact that the variation of eddy viscosity production in the insensitive structured vortex upstream of breakdown modifies the evolution of the eddy viscosity production downstream. In the context of the AVT-113 action group, Fritz and Cummings [43] report the numerical results obtained from the participating partners with respect to the VFE-2 test case. They evaluated that the main discrepancies, with respect to the subsonic regime, are in agreement with the findings along this research for regarding the baseline SA turbulence model. The application of SA, k-ω with different variations or corrections as well as a EARSM model returned deviations with respect to both the medium and sharp leading-edge shapes [43]. Focusing on the sharp shape which better correlates with the small radius used in the current calibration phase, the models were able to predict with an appropriate grade of accuracy the structured and highly stable portion of the vortex similarly to the baseline model in the current research (Fig. 4.13). In accordance are also the larger deviations that the numerical solutions encounter with respect to the experimental data as the vortex flow moves downstream approaching more unstable conditions due to the adverse pressure gradient at the trailing edge. The suction peaks are also underpredicted whereas the vortex represent a larger and more unstable structure which causes an upstream displacement of the breakdown position.

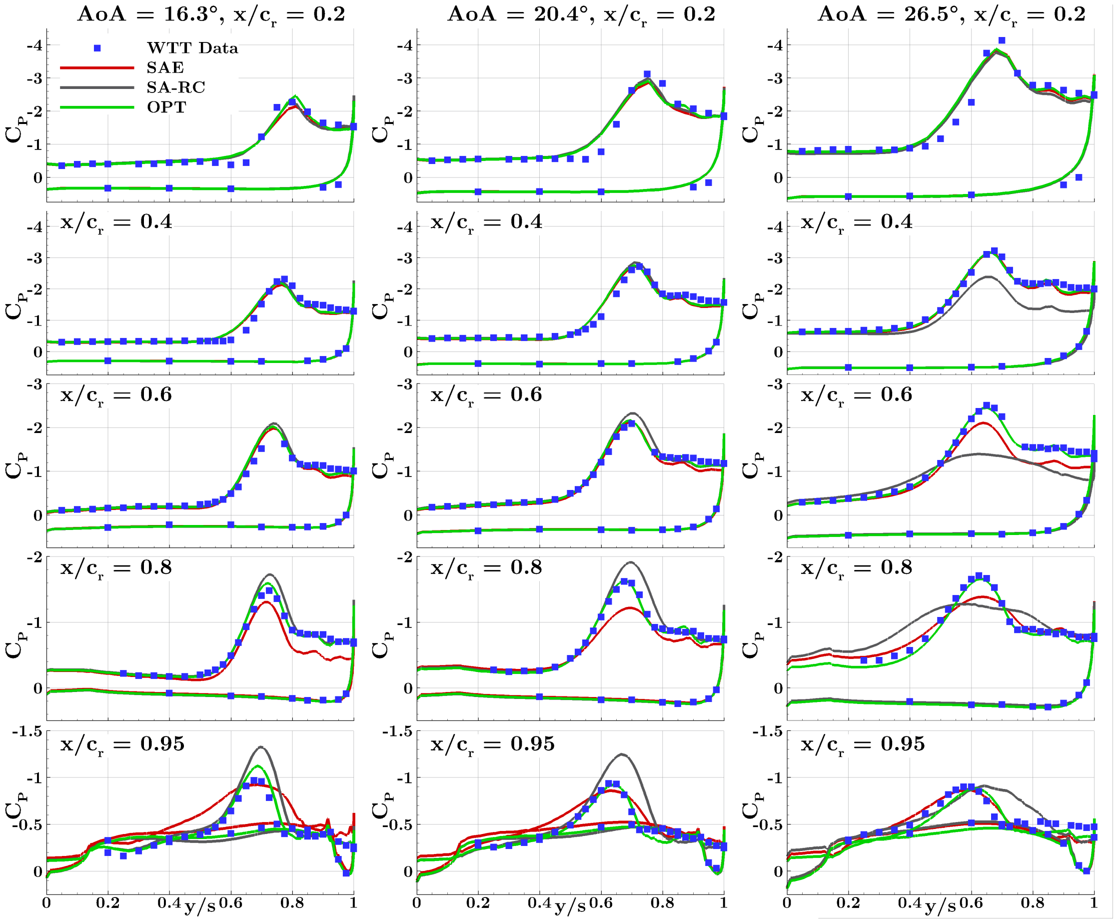

Figure 4.13: Surface C_P distribution along cross-flow sections at $x/c_r = [0.2, 0.4, 0.6, 0.8, 0.95]$ for the 65° swept delta wing with $r/c_r = 0.033\%$, $M = 0.4$ and $Re = 6 \cdot 10^6$. The data of the baseline SAE model, the SA-RC and the optimized turbulence model (Table 4.4) are compared with the steady surface pressure measurements [122]).

Application of the Spalart and Shur Rotation Correction. The Spalart and Shur rotation and curvature correction [79] is a modification of the SA model (Sec. 3.3.1) and it is investigated in order to have a second comparison with a model often used in the community for such a class of flows. It often improves a certain cluster of vortex flow types but the predictive capability may be also limited in some cases.

The application of the SA-RC model enhances the accuracy of the surface pressure distribution for the two lowest considered angles of attack at 16.3° and 20.4°. As a first evaluation, it is evident how the rotation correction improves the model accuracy in predicting the proper vortex flow stage. Instead of a fully developed vortex with breakdown instability, as obtained with the baseline SAE model, the breakdown disappears from the vortex evolution above the wing surface. The vortex maintains a structured and stable jet-type flow for a longer distance over the upper surface (Figs. 4.15, 4.16). The vortex separation position along the leading edge is not influenced by the turbulence model correction as well as the attached flow on the lower surface. This is a further indication that such regions manifest low sensitivity to turbulence model modifications and are already predicted by the baseline turbulence model to an appropriate extent. In addition, the upstream region of the vortex, which covers the region down to 40-50% of c_r, experiences almost no significant variation due to the turbulence modeling effects. This is again an indication of the insensitivity of the region to the modeling of turbulence. The SA-RC model produces the same vorticity distribution and vortical flow typology in this region (Figs. 4.15, 4.16) which consequently produces negligible differences in the suction distribution impressed on the aerodynamic surface (Fig. 4.13). Moving further downstream and, in particular, for the last cut at 95% of c_r for the two smaller angles of attack, it is possible to visualize how the vortex flow rotates around a higher vorticity peak in its sub-core region compared to the baseline SAE model. The distribution of the vorticity is similar to the structured region upstream and this exhibits how the absence of the breakdown instability permits the vortex to maintain the structured region for a longer distance. Along the vortex axis, whereas the vorticity distribution is similar, the vortex experiences a progressive dissipation of the magnitude of the vorticity value. The jet type vortex is maintained longer downstream to the trailing-edge proximity and no breakdown or reversed flow is visible from the extraction of iso-surfaces neither with u/U_∞ equal to 0.25 or 0.0. As consequence, a narrow suction footprint corresponds to a more constrained structured vortex flow which is qualitatively more in agreement with the experimental data. However, an over-prediction of the suction peak in proximity of the high values of the rotational core is present and this discrepancy increseas moving downstream. The suction peak at 95% of c_r reaches a value around -40% of the wind tunnel data for the two smaller angles of attack. In addition to this discrepancy, at 20.4° the suction has also a larger footprint in the spanwise direction. The secondary vortex is for the most part only partially influenced by the SA-RC model and the secondary peak is not increased compared to the baseline model, except for some cuts where the overall suction level in the area of the secondary vortex is increased. The effect of the correction appears to be too strong for the considered flow case.

This evaluation is confirmed by the highest angle of attack, where the breakdown is moved upstream with a significant offset from the baseline model as a clear indication of the increased strength and, consequently, instability of the vortical structure. Whereas a structured region is maintained down to 40% of c_r, a wake like flow dominates downstream as visible at the 60% of the root chord. It is shown by the vorticity contours (Fig. 4.17b) which do not manifest a structured vortex flow with a peak in the vortex core, instead the vortical structure is already deprecated into a chaotic and expanded region. The tangential velocities coming from the structured region upstream transfer momentum downstream which permit to maintain a level of vorticity in the outer border of the flow field. Such remaining rotational components progressively diffuse moving downstream as the overall vorticity values gradually decrease. It is interesting to notice how the secondary vortex structure also drastically changes from the baseline model at $x/c_r = 0.6$ due to the breakdown of the primary vortex. The breakdown of the primary vortex triggers the progressive diffusion of its structure proceeding downstream and the disappearing of the secondary vortex structure as direct consequence. The same conclusions can be confirmed by addressing the surface pressure distribution (Figs. 4.17a, 4.13) where the suction footprint suddenly reduces its maximum peak values and it covers a larger area. At 40% of the root chord, the vortex is close to break down as a structured region is visible but at a significant increase of the C_P level. The phenomenon suggests a sudden reduction in the vortex induced velocities which impress a lower vortex suction on the upper wing surface. The accuracy of the numerical simulation results in relation to the experimental data is significantly compromised by the false vortex flow stage prediction. The error is now much larger compared to the baseline turbulence model. The large region of chaotic wake flow is also clearly visible by the iso-surfaces because they show the loss of the vortical structure dominated by helicity and the appearance of an unstructured and reversed flow.

The eddy viscosity is represented in Figure 4.18 for the cross-flow sections in the proximity of the breakdown region related to the three reported angles of attack. First of all, the importance of turbulence modeling with respect to vortex flows and the employed numerical methodologies is motivated by the fact that high levels of eddy viscosity are produced inside the vortical region when applying the baseline SAE model. The eddy viscosisty distribution appears to be similar between different angles of attack at similar positions which may suggest that the employed model might be limited in flexibility of modeling such complex flow fields and it does not show a high dependency on different vortex stages and strengths. Differently, the SA-RC provide an extreme destruction of eddy viscosity in the vortex core while it remains almost not erturbated in the outer region where the feeding shear layer rolls up to form the vortex structure and in the secondary vortex region. The values of eddy viscosity of the vortical structure are not appreciable by maintaining the same visualization scale as the baseline model, showing how the reduction is a matter of orders of magnitude. The low dissipation due to the absence of μ_t in the core explains how the the core vorticity is even stronger than for the baseline model. However, except for the angle of attack of 26.5°, it is expected that a lower dissipation causes an upstream displacement of the breakdown instability due to the higher sensitivity to perturbations. The balance between the low dissipation enhancing the core vorticity which permits to strengthen the vortex structure and helicity dominated flow and the low resistance at the propagation of instabilities is therefore dependent on the angle of attack. In general, the eddy viscosity variation exhibits how the SA-RC corrected model is possibly too strong for the considered flow case and it manifests low flexibility in improving the same test case when the vortex flow typology changes reducing its predictive capability. This is particularly detrimental for the application of numerical methods to the production of large numerical datasets. The SA-RC model, likewise the baseline model, is composed of terms with related coefficients which have been calibrated for generic test cases and, therefore, could be re-calibrated to the considered flow case with the proposed methodology. However, such an approach would have detrimental limitations with respect to both flexibility and accuracy. It is considered more appropriate, as this research proposes, to isolate the effects of the turbulence model modification to terms which are exclusively connected with the vortex field and they provide more possible flexibilities from their different combinations. Moreover, when the correction is applied to a flow regime of the test case where no vortex or only weakly stable vortices are present, it is expected that the model enhancement would loose effectiveness. In such a way, the modeling of turbulence would correspond to the underlying baseline model which is already capable of a good grade of accuracy for attached flows.

Optimization Procedure and Application. The optimization methodology (Sec. 3.4.4) for the presented turbulence model modification is performed following a series of preliminary steps when a new test case is under investigation.

- Sensitivity to spatial discretization: A proper level of numerical grid fineness is provided in order to correlate the discrepancies almost exclusively to the turbulence model and its lack of accuracy for the considered test case.
- Sensitivity of the turbulence model parameters: A series of test simulations are performed to investigate the sensitivities of the different turbulence model terms on the vortex flow. Firstly, the testing phase is relevant through the formulation of the terms. It is necessary to verify that their influences on the vortex flow correspond to a physics based approach and a particular vortex type or region to be addressed. Secondly, also when approaching a new kind of vortex flow, different from the test cases in the historical application of the methodology, it is important to evaluate the sensitivities of the terms on the flow field. This suggests the best direction possible of the optimization procedure. Moreover, it permits to verify if any of the terms have no influence, if similar influence is present between some of them or if the appropriate influence in the region with the highest discrepancies is matched.
- Tuning of the optimization procedure settings: The parameters which set the optimization handling of the numerical simulations are decided accordingly in order to have a proper convergence rate between the iterations and the sensitivity evaluations. This is necessary to permit the well behavior of both the algorithm and the numerical simulations to properly progress the convergence of the model parameters. Therefore, it is important to find an equilibrium for preventing poor convergence of the inner sensitivity simulations and for having a proper sensitivity of the parameters based on the values of the increments.

Table 4.4: Optimized set of coefficients for the 65° swept delta wing with $r/c_r = 0.033\%$.

Coefficient	c_{bv1}	c_{bv4}	c_{bvh1}	c_{bvh2}	c_{bvb}
Value	0.0375	0.003	-0.02	-0.432	-0.6

After this preliminary phase and following the methodology guidelines described above, an optimization procedure (Sec. 3.4.4) is set up including the terms with the highest

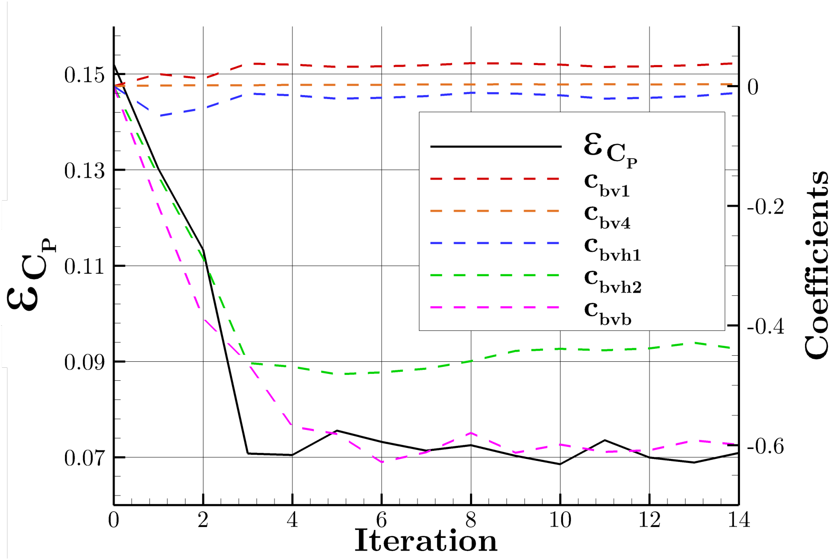

Figure 4.14: Convergence of the $\mathcal{E}_{C_P}$ and the coefficients of the turbulence model modification with sufficient sensitivity along the optimization procedure for the 65° swept delta wind with $r/c_r = 0.033\%$, $\mathrm{M} = 0.4$, $Re = 6 \cdot 10^6$ and $AoA = 20.4°$.

sensitivity and which show different influence on the vortex flow field. A first optimization is applied to the single angle of attack of 20.4° (Fig. 4.14). The average error of the pressure distribution between the numerical solution and wind tunnel data is significantly reduced by a factor of 2.3, from $\mathcal{E}_{C_P}$ of 0.152 to 0.069. From the optimization convergence plot (Fig. 4.14) it is visible how the average C_P error is improved for the major part within the first four iterations. Successively the value of the target function oscillates around similar levels and lower sensitivity is available from the parameters variation. The optimization is stopped as a convergence state is achieved. The resulting coefficients of the optimization are taken as optimum (Table 4.4). Other optimizations are started in parallel with different starting points in order to address the presence of other local optima with better performance. No direction with more potential has been found during this phase. Being the optimum the result of targeting the experimental data of a single angle of attack, an additional optimization is started from the optimal set of coefficients including also the angle of attack of 26.5°. The optimizer, however, remains in the proximity of the starting values. This outcome shows how the optimum remains valid by extending to other angles of attack of the calibration case. Hence, that no further improvements for the higher angle of attacks is achievable by the turbulence model terms indicates that the previous optimum addresses with the same sensitivity the source of discrepancies at larger AoAs. This result is consistent with the fact that the vortex flow stage and characteristics are similar between the two angles of attack. The only difference is the strength of the vortex structure but the main discrepancy remains correlated to the vortex breakdown position and the C_P level downstream. The selected set of coefficients is therefore applied to the three analyzed angles of attack to cover the

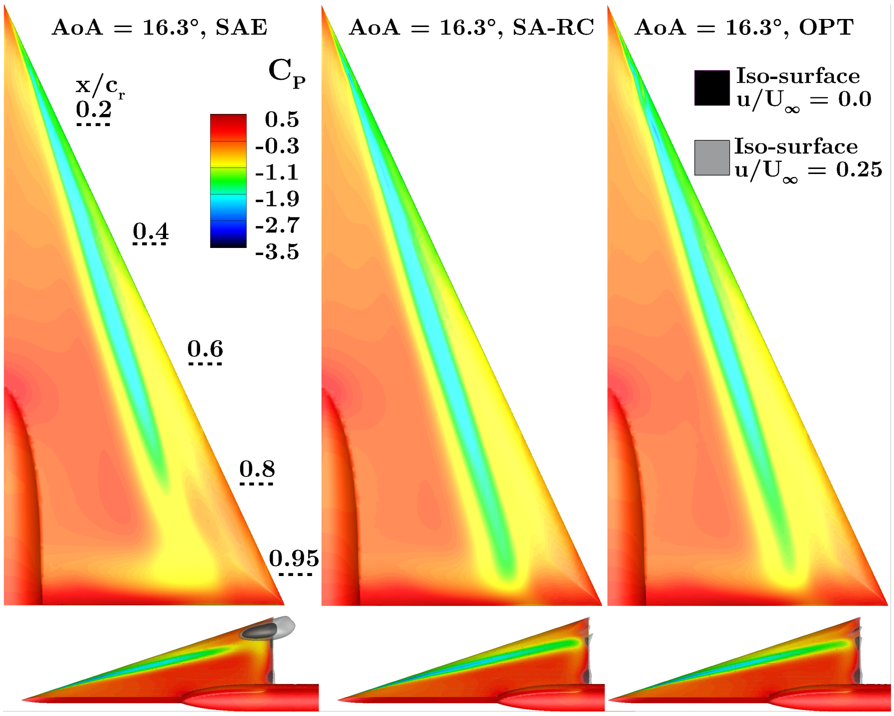

(a) Distribution of C_P on the upper surface and the u/U_∞ iso-surface.

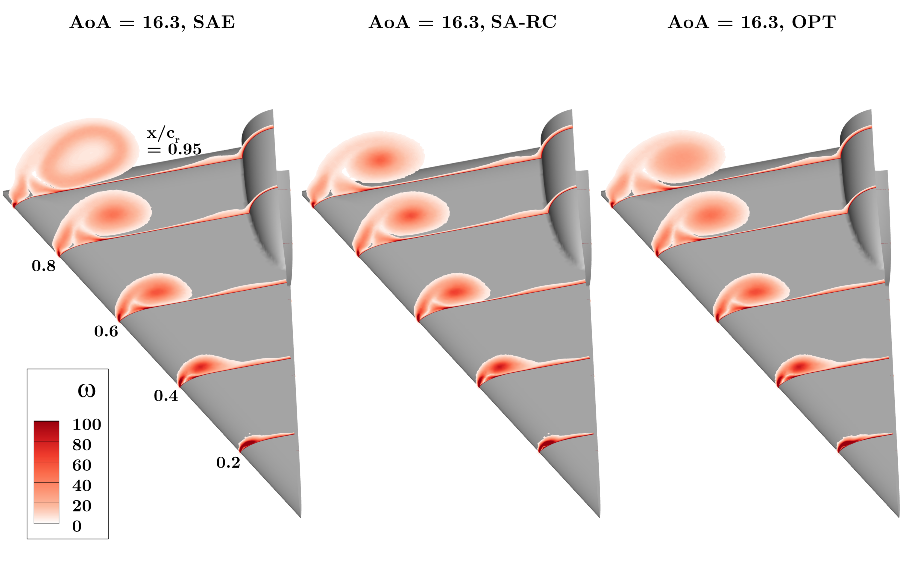

(b) Vorticity distribution along cross-flow sections at $x/c_r = [0.2, 0.4, 0.6, 0.8, 0.95]$.

Figure 4.15: Comparison of the numerical results of the baseline SAE model, the SA-RC and the optimized turbulence model (Table 4.4) for the 65° swept delta wing with $r/c_r = 0.033\%$, $M = 0.4$, $Re = 6 \cdot 10^6$ and $AoA = 16.3°$.

envelope where the main discrepancies with respect to the baseline model appear. The

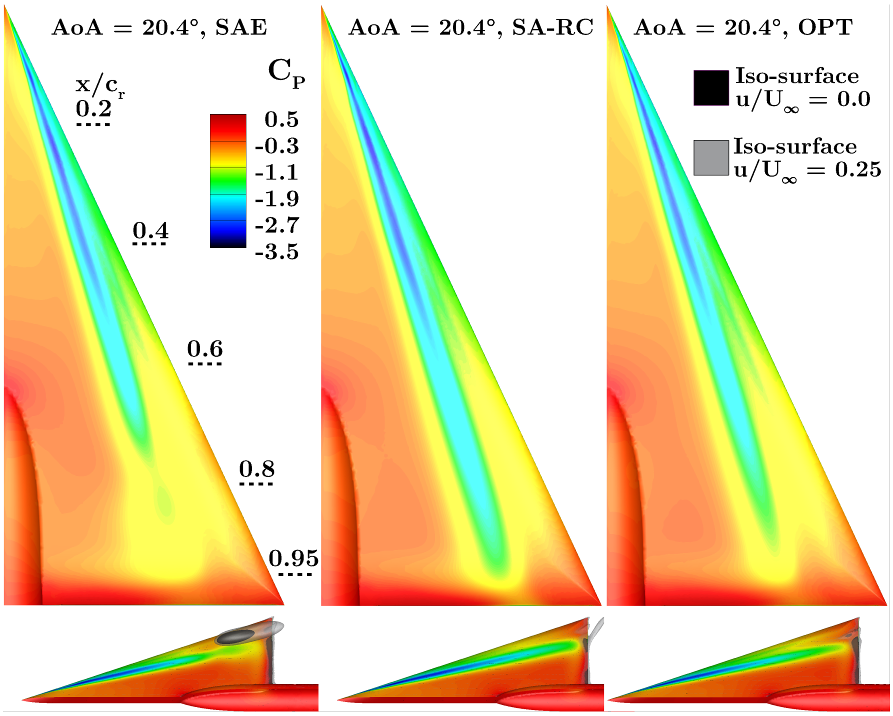

(a) Distribution of C_P on the upper surface and the u/U_∞ iso-surface.

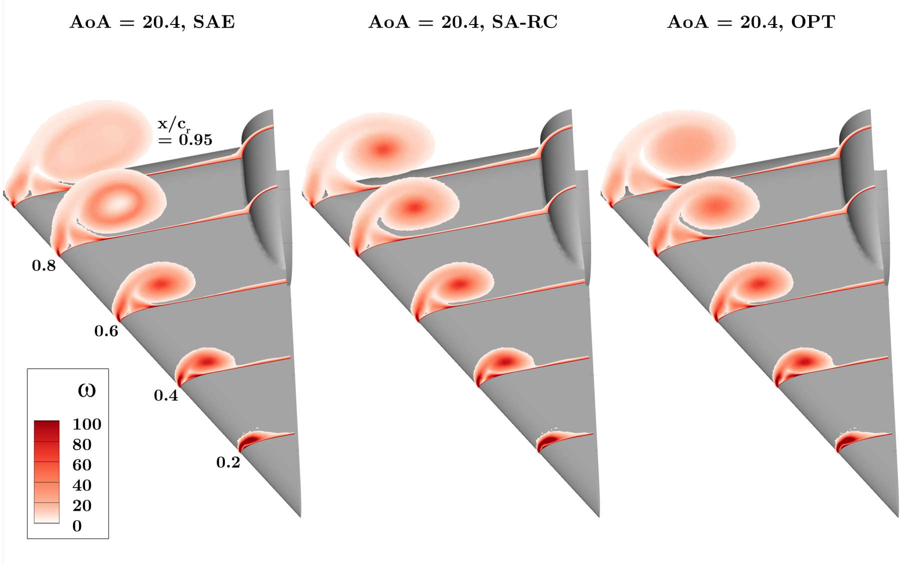

(b) Vorticity distribution along cross-flow sections at $x/c_r = [0.2, 0.4, 0.6, 0.8, 0.95]$.

Figure 4.16: Comparison of the numerical results of the baseline SAE model, the SA-RC and the optimized turbulence model (Table 4.4) for the 65° swept delta wing with $r/c_r = 0.033\%$, $M = 0.4$, $Re = 6 \cdot 10^6$ and $AoA = 20.4°$.

application of the optimum to the angle of attack of 16.3° predicts the vortex development in a different way with respect to both the baseline SAE and the SA-RC models. Whereas the breakdown is now absent and the vortex reach a fully developed stage, it does not manifest a high core vorticity until the trailing edge of the wing. The vorticity gradually diffuses along the vortex axis with lower and lower core vorticity magnitudes until they reach the order of magnitude of the tangential region and the vortex sheet separation from the leading edge (Fig. 4.15b). Such diffusive behavior of the vortex progression manifests itself already at 80% of c_r. Therefore, whereas the achieved stage of the vortex is comparable to the one provided by the SA-RC model, when moving into a more detailed visualization of the vortex flow development, substantial differences are present. This indicates that a higher order of flexibility is achievable by the turbulence model modification and its regional calibration provided by the optimization procedure. As consequence of a weaker and more diffused vorticity distribution in the rear region of the wing, the suction footprint is less pronounced compared to results from the SA-RC modeling (Fig. 4.15a). When compared with the experimental data (Fig. 4.13), the pressure distribution matches with a good grade of accuracy to the experimental data. The C_P distribution is qualitatively comparable to the SA-RC results, however, in this case also the C_P peak is predicted better and closer to the wind tunnel measurement data. The regions of the flow which have low discrepancy with the wind tunnel data and experience low sensitivity to the SA-RC model manifest the same behavior also with the optimized model.

With respect to the angle of attack, namely 20.4° a similar effect is obtained with the application of the optimized model (Fig. 4.16a). The vorticity distribution follows the same trend of a more diffused distribution with a less distinctive core region. The pressure distribution exhibits lower suction levels when compared to the SA-RC model results. Hence, a narrower suction peak is visible which is also more in agreement with the experimental data (Fig. 4.13). The error in the suction levels achieved with the SA-RC model rises with angle of attack showing again lower flexibility than the optimized model. With respect to the optimized model, it is difficult to identify regions where further improvements might be necessary. The u/U_∞ iso-surface above the wing surface exhibits a similar condition to the SA-RC model (Fig. 4.16a). However, the stagnating flow with u/U_∞ below 0.25 covers a larger region. As further confirmation of the enhanced flexibility of the optimized model compared to the other reference models, at 26.5° the optimized model maintains an accuracy improvement performance similar to the smaller incidence angles whereas the SA-RC model is not able to predict even the proper vortex flow stage. The vorticity contours (Fig. 4.17b) show how the high core values are reduced along the vortex development but the vortex structure remains stable (Fig. 4.17a). The secondary vortex is not triggered to burst by the main vortex's breakdown and it follows its progression along the vortex system. A recirculation zone is visible in proximity of the trailing edge, as seen for the smaller angles of attack (Fig. 4.17a). The comparison of the C_P distribution with the experimental data illustrates a comparable level of improvement to the other angles of attack. The flexibility of the optimized model is able to improve consistently the relevant range of angles of attack without introducing any numerical instability. A visible discrepancy remains

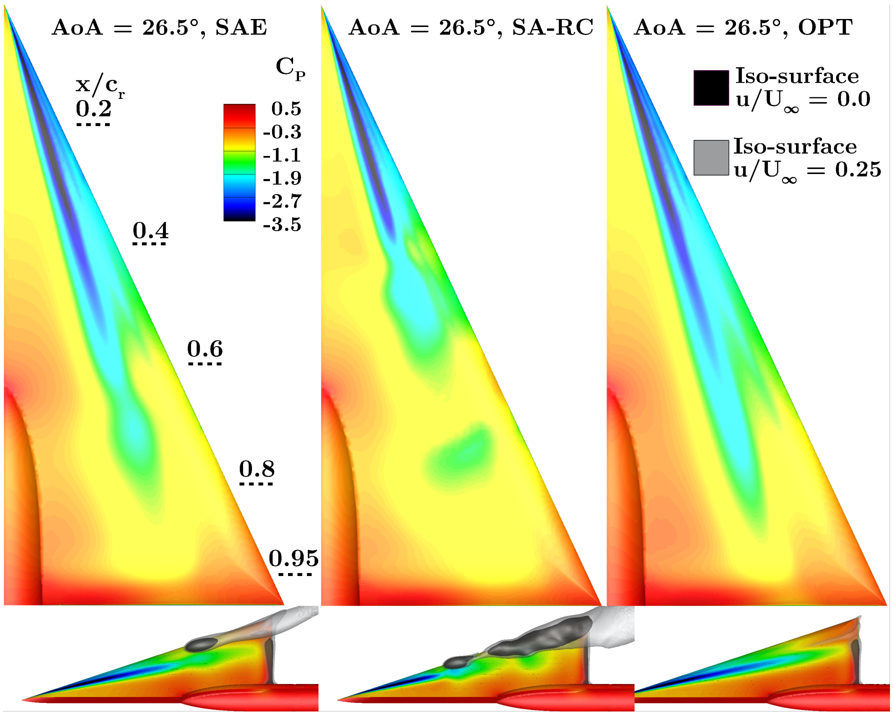

(a) Distribution of C_P on the upper surface and the u/U_∞ iso-surface.

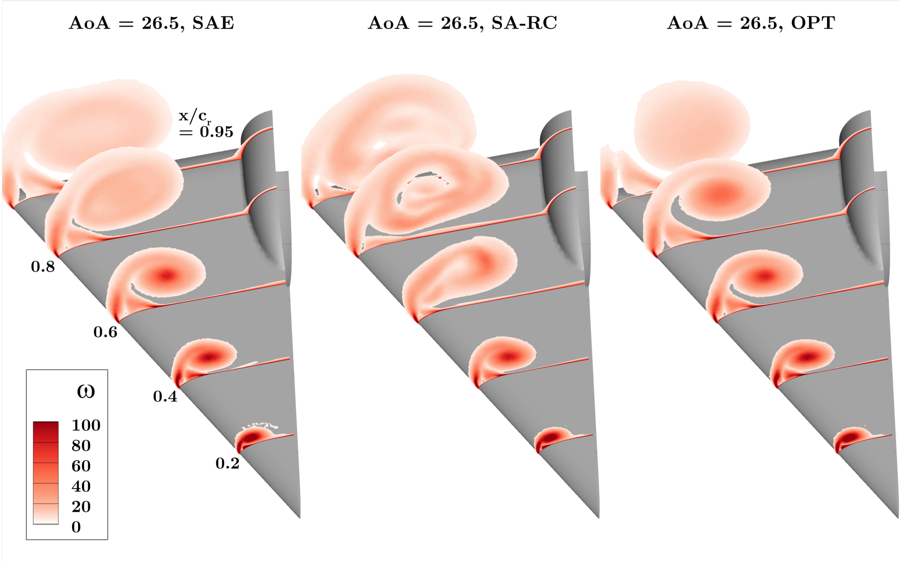

(b) Vorticity distribution along cross-flow sections at $x/c_r = [0.2, 0.4, 0.6, 0.8, 0.95]$.

Figure 4.17: Comparison of the numerical results of the baseline SAE model, the SA-RC and the optimized turbulence model (Table 4.4) for the 65° swept delta wing with $r/c_r = 0.033\%$, $M = 0.4$, $Re = 6 \cdot 10^6$ and $AoA = 26.5°$.

with respect to the rear section at 95% of c_r where the suction peak of the numerical simulation is moved outboard of about 5% of the local span. The outer region manifests a flat suction distribution similar to the wind tunnel data but at a lower suction level of about 0.1 in terms of C_P. In order to gather further insight into the difference of the analyzed turbulence models, a series of cross-flow sections are extracted at relevant positions for the three angles of attack and a contour of the eddy viscosity is shown for the three models (Fig. 4.18). The sections visualized correspond to the position of the first available experimental data downstream of the breakdown for the considered angle of attack. The variation of the eddy viscosity between the baseline SAE model and the SA-RC modification show clearly which is already known from the analysis of the vortex flow variation. The SA-RC has lower flexibility and its effect is too strong as the eddy viscosity model is dominated by destruction except for the region of the increased tangential velocities where the SA-RC is switched off. The variation provided by the optimized model differs significantly from the SA-RC effect. The eddy viscosity is not completely destroyed but countrary it is modified in accordance to the location along the vortex development. This shows how the calibration of a series of independent terms provides more flexibility to the eddy viscosity evolution in a vortical flow development as well as a higher grade of accuracy. A further indication of the potential and proper behaviour of the methodology is that the pressure distribution under the lower surface of the wing is insensitive to the turbulence model variation and calibration. This is a confirmation that the methodology is properly formulated in order to only affect the vortex field and, indirectly interacts with it. Moreover, the good match with the lower surface data indicates the quality of the experimental data as almost no turbulence model discrepancy is expected in this region and the proper calibration for attached flows of the baseline SAE model permits to have high fidelity in the numerical results. However, the cut at the latest position under the wing exhibits a certain variation in the pressure distribution. This is explainable because the cut is at the very proximity to the trailing edge and as the vortex flow leaves the wing interacts for a certain portion upstream on the lower surface. The accuracy for this specific section remains, however, of an appropriate grade.

4.4.1.2 Calibration Application and Validation Cases

Overall, the results are promising as a single optimum is able to improve a wide range of angles of attack with consistency where other available models could not. The calibration targets see their mean absolute error with the experimental data being significantly improved (Table 4.5). Moreover, the numerical simulations show no evidence of additional instability, maintaining a good solver robustness along the complete preliminary testing phase and the optimization procedure. No significant additional computational cost is introduced by the methodology, except for the optimization procedure which might cost between 10 and 100 times the numerical simulation of one angle of attack of the considered test case. However, it is expected to be reduced with experience and transfer of information from other test cases in the preliminary testing phase. Moreover, with the

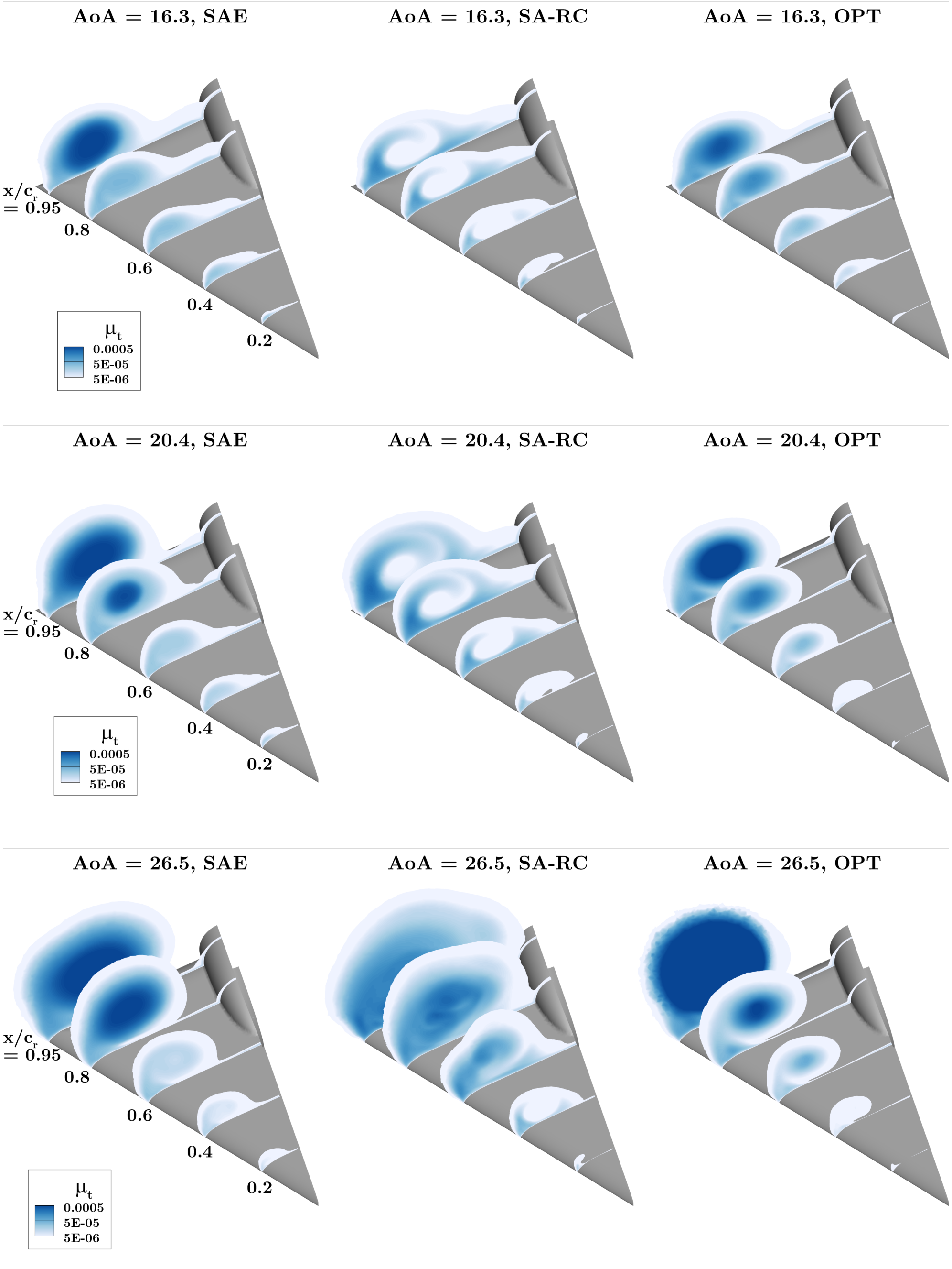

Figure 4.18: Eddy viscosity exponential distribution along cross-flow sections at $x/c_r = [0.2, 0.4, 0.6, 0.8, 0.95]$ for the 65° swept delta wing with $r/c_r = 0.033\%$, $M = 0.4$ and $Re = 6 \cdot 10^6$. The data of the baseline SAE model, the SA-RC and the optimized turbulence model (Table 4.4) are compared.

application of the methodology to large datasets, the optimization computational cost becomes negligible by proportion.

The calibration phase on the reported case is followed by the validation case in order to evaluate how consistent the improvement is over flow conditions and geometrical variations of the calibration case. With respect to this test case, the possible validation cases are spread over different Reynolds numbers, Mach numbers and also leading-edge geometries.

Validation Case Application. An important validation variation which has been the focus of research along the VitAM project also by the research partners at TUBS [109] is reported in detail [108, 130]. This validation case consists of a variation from the calibration case of the Reynolds number ($Re = 2 \cdot 10^6$) and the leading-edge shape which is now completely sharp. The surface C_P distribution is reported in Figure 4.19 where data for two angles of attack which manifest the largest discrepancies to experimental data [131] are depicted.

In general, the conclusions gathered for the calibration case and its application to the relevant angles of attack remain valid for this validation case. Hence, the sensitivity of the turbulence model is low on the lower surface and on the structured portion of the vortex, upstream of $x/c_r = 0.6$. The turbulence model optimum improves the prediction of the vortex development stage and the breakdown position is displaced downstream compared to the baseline SAE model (Fig. 4.19). At $x/c_r = 0.6$, the SAE model shows a larger suction footprint and a higher peak compared to the experimental data. This is not improved by the turbulence model variation which slightly worsen the accuracy by showing an even higher suction peak at 25.4°. However, the better prediction of the vortex flow stage enhances the modeling quality of the interaction between primary and secondary vortex structures. Hence the secondary suction foot print is in good agreement with the wind tunnel data at $x/c_r = 0.6$ for $AoA = 25.4°$. Further downstream, both angles of attack manifest a significant improvement due to the prediction of the correct vortex stage. However, the suction peaks are consistently higher than the experimental data and this suggests that the accuarcy average improvement is going to be lower than the calibration case. At the region of the flow in proximity of the cut at $x/c_r = 0.95$ for the largest angle of attack, a significant offset between the wind tunnel data and both numerical models is visible outside of the vortex peak. In conclusion, in comparison to the baseline SAE model, the improvement is significant.

Summary of the Validation Results. The results of all of the validation cases are not reported in detail but a summary of their flow and geometrical variations as well as their accuracy levels are reported in Table 4.5.

The average improvement in the accuracy related to the experimental data due to the application of the optimized model ranges between an error reduction of 10% and 26.9%. The only exception is the case with the medium leading-edge radius (with $r/c_r = 0.1\%$) with the same Reynolds number which, as an outlier, presents a reduction of only 2.2%. However, the error of the baseline turbulence model for this case is already really low

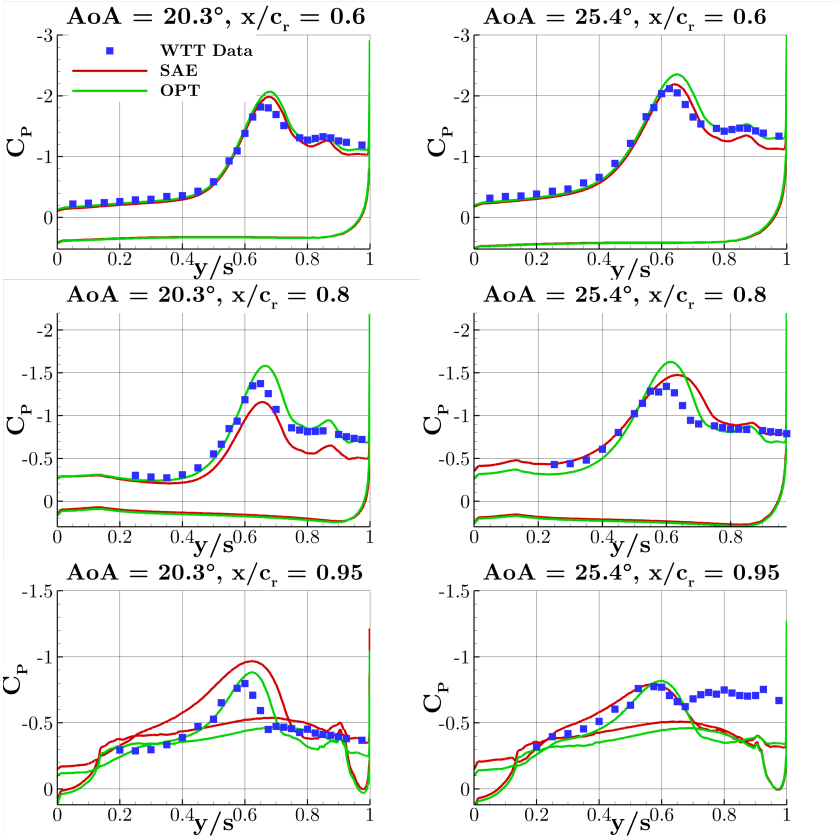

Figure 4.19: Surface C_P distribution along cross-flow sections at $x/c_r = [0.6, 0.8, 0.95]$ for the 65° swept delta wing with $r/c_r = 0.0\%$, $M = 0.4$ and $Re = 2 \cdot 10^6$. The data of the baseline SAE model and the validation of the optimized turbulence model (Table 4.4), calibrated on a different Reynolds and leading-edge shape, are compared with the steady pressure surface measurements [131]).

and, therefore, a lower sensitivity of the turbulence model modification is to be expected. This result confirms the potential and good applicability of the methodology because it does not worsen cases where the baseline model already provide good results. The same is evident when the optimized model is applied to moderate and low angles of attack where the sensitivity is even lower.

4.4.2 Non-Slender Delta Wings - Model53, Model56 and Validation Cases

In the previous section, the optimization and validation of a slender delta wing, i.e. which employs a large sweep angle, has been investigated and it has shown the potential of the present method to improve the accuracy for a relatively large spectrum of validation cases. In order to extend the application of the methodology to other topologies of delta wing shapes, in this section, the methodology is evaluated for a different cluster of cases included within this research which are non-slender delta wings. Therefore,

Table 4.5: Validation cases for the application of the optimized set of coefficients for the 65° swept delta wing with $r/c_r = 0.033\%$.

$r/c_r\%$	Re	$\mathcal{E}_{C_P,SAE}$	$\mathcal{E}_{C_P,Opt}$	$\mathcal{E}_{C_P,Opt} - \mathcal{E}_{C_P,SAE}/\mathcal{E}_{C_P,SAE}$ (%)
0.0	$2 \cdot 10^6$	0.1355	0.1195	-11.8%
0.0	$6 \cdot 10^6$	0.1349	0.0985	-26.9%
0.0333	$60 \cdot 10^6$	0.1831	0.1452	-20.6$
0.1	$2 \cdot 10^6$	0.14577	0.1276	-12.5%
0.1	$3 \cdot 10^6$	0.1934	0.1745	-10%
0.1	$6 \cdot 10^6$	0.1177	0.1150	-2.2%
All cases average	-	0.1517	0.1300	-14.3%

wings with a moderate sweep angle around 50°. Such delta wing types are of high relevance as they are found in numerous cases of application and production through the decades. Whereas highly swept wings provide a more stable vortical flow structure which delay breakdown up to high angles of attack, they have difficulties in providing an appropriate wing area, aspect ratio and proper aerodynamic characteristics. Lower swept wings are therefore commonly used as main wing and highly swept wings are usually employed as strakes which stabilize the vortical structure upstream of a lower swept main wing. As consequence of a lower sweep angle, the vortex flow characteristics change compared to highly swept delta wings. The vortex flow follows a different path through its development stages due to its inherent higher instability. The breakdown instability of the vortex structure is encountered at lower angles of attack and the suction footprint is characterized by a wider area with reduced peaks. All such differences in the flow type and development are associable physically to differences in the flow variables. As consequence, because the enhanced turbulence model is formulated with a physical fundament using flow quantities related to a vortex flow and its type, it is expected that the optimum derived for the VFE-2 test case does not improve the modeling of turbulence for test cases with drastic differences with respect to the sweep angle, which is the case of non-slender geometries.

The reference test case for the calibration phase is chosen to be the Model53 [120] geometry which has been described in section 4.1.2. Experimental data for the calibration phase are chosen in the AoA-range where the highest discrepancies with the baseline model are present, hence, between the initial breakdown and the completely stalled and vortex shed condition. This range covers the angles of attack between 20° and 30°. In parallel, the Model56 is selected as the most logic validation case being a modification of the Model53 where the sweep angle is increased by 3°. In fact, the Model56 was thought and designed to be a validation case for the Model53. Therefore, the results are reported by describing in parallel the application of the optimum to the calibration and validation cases. Consequently, additional validation cases with other differences with respect to the planform characteristics are reported in the successive section. The application of the methodology focuses on the middle-high portion of the angle-of-attack polar and high performance aircraft with comparable wing planforms commonly fly at such high incidences with a 20° deployed slat. For this reason, the Model53 and Model56 are provided with a reasonable slat deployment angle. The Model53 and Model56 offer a suitable and realistic set of cases for the evaluation of the methodology for moderate sweep angles and non-slender delta wings [108, 130]. Moreover, they inherently bring more complexity into the vortex flow topology due to the presence of the deployed leading-edge slat. The interaction between vortices is a relevant feature and it results in cross-dependences which increase the challenge of the proper calibration and flexibility of the turbulence model modification. This is a relevant step forward for the application of the methodology to a large dataset of a full aircraft configuration which employs several small geometrical variations.

The different local angle of attack at the slat's leading edge induces the separation of a second vortex of a more stable nature. The two vortices differ in terms of topology and development stage also because the separating flow at the slat has to overcome the deployment kink (Sec. 1.2.4.1) which additionally modifies the flow compared to a free vortex over the main wing surface. Moreover, their cross-interaction increases the flow complexity as it changes with the angle of attack. In particular, due to their vicinance along the rear portion of the wing, the less stable vortex breakdown provokes a triggering effect and it incepts an instability to the more stable one. Whereas the two vortices separate along the same leading-edge sweep, their difference is not only associated with a different effective angle of attack. The leading-edge slat deployment changes in fact more consistently the shape of the wing countour and surface. For this reason, the secondary vortex structure is of different nature.

Application of the SAE Baseline Model. Before the application phase of the methodology, a first overview and analysis of the available experimental data and the baseline turbulence model is of high relevance and good practice. Afterwards, the results are further analyzed into detail with a direct comparison with the optimized model. As shown in Figure 4.21a, with respect to the numerical results, the suction footprint of the first vortex appears reasonable and it clearly shows the differences to the 65° swept wing correlated with the presence of a lower sweep angle. It is evincible how the suction is relatively wider and the vortex structure influences the upper surface over a shorter distance. Downstream, the suction levels rapidly decrease. The suction peak values are comparable to the same angle of attack of the VFE-2 case but the surface area where it acts is larger. With respect to the second vortex, the vortex position appears to be closer to the leading edge. At first, in fact, the vortex highest suction is highly concentrated upstream the deployment junction because the vortex structure does not succeed to roll up over the main surface completely (Sec. 1.2.4.1). This is also evincible from the cross-flow section showing the vorticity magnitude at 32% (Fig. 4.26) where no clear vortex structure is visible at the current location but only a separated vortex sheet which turns inboard and stays confined in proximity of the surface. It eventually merges into the first vortex. An actual vortex structure may overcome the slat junction further downstream. At the cross-flow section at 72.7%, in fact, the second vortex structure is clearly visible.

The same conclusion is derived from the surface pressure distribution where the suction level imprinted by the separated vortex sheet on the slat is visible before it overcomes the slat's kink. In fact, the suction remains concentrated in the proximity of the leading edge until it moves above the deployed slat. The surface pressure distribution illustrates around 60% of the root chord (Fig. 4.21a), that there is a suction drop along the slat surface and a vortical flow generates above the main wing surface. Downstream, it generates a vortical structure with a correlated vortex suction footprint whose progression is expected by the vortex flow over a delta wing. Moreover, no strong interaction as well as vortex merging between the vortical structures is shown for the angle of attack of 20°, however, a weak cross-influence is present, mostly in the first 30% of the wing. The slat vortex sheet is fed into the main vortex upstream of the second vortex which may introduce a variation in the main vortex development as form of a weak cross-interaction (Fig. 4.27).

It is also significant to notice that the vortex structure of the first vortex exhibits relevant differences with the vortex structure at a higher sweep angle. If compared with the 65° swept delta wing of the previous section 4.4.1, no high core vorticity values are encountered that indicate a high rotational energy of its inner part. Therefore, the vortex differs significantly in its topology, development process and stages. Even though a vorticity collapse and diffusion is not present or is not strong compared to the aft-breakdown flow on the 65° swept wing, a reduction in the vorticity level is present for the vortex even before breakdown. The absence of an inner core high vorticity indicates that a wake type vortical structure is present. The lack of a pronounced viscous sub core and a less structured region correlate with a lower resistance to instability phenomena. Therefore, the progression of the vortex flow into a turbulent flow and the experience of adverse gradients of pressure make it more prone to the occurrence of vortex breakdown. Such behavior is again consistent with findings gathered from different literature sources in section 1.2 with respect to the effect of sweep angle and angle of attack to the evolution of vortex stages. When the angle of attack is increased to 25°, similar observations are gathered with regard to the first development of the apex vortex where the vortex type is similar but with a larger covered area (Fig. 4.27). As consequence, the C_P footprint is also larger and higher suction levels are induced on the wing surface. The progression of the vortex similarly provokes the reduction of the suction level along its axis. The vortex enhanced strength corresponds to a decreased stability. The vortex breakdown is displaced progressively upstreams with the increase of the angle of attack until a fully shedded vortex and stall stage is reached at the angle of attack of 28° as shown by the exprimental data for the Model53. The second vortex changes its development as the angle of attack is increased. Its deployment above the wing surface and its overcoming of the slat's kink takes place further upstream. As the vortices grow in intensity, they also experience more cross-interactions (Fig. 4.22a) and eventually completely merge in the rear part of the wing at $AoA = 28°$ (Fig. 4.24a). At $AoA = 25°$ the SAE model predicts a small but clear vortical structure above the deployed slat surface already from 32% of the root chord (Fig. 4.27). Therefore, a distinctive suction footprint is present also upstream of the "overcoming" of the slat junction (Fig. 4.22a) which was not the case for the angle of attack of 20°. Close to that position, the vortex sheet rolls above the main wing surface and it generates a vortex which influences a wider area compared to lower angles of attack. The experimental data confirm such considerations and illustrate that the accuracy of the SAE model up to this angle is not appropriate with respect to the prediction of the proper vortex stage. Improvement potential is visible with respect to the vortex progression, suction levels and cross-interaction strength. The highest grade of discrepancy of the SAE model is achieved where the breakdown dominates the flow and the experimental data predict a completely vortex shed and stall condition (Fig. 4.24a).

The validation cases selected for the Model56 are chosen with the objective to have comparable vortex flow stages. With respect to the angles of attack of 20° and 25° of the Model53, the same values are chosen for the validation case. They in fact represent a similar flow topology and vortex development stage for both cases. The higher sweep angle causes, however, the presence of a more stable vortex and a decrease with respect to the suction footprint area. Therefore, the vortex breakdown position is expected to be located downstream compared to the Model53 at the same angle of attack. With respect to the fully shedded and stall condition which is present at $AoA = 28°$ for the Model53, the angle of 30° is chosen for the validation case because it is more appropriate to perform a cross-comparison for same flow conditions.

Optimization Procedure: Model53 as Calibration Case. The accuracy of the results is evaluated in relation to the experimental data available which consists of static pressure measurements on the wing surface for a series of cross-flow sections. A first comparison with a commonly used baseline model like SAE is necessary for evaluating the starting accuracy grade and to identify the regions or points of the polar where the more severe discrepancies occurr. As evinced from the result, the general trend of the SAE model is to underpredict the instability status of the vortical structure and, hence, the breakdown phenomenon is displaced downstream compared to the experimental data. Smaller local differences are related to the level of suction of the different cuts and to the slat vortex and the position where its separation overcomes the slat junction. Being the highest amount of error concentrated on high angles of attack, the optimization is performed, after its first evaluation and sensitivity tests, on the single angle of attack of 28°. Similar sets of coefficients have been obtained by applying the methodology for combination of cases and the optimum obtained with the best performance for the calibration angles is selected (Table 4.6). The progression of the optimization procedure follows a similar course as for the 65° swept wing of the previous section (Sec. 4.4.1). The $\mathcal{E}_{C_P}$ is reduced for the most part within the first four iterations (Fig. 4.20) whereas the parameters show a partial delay in their convergence as they maintain a certain grade of oscillation. Eventually, the parameter oscillations decrease and the objective function further improves until an appropriate convergence grade is achieved. The last values of the parameters are set as the optimum of the considered calibration case. Terms which have not been included in the optimization have returned a comparable sensitivity to the other terms or they have not shown a relevant sensitivity along additional optimization procedures or preliminary sensitivity tests.

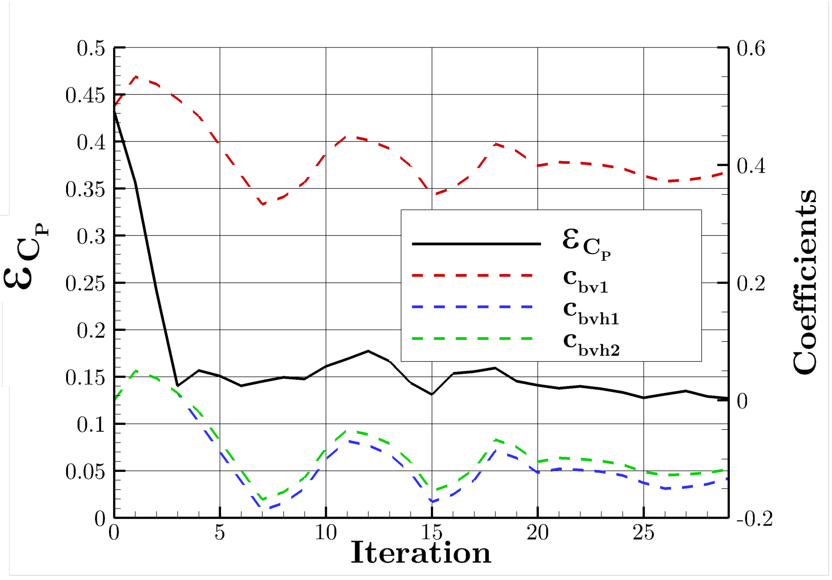

Figure 4.20: Convergence of the $\mathcal{E}_{C_P}$ and the coefficients of the turbulence model modification with sufficient sensitivity along the optimization procedure for the Model53, M = 0.15, $Re = 1.7 \cdot 10^6$ and $AoA = 28°$.

Table 4.6: Optimal set of coefficients for the Model53.

Coefficient	c_{bv1}	c_{bvh1}	c_{bvh2}
Value	0.41	-0.11	-0.10

The optimization [108] significantly reduces $\mathcal{E}_{C_P}$ with respect to the experimental data as shown in Table 4.7.

Analysis of the Calibration and Validation Results: AoA = 20°. Starting with the lowest angle of attack of 20°, the sensitivity of the numerical solution to the turbulence model is mild and this confirms the property of the methodology which does not influence negatively the solution which is already well predicted by the baseline model and where turbulence model variations have only slight effects. The breakdown location is moved slightly upstream with a displacement of around 5% of the root chord. Moreover, a particular feature is noticeable in the surface pressure distribution along the sections in the rear part of the wing (4.21a) where the experimental data indicate the presence of a third separation along the deployed slat. Another possible explanation is a different evolution of the secondary vortex which remains constrained above the slat without being able to overcome the deployment step and moving above the wing surface. This flow is only partially perturbated by the application of the optimized set of coefficients. The optimized model is, however, able to reduce the peak values of the vortex suction near the wing apex and towards the rear region of the wing. Both variations correspond

Table 4.7: $\mathcal{E}_{C_P}$ between numerical and experimental data for the Model53.

AoA °	SAE baseline	Optimized	Difference
20	0.2215	0.2267	+2.3%
25	0.1570	0.1348	-14.1%
28	0.4253	0.1411	-66.8%
Average	0.2679	0.1675	-37.46%

Table 4.8: $\mathcal{E}_{C_P}$ between numerical and experimental data for the Model56.

AoA °	SAE baseline	Optimized	Difference
20	0.2922	0.2709	-7.3%
25	0.1905	0.1609	-15.5%
28	0.2885	0.1986	-31.2%
30	0.4622	0.1182	-74.4%
Average	0.3084	0.1872	-39.3%

to a better grade of accuracy in that zone. While the highest source of discrepancy for the considered angle of attack remains concentrated on the progression of the suction level on the slat surface. It appears clearly that the turbulence model has low sensitivity with respect to the capturing or variation of this phenomenon. This suggests that in the case of a baseline turbulence model which does not capture a definite large-scale feature, it is not very probable that the calibration procedure may suddenly provoke its occurrence. The optimizer algorithm follows what the gradients of the incremental simulations returns as information based on the sensitivity of the solutions to the coefficient variations. Therefore, if at the starting point of the simulation no such feature is present, it is expected that the gradients push the optimization towards the improvement of the present flow features with high sensitivity. The optimizer is not able to "know" where to move in order to make a new feature appear. This is instead possible if different starting points of the coefficients are tested in order to find if the turbulence model formulation is able to predict it. However, with respect to this particular feature, no turbulence model variation or coefficient starting values have beend found which are able to predict it in any form. A second possibility is that the assumptions on which the turbulence model is based are too restrictive and they do not permit the modeling to properly predict such a phenomenon with any of the possible calibrations or model formulations as well. This may be evaluated either by veryfing different turbulence model formulations or moving to more complex turbulence models which is not a target of the current work. The first vortex, however, exhibits a significant grade of accuracy with respect to the C_P distribution in relation to the experimental data. This was already the case for the baseline SAE model, therefore, the capacity of not altering already properly predicted features by the turbulence model variation is confirmed. Differences are difficult to notice being

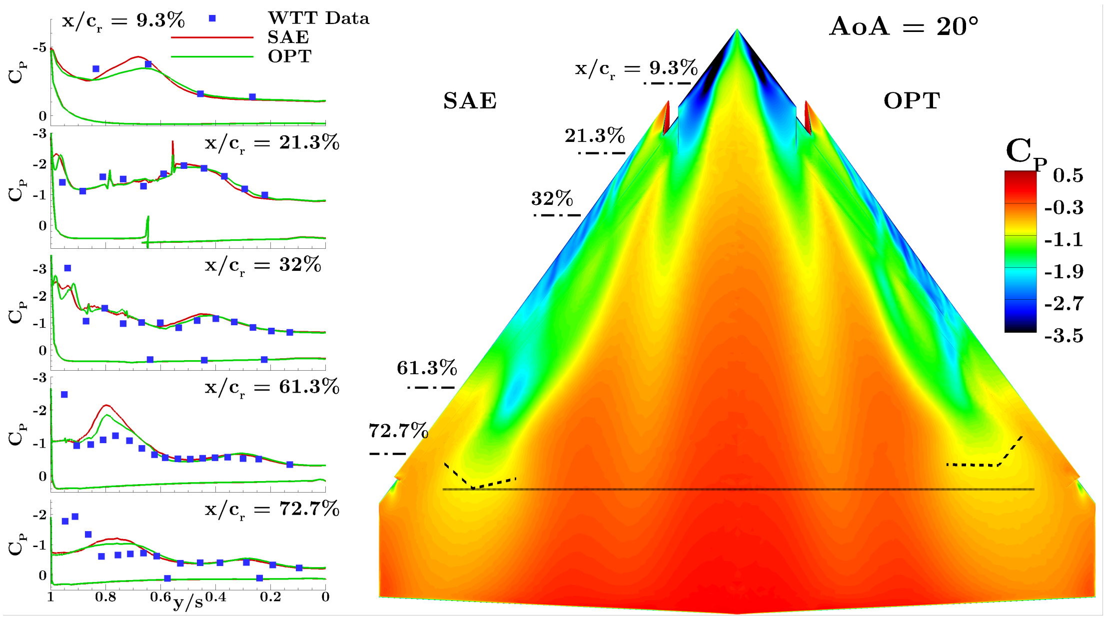

(a) Model53, Calibration case.

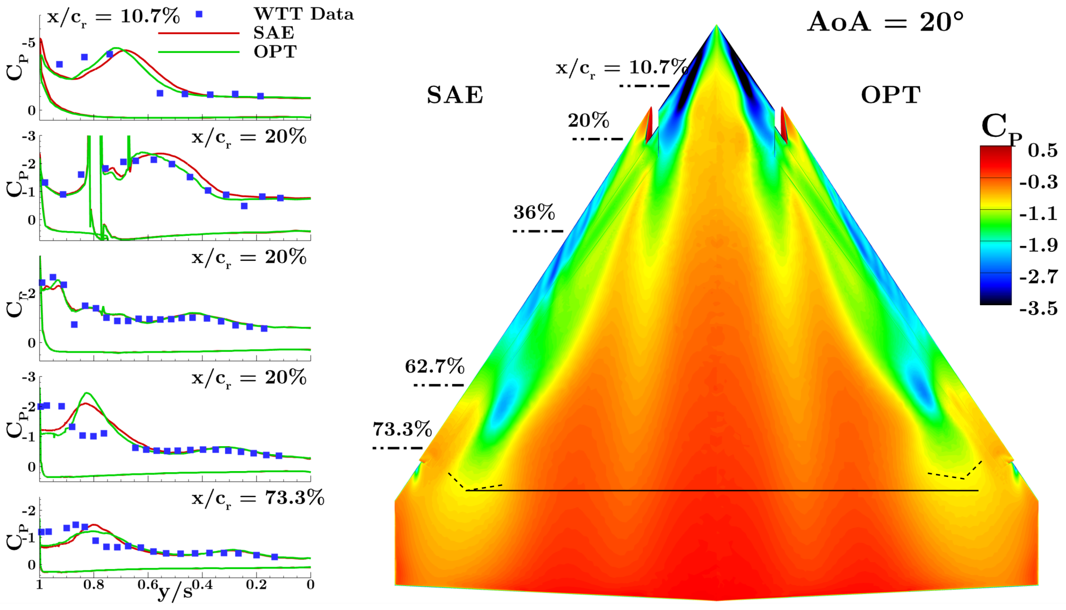

(b) Model56, Validation case.

Figure 4.21: An upper surface contour plot and 5 cross-flow sections of the surface C_P at M = 0.15, Re = $1.7 \cdot 10^6$ and AoA = 20° are reported. The original SAE model and the optimized turbulence model (Table 4.6) are compared to the experimental data.

below 0.1 of C_P. When noticeable, they relate to a further improvement of the suction level of the vortex for the section at 21.3% of c_r and the side towards the interaction region for the 32% section.

As consequence of the mismatch with the slat vortex separation and because that is the main source of discrepancy with the experimental data, the overall accuracy level is almost not varied with the turbulence model modification (Table 4.7). By visualizing the flow development along consecutive cross-flow sections of the vortex region (Fig. 4.27), it is evident how the main vortex flow shows no significant variation from the baseline model. The vortex maintains a wake type structure with no clear viscous sub-core which would be identified by a high vorticity center. The slat vortex maintains a wake type flow as well but the vortical region is larger as consequence of the fact that the suction levels drop along the vortex axis further upstream compared to the baseline model. The apex vortex shows a slightly lower intensity of the vorticity magnitude at the section located at 72.7% of c_r. Both variations confirm what is noticeable from the pressure distribution which is a displacement upstream of the breakdown instability. Moreover, the low differences present in the vorticity distribution confirm how the turbulence model variation has only slight influence on the vortical structures at this angle of attack. With respect to the eddy viscosity distribution (Fig. 4.26), its magnitude is consistently reduced for both vortices whereas its distribution shape qualitatively remains the same as consequence of the slight variation in the vortical flow topology. The variation is more significant in the less stable apex vortex where, for example at the section located at 72.7% of c_r, the eddy viscosity distribution changes qualitatively. The level of eddy viscosity reduces with the optimized model except for the inner region of the vortical structure where the flow is dominated by lower vorticity levels. However, this eddy viscosity variation results in a low influence on the vortex flow evolution as the vorticity variation is much lower than the eddy viscosity difference. This confirms again that these regions and types of vortical flow experience low sensitivity to turbulence modeling and they are already well predicted by the baseline model.

With respect to the validation case, i.e. the Model56 at the same angle of attack, the main source of discrepancy remains related to the rear portion of the wing and the evolution of the slat vortex where the vortex structure overcomes the slat junction and moves its suction peak above the wing surface. The optimized model partially modifies the vortex flow in this region without any significant improvement. This illustrates that, during the calibration phase, the model terms have not shown any significant sensitivity to the flow feature. The apex vortex is accurately predicted by both the baseline and the optimized model (Fig. 4.21b). However, the second one partially improves its C_P distribution along the first two cross-flow sections, i.e. at 10.6% and 20% of c_r. With respect to this improvement, it is interesting to notice how the direction of the variation of the suction distribution is different to the one experienced on the Model53. The vortex is now moved slightly outboard by the optimized model and the suction distribution matches the wind tunnel data with a better grade of accuracy. The same difference is evident for the suction peak predicted by the numerical results for the rear region at $x/c_r = 0.627$, where now the optimized model causes a stronger suction peak of the slat vortex to act on the wing surface. Similar observations are made with regard to the vorticity magnitude distribution along the vortex flow development (Fig. 4.29). Almost no variation is present, except in the section furthest downstream, i.e. at 73.3% of c_r, where the apex vortex shows a reduction in magnitude and the slat vortex presents a wider vortical region. This last effect is the consequence of the slight variation of the vortex development with respect to the shear layer roll-up above the main wing surface after overcoming the slat junction at the end of its progression above the deployed slat surface. The eddy viscosity is reduced consistently along the vortex, especially for the apex vortex (Fig. 4.28). The variation is similar to what evinced from the results on the calibration case at the same angle of attack. Similarly to the Model53, this variation of eddy viscosity has a low influence on the vortical structure development as it is particularly stable for the apex vortex. However, the difference in sweep angle is also evident in the different distribution of the eddy viscosity provided by the SAE model. For the Model56, in fact, the eddy viscosity distribution has a lower value in average although the qualitative distribution is comparable. The effect of the optimized model is comparable but the difference is larger in relation to the SAE model for the Model56. The sensitivity of the vortex flow solution to the eddy viscosity variation is very low as evinced for the Model53.

Analysis of the Calibration and Validation Results: AoA = 25°. The angle of attack of 25° is characterized by the upstream displacement of the breakdown location as well as the position at which the slat vortex overcome the slat junction. This is consistent with the effect of an increase in the angle of attack with regard to the development of a vortex flow (Sec. 1.2). Moreover, the vortices start to experience a significant cross-interaction. Although no complete merging into a singular structure takes place, the vortices are close enough to strongly influence each others evolution. If compared to the angle of attack of 20°, in fact, the region of low suction between the two vortices is clearly larger relative to the span width. The vortex flow stage is already properly predicted by the baseline SAE turbulence model. However, discrepancies are present with regard to the shape and the values of the surface suction distribution as well as the intensity of the vortices interaction. The application of the optimized set of coefficients influences all of the mentioned differences with the experimental data (Fig. 4.22a). The suction level and distribution is improved with a good agreement at the apex region ($x/c_r = 9.3\%$) while basically no variation is appreciable on the region upstream of the slat vortex ($x/c_r = 21.3\%$). With respect to this region, the baseline model is already able to provide accurate results. Further downstream, the optimized model improves the suction distribution of the slat vortex which is lowered as consequence of the upstream displacement of the breakdown instability. However, more complexity in the flow description is introduced by the cross-interaction between the two vortices which is presumably felt by the optimizer only as a secondary effect and as a consequence of the variation of the breakdown positions or the slat vortex development above the deployed surface. Therefore, the optimizer tries to move the breakdown of the slat vortex upstream due to its primary influence on the discrepancy, hence on the gradient sensitivity. By doing so, the cross-interaction changes and the apex vortex produces a stronger suction footprint for a longer distance. This result is detrimental for the accuracy with regard

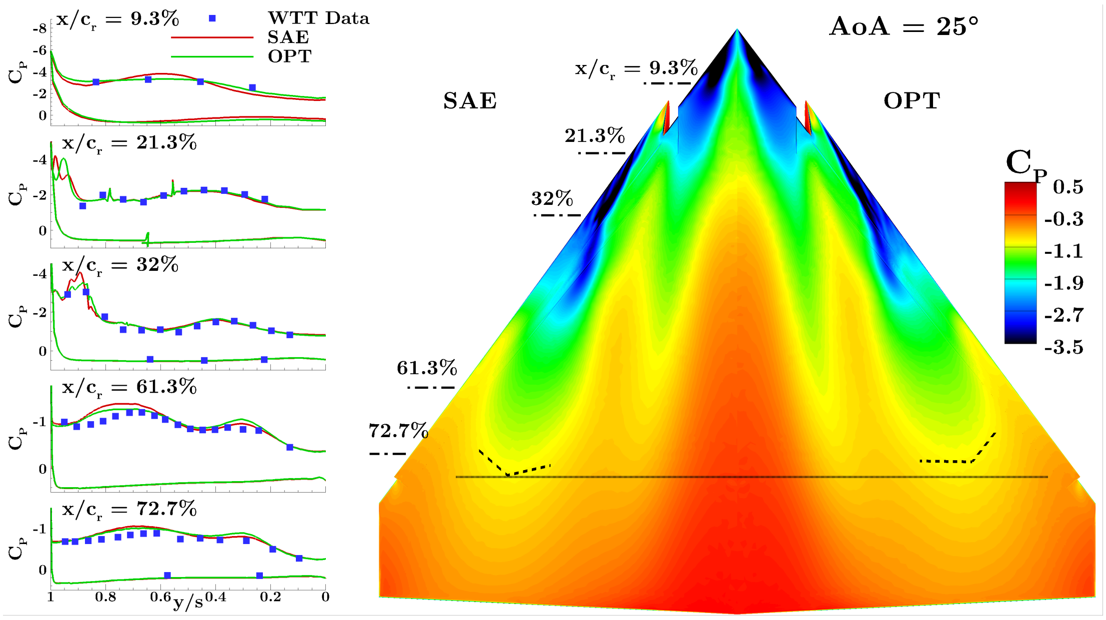

(a) Model53, Calibration case.

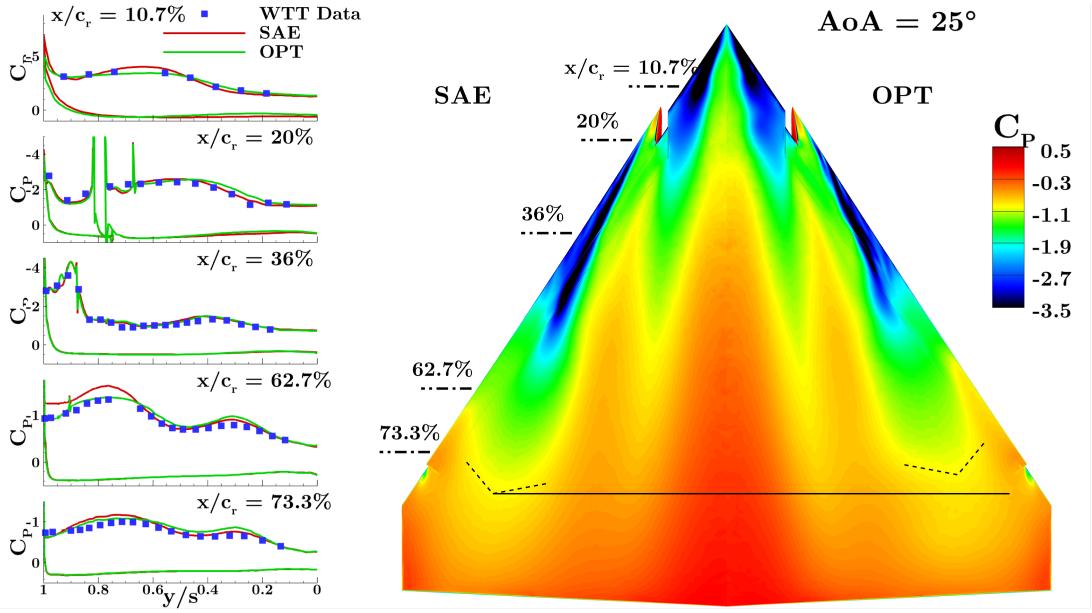

(b) Model56, Validation case.

Figure 4.22: An upper surface contour plot and 5 cross-flow sections of the surface C_P at M = 0.15, Re = $1.7 \cdot 10^6$ and AoA = 25° are reported. The original SAE model and the optimized turbulence model (Table 4.6) are compared to the experimental data.

to the first vortex. With respect to the region between the two vortices, the suction level and the shape remains the same for the two models and it manifests for both a proper grade of accuracy. It appears that the optimizer struggles to counter the interaction after having improved the source of main error which is the breakdown displacement. However, the improvement in accuracy is appreciable and important in terms of mean error with the experimental pressure distribution (Table 4.7). This is also confirmed with the application on the validation case (Table 4.8). Also for this angle of attack, it is confirmed that the lower wing surface experiences no sensitivity to the turbulence model variation. The surface pressure contour also clearly shows how the apex vortex impresses a higher suction for a longer distance.

With respect to the Model56, the starting flow topology of the baseline turbulence model is similar to the calibration case with the exception that the effects introduced by the larger sweep angle cause the suction of the apex vortex to be narrower and shorter in the axis direction (Fig. 4.22b). A more structured vortex flow type is present. The slat vortex presents a similar development to the Model53 but the breakdown position is at a different position due to the larger sweep angle. Additionally, whereas for the Model53, the transition of the slat vortex through the slat junction towards the wing upper surface is clearly visible as a kink in the suction distribution at around 30% of the root chord, this is not the case for the Model56 where the vortex exhibits no significant kink at the slat junction. In fact, the vortex follows a straight path towards its development downstream. However, with the application of the calibrated set of terms, the vortex shows a junction kink structure more similar to the one highlighted for the 53° swept wing. In general, it is interesting to notice that this is not the case for the optimized model where the vortices develop in a more similar fashion whereas the difference between the two cases is noticeable with the application of the SAE model. The main effects of the optimized model (Fig. 4.22b) are consistent with those seen for the Model53. Hence, a displacement upstream of the breakdown position with respect to the slat vortex and a reduction of the suction peak of the apex vortex occur. As consequence, a similar effect on the vortices cross-dependency is present. The slat vortex impact match better with the experimental data by employing the optimized model as visible for the section at 62.7% of c_r (Fig. 4.22b) which is actually more significant than the calibration case. A good indication that the optimizer and the additional terms grasp physical content from the calibration process and not a blind minimization. However, some local discrepancy is introduced on the inboard side of the apex vortex at 20% of c_r. This was not the case for the calibration case. In general, the predictive accuracy on the validation case appears to be properly conserved with respect to the medium range of angles of attack and the mean average error reduction is of the same order of magnitude, i.e. -14.1% for the Model53 and -15.4% for the Model56 (Tables 4.7, 4.8).

The vorticity distribution along cross-flow planes shown how the vortex develops over the wing and the slat surfaces (Fig. 4.27). For both the calibration and validation cases, almost no variation is introduced by the application of the optimized model at the first illustrated cross-flow section. This region is dominated by the single apex vortex whose structure remains stable and it is insensitive to turbulence modeling variation although a certain difference is present with respect to the eddy viscosity distribution (Fig. 4.26). Similarly to the smaller angle of attack, the application of the optimized model corresponds to a reduction of the eddy viscosity levels. However, this variation magnitude changes with the sweep angle change. At the section further downstream, the eddy viscosity variation is more significant for the Model56, in particular, for the slat vortex. Differences in the vorticity distribution are less evident than for the surface pressure. It is noticeable that the optimized model changes the stage of the slat vortex development in the middle section.

Analysis of the Validation Results: AoA = 28°. Moving to a higher incidence angle, the angle of 28° for the validation case is selected. This choice is taken due to the fact that the vortex flow development stage foreseeable from the wind tunnel data is different between the two cases. Therefore, in order to provide a better comparison between similar vortex flow stages, the angle of attack of 28° of the Model53 is compared to the one at 30° for the Model56. This further confirms the effect of a variation towards higher sweep angle which causes an offset of the vortex evolution stages towards higher angles of attack. However, the angle of attack of 28° is reported for consistency and for the analysis of an additional point in the vortex development region between a fully developed one and a complete vortex shed and stall condition.

The vortex flow stage at 28° (Fig. 4.23) corresponds to a fully developed vortex with breakdown. The breakdown position moves upstream compared to the angle of attack at 25° and the weak cross-interaction is substituted by a strong interaction at first which eventually causes the collapse of the vortices into a common structure. However, the baseline turbulence model is not able to predict such features but it still returns a weak interaction of the two vortices as solution, similarly to the solution at $AoA = 25°$ with an upstram movement of the breakdown location. In fact, the presence of two suction peaks is visible down to the section at 73.3%. The application of the optimal set of terms permits a proper solution of the vortices flow development stage with respect to the strong interaction and structures merging. As consequence, the suction distribution is signficantly improved along the slat vortex development, as visible from the section at 36% (Fig. 4.23), and downwards along the single merged structure. At the section at 10.7% the suction peak of the apex vortex is more flat and slightly lower compared to both experimental data and the baseline model. With respect to this feature, the baseline model returns a better accuracy. It is noticeable from the surface suction contour (Fig. 4.23) with the optimized model that the vicinance of the two vortical structures causes also a triggering effect of the breakdown instabilities as the locations for both vortices are close to each other on the wing surface. In general, the accuracy achieves an important improvement compared to the baseline SAE model (Table 4.8).

Predictive Capability of the ANN-Predicter. The ANN-predicter (Sec. 3.5.2.2) is applied to the validation case (Model56) at the angle of attack of 28° in order to investigate which accuracy improvement would have been possible without the availability of a previously obtained optimized model. The predicter returns a set of coefficients which differs from the Model53 (Table 4.9). The value of c_{bv1} is less destructive whereas c_{bvh1} gets really close to a zero value. The last coefficient instead is the most similar to the Model53 optimum. Overall, the magnitude of vortex destruction seems similar as the

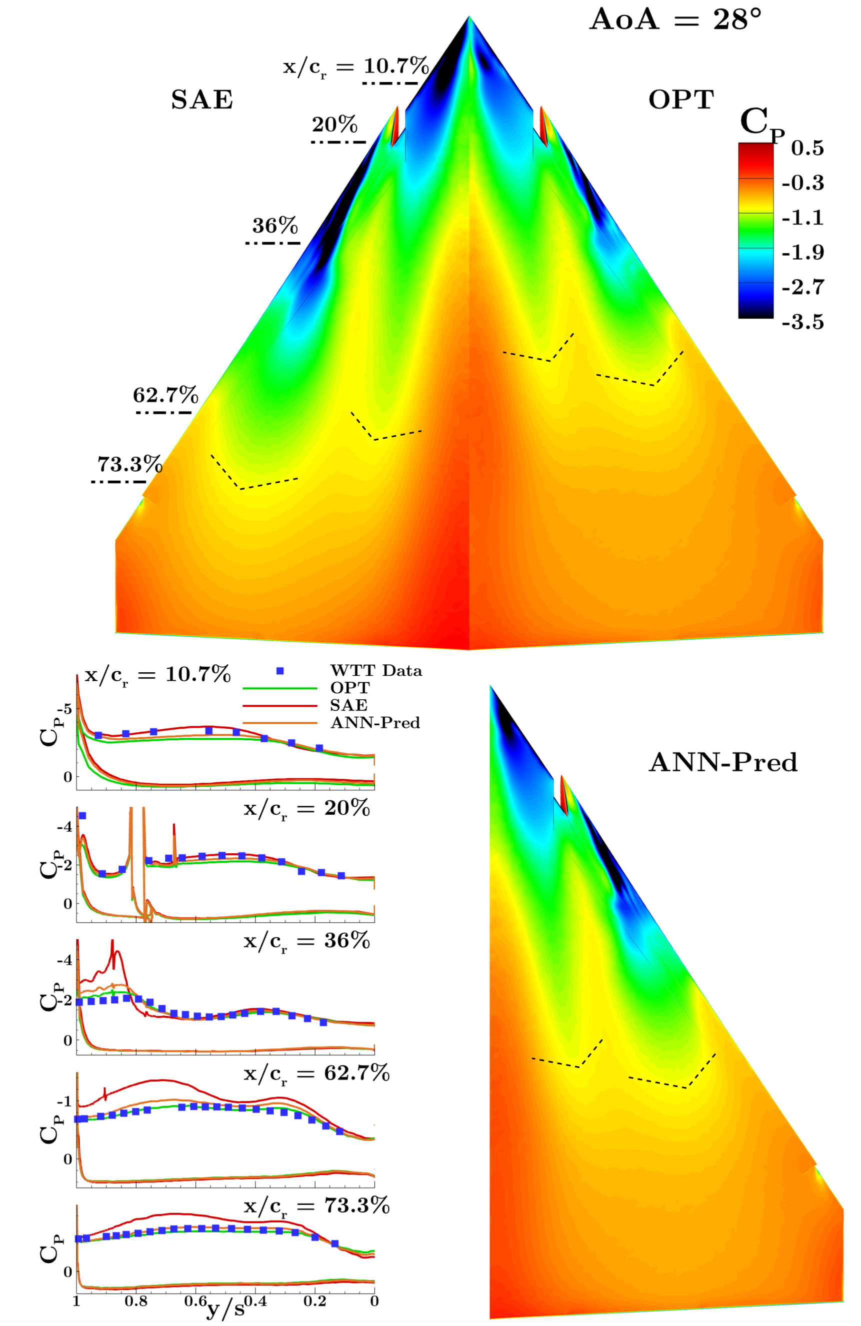

(a) Model56, Validation case.

Figure 4.23: An upper surface contour plot and 5 cross-flow sections of the surface C_P at M = 0.15, Re = $1.7 \cdot 10^6$ and AoA = 28° are reported. The original SAE model, the optimized turbulence model (Table 4.6) and the the model predicted by the ANN-predicter (Table 4.9) are compared to the experimental data.

difference between c_{bv1} and the other terms is similar to the one of the Model53 optimal coefficients. However, a different distribution of the vortex destruction is encountered in the development of the different regions of the vortices.

As illustrated in Figure 4.23, the C_P contour plots manifest a similar variation to the optimized model of the ANN-prediction from the SAE. The breakdown of the vortices is displaced further upstream. However, the displacement is smaller than the one obtained by the Model53 optimum. The cross-flow distribution of C_P confirms this result. On the one hand, the sections located at $x/c_r = 36\%$ and 62.7% clearly show how the ANN-prediction returns a C_P peak which partially differs from the experimental data although the improvement from the SAE model is significant. On the other hand, the first two sections located more upstream manifests a better accuracy level for the ANN-prediction results. The last section at $x/c_r = 73.3\%$ shows that a similar result is obtained for the two model variations although the ANN-prediction exhibits a C_P distribution closer to the experimental data.

The ANN-predicter application shows its potential for the partial improvement of newly investigated test cases which lack of experimental or high fidelity data. Moreover, this set of terms would also provide a suitable coefficients initialization for an optimization procedure dedicated to refine the accuracy based on experimental data.

Table 4.9: Set of coefficients predicted by the ANN model for the Model56 at AoA = 28°.

Coefficient	c_{bv1}	c_{bvh1}	c_{bvh2}
Value	0.267	-0.054	-0.0324

Analysis of the Calibration and Validation Results at Stall Conditions. As final vortex flow stage of the considered class of non-slender delta wings, a stall condition is analyzed. As mentioned, this flow feature is achieved at 28° angle of attack for the Model53 while it is delayed up to 30° for the Model56. The occurrence of a stall condition is clearly indicated by the experimental data along the different cross-flow sections where the suction distribution is flat along the complete wing upper surface for both the calibration and validation cases. The level of suction starts from a level around $C_P = -2$ at the apex (Fig. 4.24) and reduces progressively along the freestream direction dropping below -1. However, the numerical solutions obtained with the application of the baseline SAE turbulence model show the presence of a fully developed vortex stage where the breakdown of the vortices is moved further upstream compared to smaller angles of attack. In addition, the vortices now merge at a position corresponding to their breakdown location, i.e. around 50% of c_r. The instability of which involves both the vortical structures and it merges them together into a single chaotic wake flow similarly to what seen for the angle of attack of 28° with the Model56. The question remains about the causality of the phenomena. Hence, whether the instability of the first vortex, which bursts, triggers the breakdown of the other vortex due to the strong interaction or whether the strong interaction between the more unstable vortices cause an instability to occur at the same

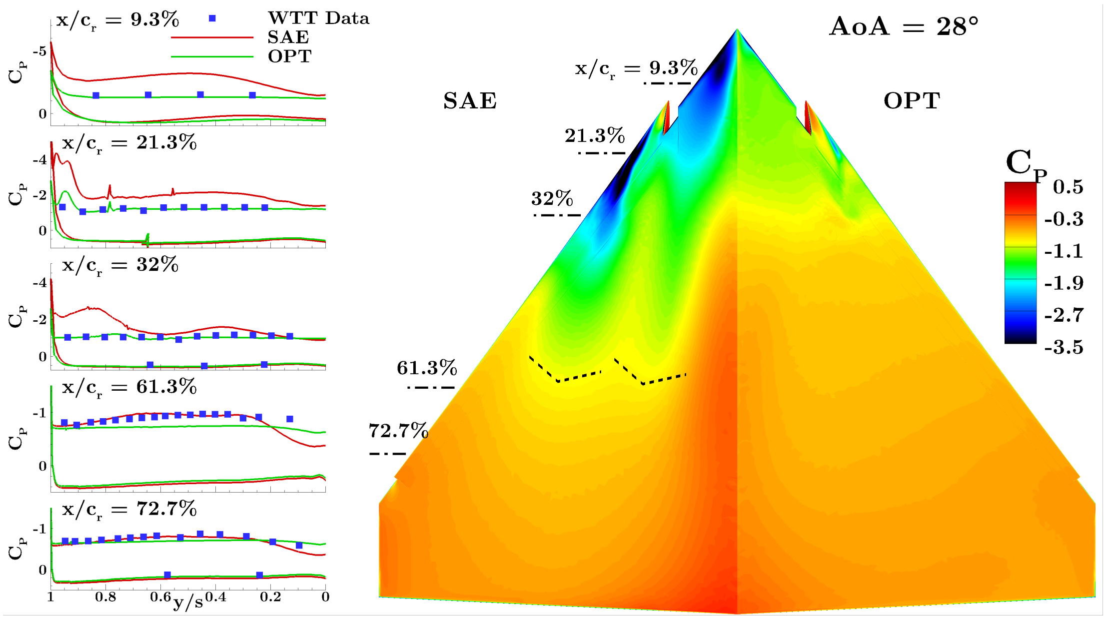

(a) Model53, Calibration case.

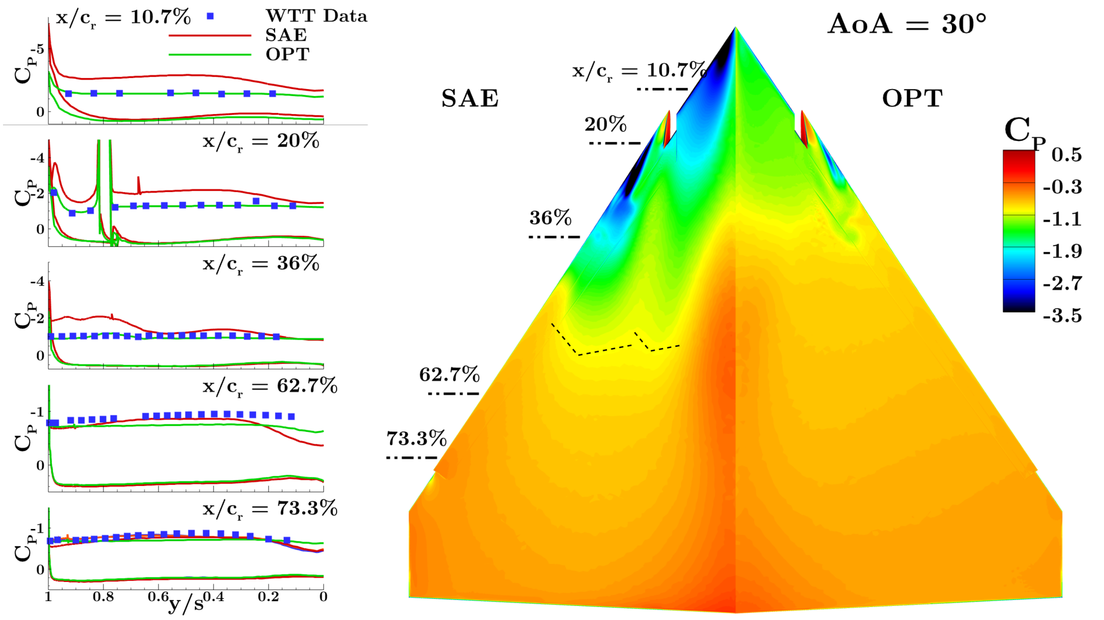

(b) Model56, Validation case.

Figure 4.24: An upper surface contour plot and 5 cross-flow sections of the surface C_P at M = 0.15, Re = $1.7 \cdot 10^6$ and AoA = [28°,30°] are reported. The original SAE model and the optimized turbulence model (Table 4.6) are compared to the experimental data.

position. The prediction of the baseline model is wrong compared to the experimental data as the vortex flow stage is represented not correctly.

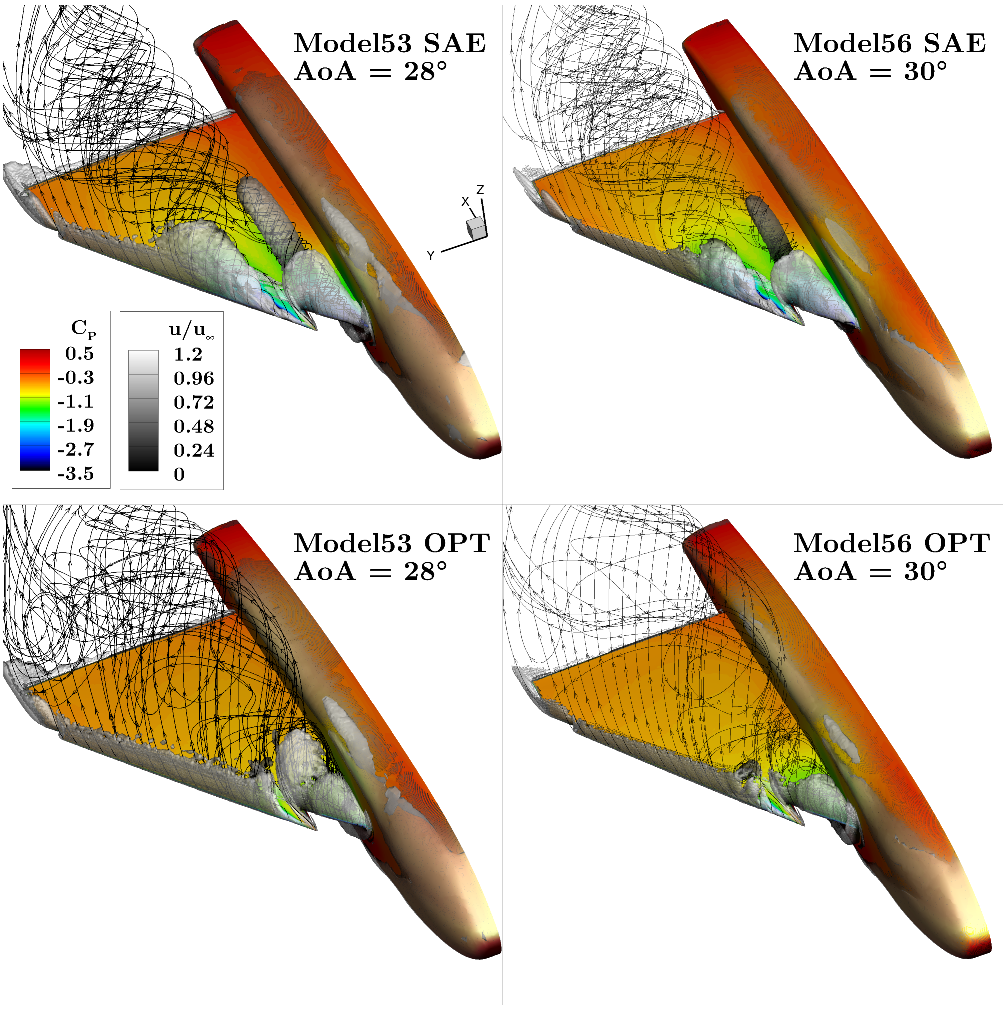

Figure 4.25: The numerical results of the Model53 and Model56 for the baseline SAE and the optimized turbulence model (Table 4.6) are here represented by means of iso-surfaces of a Q-criterion = 10 coloured with the contour of the dimensionless u component of velocity over the freestream velocity. The flow streamlines are postprocessed in order to represent the vortices. The surfaces are coloured with the C_P contour distribution.

The vorticity distribution along consecutive cross-flow planes confirms what evinced by the surface pressure distribution (Fig. 4.27). The apex vortex is similar to the one obtained for the angle of attack corresponding to 25° although the covered region is larger with respect to the first 25% of c_r. Hence, it causes a stronger footprint over the wing surface. Further downstream, a large difference is noticeable with respect to the slat vortex which already has a significant vortex structure at 32% of c_r. Moreover, the slat vortex does not present a clear vorticity peak or a jet type flow. The larger sizes of the vortices cause the merge of the two structures into a single one as visible at the cross-plane at 72.7% of c_r.

The application of the optimized model (Fig. 4.24a) on the calibration case clearly improves the numerical solution of the vortex flow as the correct development stage is predicted. A flat suction distribution is present for the whole wing which is in agreement with the experimental data. Moreover, the suction level is properly predicted with high accuracy from the apex and downstream to the middle of the wing. However, the progression of the suction level along the wing extension has partial discrepancies to the experimental data. As visible from the section at 61.3% of c_r the optimized model provides a suction level which qualitatively has a reasonable distribution but at a slightly lower suction level. This discrepancy is for the most part recovered moving further downstream where only small differences are present from the baseline model which is instead able to provide good accuracy in this region. Whereas the optimized model has been able to achieve a proper vortex flow stage it lacks sensitivity with respect to the evolution along the wing extension. Overall, the accuracy enhancement is consistent and significant.

The Q-criterion iso-surfaces (Fig. 4.25) show the drastic change of the vortex flow stage and characteristics with the application of the optimized model. With regard to the apex vortex, the baseline turbulence model provides a numerical solution which manifests a more stable vortex. An iso-surface structure is visibile until the middle portion of the wing and the contour levels of the dimensionless velocities reduce progressively until breakdown. It is interesting to notice how in the proximity of the slat separation, the geometrical discontinuity generates an effect on the first vortex due to a smaller separation structure at the slot between the leading edge and the deployed slat. The streamlines show a structured region until the iso-surfaces disappears and they merge with the slat vortex into the chaotic wake flow downstream. The iso-surface of the second vortex represent a reasonable structure if compared to the surface pressure distribution. The application of the optimized model (Fig. 4.25), as already seen for the pressure distribution, reduces the stability of the vortices which reaches breakdown more upstream and the configuration employs a stall condition except for the near apex region where a vortex is maintained down to the proximity of the slat separation. The slat vortex is completely shed into the chaotic wake. Whereas the merged burst vortex structure conserves a certain amount of rotation with the baseline model, this is not true for the optimized model where a higher grade of chaotic movement is manifested. The presence of a full stall condition may justify the issues of the optimized model to match precisely the suction levels above the rear portion of the wing. Similar conclusions can be derived from the numerical solutions of the Model56 geometry where the differences are mostly related to what already described from the surface pressure distribution. Also, for both models, the mild separations that happen above the generic fuselage appear to be only weakly influenced by the turbulence model variation which is a good indication that the variation of modeling directly affects the vortex flow fields.

The vorticity distribution exhibits variations (Fig. 4.27) which are consistent with the features analzyed from the surface pressure distribution. A fully burst vortex is already

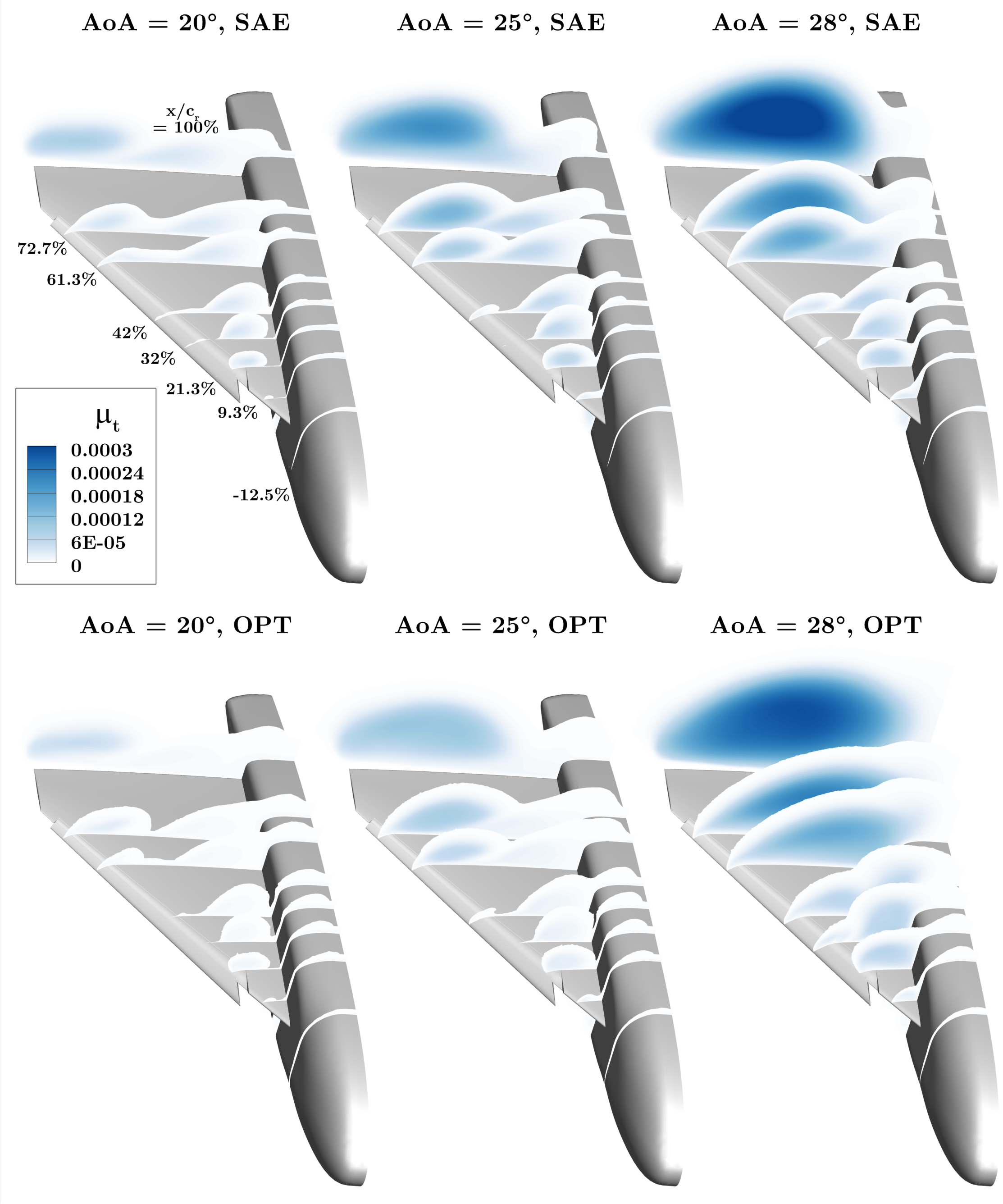

Figure 4.26: Eddy viscosity distribution along cross-flow sections at $x/c_r = [-0.125, 0.093, 0.213, 0.32, 0.42, 0.613, 0.727, 1.0]$ for the Model53 at $\mathrm{M} = 0.15$, $\mathrm{Re} = 1.7 \cdot 10^6$ and AoA = [20°,25°, 28°]. The data of the baseline SAE model and the optimized turbulence model (Table 4.6) are compared.

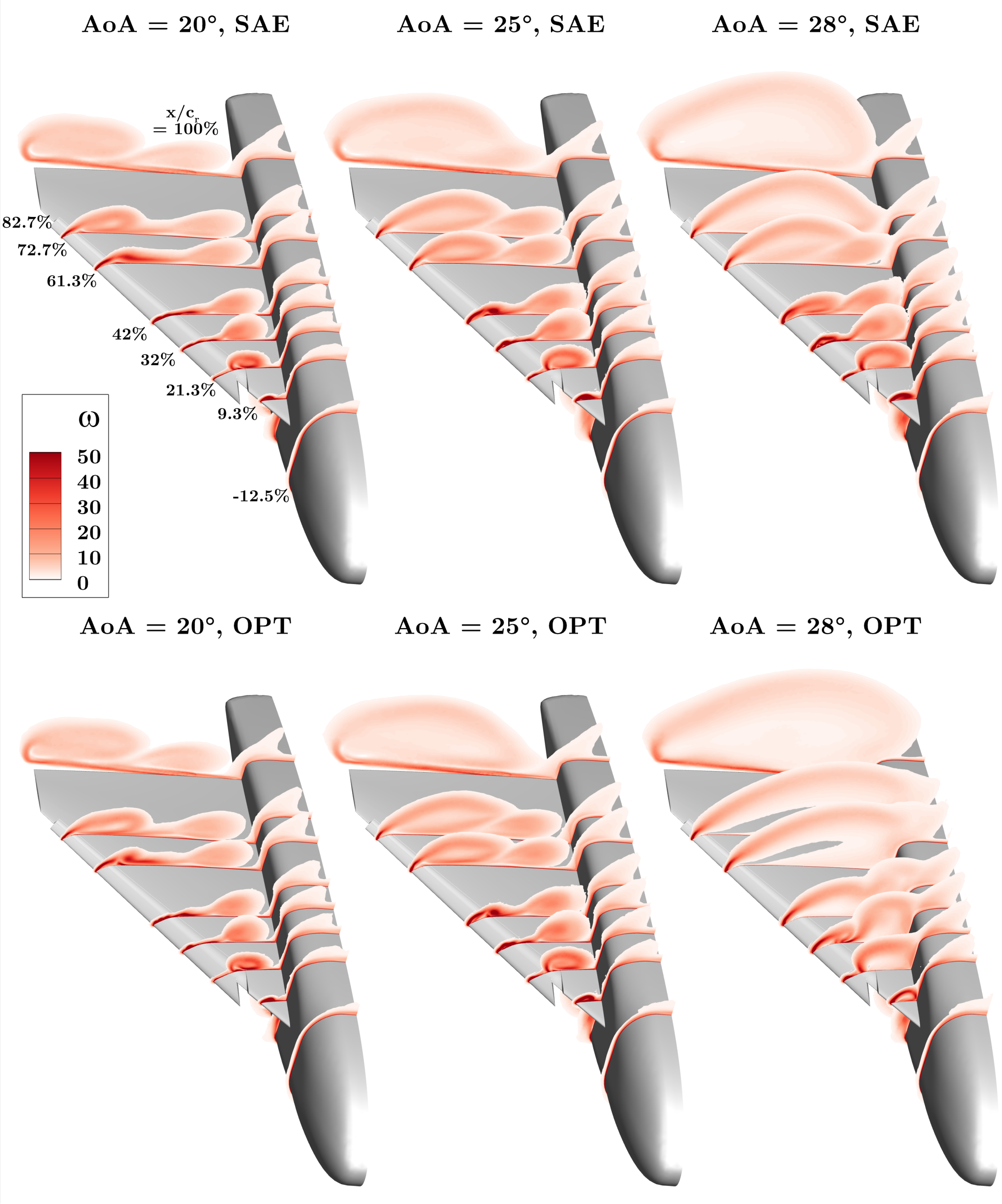

Figure 4.27: Vorticity magnitude distribution along cross-flow sections at $x/c_r = [-0.125, 0.093, 0.213, 0.32, 0.42, 0.613, 0.727, 1.0]$ for the Model53 at $\mathrm{M} = 0.15$, $\mathrm{Re} = 1.7 \cdot 10^6$ and AoA = [20°,25°, 28°]. The data of the baseline SAE model and the optimized turbulence model (Table 4.6) are compared.

present in the first region of the apex where a residual vortical structure remains far away from the wing. Only partial additional velocities which are remnants of the vortex shedding above the wing influence the wing surface. For this reason, the suction level is flat but higher above the front region of the wing. The progression of the vortices follows consistently the predicted flow stage. Therefore, the slat vortex experiences an early breakdown and shedding with merging into the vortex inboard. The slat vortex survives the extreme flow incidence for only a short distance close to the slat surface and on the region more upstream, as visible from the cross-flow plane at 21.3% of c_r. The flow downstream of the merging is similar between the two models with respect to the vorticity distribution showing that the highest sensitivities are related to the breakdown/shedding position. The last sentence is also true for the eddy viscosity distribution in the region downstream of the vortices merging (Fig. 4.26). In the region upstream differences are present. Although the turbulence model modification provides an increased destructive behavior of the model inside the vortical structure, the eddy viscosity is higher with the optimized model. This is due to the fact that indeed the application of the turbulence model employs more eddy viscosity destruction but with respect to the same flow stage. As the vortex flow stage changes, however, as consequence of the application of the optimized model, the eddy viscosity increases due to the presence of a burst and chaotic flow state. The presence of a different and more turbulent flow stage dominates the increase of eddy viscosity levels but its presence is originally caused by the more destructive nature of the optimized model. Therefore, when comparing the baseline and the optimized model at the same coordinate of the cross-flow plane, it is reasonable that the second provides a stronger eddy viscosity distribution.

When applied to the Model56 case, the effect on the vortex flow solution is similar and a comparable amount of accuracy improvement is achieved (Table 4.8). As already mentioned the same flow condition is achieved on the angle of attack of 30° due to the higher stability provided by the higher sweep angle to the vortical structure. The suction level is properly predicted until the mid-rear portion of the wing where a slight underprediction is obtained by the optimized model. With respect to the vorticity distribution along the cross-flow planes (Fig. 4.29), the effect of the optimized model is comparable to what experienced on the calibration case. However, the effect appears to be stronger at the location farthest downstream where the vortical region is more expanded and the tangential velocity magnitudes acting on the wing's upper surface are reduced. This region shows more sensitivity to the optimized model and the surface pressure distribution exhibits a better grade of accuracy compared to the Model53 calibration cases. The eddy viscosity distribution (Fig. 4.28) clearly exhibits the effect of its increased destruction already at the region close to the wing's apex. The shape is also modified as it follows the expansion of the vortical structure due to the stronger inclination to instability provided by a lower turbulent dissipation effect. The section at 73.3% manifests differences as well, due to the variation in the vortical wake structure.

The application of the methodology confirms its good potential already reported for a different class of delta wings in the previous section 4.4.1. First of all, the optimization procedure coupled with a preliminary phase of sensitivity analysis permits to obtain a relevant grade of accuracy improvement for the calibration target. This is performed with a suitable grade of effort in terms of user's time and computational costs. Moreover, the optimized model is not detrimental to the stability, convergence rate or computational cost of the numerical simulations when applied to both the calibration and validation case. The model offers a good flexibility in improving the validation case with a comparable grade of accuracy. It confirms the promising potential of being applicated for the accuracy enhancement of a large dataset of cases which share a common baseline case used as calibration target.

Additional Validation Cases: the AVT-183 53° Diamond Wing and the 55° Swept Blended Wing Body The validation of the optimum related to the Model53 on the Model56 has shown the potential of the methodology to be applied on a large dataset of small geometrical variations. This is of high relevance with regard to the application in an industrial framework where a series of small consecutive variations are tested iteratively for a baseline geometry. If the vortex flow characteristic is not or only slightly affected by the variation, it is assumed that the turbulence model calibration maintains consecutively a high part of its accuracy improvement. This is what we can see as the extension of the model calibration from a baseline geometry and extending it inside a certain range of variations.

Another possibility to further extend the methodology is to follow a different analysis. In this sense, it is possible to correlate a calibrated turbulence model with the topology of the vortex flow as well as the features which have been most significantly affected and improved. If this is clearly identified by the analysis of the effect on the calibration case, the same turbulence model is expected to improve other test cases where similar flow features or vortex characteristics/stages are present. Taking as example the Model53/56 cases, it has been shown how certain flow features are mainly addressed by the turbulence model calibration due to the fact that the optimizer algorithm follow the most sensitive flow characteristics in relation to the coefficients variations. Therefore, the breakdown displacement is improved for both considered cases in a consistent manner. The same conclusion can be made with respect to the accurate prediction of the stall condition. As a consequence, if a new test case is evaluated and a similar vortex flow topology appears at comparable angles of attack and geometric macro characteristics of the wings, i.e. sweep angle or leading-edge radius, the application of the same turbulence model has a high predictive capability and it maintains a significant portion of the accuracy improvement.

In parallel to the direct application of the Model53 optimum to comparable cases for the same flow and geometrical parametric cluster, the results obtained with the ANN-predicter (Sec. 3.5.2.2) are cross-plotted and compared.

To verify this, two test cases are here reported which enclose such comparable flow cases. These are the SAGITTA 55° swept blended wing body (Sec. 4.1.3) and the AVT-183 53° swept diamond wing (Sec. 4.1.1).

SAGITTA: 55° Swept Blended Wing Body. The present test case consists of a 55° swept blended wing body called SAGITTA and it has been described in section 4.1.3.

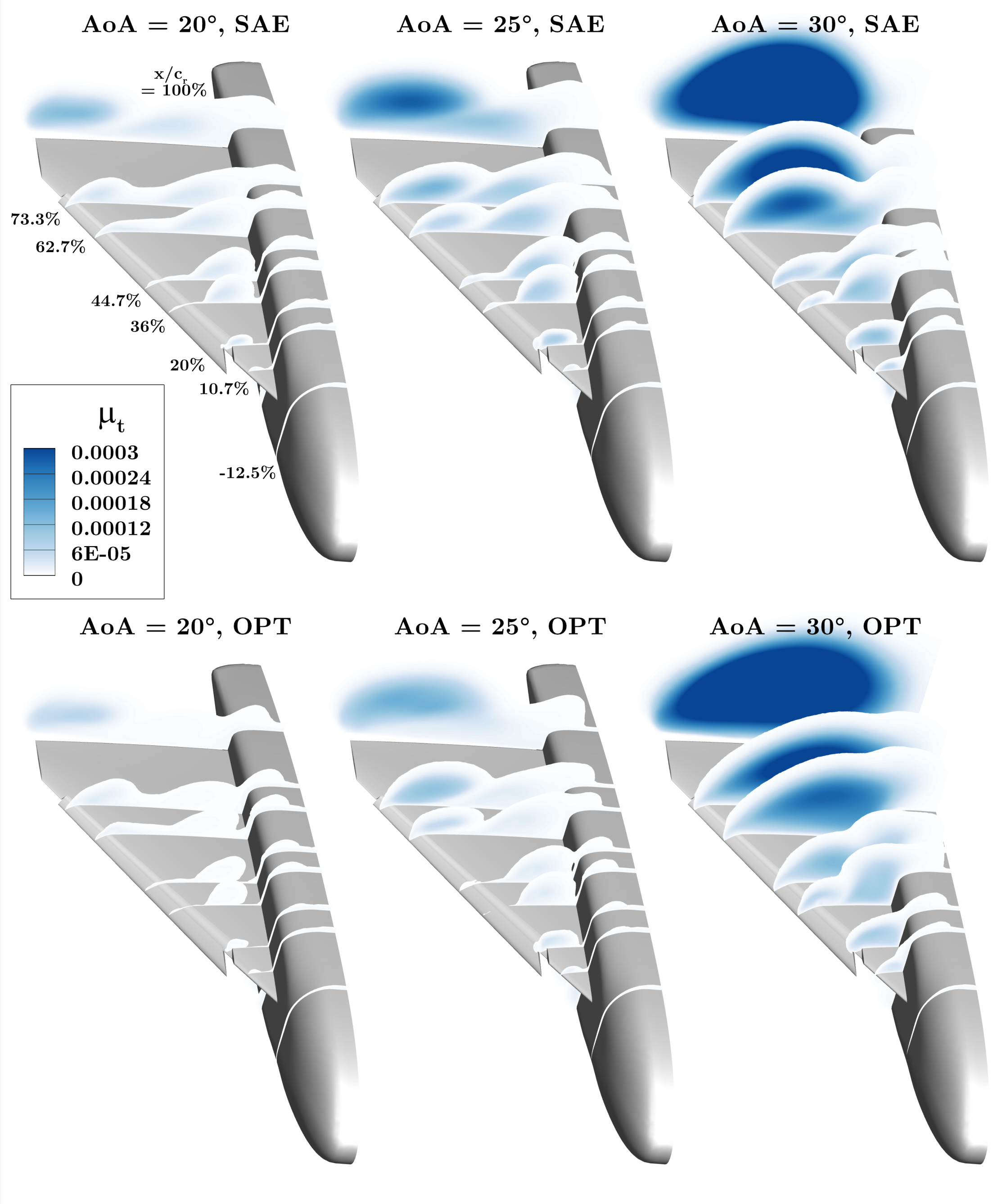

Figure 4.28: Eddy viscosity distribution along cross-flow sections at $x/c_r = [-0.125, 0.107, 0.20, 0.36, 0.447, 0.627, 0.733, 1.0]$ for the Model56 at $\mathrm{M} = 0.15$, $\mathrm{Re} = 1.7 \cdot 10^6$ and AoA = [20°,25°, 30°]. The data of the baseline SAE model and the optimized turbulence model (Table 4.6) are compared.

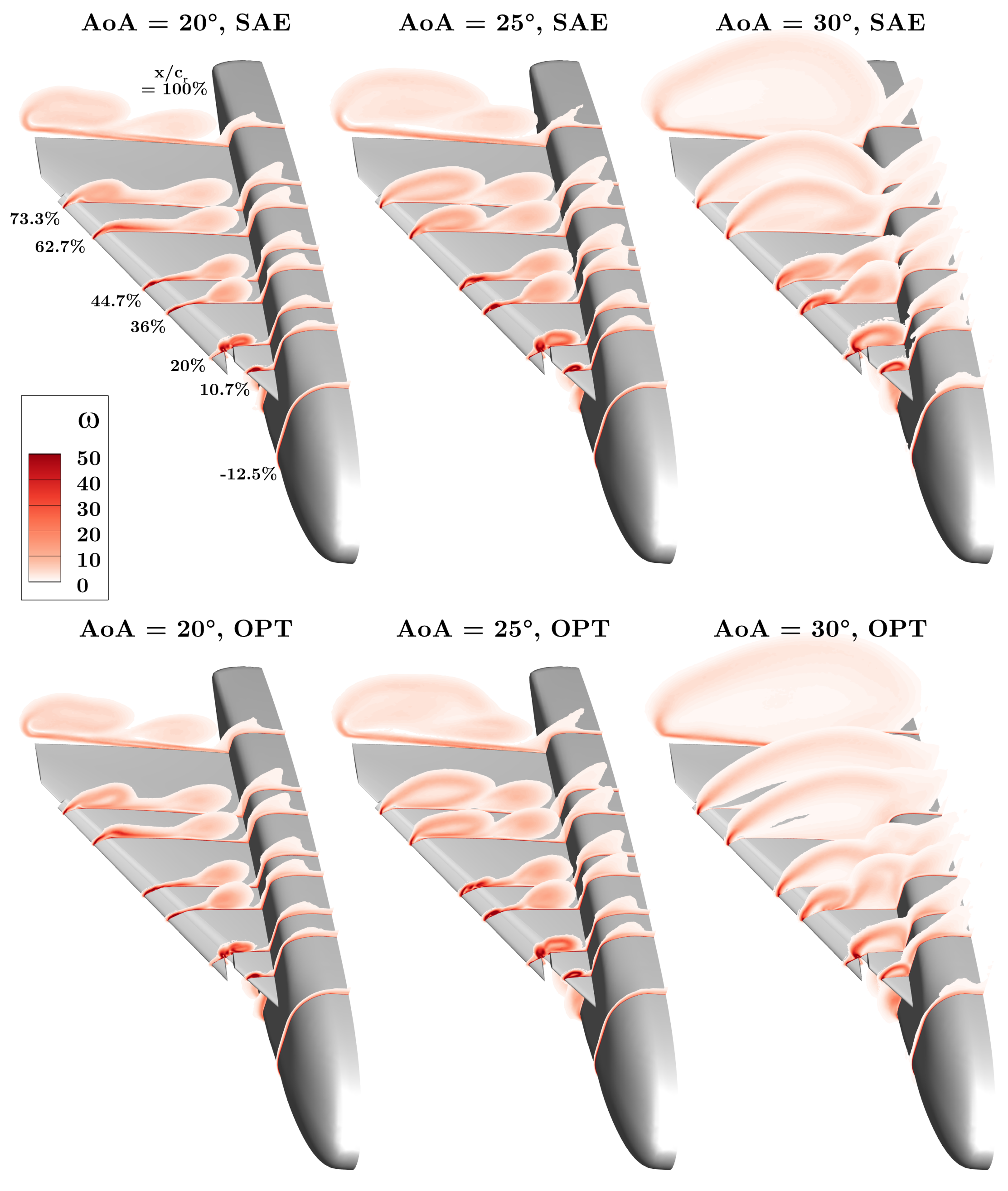

Figure 4.29: Vorticity magnitude distribution along cross-flow sections at $x/c_r = [-0.125, 0.107, 0.20, 0.36, 0.447, 0.627, 0.733, 1.0]$ for the Model56 at $\mathrm{M} = 0.15$, $\mathrm{Re} = 1.7 \cdot 10^6$ and AoA = [20°,25°, 30°]. The data of the baseline SAE model and the optimized turbulence model (Table 4.6) are compared.

Due to the availability of experimental data at high angles of attack and its medium sweep angle, it is chosen as a validation case of the optimum derived from the Model53 and the testing of the ANN-predicter extension [116]. This test case employs some major differences compared to the Model53. First of all, the sweep angle is 2° larger but also the other geometrical parameters of the planform are substantially different. In particular, the body thickness which is significantly larger. The leading-edge curvature is low and the rounded leading edge causes a partially developed vortex to take place up to moderate angles of attack. Since this application is thought as a validation case of the Model53 optimum, the section of angles of attack where a fully developed vortex with breakdown or stall condition dominate the flow is selected for this purpouse. The selected angle-of-attack spans between 32° and 40°. The flow condition is also partially different being the flow regime at a Mach number of 0.1. The wind tunnel model is a full span model and it has also been measured at the W/T-A wind tunnel facility at TUM-AER.

The numerical simulation with the baseline SAE model are performed as starting basis. This permits to investigate the vortex flow features which characterize the validation target data, i.e. the surface pressure distribution. In this way, experience is also gathered with respect to the correlation of the modeling sensitivity and the flow regions with the largest discrepancy. It is noticeable that the differences in the geometrical parameters compared to the Model53 cause a different positioning of the vortex flow stages along the angle-of-attack polar (Fig. 4.30). Whereas at $AoA = 28°$ a stall condition is achieved for the Model53, here a suction footprint caused by a vortical separation remains up to $AoA = 36°$. In general, the SAE baseline model provides a good level of accuracy on this test case up to $AoA = 36°$ whereas more difficulties occur in predicting the proper evolution of the incipient vortex separation at low to moderate angles of attack [74] where also multiple vortical structures may take place along the single leading-edge extension. At $AoA = 32°$ and $AoA = 36°$ the baseline SAE model is able to properly predict the right vortex flow stage but at $AoA = 40°$ it mispredicts it. In that case, it does not indicate a stall condition as illustrated by the wind tunnel data (Fig. 4.30). At the cross-flow section of $x/c_r = 0.1$ for $AoA = 32°$, a clear suction peak induced by a healthy vortical structure is shown by the experimental data (Fig. 4.30). The baseline SAE model shows the same vortex flow stage with an overprediction of the suction peak and some differences in the outer region between the peak and the leading edge. The vortex is fully developed and its separation fixed at the apex. Inboard, the flow is fully attached and it is properly predicted by the SAE model as expected. At $x/c_r = 0.2$, the suction peak level drops as the vortex region expands and the SAE model provides a similar qualitative distribution with a peak overprediction. Further downstream, the accuracy improves as the suction distribution is closer to the wind-tunnel data. Moving to the angle of attack of 36°, the vortex flow stage tends towards a stall condition but a vortex structure is still present. The suction distribution is flatter and at lower peak levels. The SAE model sees its accuracy being reduced as the overprediction of the suction peak is more significant. From $x/c_r = 0.4$ and downstream, the accuracy improves and the numerical results are considerably close to the experimental values. At $AoA = 40°$, the baseline SAE manifests a wrong vortex flow stage compared to the experimental data where a fully stall condition is evident. The discrepancies are considerable with respect to both the distribution shape and, consequently, the C_P values. The experimental data show that a completely flat C_P distribution is present along the whole surface. By looking in general at the vortex progression between the three reported angles of attack, it appears that the wind tunnel data exhibit a much faster transition to a stall condition compared to the baseline SAE model. This is expected to be related to the lack of accuracy in representing the real dissipative content of a turbulent vortex flow under the constraint of the Boussinesq assumption and the calibration for a fundamental and fully attached aerodynamic flow.

The optimal set of coefficients available from the calibration performed on the Model53 (Table 4.6) is applied to this test case as a validation process to investigate the predictive capability of an optimum and the proposed methodology to a cluster in the parametric space of cases around the identification of the original calibration case. The Model53 optimum provides interesting results already at the angle of attack of 32°. The main discrepancy of the SAE baseline model is substantially reduced in the front part of the wing. The suction peak of the region near the apex is significantly improved, the suction levels match with the experimental data. The region inboards is not influenced by the modeling modification. Moving to the section at $x/c_r = 0.2$, the peak level is also reduced to an appropriate level, closer to the peak level visible from the experimental distribution. However, the position of the vortex appears to be slightly displaced outwards, which is not in agreement with the wind tunnel data. Further downstream, the reduction of the suction level is too strong and it determines an underprediction of the experimental suction distribution. The discrepancy on the rear part is, however, retained under an acceptable level of error with the experimental data. By increasing the angle of attack to 36°, the C_P distribution is far closer to the experimental values. Also here the suction peak is slightly displaced outwards. However, at $x/c_r = 0.2$ in particular, the application of the Model53 optimum reduces the C_P values in the right direction until it underpredicts the experimental values with a considerable offset. The same effect but with a lower discrepancy to the experimental data is also visible downstream. Similarly to the Model53 and Model56 cases, the wake flow employs a higher grade of complexity and also the enhanced model struggles to improve its suction footprint with the same grade of improvement as upstream. At $AoA = 40°$, the wrong vortex stage predicted by the baseline model is substitued by a stall condition with the enhanced model. This is also in agreement with the results seen for the calibration case. The suction distribution is flat along the whole extension but a substantial offset in the C_P values is present. The application of the turbulence model calibrated on a different test case has shown its potential when the experience of the modeler is applied in order to identify the analogies with respect to the vortex flow characteristics and development type. Therefore, the methodology shows potential when applied to a reasonable cluster of cases around the calibration target.

In order to analyze the potential of the ANN-predicter extension [116], the features describing the SAGITTA test case at 36° angle of attack are injected in the neural network as input features. The predicter returns a set of coefficients reported in Table 4.10. The modeler may already see from the past experience that the predicter is going in a

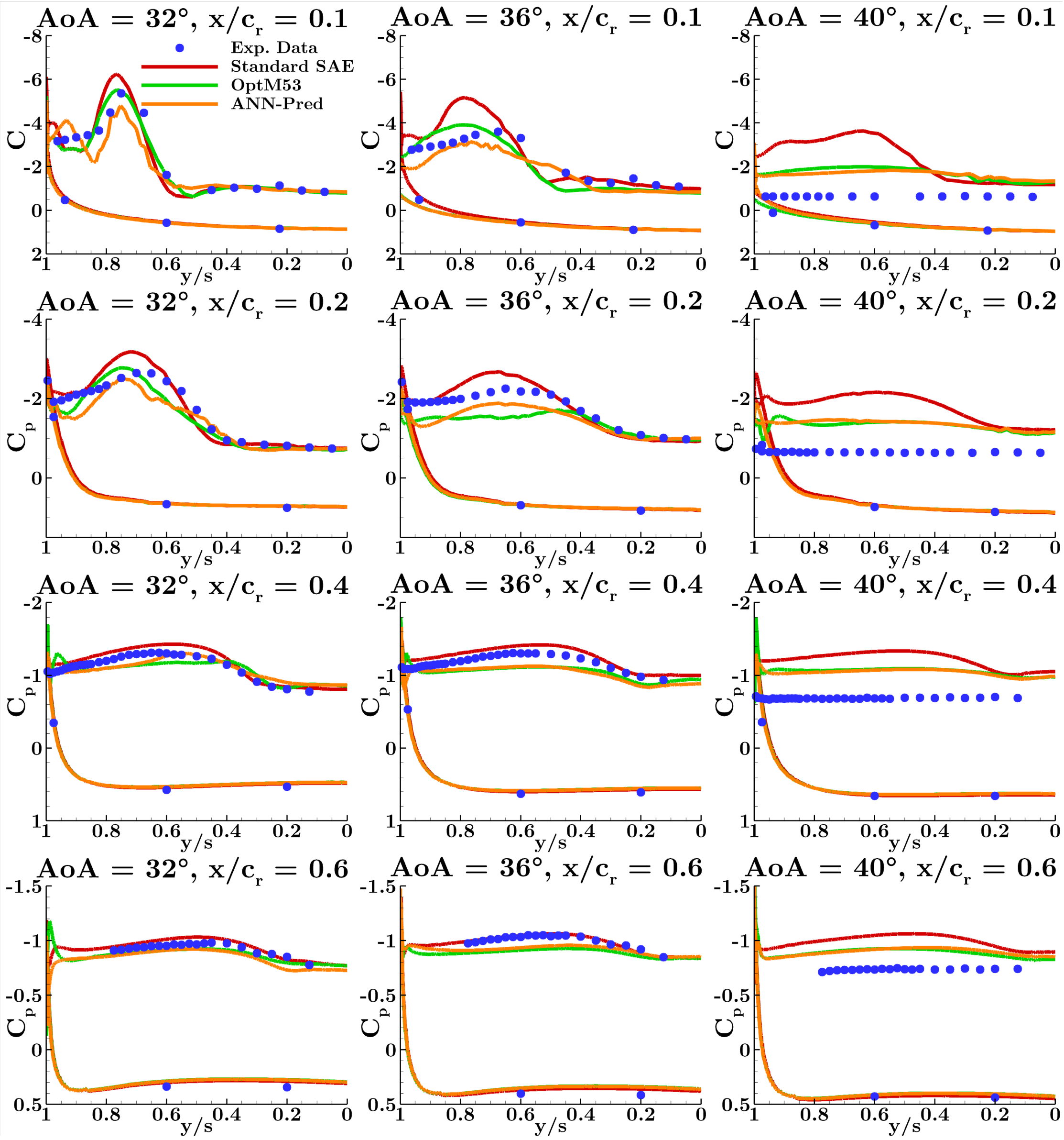

Figure 4.30: The surface C_P distribution along cross-flow sections at $x/c_r = [0.1, 0.2, 0.4, 0.6]$ for the SAGITTA blended wing body is shown at $M = 0.1$, $Re = 1.77 \cdot 10^6$ and the angles of attack of 32°, 36° and 40°. The data of the baseline SAE model, the optimized turbulence model for the Model53 calibration case (Table 4.6) and the model predicted by the ANN-predicter (Table 4.10) are compared with the steady pressure surface measurements.

plausible direction, which is similar to the optimum derived for the Model53 calibration. However, some details of the prediction are interesting. The value of c_{bvh1} is practically 0 whereas the other terms are near the half of the values for the Model53 optimum.

The predicter indicates no relevant sensitivity captured by the structured part of the vortex, identified by c_{bvh1}. The application of the predicted set of coefficients introduces a substantial variation of the vortices development (Fig. 4.30). Starting from the angle of attack of 32°, the direction of variation is in general comparable to the one provided by the Model53 optimum. At the cross-flow section at $x/c_r = 0.1$, the main suction peak is reduced compared to the baseline model but the reduction is too large. The suction peak is lower compared to the experimental data and a substantial difference is visible with respect to the region between the C_P peak and the leading edge, here the physical representation of a secondary separation appears to be wrong and the accuracy is reduced. The attached flow inboard is not affected also by this turbulence model variation. At $x/c_r = 0.2$, the C_P distribution is similar to the Model53 optimum except for a mild offset in the C_P positive direction. The inner side of the vortex suction curve is slightly improved, this is valid also downstream at $x/c_r = 0.4$. At $x/c_r = 0.4$ and $x/c_r = 0.6$, no variation from the baseline model is introduced in proximity of the leading edge which is instead visible for the Model53 optimum. It may be significant that in that region the c_{bvh1} has the largest sensitivity. With respect to the C_P distribution at $x/c_r = 0.6$, it is really close to the results obtained with the Model53 optimal model. Moving to 36°, the difference between the two versions of the enhanced models is similar. Hence, at the near-apex region the suction distribution is slightly lower for the ANN-prediction and, in this case, the distribution is close to the wind tunnel data. The distribution shape also changes and the inboard region manifests a different distribution. However, the peak span-wise position is different compared to the experimental data. At $x/c_r = 0.2$, the numerical results have the largest difference between the two model variations. The C_P distribution is significantly improved by the ANN-predicted model whereas the suction levels remain lower than the experimental data. From $x/c_r = 0.4$ and downstream, no appreciable variation is visible. With regard to the highest angle of attack at 40°, the results between the Model53 optimum and the ANN-prediction are really close except for a slight difference at the region near the wing apex. This is an indication that a much stronger eddy viscosity destruction is necessary for this stalled flow stage but this would provoke a drop in accuracy in the previously analyzed angles of attack. However, this is a good indication that both an optimum of a different test case and the ANN-predicter are able to find a good compromise for the considered angles of attack.

Table 4.10: Turbulence model coefficients predicted by the ANN model for the SAGITTA blended wing body.

Coefficient	c_{bv1}	c_{bvh1}	c_{bvh2}
Value	0.23378	-0.001	-0.040

The results have shown again that an optimum derived for a certain class of vortex flow like the Model53 at high angles of attack may be applied, based on previous experience, to a cluster around the calibration case in the parametric space of vortex flow stages. The potential of extending further the predictive capability based on previously optimization procedure is also shown by the application of a model which is predicted by the ANN-predicter fed with geometrical and flow condition parameters of the target flow. To confirm these promising results, another similar validation is performed on the AVT-183 diamond wing.

AVT-183 53° Diamond Wing. The geometry has been described in Section 4.1.1 and, except for the leading-edge sweep angle which is equal, the planform geometry differs from the Model53 with respect to the geometrical parameters (Table 4.1). A significant difference is present with respect to the leading-edge curvature because its value is smaller for the AVT-183 wing with consequent diversity in the vortex structure and development over the angle-of-attack polar. For example, in the range of lower angles of attack, the vortex develops in a partially separated stage. Hence, the separation onset of the vortex is not fixed along the leading-edge extension but it starts at a certain distance from the wing's apex and moves upstream progressively as the angle of attack is increased. This range of angles of attack has been the target of a parallel optimization procedure and it is reported in Section 4.4.3. With respect to the validation of the Model53 optimum, the relative set of coefficients is designated for the application to low-swept delta wings employing fully separated vortices and manifesting a breakdown and/or a stall condition. Therefore, its target of predictive capability consists of the range of higher angles of attack of similar planform shapes. In the case of the AVT-183 diamond wing the application target [130, 108] is the range between $AoA = 28°$ and $AoA = 32°$.

The wind tunnel model (Fig. 4.1) consists also of a half model like the Model53 and it has been measured in the same wind tunnel facility (W/T-A) at TUM-AER. The peniche is composed of a 90-mm perpendicular extrusion of the root wing profile which is substantially different from the solution adopted on the calibration case. It is expected that an extruded peniche has a significant influence on the regions at high angles of attack where the flow separates around it and it inevitably interacts with the vortex structure. Whereas on the Model53, the fuselage and peniche module have been constructed to guarantee a more realistic behavior at high angles of attack. Moreover, the presence of a swept trailing edge, which encloses the diamond planform shape, alters the adverse pressure gradient direction and magnitude. This correlates with a different breakdown evolution at the higher angles of attack. Additionally, the calibration case comprehends a leading-edge slat deflection of -20° whereas here no slat is available. The AVT-183 diamond wing always manifests a single vortex and it does not include the complex phenomenologies present on the Model53, i.e. multiple vortices and interactions. As a consequence of the mentioned differences, the validation of the optimum is challenging but it provides relevant information about the range of applicability of such a methodology. It permits to evaluate how detrimental it is to the modeling accuracy improvement when significant variations from the calibration case are present. The diamond wing case remains at a reasonable variation level with respect to the geometrical and flow parameter variations.

First of all, the numerical solutions provided by the baseline SAE model are analyzed. Hence, the main source of error is correlated to particular regions or conditions of the vortex flow. This permits to gather further experience about the modeling correlations

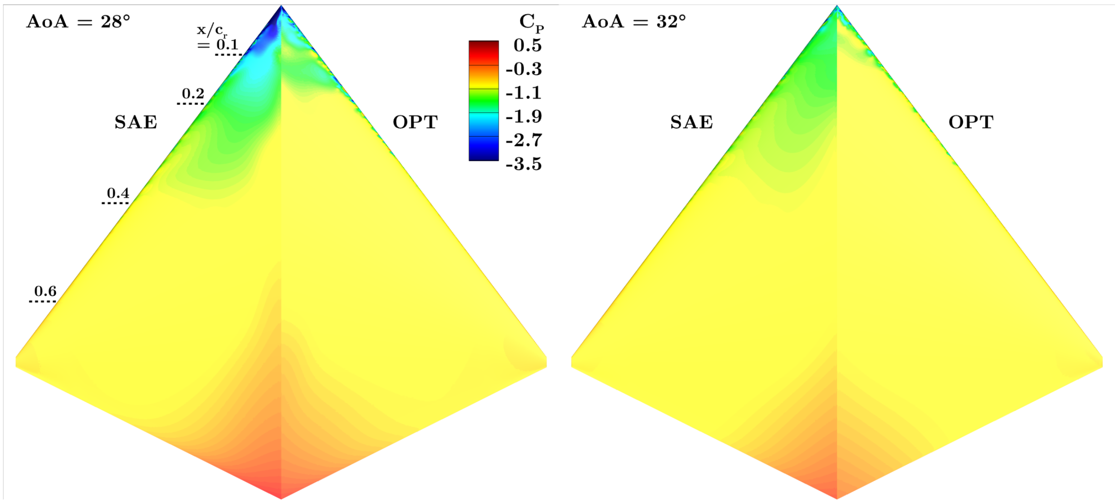

Figure 4.31: The surface C_P distribution for the AVT-183 53° swept diamond wing is shown at $M = 0.15$, $Re = 2.7 \cdot 10^6$ and the angles of attack of 28° and 32°. The data of the baseline SAE model and the optimized turbulence model for the Model53 calibration case (Table 4.6) are compared.

between the main sources of error and the improvement potential with the methodology application. By applying the baseline SAE model, the numerical solution manifests a developed vortical structure without full stall up to $AoA = 32°$. The differences between AoA = 28° and 32° shows that the stall condition is getting closer to appear as the angle of attack increases. In fact, the suction distribution reduces its peak values between the two angles of attack and its distribution manifests a progressively flatter shape along the wing's span (Fig. 4.31). The separation onset is clearly fixed at the wing apex at this range of angles of attack. However, the presence of the peniche does play an important role for the vortex separation type and stall condition. This increases, certainly, the differences of the flow with respect to the Model53. This is visible mostly for the AoA = 32° where (Fig. 4.31) the suction footprint at the apex nearby illustrates how the vortex structure is generated by a separation taking place further inboard compared to the wing's root. The flow would therefore be of different nature if the wing is isolated from the peniche. With respect to the vortex development, it is possible to visualize how the vortex suction levels drop between 10% and 20% of c_r for the angle of attack of 28° as consequence of the breakdown instability. This characteristic is comparable with the Model53 pressure distribution at the same angle of attack. Moreover, suction levels of $C_P = -1$ are reached downstream to $x/c_r = 0.3$ for AoA = 28° of the AVT-183 diamong wing. This is also valid for the Model53. Downstream, the suction level drop is more marked for the Model53 whereas the drop is mild on the diamond wing. In fact, zones of C_P lower than -0.5 are only visible in the inner-rear region where the influence of the vortex wake is negligible. It appears as the breakdown instability on the Model53 takes place where the main and slat vortex trigger each other. It takes place further downstream and it is more abrupt if compared to the AVT-183 wing. The drop of suction covers a shorter distance in the x-direction. The surface pressure distribution at AoA = 30° shows how the main differences to the lower angle of attack of 28° are present in the near-apex region because of the vortex higher instability level and incipient stall condition.

The cross-flow sections (Fig. 4.32) show how a significant suction peak for the baseline SAE model is only present at the apex-region of the lower angle of attack. The suction distribution is then flat downstream of breakdown. The spanwise C_P distribution acquires more curvature moving downstream where the increased wing span permits the vortex wake flow not to cover the whole surface. Moreover, the suction level of the "flat" pressure distribution region decreases moving downstream. Between the angles of attack of 30° and 32° there are not many differences with regard to the suction distribution provided by the baseline SAE model. The suction distribution is flat already at the first cross-flow cut and it exhibits how the vortex has reached a stall condition. With respect to the experimental data, they manifest the presence of a stall condition already at $AoA = 28°$. The suction at the near-apex region indicated by the numerical results with the baseline SAE is, in fact, not present in the experiments whereas a flat distribution is shown. Moreover, while the correct vortex stall condition is predicted by SAE for the larger angles of attack, the suction level illustrated by the experimental data is significantly lower. This indicates how the chaotic stalled flow around the diamond wing maintains a certain content of tangential velocities which interact with the surface. The discrepancies with the experimental data of the baseline SAE model reduce moving downstream for AoA = 28°, where the accuracy acquires appropriate levels, and for $AoA = 30°$ as well where the accuracy is significantly better. Such behaviors show already some similarities which have been seen on the Model53. The first step of applying the SAE baseline model has highlighted important information about the sources of discrepancy and the similarities with the calibration case. The successive step is to apply the optimal set of coefficients.

The application of the model optimized on the Model53 calibration case (Table 4.6) results in a significant variation of the vortex flow prediction as well as an improvement of the accuracy level of the numerical simulations (Table 4.11). With the optimized model, a fully stall condition is predicted already at $AoA = 28°$ and the pressure distribution correlates accordingly with the experimental data at the cross-flow sections of $x/c_r = [0.1, 0.2]$. The suction distribution is flatter and at a lower C_P value. Moving downstream, the optimized model is mildly detrimental to the numerical results accuracy in a surprisingly similar way to the Model53 accuracy on the second half of the wing surface. This indicates more global characteristics of the turbulence model limitation to properly predict both the vortex stall condition upstream and the development of the chaotic wake flow which may necessitate of further complexity in the modeling formulation or to reduce the scale resolving limit and removing the Boussinesq assumption. However, the accuracy obtained is appropriate (Table 4.11) and it reaches a similar average value to the one reached by the calibration case (Table 4.7). The accuracy improvement is also very important at larger angles of attack where the optimized model moves in the direction of the experimental data along all sectional chordwise stations. At $AoA = 32°$, the suction distribution is improved by narrowing down the offset to the experimental data whereas it maintains a proper qualitative distribution. However, it lacks effectivity to completely match the experimental data. It is also important to notice that the pressure distribution on the lower wing surface is not altered by the application of the optimized model as already seen for all the other test cases. This behavior is favourable because it indicates that the model's variation has effectivity exclusively inside vortex/highly separated regions.

In conclusion, the application of the optimized model for low-medium swept delta wings is able to significantly improve the computational results for the range of angles of attack dominated by the same vortex flow stages as the calibration case. The accuracy improvement rate is comparable to the one of the calibration case. Moreover, similarities to the calibration case are shown with regard to the correlation of the vortex flow stage and type and the effect of the variation of turbulence modeling. Hence, the results illustrate how the optimization performed on the Model53 has targeted the mathematical error coming from the experimental data and it has responded by increasing the physical content which is modeled by the additional terms. This modeling enhancement is confirmed by this validation case. These results form an important confirmation of the possibility to apply the methodology for a series of low to mild geometrical and flow field modifications from the original calibration case thanks to the experience from past test cases and the physical understanding of the vortex flow type, characteristics and sensitivity to the turbulence model variation.

Table 4.11: $\mathcal{E}_{C_P}$ between numerical and experimental data for the AVT-183 diamond wing.

AoA °	SAE baseline	Optimized	Difference
28	0.163	0.1388	-14.85%
30	0.278	0.1283	-53.85%
32	0.411	0.2721	-33.8%
Average	0.284	0.1797	-36.72%

With respect to the application of the ANN-predicter (Sec. 3.5.2.2), the flow and geometrical conditions are given as input features to the ANN with a target angle of attack equal to 32°. Here, the decision to use the maximum angle of attack is based on the experience of the user and the analysis of the flow predicted by the SAE model. In fact, it is evident that the target range of AoAs share a similar vortex flow stage misprediction to the Model53 calibration case, i.e. correlated with the breakdown and stall region. Therefore, in order to furnish more emphasis to the ANN-predicter with respect to this region of the vortex development stage, the highest angle of attack is given as prediction target [116]. The resulting coefficients are reported in Table 4.12. Possible improvement of the ANN extension of the methodology is evident from this application. The direction and the obtained set of coefficients is similar to the Model53 optimum which is a sign that the ANN-weights correlate the high angles of attack region and the low sweep angle to the Model53 results. By extending the availability of the data for the learning process in the future, it is expected to further improve the capability of the

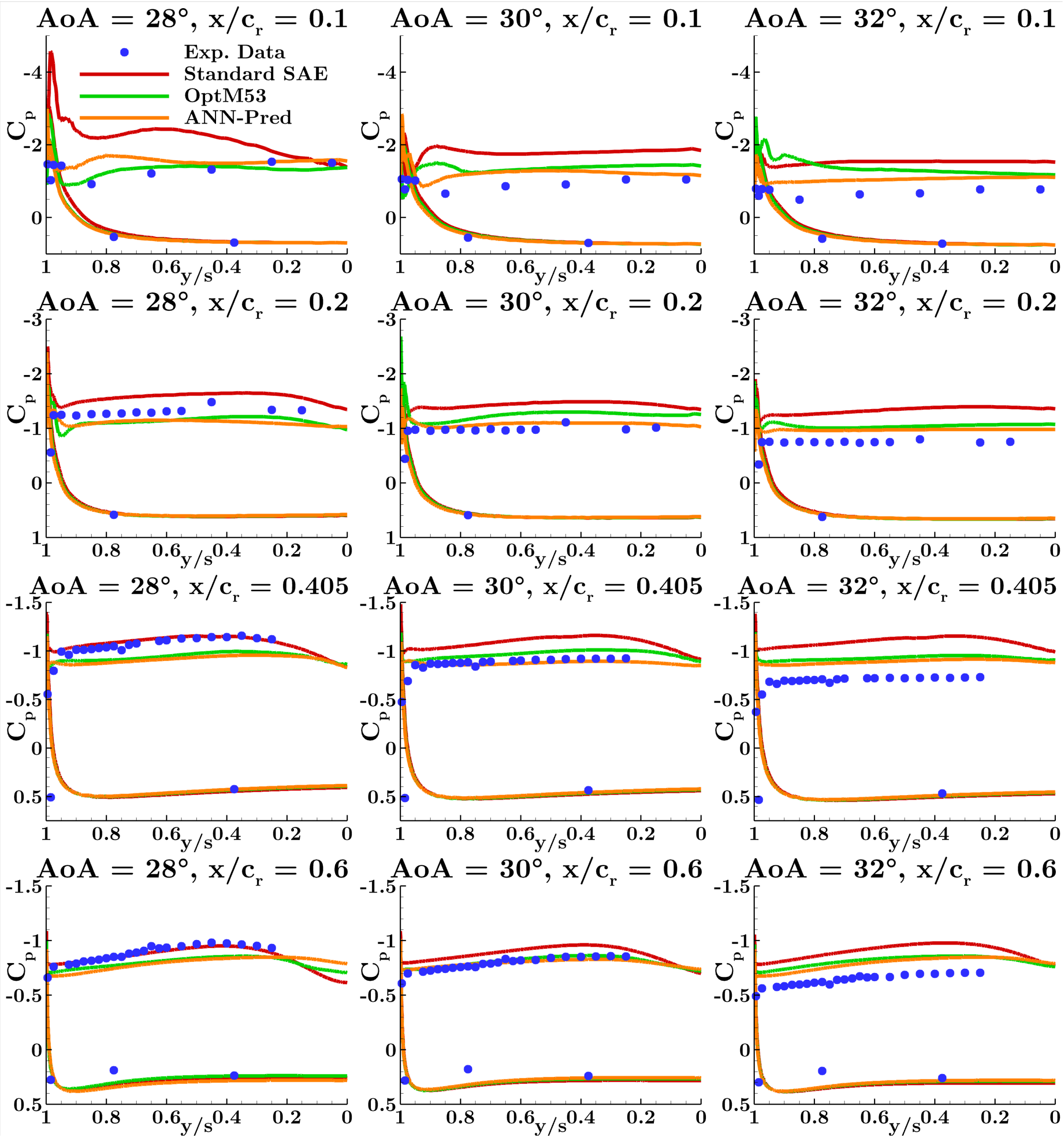

Figure 4.32: Surface C_P distribution along cross-flow sections at $x/c_r = [0.1, 0.2, 0.4, 0.6]$ for the AVT-183 53° swept diamond wing is shown at $M = 0.15$, $Re = 2.7 \cdot 10^6$ and the angles of attack of 28°, 30° and 32°. The data of the baseline SAE model, the optimized turbulence model for the Model53 calibration case (Table 4.6) and the model predicted by the ANN-predicter (Table 4.12) are compared with the steady pressure surface measurements.

predicter to find new solutions. With this application, it shows that the main direction of the prediction is similar to what a human would suggest, however the exact values appear to come from a “deeper understanding” of the features correlations. Hence, the result is a first confirmation of the potential of the methodology extension.

In particular, the coefficients highlight how the main contribution to the eddy viscosity destruction is given by the c_{bv1} term whereas the other two terms have smaller values but of different signs. This suggests that the predicted model employs a different distribution of destruction between the structured region of the vortex where some eddy viscosity production is necessary — effectively the c_{bvh1} term contributes only in part to reduce the dominant c_{bv1} destruction — and the wake flow where additional destruction is provided by the c_{bvh2} coefficient.

Table 4.12: Turbulence model coefficients predicted by the ANN model for the AVT-183 diamond wing.

Coefficient	c_{bv1}	c_{bvh1}	c_{bvh2}
Value	0.2479	-0.02574	0.04235

The detailed results are interesting and significant (Fig. 4.32). The accuracy enhancement is comparable to the Model53 optimum application. This means that if this test case would lack of experimental data, the methodology extension would have permitted to find a similar level of accuracy improvement without the need of the user experience or the availability of optimal set of coefficients on previous similar test cases. Such an extension of the predictive capability of the methodology was, in fact, the original motivation of the implementation of an ANN-predicter. In detail, at $AoA = 28°$ the ANN-prediction still presents a small suction peak at the first cross-flow section which is in less agreement with the experimental data compared to what achieved with the Model53 optimum. However, the suction distribution further inboard is better predicted. With respect to the sections further downstream, the distribution and accuracy levels are comparable to the Model53 optimal set of coefficients. It is noted that the angle of attack of 28° provides the most different flow condition from the prediction target. Moving to $AoA = 30°$, the accuracy enhancement of the ANN-prediction is significant and the results are better than the ones obtained by the Model53 optimum. This is expected as the target angle injected into the ANN-predicter is the $AoA = 32°$ case where the vortex flow stage is also the closest to the target of the Model53 calibration. At the first section, the C_P distribution is qualitatively better predicted and both the regions inboard and outboard, in proximity to the leading edge, manifest suction levels which are closer to the experimental data. The numerical results are even more accurate moving downstream where the qualitative distribution is similar to the optimal Model53 coefficients but at suction levels which properly match the experimental values. It is interesting to notice that the ANN-predicter has been able to improve the suction levels of the wake region compared to the optimum of the Model53. However, this may be motivated by the fact that the wake region of the Model53 included a higher grade of complexity due to the presence of the second slat vortex and its interaction with the main vortex. The phenomenology of which is of high complexity and it may deteriorate the modeling quality under the Boussinesq assumption constraints. The AVT-183 wing manifests a single vortical structure which is inherently less challenging from a modeling point of view. The prediction target of $AoA = 32°$ manifests a grade of improvement which is similar to the other angles of attack and the optimized model. At the first section at $x/c_r = 0.1$, the qualitative distribution is improved compared to the other models. The suction levels are also closer to the experimental data but a certain difference is maintained. Further downstream, the C_P distribution is similar to what is achieved with the validation of the Model53 coefficients and only a slight improvement of the suction levels is evident. In general, the results are of high significance as they show the potential of the methodology extension and the capability of the combination of the optimization procedure and the ANN-predicter to further extend the application range of such a class of turbulence model corrections.

4.4.3 Separation Onset Improvement of a Diamond Wing

The diamond wing has been employed as validation case for the low-swept delta wings in the previous section 4.4.2. However, the main target of the case (Sec. 4.1.1) is the investigation of the incipient vortex separation at its rounded leading edge for low and moderate angles of attack. This has been also the target for the application of the proposed methodology. Firstly, it is important to point out that the optimum derived for the high range of angles of attack on the Model53 (Table 4.6) is not appropriate for the improvement of this test case at moderate angles of attack. In fact, it would worsen the numerical simulations accuracy. This is a drawback of the regional calibration for configurations which employ rounded leading edges and cover both the angle-of-attack ranges of a partially developed vortex stage and a fully developed stage with breakdown or stall. The physical characteristics are so drastically different that a calibrated model which is able to improve both without worsening the other has not been possible with the available terms. Therefore, a new optimization procedure is performed on the experimental data available for partially developed conditions.

Optimization Procedure. The sensitivity of the numerical solution to the turbulence model extension is tested and it shows its potential for the application. However, the dependency of the position of vortex separation to the model's coefficients is less clear due to the fact that the terms have been formulated with the vortex development above the wing as physical reference. At this point of the research work, the majority of the methodology applications concentrate on vortex breakdown, wake or evolution. Additionally, the separation onset of a vortex is a particularly sensitive feature to turbulence modeling as acknowledged from previous works performed on this configuration along the associated NATO task group [68, 69]. In order to overcome such complexities, as suggested in the procedure description and guidelines (Sec. 3.4.4), a proper sensitivity analysis is performed by testing the different available terms. Then, different starting points and combinations of terms are analyzed. The necessity to include three angles of attack in the optimization toolchain has been proven to be relevant for improving the accuracy consistently along the different angles of attack (Fig. 4.33). The best direction is selected and its optimum is derived after its convergence (Table 4.13). As it can be seen, the values are significantly different from the one derived on the Model53 for large angles of attack (Table 4.6). The optimization procedure is performed initially with

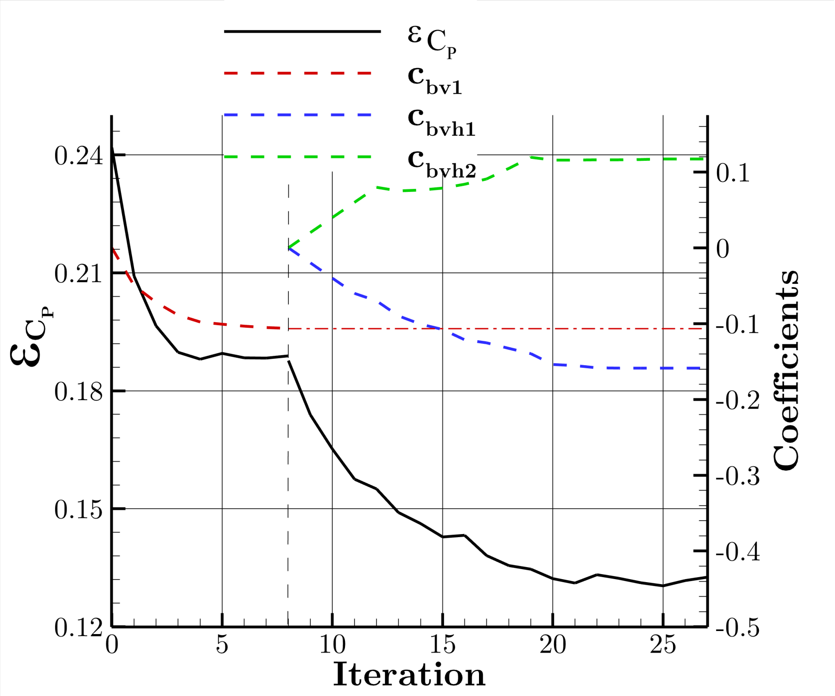

Figure 4.33: Convergence of the $\mathcal{E}_{C_P}$ and the coefficients of the turbulence model modification with sufficient sensitivity along the optimization procedure for the AVT-183 diamond wing, M = 0.15, $Re = 1.7 \cdot 10^6$ and $AoA = [10°, 15°, 20°]$.

the c_{bv1} term. This is the closest term to the source term from the baseline model and previous experience suggests to test it as first one. After reaching a minimum of the $\mathcal{E}_{C_P}$, the optimization procedure is continued by fixing the $c_{bv1} = -0.1125$ value and continuing with the two additional terms c_{bvh1} and c_{bvh2}. The calibration shows that the minimization function converges to a lower level of error. The optimization exhibits no further sensitivities to other terms afterwards. It is interesting to notice that the two additional terms (c_{bvh1} and c_{bvh2}) manifests an opposite sensitivity and they converge to two opposite directions, i.e. positive and negative, but with different absolute values. The non-linearity and complexity underlying this result is not trivial to grasp. The $c_{bv1} = -0.1125$ is converged to a negative direction which already causes the vortex onset to be moved closer to experimental data. Afterwards, the two additional terms further refine the accuracy of the numerical simulations for both the separation onset and the vortex development above the wing surface.

Numerical Results and Comparison with Experimental Data. The surface distribution of C_P in Figure 4.34 illustrates the two consecutive cross-flow sections which enclose the separation onset between them. In general, the SAE baseline model has the tendency

Table 4.13: Optimal set of coefficients for the AVT-183 diamond wing for $AoA = [10°, 15°, 20°]$ for the improvement of the separation onset.

Coefficient	c_{bv1}	c_{bvh1}	c_{bvh2}
Value	-0.1125	-0.158	0.117

to solve the separation onset too far upstream when compared with the wind tunnel measurements. The angle of attack of 12° is not included in the optimization procedure. The improvement is significant and consistent for the considered range of angles of attack. The separation onset is predicted at a correct position, in agreement with the experimental data, for all the angles of attack. As a downstream effect, the development of the vortex above the wing surface is drastically improved with respect to both position in the spanwise direction and levels of suction peaks. The results illustrate the correct prediction of the separation onset is of major importance to achieve a proper grade of accuracy for partially developed vortices. The improvement is consistent along the different angles of attack. Numerical simulations are performed also with the SA-RC model and the corresponding results manifest an inverse effect on the surface pressure characteristics. Hence, the accuracy is much worse than the optimized model but also of the baseline model. The separation onset is moved further upstream by the SA-RC model. This is expected by the results of the optimization procedure. In fact, the outcome of the optimization is that in this flow scenario a higher content of eddy viscosity production is necessary, with the optimum coefficients dominated by negative values. The SA-RC model is notoriously highly destructive and, therefore, it influences the onset prediction in the wrong direction. Consequently, the numerical results manifest a lower grade of agreement with the wind tunnel data. Moreover, high numerical oscillations are introduced in the solver convergence. In the scenario of small angles of attack and, in particular, with rounded leading-edge shapes, the usage of SA-RC is not recommended.

Summary and Outlook. The average $\mathcal{E}_{C_P}$ in the range of angles of attack between 10° and 20° is reduced by 45% from a mean value of 0.242 to 0.1326. Whereas the accuracy improvement is not in question, the problem of having a different optimum between small and high angles of attack remains. As an outlook, the possibility to include new terms which only affect the separation onset could improve both the partially and fully developed stages of the same configuration. Another possibility is to employ the zonal methodology (Sec. 3.5.1) where a global zone acts on the vortex development above the wing whereas a second zone is dedicated to the leading-edge proximity where the separation onset takes place. A new term was also tested which would concentrate its influence on the leading-edge proximity and it was based on the pressure gradient magnitude and direction. However, its development has been abandoned for the moment due to the continous encountering of numerical issues with regard to stability and due to the secondary importance of partially developed vortices for the current research.

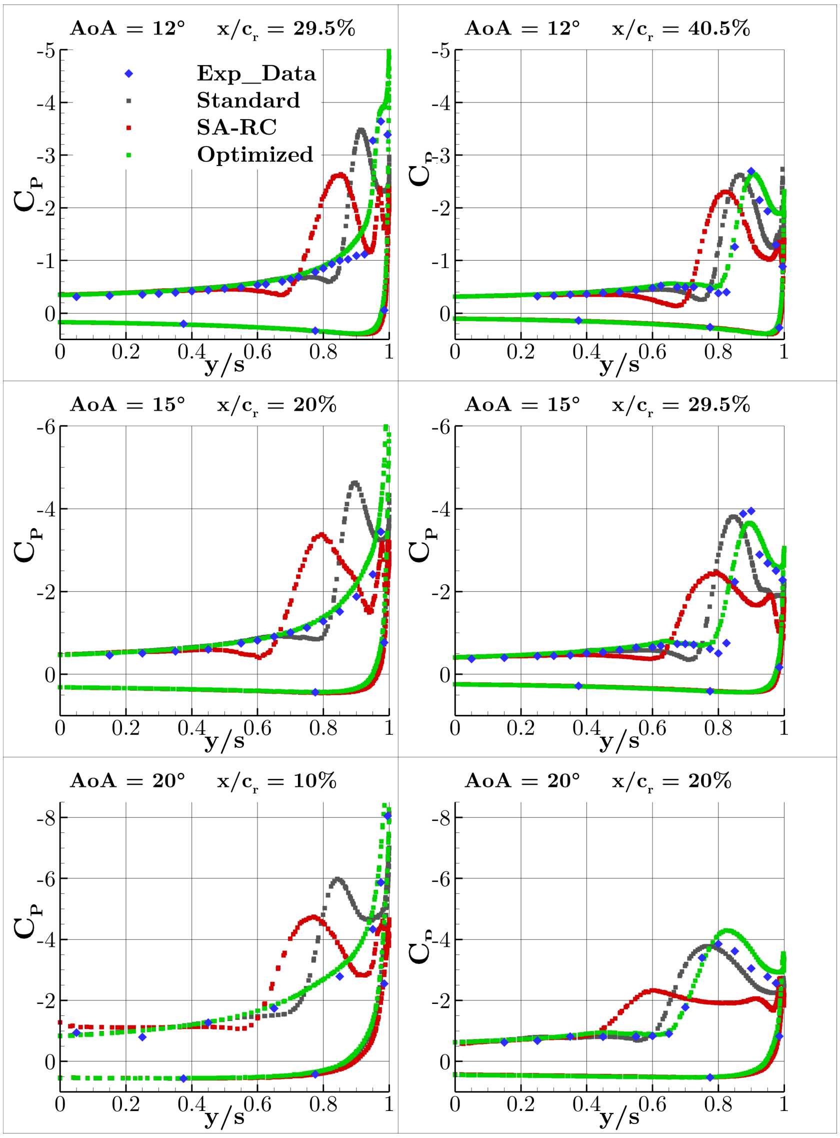

Figure 4.34: Surface C_P distribution along cross-flow sections at up and downstream of the separation onset for the AVT-183 53° swept diamond wing is shown at $M = 0.15$, $Re = 2.7 \cdot 10^6$ and the angles of attack of 12°, 15° and 20°. The data of the baseline SAE model, the SA-RC model and the optimized turbulence model are compared with the steady pressure surface measurements.

In conclusion, the possibility to improve the separation onset and the potential of the methodology is significant.

4.4.4 60° Swept Delta Wing: Analysis of the Predictive Capability Extension

In this section, the predictive capability extension provided by the ANN-predicter is investigated (Sec. 3.5.2.2) on a test case which shares less similarities to the others included in the training dataset. The test case consists of the rapidly manufactured 60° swept delta wing (DW60) which has been described in Section 4.1.4. The sweep angle is, in fact, different from the other test cases. Moreover, the application of the optimum derived on the moderate sweep angle of the Model53 does not improve the accuracy of the DW60 case. Same result is obtained if the optimum for the 65° delta wing case is employed. Additionally, this is an example of a test case where the experience of the user is not enough to find a good optimum that can enhance the accuracy. Without experimental data, however, the information gathered from the other test cases would not be enough for a substantial improvement in the numerical results. For these reasons, the ANN-predicter model is applied to this test case in order to analyze if an improvement is achievable for a different geometry. The ANN-predicter returns a

Table 4.14: Set of coefficients predicted by the ANN model for the DW60.

Coefficient	c_{bv1}	c_{bvh1}	c_{bvh2}
Value	0.2757	0.0345	-0.027

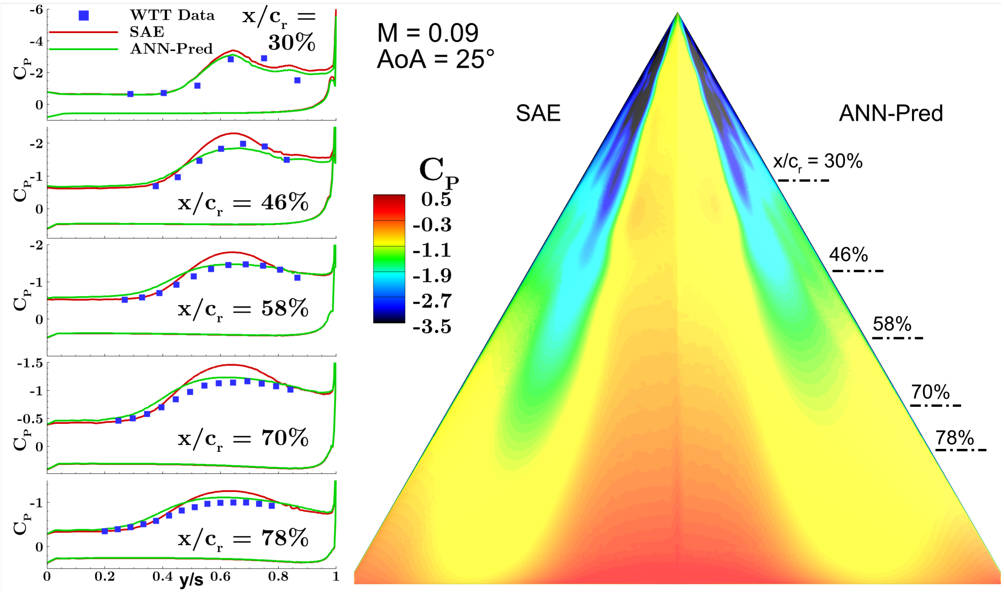

Figure 4.35: An upper surface contour plot and 5 cross-flow sections of the surface C_P at M = 0.09, Re = $0.7 \cdot 10^6$ and AoA = 25° are reported. The original SAE model and and the model predicted by the ANN-predicter (Table 4.14) are compared to the experimental data.

set of coefficients (Table 4.14) which is closer to the Model53 optimum than the VFE-2 one. Therefore, the Model53 optimum would have been a good starting point for further refining the optimization of this geometry by using experimental data. The major contribution to the predicted calibration is given by the $c_{bv1} = 0.2757$ term which introduces additional eddy viscosity destruction in the vortex flow. The other terms $c_{bvh1} = 0.0345$ and $c_{bvh2} = -0.027$ indicate that an additional content of destruction is injected in the structured part of the vortex whereas additional production is provided to the wake flow. It is interesting to notice that the absolute values of the last two coefficients are comparable but contribute to the eddy viscosity production in opposite directions.

The C_P contour of the wing upper surface at $AoA = 25°$ (Fig. 4.35), provided by the SAE baseline model, exhibits the presence of a vortex structure separating along the whole leading-edge extension. A relatively strong secondary vortex is also clearly visible and it generates a C_P peak which is comparable to the primary one whereas its cross-flow size is significantly smaller. The secondary suction footprint is evident until around 50% of c_r. The primary vortex changes its structure around that position. Its C_P footprint suddenly expands as the vortex cross-section enlargement takes place and its suction peak drops at 20% of c_r downstream until it reaches a wider cross-flow section with lower values around $C_P = -1.2$ at $x/c_r = 0.75$. The application of the ANN-predicted calibration of the model exhibits some differences compared to the baseline model (Fig. 4.35). Upstream of $x/c_r = 0.2$ the vortex footprint is comparable to the SAE. This confirms once again that the structured region of the vortex employs a low sensitivity to turbulence model variations. Both the primary and secondary footprints manifest lower suction levels compared to the SAE model. The model variation moves the breakdown instability upstream, similarly to the effect for other test cases, e.g. the Model53 and Model56 results at $AoA = 25°$ (Fig. 4.22). The vortex is less stable and the widening of the suction cross-section is now located further upstream, at around $x/c_r = 0.35$. Qualitatively the pressure contours for the two turbulence models are not very different, they exhibit the same development stage of the vortex flow. However, the variations of the suction distributions are significant for the proper prediction of the aerodynamic characteristics of this kind of delta wings. The variations are better appreciable by comparing the C_P distribution along surface cross-sections (Fig. 4.35). The cross-section at $c_r = 30\%$ exhibits the reduction of the suction levels with the ANN-predicted model but the C_P distribution retains the same qualitative shape. The experimental data show a good grade of agreement in the inboard region whereas the solution of the vortex footprint is improved by the ANN model with respect to the level of suction of the secondary and primary peaks. However, the wind tunnel data show that a larger vortex should be present at this location of the wing. With respect to the other cross-sections downstream, the SAE model indicates a higher suction peak compared to the experimental data. However, the inboard region matches properly with the wind tunnel data. The application of the ANN predicted model significantly improves the accuracy in capturing the correct distribution and values of the vortex suction. The only region which is slightly not captured in full detail is the inboard region. In general, the improvement of the vortex development and the associated suction distribution with the ANN model is significant and it exhibits the potential of the application of this additional methodology for extending the predictive capability based on the acquired data set on previous test cases.

4.4.5 Multiple Swept Delta Wings: Multiples Vortices and Interaction

The following test cases are representative for the class of vortical flows which are generated from a multiple swept delta wing configurations. Hence, a wing planform which employs different sectors of different leading-edge sweep angles. The presence of different sweep angles cause the evolution of distinct vortices, if the related wing segments in relation to other sections and if the junction angles, i.e. the difference of the sweep angles of two consecutive wing sections, are large enough. Multiple vortices may interact (Section 1.2.2.2) and the type of interaction and strength changes with the sweep angle difference as well as the angle of attack. Therefore, the complexity of the flow increases and additional sources of turbulence modeling sensitivities and possible lack of accuracy are present. Multiple swept delta wings have gathered progressively more interest due to the additional potential for the achievement of higher aerodynamic performance with regard to the requirements associated with new-generation of highly agile aircraft. For these reasons, this class of flows is relevant for the application of the methodology because of the state-of-the-art importance of such configurations. It permits to investigate the capability to improve a high-level complexity flow. In particular, it is important to further test the turbulence model flexiblity and accuracy improvement when different vortices of different evolution stages are present and their interaction changes along the target angle-of-attack polar. The predictive capability is a quality which needs to be maintained along a certain range of cases and needs to be evaluated.

In this section, two configurations are reported which are the Erickson's double delta wing and the generic triple delta wing from the AVT-316 task group. Their descriptions are reported respectively in Section 4.1.6 and Section 1.2.2.2.

4.4.5.1 Erickson's Double Delta Wing

A double delta wing configuration is composed of two distinct sections and, in most cases, consists of a strake and a main wing section. A strake is characterized by a larger sweep angle which contributes to the generation of a stable vortex. The objective is to combine the characteristics of such a vortex with a less stable vortex generated by the lower sweep angle of the main wing section. Compared to a configuration without the strake portion, it is possible to delay the occurrence of breakdown and, hence, the stall condition. The structured stable vortex is able to stabilize also the second vortical structure and extend the angle-of-attack range. Therefore, such configurations are of high interest for the development of high maneuverability aircraft.

In this section, a double delta wing configuration is investigated and the turbulence model optimization methodology is applied [107]. The wing is composed of a 76° swept strake section and a 40° swept main wing section. The NASA report by Erickson [127] provide experimental data for different Mach numbers and junction geometries. Here, the case with a Mach number of 0.5 and the baseline fillet is reported which consists of the geometrical intersection of the two leading edges in a common junction point. The experimental data are available as Pressure Sensitive Paint (PSP) images which are employed to compare the surface pressure distribution of the numerical results. A limited number of surface pressure stationary measurements are also available. The optimization procedure is applied with the integral forces as target due to the small number of pressure points available. Moreover, this is also performed to verify the application of the methodology by targeting exclusively integral force data because, in the context of the development of an aircraft, the availability of data may be restricted to this topology of data. Therefore, for this test case the results obtained with the application of the methodology towards the integral forces are compared to the pressure data for confirmation.

Table 4.15: Optimal set of coefficients for the Erickson's double delta wing.

Coefficient	c_{bv1}	c_{bv2}	c_{bvh1}	c_{bvb}
Value	0.059	0.061	0.062	0.16

The Mach number is 0.5 featuring of a compressible subsonic case and the angles of attack investigated cover the range between 10° and 20°. Such values are too low for reaching the breakdown condition of the vortex separating at the strake. With respect to the wing vortex, such values are large enough to encounter a fully developed vortex with breakdown instability. The junction fillet is relatively highly swept, e.g. 36°. The interaction between the vortices is of strong magnitude and it increases by moving to higher angles of attack (Sec. 1.2.2.2). Moreover, with the leading edges characterized by a sharp contour shape, the occurrence of a partially developed vortex is not observed on any of the two wing sections, i.e. the separation onsets are fixed at the apex and at the junction.

Optimization Procedure Results. The optimization procedure is performed by including two different points of the angle-of-attack polar, i.e. $AoA = 18°$ and $AoA = 20°$ [107]. The included turbulence model terms provide the best sensitivities to the numerical solution and the lowest superposition of effects. Different optimization procedures are tested to analyze the presence of local optima and they have provided a similar accuracy improvement by employing different combinations of the coefficient values. However, there are no indications that drastic additional improvements may be achieved with further locality investigations. Hence, the simplest optimization with the best general result [107] is chosen to define the optimal set of coefficients (Table 4.15). This means, in this context, the optimum derived from the procedure which includes the more utilized terms and the less "exotic" starting values, i.e. closest to zero.

Numerical results. The optimal set of turbulence model coefficients provides a significant reduction of the average error of the considered aerodynamic data. By considering

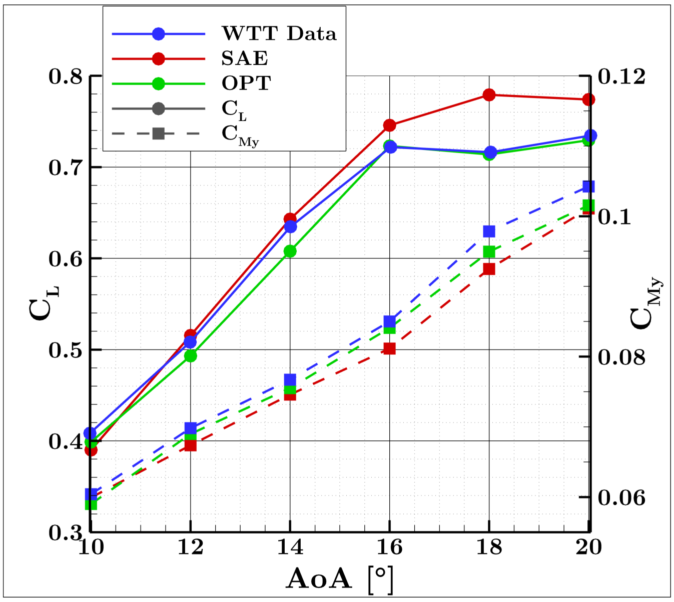

Figure 4.36: C_L and C_{My} versus AoA for the experimental data [127], the baseline SAE model and the optimized model (Table 4.15).

the whole angle-of-attack polar (Fig. 4.36), the average C_L error is reduced from 0.0267 to 0.0073 whereas the average error for C_{My} from 0.0029 to 0.00153, i.e. respectively by factors of 3.65 and 1.9. The aerodynamic coefficient plots versus the angle of attack (Fig. 4.36) show how the improvement is significant for angles higher than $AoA = 14°$, where the lift coefficients lie basically on top of the experimental data whereas for the pitching moment the deviation is improved but it maintains a certain error. In particular, at $AoA = 20°$, the C_{My} value shows almost no variation to the baseline model. The variation of the aerodynamic coefficients indicate that the optimized model is adding up destruction of eddy viscosity in the vortex structures which results in higher sensitivity to instabilities and it moves the breakdown phenomenon further upstream.

The surface pressure contour plot obtained by the baseline SAE model at $AoA = 20°$ (Fig. 4.37) illustrates how the flow topology is similar to the distribution of the PSP results. The strake vortex impresses a stronger suction which is also evident from the cross-flow section at $x/c_r = 0.25$ (Fig. 4.37) in comparison to the surface pressure measurements. The qualitative distribution of the vortex footprint is comparable but at a higher level of suction. The well structured strake vortex is less sensitive to the turbulence model modification and the suction footprint matches the baseline SAE model. This is consistent with previous test cases (Sec. 4.4.1). Moving in proximity of the fillet junction, it is evident that a strong vortex-vortex interaction takes place. The high junction angle and the small strake span causes the vicinity of the vortical structures, thus a strong interaction is observed. The suction footprint of the aft wing is much stronger than the strake one. It is more unstable nature causes its breakdown to happen before the strake one. From the PSP visualization, this is evident as an abrupt suction

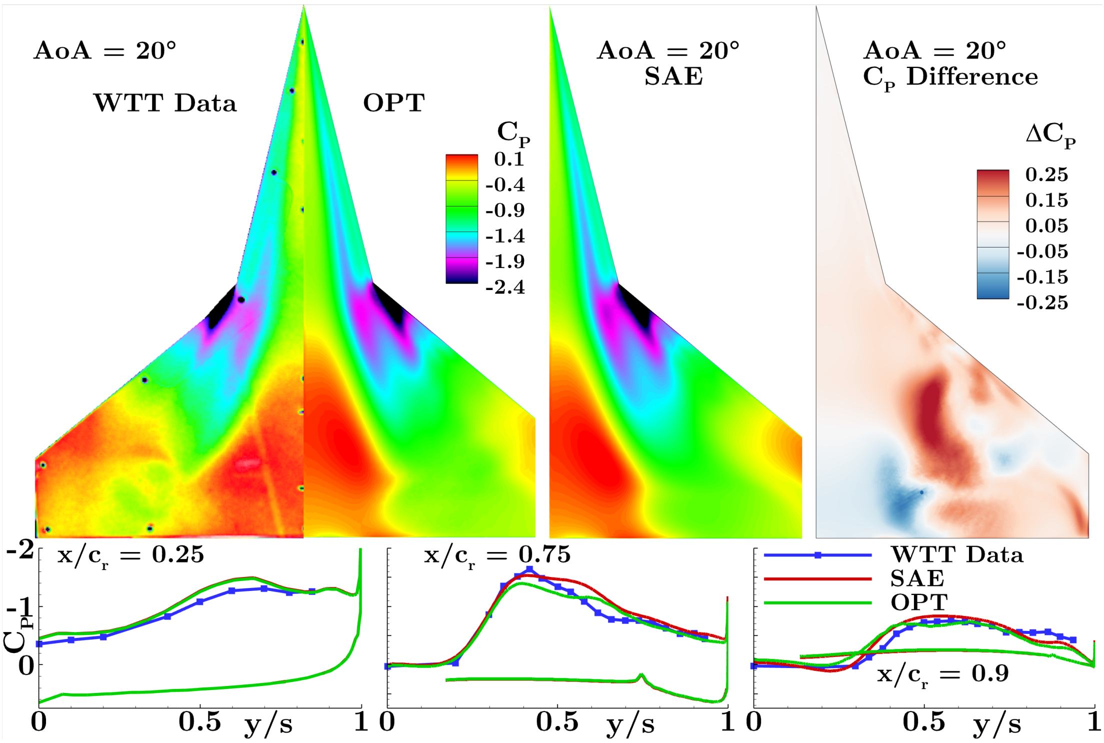

Figure 4.37: The surface C_P distribution at 20° angle of attack is show as a top view of the wing planform and along cross-flow sections at $x/c_r = [0.25, 0.75, 0.9]$ for the Erickson's double delta wing [127]. The data of the baseline SAE model and the optimized turbulence model (Table 4.15) are compared with the PSP and steady surface pressure experimental data. A difference plot between the optimized and baseline SAE model is also shown.

reduction of the outboard vortex and takes place upstream of a similar behavior for the inboard vortex. As known from the literature (Sec. 1.2.2.2), the breakdown of one structure may induce the instability of an interacting vortex. This happens to be one of these cases. This complex interaction is less evident with the SAE results. The SAE baseline model provides a stronger suction for both vortices and their development downstream is different. In fact, their breakdowns appear to take place simultaneously at the same position. Moreover, this position is locateddownstream of the one highlighted by the experimental data. This is also evident by the discrepant spanwise distribution of C_P at the $x/c_r = 0.75$ section. The numerical results show a double peak distribution whereas the experimental data suggest that the suction distribution is dominated by the strake vortex whereas the wing vortex has already undergone a breakdown phenomenon and it has been dissipated into the inboard vortex. The qualitative distribution is not improved by the optimized model whereas it improves the suction level by displacing the breakdown upstream. This indicates how the optimization is able, on the one hand, to target the need of additional eddy viscosity destruction to improve the mean breakdown position. On the other hand, it has not been able to address the lack of modeling complexity required to adjust the vortex-vortex interaction and merging features. This has also been the case for the Model53 and Model56 results (Sec. 4.4.2) where the complexity is even higher. The mean absolute error has been significantly improved. Downstream of the breakdown location, the PSP measurements exhibit a highly chaotic wake flow where an oscillating surface suction distribution appears. Due to the breakdown displacement with the optimized model, a more accurate level of suction is predicted compared to the baseline SAE model. However, discrepancies to the experimental data are evident as consequence of the misprediction of the vortex interactions strength and type. The difference in C_P between the optimized and the baseline model is plotted (Fig. 4.37). The major difference corresponds to the breakdown proximity and the wake downstream. The offset of the breakdown position causes an increase of C_P in the region.

The surface C_P distribution of the optimized model compared to the PSP data is plotted for the angles of attack of 14° and 18° (Fig. 4.38). The vortex flow stage is also properly predicted by the numerical results. At lower angles of attack, as visible for $AoA = 14°$, the interaction of the vortices is much less intense as they do not merge. They maintain two separate structures and, consecutively, two distinct suction footprints. However, the optimized model predicts a more stable outboard vortex for which the high suction region is maintained for a longer distance. With respect to $AoA = 18°$, the flow type and numerical discrepancies appear to be really similar to thoe experienced at the angle of attack of $AoA = 20°$.

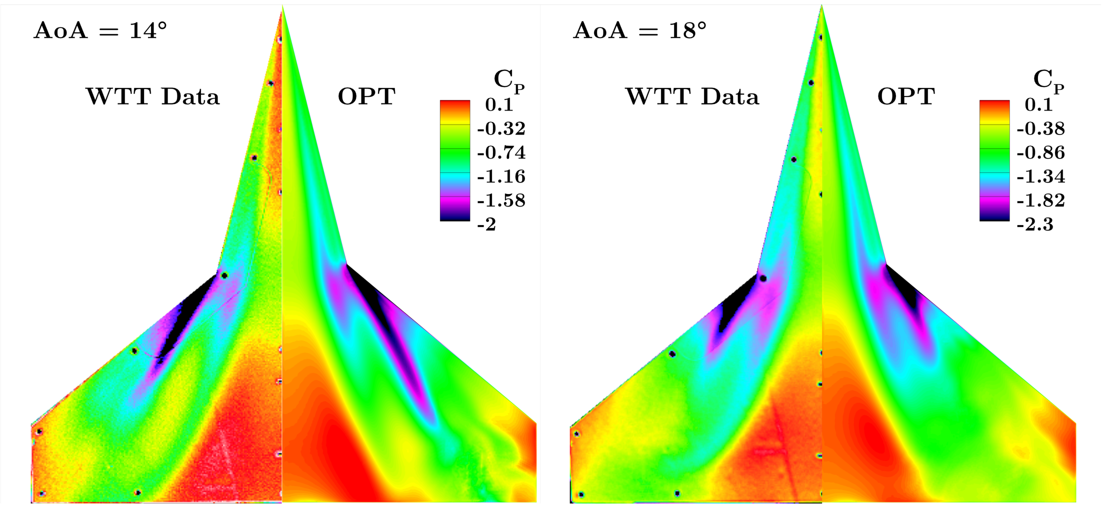

Figure 4.38: The surface C_P distribution at 14° and 18° angle of attack is show as a top view of the wing planform for the Erickson's double delta wing [127]. The data of the optimized turbulence model (Table 4.15) are compared with the PSP experimental data.

In conclusion, the optimization procedure has been able of improving the numerical results of a test case which disposes of multiple and interacting vortical structures by means of integral aerodynamic forces as calibration data. Whereas a modeling limitation is encountered with respect to the proximity of the vortex interaction and breakdown displacement region, the mean absolute error is significantly improved. The optimal set of coefficients is chosen as possible candidate for similar flow cases where interacting vortices at similar sweep and junction angles dominate the target flow.

4.4.5.2 Triple Delta Wing Configuration

In this section, the numerical results for the AVT-316 triple delta wing configuration (Sec. 4.1.7) are reported. Experimental data are available for a large spectrum of geometrical and flow condition variations. Here, results are reported for the most interesting angles of attack at two different compressibility regimes: a compressible subsonic case at Mach 0.5 and a transonic case at Mach 0.85. For the transonic cases, additional complexity is introduced by the presence of the vortex-shock interactions. Moreover, the planform itself employs already a significant level of vortex flow complexity and a high grade of challenge for the methodology application. The first sweep angle which covers the front of the strake portion is in fact an additional geometrical feature which significantly influence the strake vortex generation and separation [74]. In order to evaluate the flexibility of previously optimized models to improve new test cases, the optimal set of coefficients derived from the Erickson's double delta wing (Table 4.15) has been applied to the subsonic case (OPT-DD). To extend the comparison to the available vortex correction at the state of the art, results with the Spalart and Shur correction (SA-RC) are also compared [79]. Moreover, new optimization procedures are performed for the subsonic and the transonic conditions. It appears evident from the first sensitivity tests that different optimizations are necessary for the two flow regimes. The transition from a subsonic case to a transonic case introduces new features to the vortex flow typology and development which induces a significant difference with respect to the correct modeling of turbulence. As consequence, the correction terms of the proposed methodology needs to be recalibrated. This is an important lesson to be further analyzed for the extension of the methodology to a larger spectrum of transonic regimes. As consequence, whereas the Erickson's double delta wing represents a good candidate for the accuracy enhancement of the subsonic numerical results, its potential is drastically reduced for the transonic case. As additional comparison, the zonal extension (Sec. 3.5.1) of the turbulence model formulation is applied to the transonic case to investigate how much additional flexibility and accuracy potential is gained compared to a traditional calibration for terms valid on the complete domain.

Calibration for the Subsonic Condition. Due to the complexity of the vortex flow type with multiple interacting or merging vortices, three different swept wing sections and the high angles of attack covering the full development of vortices with breakdown instabilities, a series of sensitivity analysis needed in advance. Different optimization procedures are tested to investigate the locality of the descent to optima of the minimization function. The best optimization result in terms of accuracy improvement is selected as optimum (Table 4.16). It has not shown the necessity of the inlcusion of all the modeling terms and different starting values of the coefficients. However, the necessity to include different angles of attack covering a large part of the angle-of-attack

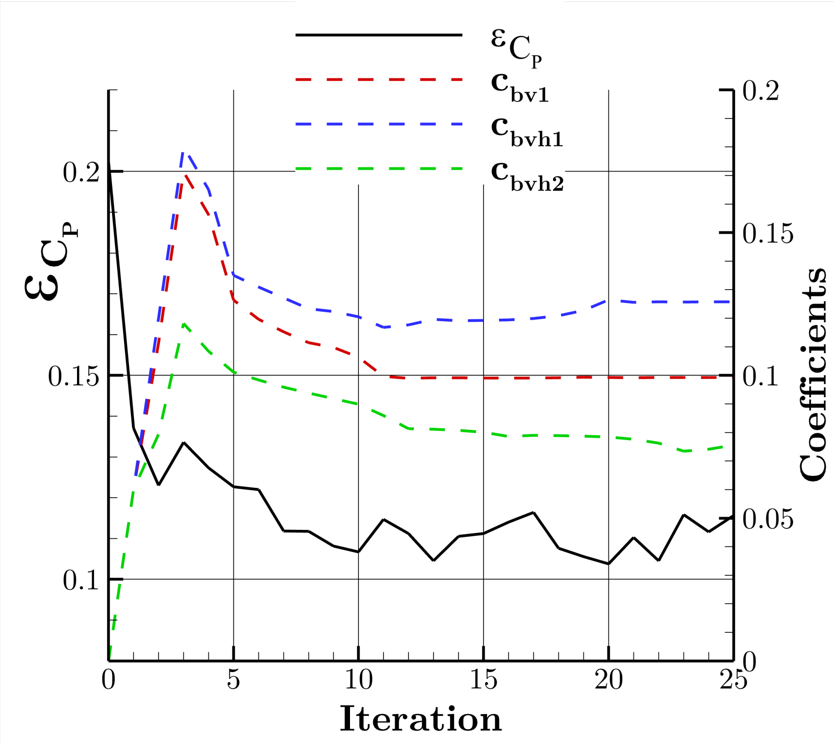

Figure 4.39: Convergence of the $\mathcal{E}_{C_P}$ and the coefficients of the turbulence model modification with sufficient sensitivity along the optimization procedure for the AVT-316 triple-delta wing configuration, M = 0.5, $Re = 8.93 \cdot 10^6$ and $AoA = [24.0, 32.0, 40.0]°$.

polar has been manifested. Hence, three angles of $AoA = [24.0°, 32.0°, 40.0°]$ are included. The resulting optimal coefficients (OPT) follows at first a similar sensitivity direction from the starting base, i.e. the baseline SAE model. The positive coefficients indicate the gradients leading to a destructive direction. At the beginning, the sensivity is quite large and the optimizer pushes the coefficients in the direction by employing the maximum increments allowed by the optimization user-defined settings. This is valid for c_{bv1} and c_{bvh1} until the fourth iteration whereas c_{bvh2} sees its sensitivity being reduced from the third iteration (Fig. 4.39). At the fifth iteration, the optimizer perceives the overshooting of destruction employed by that rapid descent and the coefficients are consequently re-adjusted into more moderate values thanks to the reversal of sensitivity. In this second portion of the optimization, the differences between the terms sensitivities come into play and they converge to different coefficient levels. c_{bv1} converges closely around 0.1 whereas the other two terms manifest a converging value which share a similar offset from the c_{bv1} but in opposite directions, i.e. $c_{bvh1} = 0.126$ and $c_{bvh2} = 0.078$.

Description of results. The most peculiar angles of attack are selected for comparing the numerical results and investigate the effect of the modeling of turbulence with the accuracy towards the experimental data. In general, the baseline turbulence model (SAE)

Table 4.16: Optimal set of coefficients for the AVT-316 triple delta wing at M = 0.5.

Coefficient	c_{bv1}	c_{bvh1}	c_{bvh2}
Value	0.0992	0.126	0.078

underperforms as expected. At $AoA = 16°$, the SAE model is able to predict a vortex flow distribution similar to that captured by the wind tunnel data (Fig. 4.40). The inboard vortex strongly interacts with the outboard vortex, they merge and induce a suction footprint down to the traling edge. In the proximity of the forward wing section, the distribution matches with experimental data except for the suction impressed on the fuselage side which is significantly stronger for the experimental data. This discrepancy is maintained but it decreases downstream. From the C_P contour plotting, it is also evident that the numerically predicted vortex suction over the strake region is stronger than for the experimental data whereas it indicates to proper values as the intersection is approached. With respect to the fuselage suction and this region of the vortex flow, low sensitivities are experience by the other turbulence model variations except for the SA-RC model which appears to bee too abrupt for this kind of vortex. The suction values are larger in the levcon region. By moving further downstream, $x/c_r = 0.475$, all the employed turbulence models manifest an appropriate accuracy. However, the peak value is improved by both the validation optimum from the Erickson case and the newly derived optimum. The region of the secondary separation is predicted with less accuracy by the SA-RC model whereas low sensitivities are shown by the optimized models compared to the baseline one. The next section manifests the strong interaction between the two vortices and large complexities in the flow physics arise. Whereas the baseline SAE model overpredicts both the inboard and the outboard C_P peaks, the other models improves exclusively the inboard one. The outboard vortex is more insensitive to turbulence modeling but the wind tunnel data show a lower suction level. The enhanced improvement is provided by the calibrated model but it is also the one which shows a more pronounced overprediction of the outer vortex suction. With respect to the section located most downstream, at $x/c_r = 0.825$, all the employed models exhibit a proper full merging of the vortices into a single suction “bell-shaped distribution”. The baseline model shows the largest discrepancies to the experiment where a extended region is covered by the vortex suction and the peak is mildly higher. The two optimized models share a similar distribution, where the peak values are closer to the experimental data. However, they still cover a larger suction region similar to the SAE results. The SA-RC model introduces higher destruction and high oscillations are present in the numerical solution. The distribution is close to the optimized models. With an angle of attack of 24°, the outboard vortex merges into the inboard flow after a very short distance. This is visible by the C_P distribution of the PSP measurements (Fig. 4.41). The SAE model is not able to predict the merging of the two vortices but it still exhibits a small independent outboard vortex in the proximity of the sweep kink. Whereas the surface contour of C_P appear reasonable for the SA-RC model and the Rrickson’s test

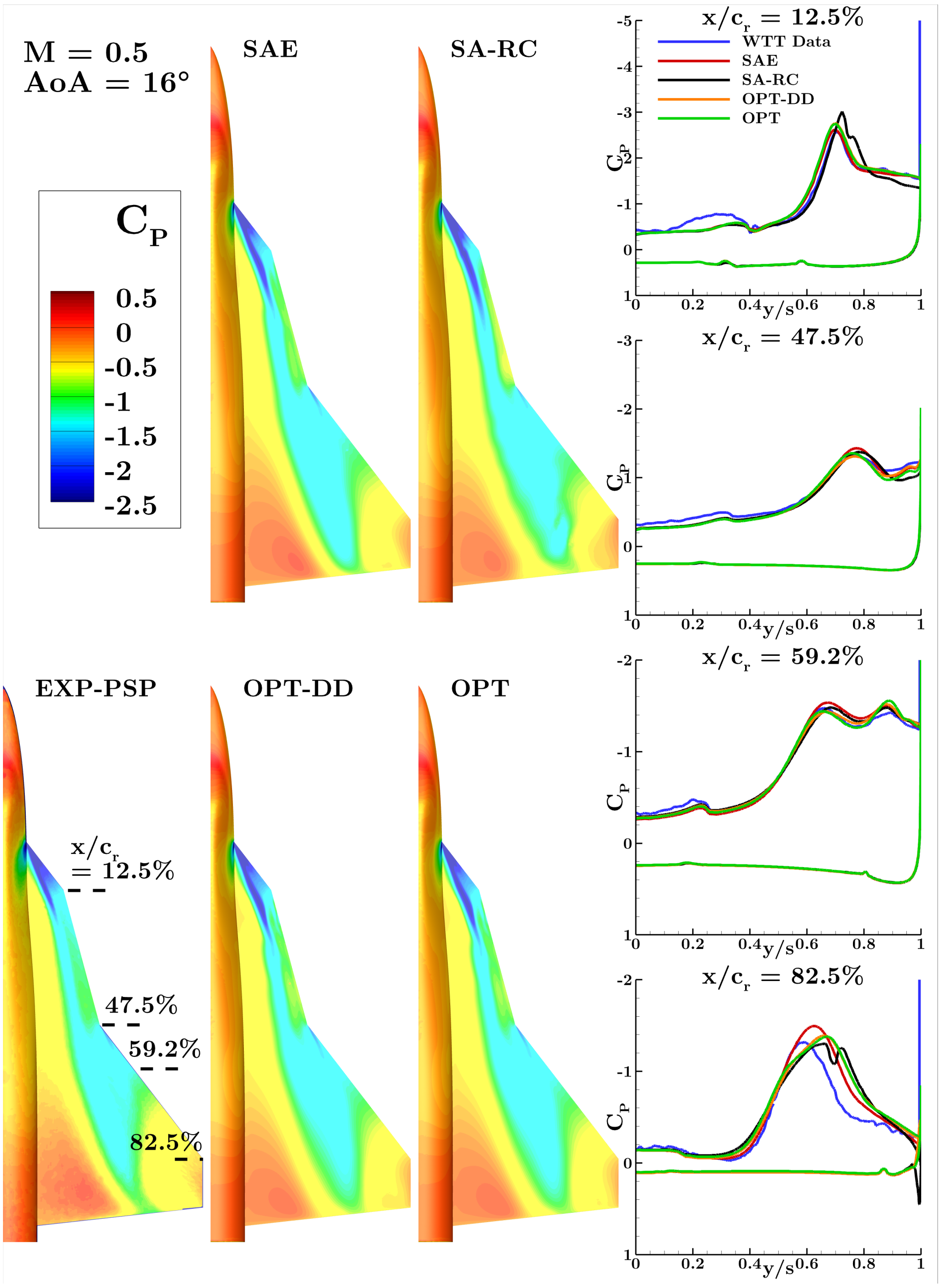

Figure 4.40: The upper surface C_P distribution is visualized by means of surface contour plots and 4 cross-flow sections ($x/c_r = [0.125, 0.475, 0.592, 0.825]$) at M = 0.5, $Re = 8.93{\cdot}10^6$ and $AoA = 16.0°$. The baseline SAE model, the SA-RC model, the model precedently optimized on the Erickson's double delta wing (Table 4.15) and the optimized turbulence model (Table 4.16) are compared to the PSP experimental data.

case optimum, a small overprediction of the outboard vortex is shown by the model optimized towards this same test case. At the first section cut at $x/c_r = 0.125$, the OPT model shows the best accuracy with respect to both the vortex suction footprint and the outward distribution, therefore it appears it is the best model for the levcon region. The baseline SAE model overpredicts the suction peak similarly to what is modeled by the Erickson's optimum. The SA-RC model reduces the suction peak but changes the C_P footprint area in an erroneous fashion. Moving to the strake-wing proximity, at $x/c_r = 0.475$, the SAE shows the largest discrepancy from the experimental data whereas the best accuracy improvement is provided by the SA-RC model. Both turbulence models which employ the proposed methodology change the vortex flow in the right direction but the corresponding results do not match the wind tunnel data. At $x/c_r = 0.592$ and $x/c_r = 0.825$, the numerical results show consistency with respect to the models accuracies as consequence of the downstream effect of a better prediction at the planform kink. The SAE manifests the largest deviation with respect to the strength of the vortex; the vortex stability is high and this avoids the breakdown instability and the merging of the vortices to take place. The OPT model improves the distribution but it does not match the experimental data like the other models do. In particular, the OPT-DD is able to almost perfectly match the two vortices coexistence at $x/c_r = 0.592$ and the C_P distribution downstream as well. It is important to notice that the OPT-DD has been calibrated on a range of moderate angles of attack up to 20°, which may be the cause of its better accuracy in this region. However, it is curious but also important to notice that an optimum calibrated for a different test case manifests consistent accuracy improvements even with drastical geometrical variations. This shows potential with respect to the predictive capability extension with the proposed methodology. At $AoA = 32°$, the vortex flow represented by the PSP experiments (Fig. 4.42) exhibits a similar development stage to the case of $AoA = 24°$ case whereas the breakdown and the drop in suction moves upwards. Moreover, the vortex cross section increases and therefore, it covers a larger portion of the wing surface and the two vortices merge directly at the strake-wing intersection. Similarly to lower angles of attack, the SAE baseline manifests a different vortex flow stage and it largely deviates from the experimental data. The vortex is too stable, the C_P distribution shows larger suction levels and a wrong distribution. Moreover, the vortices merging into a singular structure is located farther downstream. At $x/c_r = 0.125$, the suction level and distribution is significantly improved by all the turbulence models. The best performance in terms of accuracy is given by the dedicated optimum OPT as the corresponding results properly matches with the experimental data. Qualitatively speaking, the distribution shape is appropriate also with the other corrections but the Erickson's validation model underpredicts the C_P levels whereas the SA-RC model overpredicts them. The fuselage suction shows very low sensitivity to the modeling of turbulence and it does not indicates an accurate solution. Moving downstream, at $x/c_r = 0.475$, all the models results in a significant improvement compared to the SAE model but the resultant C_P distribution shape is not completely correct and a wider suction footprint is obvious. The SA-RC model properly predicts the vortex suction, in particular the central region, whereas it maintains a certain offset to the experimental data outboard, close to the leading edge. It also improves

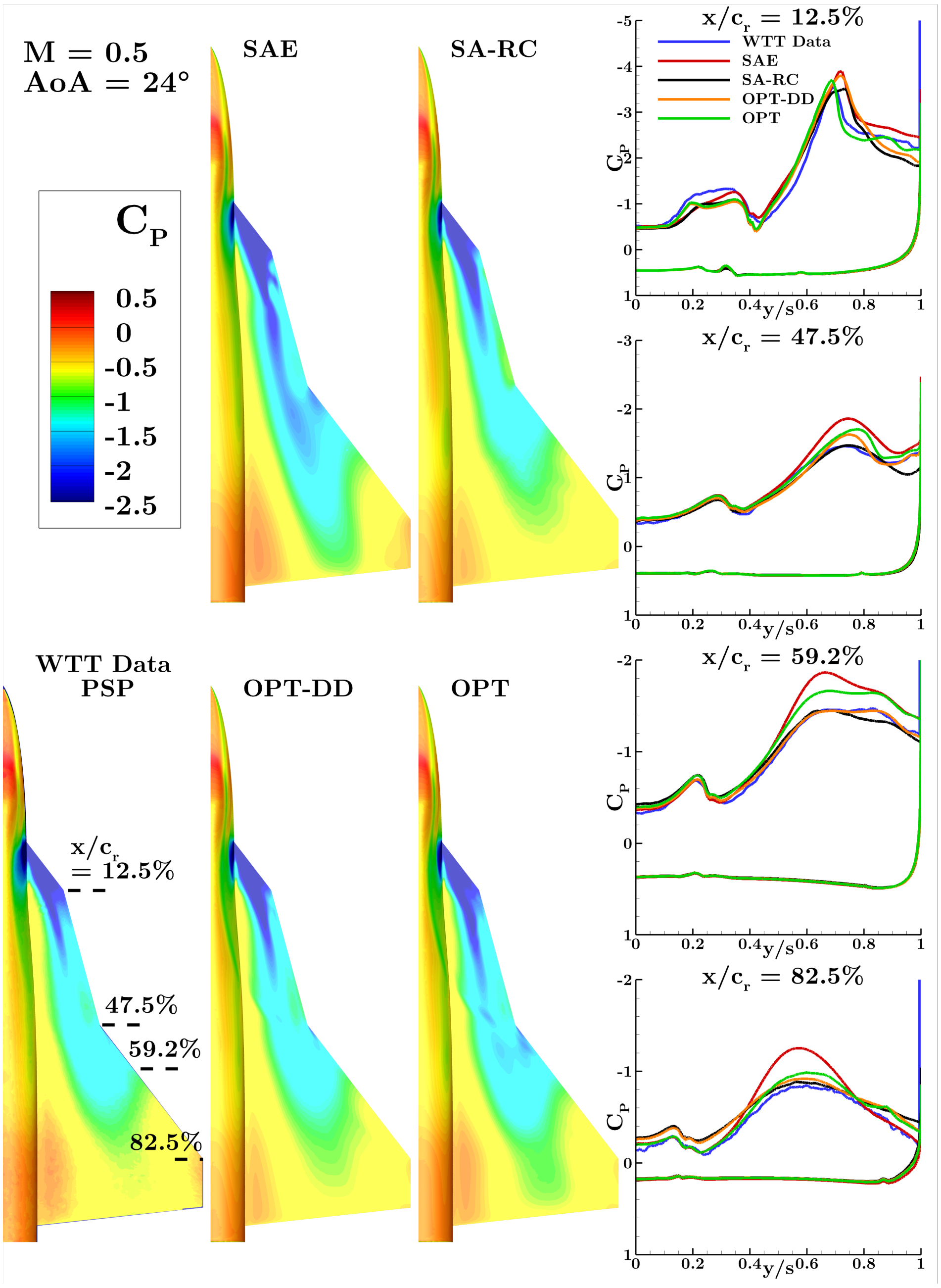

Figure 4.41: The upper surface C_P distribution is visualized by means of surface contour plots and 4 cross-flow sections ($x/c_r = [0.125, 0.475, 0.592, 0.825]$) at M = 0.5, $Re = 8.93{\cdot}10^6$ and $AoA = 24.0°$. The baseline SAE model, the SA-RC model, the model precedently optimized on the Erickson's double delta wing (Table 4.15) and the optimized turbulence model (Table 4.16) are compared to the PSP experimental data.

the fuselage vortex suction whereas the other models still exhibit low sensitivity with respect to this flow feature. The OPT model shows a higher accuracy compared to the OPT-DD for the suction values in the central region, the distribution is similar but with an almost constant offset. The same comments can be made for the successive cross-flow section at $x/c_r = 0.592$. With respect to the wake flow, all the models improve the numerical results compared to the baseline model with a similar grade of accuracy. They are really close in terms of shape and suction levels to the experimental data. The fuselage suction is also considerably improved in this region. In general, it is shown that the OPT model exhibits here the best improvement rate whereas the OPT-DD accuracy slightly drops. However it is still really effective in improving the predicted vortex flow stage and the suction levels.

Finally, the highest angle of attack of 40° (Fig. 4.43) shows a singular and unstable strake vortex with no outboard vortex separation at the wing intersection. Hence, only the strake vortex is present and it dominates the full wing extension. On this case, a clear distinction is present between the strake and the wing regions. On the one hand, the strake flow is significantly improved by the optimized models, at $x/c_r = 0.125$, even though no sensitivity is evident between the OPT and the OPT-DD. They improve the vortex flow prediction to a proper flat distribution similar to the experiment. However, the modification is too strong and a clear offset is established between the experimental and the numerical distributions. The SA-RC has a similar influence but even stronger. As the cuts further downstream are analyzed, it is evident how the optimized models and the SA-RC model get closer to each other and how the SAE baseline model becomes progressively the most accurate one to describe the wake-like flow at $x/c_r = 0.825$ where it properly matches the wind tunnel data. This is an effect which has been already seen for other optimizations like the one on the Model53 (Sec. 4.4.2) at the condition of fully stalled flow. It means that the wake-like flow after breakdown in the proximity of a stall condition is such a complex flow type that it is difficult to improve it together with the strake flow upstream by remaining inside the Boussinesq limitation.

The results have illustrated how the baseline SAE model is inaccurate for the reported test cases along different flow stages related to the analyzed angles of attack. The SA-RC model is, in this case, a good candidate to partially improve the modeling but the proposed methodology extension offers the possibility to enhance even further the accuracy improvement. It is also very important to see how the optimum derived from a different test case, i.e. the optimum of the Erickson's double delta wing, is able to significantly improve the results at a similar overall level to the dedicated optimization.

Calibration for the Transonic Condition: Global and Zonal Methods. As a first sensitivity test, the optima used in the subsonic condition have also been applied to the transonic condition at M = 0.85. However, although they modify the eddy viscosity vortex destruction in the right direction, they are only able to improve the results accuracy towards the experimental data to some extent. Whereas it is important to notice that a certain grade of improvement is maintained and the results are not becoming worse. A new calibration procedure is performed with the transonic experiments as tar-

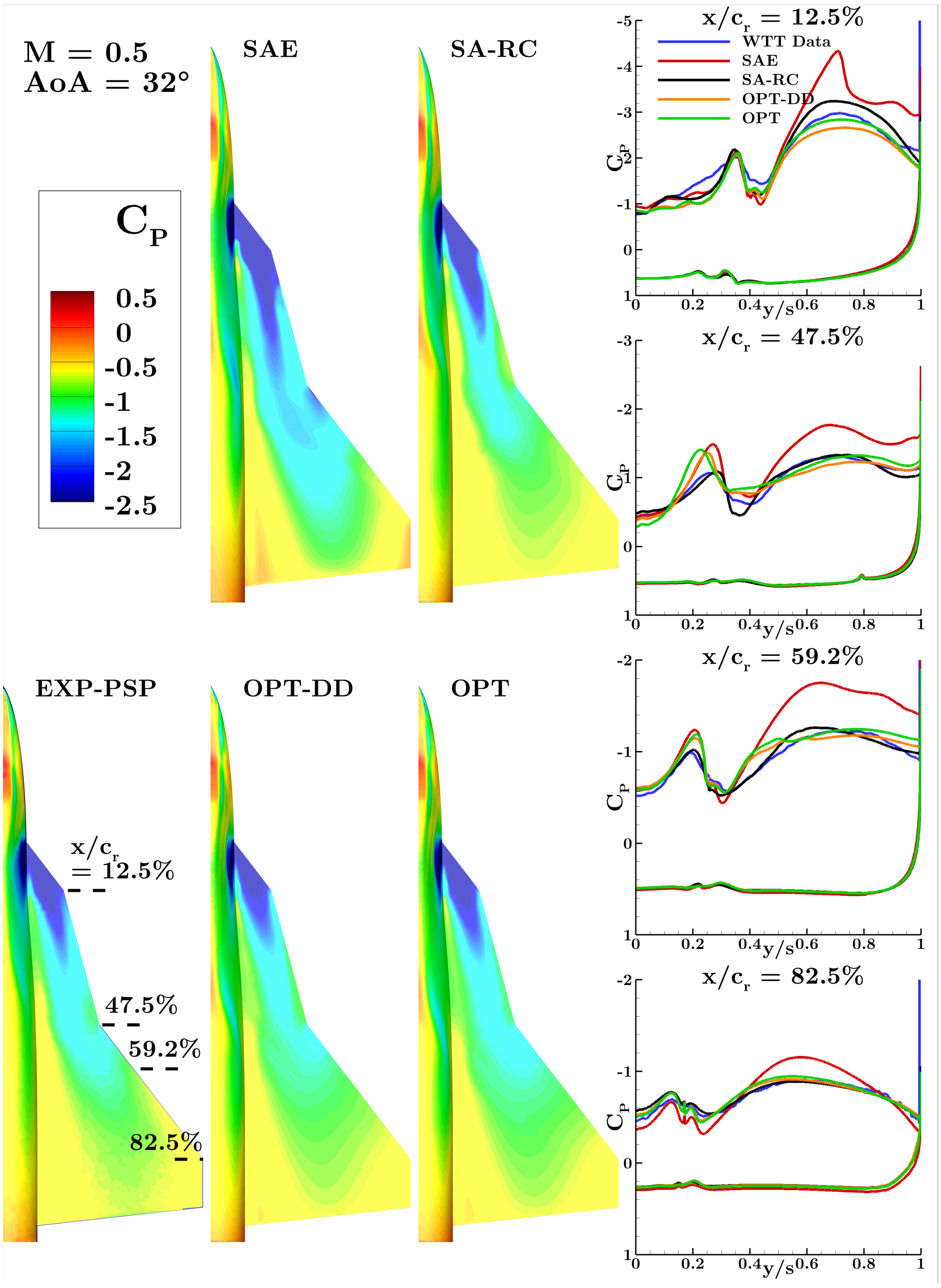

Figure 4.42: The upper surface C_P distribution is visualized by means of surface contour plots and 4 cross-flow sections $(x/c_r = [0.125, 0.475, 0.592, 0.825])$ at M = 0.5, $Re = 8.93 \cdot 10^6$ and $AoA = 32.0°$. The baseline SAE model, the SA-RC model, the model precedently optimized on the Erickson's double delta wing (Table 4.15) and the optimized turbulence model (Table 4.16) are compared to the PSP experimental data.

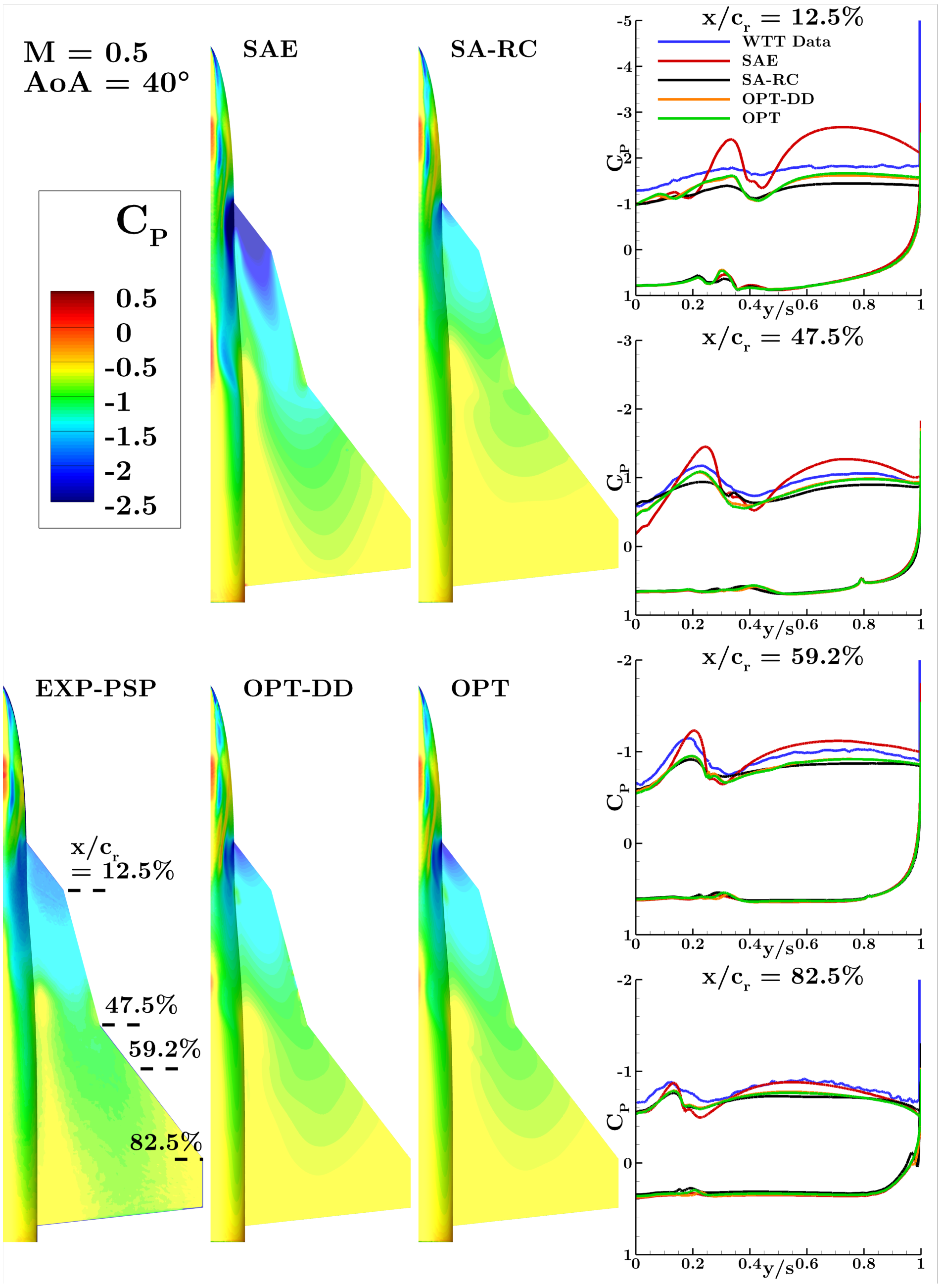

Figure 4.43: The upper surface C_P distribution is visualized by means of surface contour plots and 4 cross-flow sections ($x/c_r = [0.125, 0.475, 0.592, 0.825]$) at M = 0.5, $Re = 8.93 \cdot 10^6$ and $AoA = 40.0°$. The baseline SAE model, the SA-RC model, the model precedently optimized on the Erickson's double delta wing (Table 4.15) and the optimized turbulence model (Table 4.16) are compared to the PSP experimental data.

get (Fig. 4.45). In addition to the main optimization routine, the zonal methodology is used to investigate the possible advantages in terms of accuracy enhancement by having independent turbulence model corrections for different geometrical pre-defined zones (Sec. 3.5.1). For this geometry in particular, a zone is defined around the main wing from the intersection between the strake high sweep and the wing lower sweep to the wake region behind it. The first set of coefficients works on the whole domain except for the outboard vortex, and it is referred to as the strake zone, whereas the second set of coefficients refers to the outboard vortex on the main wing zone (Fig. 4.44).

The optimal set of coefficients for the transonic case (Table 4.17) manifest similar sensitivities with respect to the applied terms. Therefore, the same terms are calibrated in the optimization procedure. However, the values of the coefficients are significantly larger, by a factor of around 3 to 4 depending on the coefficient, compared to the subsonic case. This indicates that, firstly, the baseline SAE model has larger drawbacks for a transonic flow condition where the complexity of the flow is severely enhanced by the combination of compressibility effects and the highly vortical flow (Sec. 1.2.3). Secondly, the methodology extension needs to introduce a significant increase of eddy viscosity destruction in the vortex flow field in order to achieve an accuracy improvement compared to the subsonic case.

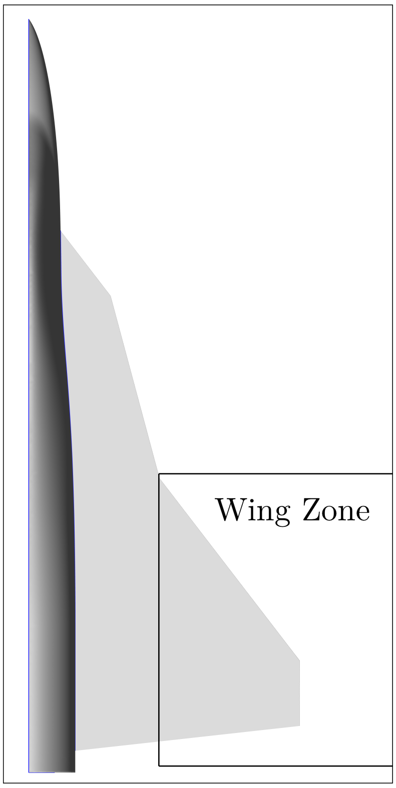

Figure 4.44: Visualization of the wing zone boundaries for the application of the zonal methodology.

From the convergence history of the optimizations, the improvement of the mean absolute error is comparable between the two methods, i.e. the global calibration and the zonal approach, but a significant difference is evident between the two sets of terms of the zonal method. Whereas the set of terms active on the strake zone is similar in terms of direction and magnitude of the corrective coefficients, the wing zone presents an even larger need of vortex destruction of the optimized turbulence model. The values are comparable between the different additional terms. This shows that a different sensitivities are present between the two vortex structures (Table 4.18). In order to highlight the accuracy improvement for the transonic cases and the possible advantages of the application of the zonal methodology, the results for both models and the most interesting angles of attack, i.e. $AoA = 32.0°$ and $40.0°$, are reported. The SA-RC model is also tested to address its flexibility between two different states of compressibility.

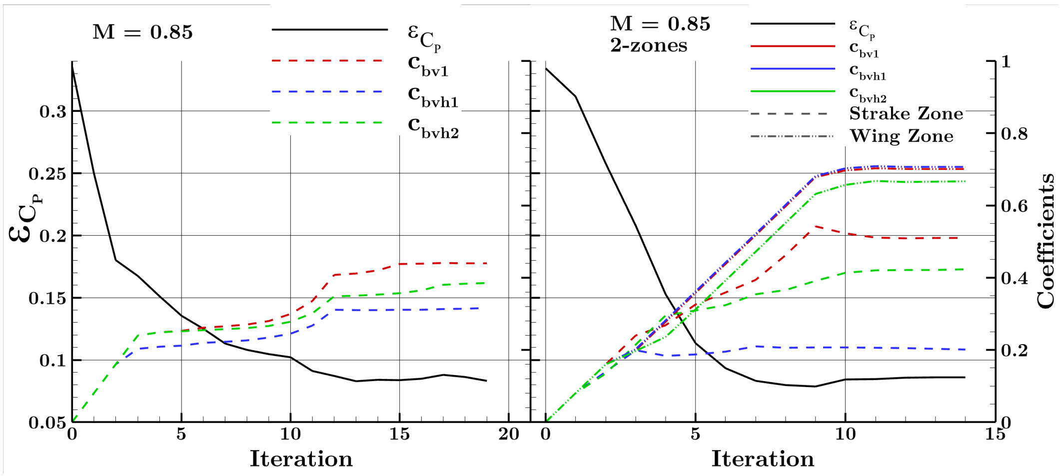

Figure 4.45: Convergence of the $\mathcal{E}_{C_P}$ and the coefficients of the turbulence model modification with sufficient sensitivity along the optimization procedure for the AVT-316 triple-delta wing configuration with and without the zonal method, M = 0.85, $Re = 12.53 \cdot 10^6$ and $AoA = [24.0, 32.0, 40.0]°$.

Table 4.17: Optimal set of coefficients for the AVT-316 triple delta wing at M = 0.85.

Coefficient	c_{bv1}	c_{bvh1}	c_{bvh2}
Value	0.4402	0.31555	0.385365

Results for the Transonic Condition. The angles of attack which highlight the largest variations and sensitivities to the turbulence model modifications are reported. Starting with the angle of attack of 32.0° (Fig. 4.46) and comparing it to the corresponding subsonic case (Fig. 4.42), it is possible to evince how the vortex flow development and characteristics are significantly different. The transonic case shows a drastically lower suction level along the whole wing extension. The flow appears to be already completely stalled on the outboard wing and close to that stage at the strake as well. The suction distribution along the cross-flow sections is completely flat which confirms the contour plots and its difference to the subsonic case. The same flow stage is of course maintained at the largest angle of attack of 40° for the transonic case and this is clearly also different from the subsonic case.

With the application of the baseline SAE model, a significantly different flow is represented by the numerical results. A large deviation from the experimental data with respect to the C_P distribution is shown and a fully developed vortex is present on the strake and the outboard wing which interact and merge on the rear part of the planform (Fig. 4.46). An inaccurate result is here also visible with respect to the fuselage flow. The fuselage vortex predicted by the baseline model manifests a significant suction footprint compared to the experimental data which also interacts with the wing vortical structures and produce a complex and highly unstable flow which is not represented by

Table 4.18: Optimal set of coefficients for the AVT-316 triple delta wing at M = 0.85 performed with the zonal methodology.

Coefficient	Global zone			Wing zone		
-	c_{bv1}	c_{bvh1}	c_{bvh2}	c_{bv1}	c_{bvh1}	c_{bvh2}
Value	0.5224	0.2067	0.414	0.6971	0.7024	0.6566

the experimental data. This is evident along the whole wing extension but particularly at the section $x/c_r = 47.5\%$. Therefore, the baseline model is not able both qualitatively and quantitatively to predict accurate numerical results.

The SA-RC model exhibits a variation of the numerical results which moves in the right direction towards the flow documented by the experimental data. At $AoA = 32.0°$, however, an important level of discrepancy is maintained with respect to the strake flow and the fuselage suction. The flow stage is close to a stall condition but not completely as it is exhibited by the experimental data. The surface C_P distribution is closer to the PSP data but it shows a reduced predictive capability compared to the subsonic case where it performs better. At $AoA = 40°$, a stall stage is achieved and a flat surface C_P distribution is obtained which qualitatively is close to the experimental distribution but a certain offset of around $\Delta C_P = 0.2$ is present. The advantages of the proposed methodology is reported for both the global and the zonal variants. The globally optimized model (OPT) applied to the angle of attack of 32.0° provides a solution with a fully stalled condition similar to the PSP data. The C_P distribution is flat and close to the wind tunnel data. The fuselage flow is also significantly improved. A slight offset to the PSP data is present at the first section $x/c_r = 12.5\%$. At $AoA = 40°$, the improvement is even better and the numerical results matche with the experimental data. However, a larger deviation is present for the C_P distribution on the fuselage. The improvement obtained with the zonal methodology is just slightly appreciable. The offset from the experimental data is even more reduced, in particular at $AoA = 32.0°$, and a lower suction level is shown in the proximity of the strake and wing intersection where the second zone starts to be active.

Conclusive Analysis. In conclusion, the baseline SAE model creates the largest discrepancies from the experimental data compared to the other investigated models. The application of the SA-RC model, in this case, permits an improvement of the vortex stage solution which is in agreement with that illustrated by the experimental data. Nevertherless, a partial discrepancy in the C_P levels remains. This is true, in particular, for the transonic cases and the largest angles of attack at subsonic conditions. The optimum derived from the Erickson's double delta wing is applied to the AVT-316 triple-delta wing in order to investigate its predictive capability for a different configuration. In this way, the capability of the methodology of improving a cluster of cases around its calibration point is investigated. Moreover, two dedicated optimization procedures are performed. The improvement in terms of accuracy is comparable between the Erickson's optimum and the dedicated one, except for some local differences. This confirms

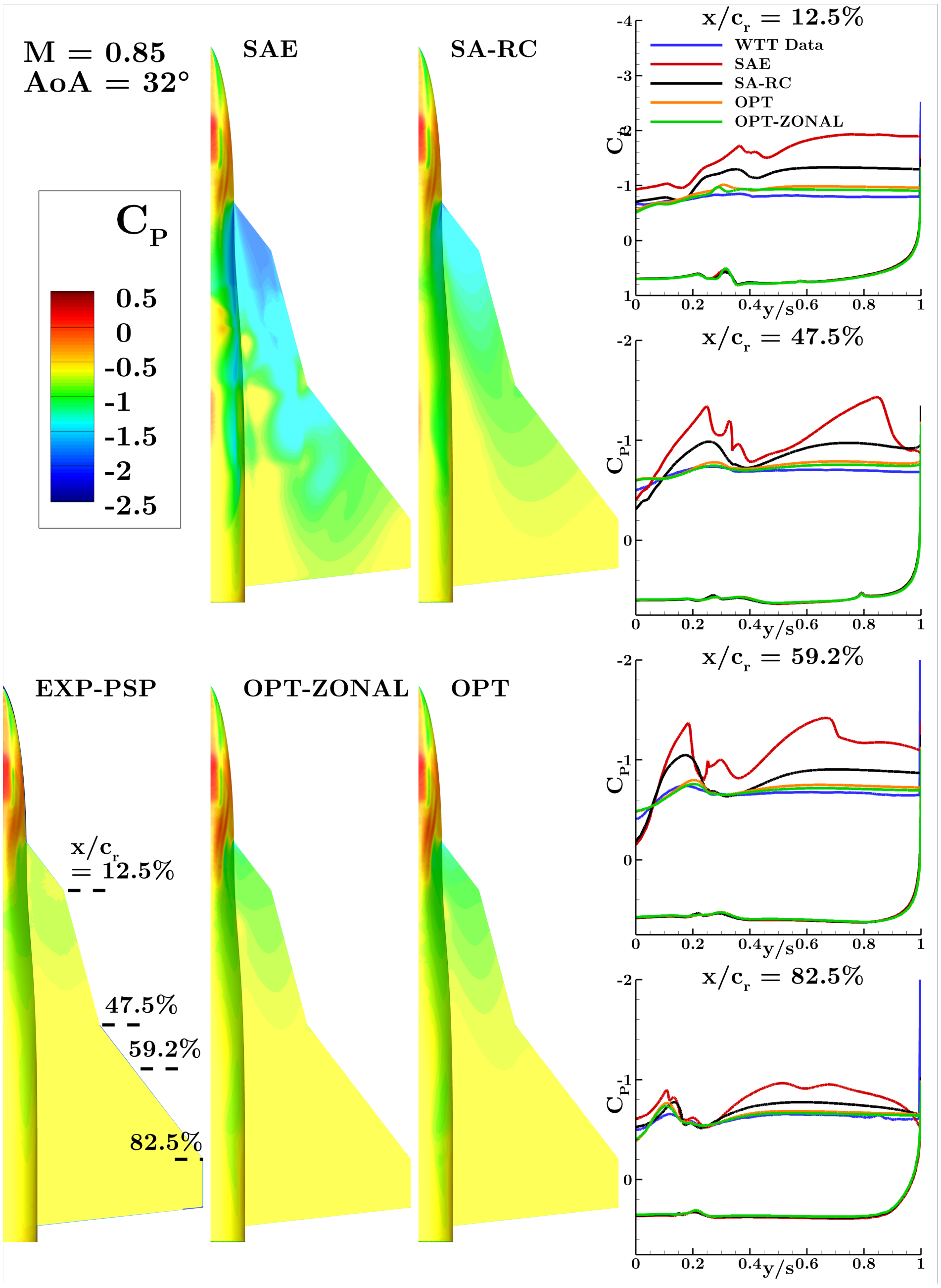

Figure 4.46: The upper surface C_P distribution is visualized by means of surface contour plots and 4 cross-flow sections ($x/c_r = [0.125, 0.475, 0.592, 0.825]$) at M = 0.85, $Re = 12.53 \cdot 10^6$ and $AoA = 32.0°$. The baseline SAE model, the SA-RC model, the model precedently optimized on the Erickson's double delta wing (Table 4.15) and the optimized turbulence models with a global (Table 4.17) and zonal formulation (Table 4.18) are compared to the PSP experimental data.

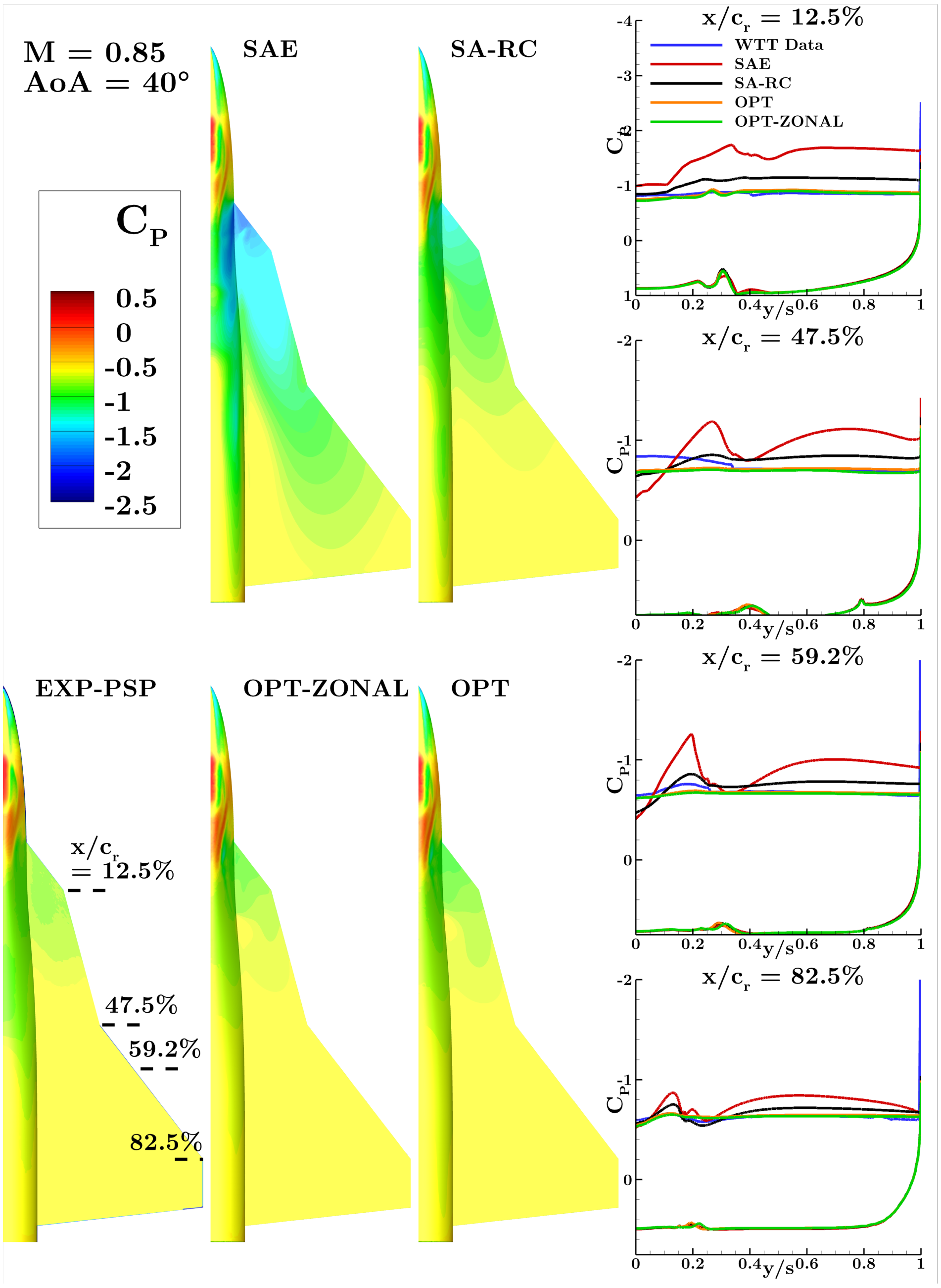

Figure 4.47: The upper surface C_P distribution is visualized by means of surface contour plots and 4 cross-flow sections ($x/c_r = [0.125, 0.475, 0.592, 0.825]$) at M = 0.85, $Re = 12.53 \cdot 10^6$ and $AoA = 40.0°$. The baseline SAE model, the SA-RC model, the model precedently optimized on the Erickson's double delta wing (Table 4.15) and the optimized turbulence models with a global (Table 4.17) and zonal formulation (Table 4.18) are compared to the PSP experimental data.

the possibility to employ an optimum for a reasonably large cluster of cases around its calibration target. The zonal methodology is employed in the transonic regime but, in this case, it introduces only a slight variation compared to the global optimum. At $AoA = 32°$ the zonal model returns a similar distribution to the global one with a mild offset in the direction of the experimental C_P distribution. The zonal methodology works as expected and it has potential to improve even further cases where vortex structures are more independent. In general, the methodology is able to improve the accuracy also for the multiple-delta-wing and complex configurations.

5 Conclusion and Outlook

Results Summary and Final Assessment

The numerical solution of vortex dominated flows is a challenging task. The employment of Reynolds-Averaged Navier-Stokes equation and on delta wings. The main issues related to the efficiency and accuracy of the generation of a large data sets for the aerodynamic design and development of an highly agile aircraft. The selection of scale resolving turbulence models is not suitable due to the computational costs and the detrimental effects to the numerical stability. Both factors are important for the successfull generation of a large aerodynamic data set under a restrained time frame. During the collaboration established in the context of the Advanced Understanding via the Virtual Aircraft Model project, a methodology to enhance the Spalart-Allmaras one-equation eddy-viscosity model by exploiting the information from experimental data is developed. The baseline model is augmented with a series of production-like terms which are exclusively active in the vortex flow field by means of a vortex identifier quantity. This identifier is positive only in the vortex dominated flow region. No modeling alteration is introduced in the solution of the boundary layer regions where an attached flow is present. The additional terms influence the production of eddy viscosity differently for different regions or types of the leading-edge vortex. The enhanced modeling flexibility combined with an automatic calibration procedure with experimental data permits to increase the grade of accuracy at the cost of a decrease of the globality.

An optimum results valid for a relatively large cluster of cases around the calibration points. In this way, the optimized model adds accuracy for a full aerodynamic dataset based on a common aircraft/wing baseline. The predictive capability has been investigated throughout the work by applying an optimum for a series of different test cases or geometrical and/or flow condition variations. The calibration has permitted to improve the accuracy significantly in most cases. The accuracy enhancement decreases as the same optimum is applied for validation to cases with larger differences. The optimization procedure is performed for a 65° swept delta wing and validated on a series of available variations which include different leading-edge shapes, Reynolds numbers and Mach numbers. The results have illustrated that, as expected, the accuracy improvement is reduced with these variations but a significant level of improvement is maintained for the investigated cases. A similar process has been performed with the 53° swept Model53. In order to investigate a cluster of cases with a moderate sweep angle, the Model53 optimum is validated on different test cases like the Model56, the AVT-183 diamond wing and the SAGITTA blended wing body configuration. The prediction of the breakdown position and the stall condition has been significantly improved. Afterwards, multi-delta wing configurations have been employed for the methodology application. The Erickson's double delta wing and the AVT-316 triple delta wing are calibrated. Here, the double delta wing optimum has shown a good predictive capability also for the subsonic case of the triple delta wing geometry. Moreover, the zonal methodology is applied on the AVT-316 configuration, to show its proper formulation. The zonal method is an extension of the turbulence model enhancement where different geometrical zones of the flow domain are defined and different values of the turbulence model coefficients are valid in the respective zones of influence. This extension exhibits high potential for cases where multiple and different vortices are present.

An Artificial Neural Network method is used to learn from the past optimization procedures and to predict a set of coefficients for a new test case where no experimental data are available. Results are reported for four test cases including the Model56, the AVT-183 diamond wing, the SAGITTA blended wing body and the 60° swept DW60 delta wing. The results exhibit a suitable grade of accuracy increase although slightly lower, as expected, than what is possible to achieve by the optimization procedure where experimental data are available.

In general, the research has been successfull in its task to find a methodology which is able to increase the accuracy of RANS simulation employing an eddy-viscosity model for predicting large-scale leading-edge vortical flows. Moreover, the extensions of the model are formulated in order to expand the accuracy improvement potential, in the case of the zonal method, and the predictive capability, in the case of the artificial neural network approach. The results are consistent throughout the reported test cases. No significant computational costs are added compared to the baseline turbulence model. No numerical instability is introduced and the boundary layer is unaltered by the turbulence model variation. The predictive capability around the calibration target related to experimental data is powerful enough to apply the method for the generation of aerodynamic data sets around a common baseline aircraft/wing.

Outlook and Future Development

The methodology may be further expanded in several directions. A larger spectrum of vortex flow stages may be optimized as new experimental data are available for other geometries and flow conditions. These data would improve the experience about the methodology predictive capability and accuracy enhancement. Moreover, it would give the modeller further information about the main dependencies of the required coefficients for different vortex flow types and stages. Additionally, a larger dataset of optimization procedures increases the predictive capability of the artificial neural network model.

The additional model terms can be translated for two-equation eddy viscosity models. A similar approach of additial terms may also be applied for a different flow case outside of vortex flows. Otherwise, a model enhancement based on similar terms may be introduced in a scale adaptive or Reynolds stress model. There are several possibilities to exploit the experience acquired from this work towards other directions.

New terms may be formulated which relates to vortex types which were not encountered with the reported test cases. A different direction may be the formulation of a different neural network approach which learns the dependence of the local vortex flow together with the global geometry and flow condition to the eddy viscosity production. The training data would be the results obtained with the optimized model or high fidelity numerical simulations.

In general, the high potential shown with the proposed methodology is enough for its application to the generation of an aerodynamic dataset. It is expected that with its continous application throughout different design loops or new geometries/flow condition, new experience is gathered and/or new problems are encountered. Either way, the modeller may exploit the new conditions to enhance the accuracy and the predictive capability even more.

Bibliography

[1] C. Breitsamter. *Turbulente Strömungsstrukturen an Flugzeugkonfigurationen mit Vorderkantenwirbeln.* PhD thesis, Technische Universität München, Herbert Utz Verlag Wissenschaft, 1997. ISBN 3-89675-201-4.

[2] K. A. Sørensen. Vitamin-abc, overview of airbus d&s activities in vitam. 2018.

[3] K. A. Sørensen. Industrialization of recent developments in numerical dataset generation. *VitAM Final Report: Airbus Defence and Space*, 2020.

[4] P. Schuster. The end of moore's law: Living without an exponential increase in the efficiency of computational facilities. *Complexity*, 21(S1):6–9, 2016. `doi:10.1002/cplx.21824`.

[5] E. Torenbeek and H. Wittenberg. *Flight physics: Essentials of aeronautical disciplines and technology, with historical notes.* 01 2009. `doi:10.1007/978-1-4020-8664-9`.

[6] R. Whitford. *Design for air combat.* London : Jane's, 1987.

[7] S. Kida and H. Miura. Identification and analysis of vortical structures. *European" Journal of Mechanics - B/Fluids*, 17(4):471 – 488, 1998. Special Issue Dynamics and Statistics of Concentrated Vortices in Turbulent Flow (Euromech Colloquium 364). `doi:10.1016/S0997-7546(98)80005-8`.

[8] M. Visbal. *Computed unsteady structure of spiral vortex breakdown on delta wings.* `doi:10.2514/6.1996-2074`.

[9] D. Hummel. Experimental investigation of the flow on the suction side of a thin delta wing. *NASA Technical Memorandum 75897*, 1981.

[10] C. Breitsamter. Unsteady flow phenomena associated with leading-edge vortices. *Progress in Aerospace Sciences*, 44(1):48 – 65, 2008". `doi:10.1016/j.paerosci.2007.10.002`.

[11] R. Nelson and K. Visser. Breaking down the delta wing vortex: The role of vorticity in the breakdown process. *AGARD Symposium on Vortex Flow Aerodynamics*, 10 1990.

[12] D. Hummel. On the vortex formation over a slender wing at larg angles of incidence. *High Angle of Attack Aerodynamics, CP-247, AGARD*, pages 15–1–15–17, 1979.

[13] E. C. Polhamus. Predictions of vortex-lift characteristics by a leading-edge suctionanalogy. *Journal of Aircraft*, 8(4):193–199, 1971. `doi:10.2514/3.44254`.

[14] N. T. Frink. Numerical analysis of incipient separation on 53-deg swept diamond wing. *53rd AIAA Aerospace Sciences Meeting*, 2015. `doi:10.2514/6.2015-0288`.

[15] X. Z. Huang. Critical assessment of test cases on vortex breakdown over slender delta wing under static model conditions, 2009.

[16] W. H. Wentz and D. L. Kohlman. Wind tunnel investigations of vortex breakdown on slender sharp–edged wings. *NASA Research Grant NGR-17-002-043, University of Kansas Center of Research, Inc., Engineering Sciences Division, Report FRL 68-013*, 1968.

[17] A. Ayoub and B. Mclachlan. *Slender delta wing at high angles of attack - A flow visualization study.* `doi:10.2514/6.1987-1230`.

[18] N. C. Lambourne and D. W. Bryer. The bursting of leading-edge vortices–some observations and discussion of the phenomenon. *ARCR & M.*, 3282:1–36, 1962.

[19] M. G. Hall. Vortex breakdown. *Annual Review of Fluid Mechanics*, 4(1):195–218, 1972. `doi:10.1146/annurev.fl.04.010172.001211`.

[20] F. Payne. *Structure of leading-edge vortex flows including vortex breakdown.* PhD thesis, Notre Dame University, IN (USA), 1987.

[21] I. Gursul. Review of unsteady vortex flows over delta wings. *Journal of Aircraft - J AIRCRAFT*, 42:299–319, 03 2005. `doi:10.2514/1.5269`.

[22] M. V. Ol and M. Gharib. Leading-edge vortex structure of nonslender delta wings at low reynolds number. *AIAA Journal*, 41(1):16–26, 2003. `doi:10.2514/2.1930`.

[23] G. Erickson. *Vortex Flow Correlation*, chapter Northrop Corporation. 1981.

[24] J. K. Harvey. Leading-edge vortex structure of nonslender delta wings at low reynolds number. *Journal of Fluid Mechanics*, 14(4):585–592, 1962. `doi:10.1017/S0022112062001470`.

[25] K. Iwanski, T. Ng, and R. Nelson. *An experimental investigation of delta wing vortex flow with and without external jet blowing.* `doi:10.2514/6.1989-84`.

[26] D. Hummel. Vortex formation over double-delta wings. *Congress of the International Council of the Aeronautical Sciences, Seattle*, 1982.

[27] G. Erickson and L. Rogers. *Experimental study of the vortex flow behavior on a generic fighter wing at subsonic and transonic speeds.* `doi:10.2514/6.1987-1262`.

[28] D. S. Miller and R. M. Wood. Leeside flows over delta wings at supersonic speeds. *Journal of Aircraft*, 21(9):680–686, 1984. `doi:10.2514/3.45014`.

[29] J. F. Wendt. Compressibility effects on flows around simple components. *AGARD Lecture Series on High Angle-of-Attack Aerodynamics*, 121, 1982.

[30] Q. Deng and I. Gursul. Effect of leading-edge flaps on vortices and vortex breakdown. *Journal of Aircraft*, 33(6):1079–1086, 1996. `doi:10.2514/3.47060`.

[31] D. M. Rao. Leading edge vortex-flap experiments on a 74 deg. delta wing. *NASA Contractor Report 159161, Old Dominion University Research Foundation*, 1979.

[32] D. M. Rao. Leading-edge vortex flaps for enhanced subsonic aerodynamics of slender wings. *Congress of the International Council of the Aeronautical Sciences, Munich*, 1980.

[33] A. Bergmann and D. Hummel. *Aerodynamic effects of canard position on a wing body configuration in symmetrical flow*. `doi:10.2514/6.2001-116`.

[34] S. B. Pope. *Turbulent Flows*. Cambridge University Press, 2000. `doi:10.1017/CBO9780511840531`.

[35] S. G. Saddoughi and S. V. Veeravalli. Local isotropy in turbulent boundary layers at high reynolds number. *Journal of Fluid Mechanics*, 268:333–372, 1994. `doi:10.1017/S0022112094001370`.

[36] F. Menter. *Turbulence Modeling for Engineering Flows*. URL: `https://www.ozeninc.com/wp-content/uploads/2021/01/Turbulence-Modeling-for-Engineering-Flows.pdf`.

[37] P. Durbin and T. Shih. An overview of turbulence modeling. *WIT Transactions on State-of-the-art in Science and Engineering*, 15, 2005.

[38] D. Wilcox. *Turbulence modeling - An overview*. `doi:10.2514/6.2001-724`.

[39] P. Spalart and S. Allmaras. A one-equation turbulence model for aerodynamic flows. *AIAA*, 439, 01 1992. `doi:10.2514/6.1992-439`.

[40] Turbulence modeling resource. URL: `https://turbmodels.larc.nasa.gov/`.

[41] J. R. Edwards and S. Chandra. Comparison of eddy viscosity-transport turbulence models for three-dimensional, shock-separated flowfields. *AIAA Journal*, 34(4):756–763, 1996. `doi:10.2514/3.13137`.

[42] N. Frink, P. Murphy, H. Atkins, S. Viken, J. L. Petrilli, A. Gopalarathnam, and R. Paul. Status of computational aerodynamic modeling tools for aircraft loss-of-control - invited. 2016.

[43] W. Fritz and R. M. Cummings. Lessons learned from the numerical investigations on the vfe-2 configuration. *NATO STO, Summary Report of Task Group AVT-113, Chapter 34. Understanding and Modeling Vortical Flows to Improve the Technology Readiness Level for Military Aircraft*, 2009.

[44] L. A. Schiavetta, O. J. Boelens, S. Crippa, R. M. Cummings, W. Fritz, and K. J. Badcock. Shock effects on delta wing vortex breakdown. *Journal of Aircraft*, 46(3):903–914, 2009. `doi:10.2514/1.38792`.

[45] R. Cummings and A. Schutte. *Detached-Eddy Simulation of the Vortical Flowfield about the VFE-2 Delta Wing.* `doi:10.2514/6.2008-396`.

[46] A. Rizzi, O. Boelens, A. Jirasek, and B. K. *What Was Learned from Numerical Simulations of F-16XL (CAWAPI) at Flight Conditions.* `doi:10.2514/6.2007-683`.

[47] A. W. Rizzi. *What was Learned in Predicting Slender Airframe Aerodynamics with the F16-XL Aircraft.* `doi:10.2514/6.2014-0759`.

[48] O. J. Boelens, K. J. Badcock, S. Görtz, S. Morton, W. Fritz, S. L. Karman, T. Michal, and J. E. Lamar. F16-xl geometry and computational grids used in cranked-arrow wing aerodynamics project international. *Journal of Aircraft*, 46(2):369–376, 2009. `doi:10.2514/1.34852`.

[49] M. Tomac, A. Rizzi, and A. Jirásek. Computational fluid dynamics predictions of control-surface effects for f-16xl aircraft. *Journal of Aircraft*, 54(2):395–408, 2017. `doi:10.2514/1.C033260`.

[50] M. Tomac, A. Jirasek, and A. Rizzi. Hybrid reynolds-averaged navier–stokes/large-eddy simulations of f-16xl in low-speed high-alpha flight. *Journal of Aircraft*, 54(6):2070–2076, 2017. `doi:10.2514/1.C034283`.

[51] S. M. Hitzel. *Vortex Flows of the F-16XL Configuration - CAWAPI-II Free-Flight Simulations.* `doi:10.2514/6.2014-0758`.

[52] S. M. Hitzel. *Free-Flight High AoA Flows Simulation at Sub- and Transonic Speeds - F-16XL (CAWAPI-3).* `doi:10.2514/6.2015-2871`.

[53] S. M. Hitzel. Sub- and transonic vortex breakdown flight condition simulations of the f-16xl aircraft. *Journal of Aircraft*, 54(2):428–443, 2017. `doi:10.2514/1.C033246`.

[54] W. Fritz, M. B. Davis, S. L. Karman, and T. Michal. Reynolds-averaged navier-stokes solutions for the cawapi f-16xl using different hybrid grids. *Journal of Aircraft*, 46(2):409–422, 2009. `doi:10.2514/1.35106`.

[55] M. A. Park, K. S. Abdol-Hamid, and A. Elmiligui. F-16xl hybrid reynolds-averaged navier–stokes/large-eddy simulation on unstructured grids. *Journal of Aircraft*, 54(6):2027–2049, 2017. `doi:10.2514/1.C034028`.

[56] S. M. Hitzel. High-angle-of-attack f-16xl flight simulations at sub- and transonic speeds. *Journal of Aircraft*, 54(6):2014–2026, 2017. `doi:10.2514/1.C034025`.

[57] A. J. Lofthouse and R. M. Cummings. Numerical simulations of the f-16xl at flight-test conditions using delayed detached-eddy simulation. *Journal of Aircraft*, 54(6):2077–2099, 2017. `doi:10.2514/1.C034045`.

[58] A. Schütte, O. J. Boelens, T. Loeser, and M. Oehlke. *Prediction of the Flow around the X-31 Aircraft using two different CFD methods*. `doi:10.2514/6.2010-4692`.

[59] R. Cummings, A. Schütte, S. Schmidt, D. Hummel, E. Milanov, R. Konrath, Z. Zlatev, T. Loeser, C. Simonsen, O. M., G. Anne, D. Otter, J.-F. Roy, S. Hitzel, D. Rohlf, D. Pallek, E. Roosenboom, A. Schröder, K. Petterson, and S. Perkins. Assessment of stability and control prediction methods for nato air and sea vehicles. 04 2012. `doi:10.14339/RTO-TR-AVT-161`.

[60] O. J. Boelens. *CFD Analysis of the Flow Around the X-31 Aircraft at High Angle of Attack*. `doi:10.2514/6.2009-3628`.

[61] A. Schütte, D. Hummel, and S. M. Hitzel. *Numerical and experimental analyses of the vortical flow around the SACCON configuration*. `doi:10.2514/6.2010-4690`.

[62] A. Schütte, K. C. Huber, N. T. Frink, and O. J. Boelens. Stability and control investigations of generic 53 degree swept wing with control surfaces. *Journal of Aircraft*, 55(2):502–533, 2018. `doi:10.2514/1.C033700`.

[63] N. T. Frink. *Numerical Analysis of Incipient Separation on 53-Deg Swept Diamond Wing*. `doi:10.2514/6.2015-0288`.

[64] D. Vallespin, A. D. Ronch, K. J. Badcock, and O. Boelens. Vortical flow prediction validation for an unmanned combat air vehicle model. *Journal of Aircraft*, 48(6):1948–1959, 2011. `doi:10.2514/1.C031385`.

[65] M. Paul and M. Rein. Transonic numerical and experimental evaluation of unconventional lambda wing control surfaces. *Journal of Aircraft*, 54(3):1139–1149, 2017. `doi:10.2514/1.C034080`.

[66] R. Cummings and A. Schütte. The nato sto task group avt-201 on extended assessment of stability and control prediction methods for nato air vehicles. 2014.

[67] A. Jirasek, R. M. Cummings, A. Schuette, and K. C. Huber. *The NATO STO AVT-201 Task Group on Extended assessment of Stability an Control Prediction Methods for NATO Air Vehicles: Summary, Conclusions and Lessons Learned*. `doi:10.2514/6.2014-2394`.

[68] J. M. Luckring, O. J. Boelens, C. Breitsamter, A. Hövelmann, F. Knoth, D. J. Malloy, and S. Deck. Objectives, approach, and scope for the avt-183 diamond-wing investigations. *Aerospace Science and Technology*, 57:2 – 17, 2016. Diamond Wing Aerodynamics. `doi:10.1016/j.ast.2016.05.025`.

[69] N. T. Frink. *Numerical Analysis of Incipient Separation on 53-Deg Swept Diamond Wing*. `doi:10.2514/6.2015-0288`.

[70] A. Buzica, L. Debschütz, F. Knoth, and C. Breitsamter. Leading-edge roughness affecting diamond-wing aerodynamic characteristics. *Aerospace*, 5(3), 2018. `doi:10.3390/aerospace5030098`.

[71] S. M. Hitzel, O. J. Boelens, and A. Hövelmann. *Vortex Development on the AVT-183 Diamond Wing Configuration - Numerical and Experimental Findings*. `doi:10.2514/6.2015-0289`.

[72] O. J. Boelens, J. M. Luckring, C. Breitsamter, A. Hövelmann, F. Knoth, D. J. Malloy, and S. Deck. *Numerical and Theoretical Considerations for the Design of the AVT-183 Diamond-Wing Experimental Investigations (Invited)*. `doi:10.2514/6.2015-0062`.

[73] A. Hövelmann and C. Breitsamter. Leading-edge geometry effects on the vortex formation of a diamond-wing configuration. *Journal of Aircraft*, 52(5):1596–1610, 2015. `doi:10.2514/1.C033014`.

[74] S. Pfnür, S. Oppelt, and C. Breitsamter. Yaw-control efficiency analysis for a diamond wing configuration with outboard split flaps. *CEAS Aeronautical Journal*, 10, 11 2018. `doi:10.1007/s13272-018-0340-1`.

[75] A. Hövelmann, A. Winkler, S. Hitzel, K. Richter, and M. Werner. Analysis of vortex flow phenomena on generic delta wing planforms at transonic speeds. 11 2018.

[76] S. Pfnür and C. Breitsamter. Leading-edge vortex interactions at a generic multiple swept-wing aircraft configuration. *Journal of Aircraft*, 56(6):2093–2107, 2019. `doi:10.2514/1.C035491`.

[77] A. Schütte and R. Marini. *Computational Aerodynamic Sensitivity Studies for Generic Delta Wing Planforms*, pages 338–348. 01 2020. `doi:10.1007/978-3-030-25253-3_33`.

[78] B. Chaouat. The state of the art of hybrid rans/les modeling for the simulation of turbulent flows. *Flow, Turbulence and Combustion*, 99:279 – 327, 2017.

[79] M. L. Shur, M. K. Strelets, A. K. Travin, and P. R. Spalart. Turbulence modeling in rotating and curved channels: Assessing the spalart–shur correction. *AIAA Journal*, 38(5):784–792, 2000. American Institute of Aeronautics and Astronautics.

[80] J. H. G. Howard, S. V. Patankar, and R. M. Bordynuik. Flow predictions in rotating ducts using coriolis-modified turbulence models. *Journal of Fluids Engineering*, 102(4):456–461, 1980.

[81] B. E. Launder, C. H. Priddin, and B. I. Sharma. The Calculation of Turbulent Boundary Layers on Spinning and Curved Surfaces. *Journal of Fluids Engineering*, 99(1):231–239, 03 1977. `doi:10.1115/1.3448528`.

[82] D. Degani and L. B. Schifft. Computation of turbulent supersonic flows around pointed bodies having crossflow separation. *Journal of Computational Physics*, 66(1):173–196, 1986. `doi:10.1016/0021-9991(86)90059-8`.

[83] S. W. Park and M. K. Chung. Curvature-dependent two-equation model for prediction of turbulent recirculating flows. *AIAA Journal*, 27(3):340–344, 1989. `doi:10.2514/3.10117`.

[84] P. R. Spalart and M. L. Shur. On the sensitization of turbulence models to rotation and curvature. *Aerospace Science and Technology*, 1(5):297 – 302, 1997. `doi:10.1016/S1270-9638(97)90051-1`.

[85] S. Hitzel. Sub- and transonic vortex breakdown flight condition simulations of the f-16xl aircraft. *Journal of Aircraft*, 54(2):428–443, 2017. `doi:10.2514/1.C033246`.

[86] S. Ali, K. J. Elliott, E. Savory, C. Zhang, R. J. Martinuzzi, and W. E. Lin. Investigation of the Performance of Turbulence Models With Respect to High Flow Curvature in Centrifugal Compressors. *Journal of Fluids Engineering*, 138(5), 12 2015. `doi:10.1115/1.4031779`.

[87] G. Subbian and R. Radespiel. Assessment of extensions for an eddy viscosity turbulence model for vortical flows. In A. Dillmann, G. Heller, E. Krämer, C. Wagner, C. Tropea, and S. Jakirlić, editors, *New Results in Numerical and Experimental Fluid Mechanics XII*, pages 131–140, Cham, 2020. Springer International Publishing.

[88] P. E. Smirnov and F. R. Menter. Sensitization of the SST Turbulence Model to Rotation and Curvature by Applying the Spalart–Shur Correction Term. *Journal of Turbomachinery*, 131(4), 07 2009. `doi:10.1115/1.3070573`.

[89] T. H. Shih, J. Zhu, W. Liou, K. Chen, N. Liu, and J. Lumley. Modeling of turbulent swirling flows. *NASA Technical Memorandum*, 09 1997.

[90] T. J. Craft, B. E. Launder, and K. Suga. Development and application of a cubic eddy-viscosity model of turbulence. *International Journal of Heat and Fluid Flow*, 17(2):108 – 115, 1996. `doi:10.1016/0142-727X(95)00079-6`.

[91] K. S. Abdol-Hamid. *Development of kL-Based Linear, Nonlinear, and Full Reynolds Stress Turbulence Models.* `doi:10.2514/6.2019-1878`.

[92] B. Parmar, E. Peters, K. E. Jansen, A. Doostan, and J. A. Evans. *Generalized Non-Linear Eddy Viscosity Models for Data-Assisted Reynolds Stress Closure.* `doi:10.2514/6.2020-0351`.

[93] W. Zhang, Z. Ma, Y. Yu, and C. Hong-Xun. Applied new rotation correction – sst model for turbulence simulation of centrifugal impeller in the rotating frame of reference. *Journal of Hydrodynamics, Ser. B*, 22(5, Supplement 1):404 – 407, 2010. `doi:10.1016/S1001-6058(09)60227-4`.

[94] A. Hellsten. *Some improvements in Menter's k-omega SST turbulence model.* `doi:10.2514/6.1998-2554`.

[95] S. K. Arolla and P. A. Durbin. Modeling rotation and curvature effecorrectioncts within scalar eddy viscosity model framework. *International Journal of Heat and Fluid Flow*, 39:78 – 89, 2013. `doi:10.1016/j.ijheatfluidflow.2012.11.006`.

[96] B. A. Pettersson Reif, P. Durbin, and A. Ooi. Modeling rotational effects in eddy-viscosity closures. *International Journal of Heat and Fluid Flow*, 20(6):563 – 573, 1999. `doi:10.1016/S0142-727X(99)00056-9`.

[97] A. S. Stabnikov and A. V. Garbaruk. Testing of modified curvature-rotation correction for k-ω SST model. *Journal of Physics: Conference Series*, 769:012087, nov 2016. `doi:10.1088/1742-6596/769/1/012087`.

[98] A. Asnaghi, U. Svennberg, and R. E. Bensow. Evaluation of curvature correction methods for tip vortex prediction in sst k turbulence model framework. *International Journal of Heat and Fluid Flow*, 75:135 – 152, 2019. `doi:10.1016/j.ijheatfluidflow.2018.12.002`.

[99] X. Zhang and R. K. Agarwal. *Development of Various Rotation and Curvature Corrections for Eddy-Viscosity Turbulence Models.* `doi:10.2514/6.2018-0591`.

[100] R. H. Bush, T. S. Chyczewski, K. Duraisamy, B. Eisfeld, C. L. Rumsey, and B. R. Smith. *Recommendations for Future Efforts in RANS Modeling and Simulation.* `doi:10.2514/6.2019-0317`.

[101] F. Menter, A. Matyushenko, and R. Lechner. Development of a generalized k-two-equation turbulence model. 2018.

[102] K. Duraisamy, G. Iaccarino, and H. Xiao. Turbulence modeling in the age of data. *Annual Review of Fluid Mechanics*, 51(1):357–377, 2019. `doi:10.1146/annurev-fluid-010518-040547`.

[103] A. P. Singh, S. Medida, and K. Duraisamy. Machine learning-augmented predictive modeling of turbulent separated flows over airfoils, 2016. `arXiv:1608.03990`.

[104] Y. Zhu and N. Dinh. A data-driven approach for turbulence modeling, 2020. `arXiv:2005.00426`.

[105] J. Wu, H. Xiao, and E. Paterson. Physics-informed machine learning approach for augmenting turbulence models: A comprehensive framework. *Physical Review Fluids*, 3(7), Jul 2018. `doi:10.1103/physrevfluids.3.074602`.

[106] Y. Zhao, H. D. Akolekar, J. Weatheritt, V. Michelassi, and R. D. Sandberg. Rans turbulence model development using cfd-driven machine learning. *Journal of Computational Physics*, 411:109413, 2020. `doi:10.1016/j.jcp.2020.109413`.

[107] M. Moioli, C. Breitsamter, and K. Sørensen. Parametric data-based turbulence modelling for vortex dominated flows. *International Journal of Computational Fluid Dynamics*, 33(4):149–170, 2019. `doi:10.1080/10618562.2019.1617857`.

[108] M. Moioli, C. Breitsamter, and K. Sørensen. Turbulence modeling for leading-edge vortices: An enhancement based on experimental data. *AIAA Journal*, 0(0):1–18, 0. `doi:10.2514/1.J060062`.

[109] G. Subbian, A. C. Botelho e Souza, R. Radespiel, E. Zander, N. Friedman, T. Moshagen, M. Moioli, C. Breitsamter, and K. A. Sørensen. Calibration of an extended eddy viscosity turbulence model using uncertainty quantification. *AIAA Scitech 2020 Forum*, 2020. `doi:10.2514/6.2020-1031`.

[110] J. Hunt, A. Wray, and P. Moin. Eddies, streams, and convergence zones in turbulent flows. *Studying Turbulence Using Numerical Simulation Databases*, -1:193–208, 11 1988.

[111] V. Kolář. Vortex identification: New requirements and limitations. *International Journal of Heat and Fluid Flow*, 28(4):638–652, 2007. `doi:10.1016/j.ijheatfluidflow.2007.03.004`.

[112] C. Truesdell. Two measures of vorticity. *Indiana University Mathematics Journal*, 2:173–217, 1953.

[113] J. Jeong and F. Hussain. Hussain, f.: On the identification of a vortex. jfm 285, 69-94. *Journal of Fluid Mechanics*, 285:69 – 94, 02 1995. `doi:10.1017/S0022112095000462`.

[114] Y. Liu, L. Lu, L. Fang, and F. Gao. Modification of spalart–allmaras model with consideration of turbulence energy backscatter using velocity helicity. *Physics Letters A*, 375:2377–2381, 06 2011. `doi:10.1016/j.physleta.2011.05.023`.

[115] C. Shorten and T. M. Khoshgoftaar. A survey on image data augmentation for deep learning. *Journal of Big Data*, 6(1):60, Jul 2019. `doi:10.1186/s40537-019-0197-0`.

[116] M. Moioli, C. Breitsamter, and K. Sørensen. Turbulence model extension for vortex dominated flows and optimization with experimental data. 01 2021. `doi:10.23967/wccm-eccomas.2020.349`.

[117] M. Abadi, P. Barham, J. Chen, Z. Chen, and A. e. a. Davis. Tensorflow: A system for large-scale machine learning, 2016. `arXiv:1605.08695`.

[118] B. Xu, N. Wang, T. Chen, and M. Li. Empirical evaluation of rectified activations in convolutional network, 2015. `arXiv:1505.00853`.

[119] A. Hövelmann. *Analysis and Control of Partly-Developed Leading-Edge Vortices*. Dissertation, Technische Universität München, München, 2016. URL: `http://mediatum.ub.tum.de/?id=1293614`.

[120] M. Moioli, C. Reinbold, K. Sørensen, and C. Breitsamter. Investigation of additively manufactured wind tunnel models with integrated pressure taps for vortex flow analysis. *Aerospace*, 6:113, 10 2019. `doi:10.3390/aerospace6100113`.

[121] J. Chu and J. M. Luckring. Experimental surface pressure data obtained on 65° delta wing across reynolds number and mach number ranges - volume 1 – sharp leading edge. *NASA Technical Memorandum 4645*, 1996.

[122] J. Chu and J. M. Luckring. Experimental surface pressure data obtained on 65° delta wing across reynolds number and mach number ranges - volume 2 – small-radius leading edge. *NASA Technical Memorandum 4645*, 1996.

[123] J. Chu and J. M. Luckring. Experimental surface pressure data obtained on 65° delta wing across reynolds number and mach number ranges - volume 3 – medium-radius leading edge. *NASA Technical Memorandum 4645*, 1996.

[124] W. Fritz and R. M. Cummings. What was learned from the numerical simulations for the VFE–2? *AIAA Paper 2008-0399*, 2008. `doi:10.2514/6.2008-399`.

[125] S. Crippa and A. Rizzi. Steady, subsonic CFD analysis of the VFE–2 configuration and comparison to wind tunnel data. *AIAA Paper 2008-397*, Jan. 2008. `doi:10.2514/6.2008-397`.

[126] R. M. Cummings and A. Schütte. Detached–eddy simulation of the vortical flow field about the VFE–2 delta wing. *Aerospace Science and Technology*, 24(1):66–76, 2013. `doi:10.1016/j.ast.2012.02.007`.

[127] G. Erickson and H. A. Gonzalez. Wind tunnel application of a pressure-sensitive paint technique to a double delta wing model at subsonic and transonic speeds. 2006.

[128] S. M. Hitzel, A. Winkler, and A. Hövelmann. Vortex flow aerodynamic challenges in the design space for future fighter aircraft. In A. Dillmann, G. Heller, E. Krämer, C. Wagner, C. Tropea, and S. Jakirlić, editors, *New Results in Numerical and Experimental Fluid Mechanics XII*, pages 297–306, Cham, 2020. Springer International Publishing.

[129] T. Gerhold. Overview of the hybrid rans code tau. In N. Kroll and J. K. Fassbender, editors, *MEGAFLOW - Numerical Flow Simulation for Aircraft Design*, pages 81–92, Berlin, Heidelberg, 2005. Springer Berlin Heidelberg.

[130] M. Moioli, C. Breitsamter, and K. Sørensen. Turbulence modeling for leading-edge vortices: an enhancement based on experimental data. *AIAA Scitech 2020 Forum*, 2020. `doi:10.2514/6.2020-1032`.

[131] R. Konrath, C. Klein, R. Engler, and D. Otter. Analysis of psp results obtained for the vfe-2 65 delta wing configuration at sub- and transonic speeds. *44th AIAA Aerospace Sciences Meeting and Exhibit*, 2006. `doi:10.2514/6.2006-60`.

[132] R. Hague, I. Campbell, and P. Dickens. Implications on design of rapid manufacturing. *Proceedings of the Institution of Mechanical Engineers, Part C: Journal of Mechanical Engineering Science*, 217(1):25–30, 2003. `doi:10.1243/095440603762554587`.

[133] A. Kirchheim, H. Dennig, and L. Zumofen. Why education and training in the field of additive manufacturing is a necessity. In M. Meboldt and C. Klahn, editors, *Industrializing Additive Manufacturing - Proceedings of Additive Manufacturing in Products and Applications - AMPA2017*, pages 329–336, Cham, 2018. Springer International Publishing.

[134] A. Springer. Evaluating aerodynamic characteristics of wind-tunnel models produced by rapid prototyping methods. *Journal of Spacecraft and Rockets*, 35(6):755–759, 1998. `doi:10.2514/2.3412`.

[135] C. Tyler, W. Braisted, and J. Higgins. Evaluation of rapid prototyping technologies for use in wind tunnel model fabrication. 01 2005. `doi:10.2514/6.2005-1301`.

[136] R. Hildebrand, R. Eidson, and C. Tyler. *Development of a Low Cost, Rapid Prototype, Lambda Wing-Body Wind Tunnel Model*. `doi:10.2514/6.2003-3818`.

[137] C. Aghanajafi, S. Daneshmand, and A. Nadooshan. Influence of layer thickness on the design of rapid-prototyped models. *Journal of Aircraft*, 46(3):981–987, 2009. `doi:10.2514/1.39702`.

[138] C. Aghanajafi and S. Daneshmand. Integration of three-dimensional printing technology for wind-tunnel model fabrication. *Journal of Aircraft*, 47(6):2130–2135, 2010. `doi:10.2514/1.C031032`.

[139] Polymaker, polylitetm pla. `https://eu.polymaker.com/product/polylite-pla/`. Accessed: 2022-01-01.

[140] Zoc33 miniature pressure scanner. available online:. `http://scanivalve.com/media/28028/zoc33_1603.pdf`. Accessed: 2022-01-01.

A Additive Manufacturing of Wind Tunnel Models with Integrated Pressure Taps

A.1 Motivation and State of the Art

The present work rely significantly on the availability of high-fidelity experimental data for the several geometrical and flow condition combinations which characterize different vortex flow topologies. However, the availability of experimental data during a pre-design or conceptualization phase of a vortex dominated wing is usually limited to previously investigated cases with a certain degree of similarity or to a small sub-set of the configurational variations of interest. The main limitation that determines this availability is the production of traditional wind tunnel models which is expensive with regard to time and costs. They are fabricated by means of a complex procedure of different stages of Computer Numerical Control (CNC) machining and surface finishing. Moreover, the production complexity increases further when the target of the experiment consists of the measurement of the steady pressure on the model surface. This requires the fabrication of pressure taps drilled through the model surface with an appropriate positioning and perpendicularity precision while maintaining the lowest diameter size possible.

In a preliminary phase of conceptualization or pre-designs, it is often of secondary importance to have the highest quality of the data. It is more relevant to have the possibility to measure several variations of a geometry at lower costs and time with a fidelity grade which is high enough for investigating the vortex flow field, validate numerical results and utilize the data in the turbulence model conditioning for further accuracy improvement or generalization. One possible solution is the introduction of a different methodology for the wind tunnel model production which offers the best balance between costs and quality. The methodology needs to be suitable for the fast production of geometries of high complexity with an appropriate flexibility, material strength and finishing accuracy. The adoption of an additive manufacturing technique is selected as the most promising possibility.

Such class of fabrication techniques share the process of additively joining particles or layers of raw material. The material and the medium of energy for the fusion vary among the different types. The first technique introduced was Stereolitography (SLA) which employs an ultraviolet beam that solidifies the deposited photopolymer resin on a surface. Selective Laser Sintering (SLS) uses a laser beam to fuse the material powder layer by layer. Finally, the Fused Deposition Modeling (FDM) avoid the usage of any beam, which permits to decrease the costs of the device. It extrudes a thermoplastic material by means of a nozzle mounted on a heated head which maintains the material at a temperature above its solidification point and deposits it layer by layer. FDM is selected as the most suitable methodology for the current research considering the time and cost requirements for prototype production. Moreover, FDM devices permit a proper flexibility in the setup of the several deposition procedure parameters which allows further optimization and improvement of the prototype quality by following an empirical approach.

During the last years the additive manufacturing technology has been progressively improving with regard to its quality, efficiency and economical requirements. One of the main advantages is the possibility to drastically reduce, almost to a negligible level compared to traditional fabrication methodologies, the additional production cost related to additional geometrical complexity. In this sense, additive manufacturing techniques are referred to as ”complexity for free” processes [132, 133] and the costs of a prototype production is estimated by the printed volume and the material used. This characteristic provides potential for the fabrication of single prototypes or small-scale production of complex geometries. In this sense, the methodologies are also often referred to as ”rapid prototyping” techniques. Wind tunnel models correspond to such a production target.

This idea has been already investigated since 1998 [134, 135] where a main limitation is recognized in the material strength of the thermoplastic material used in the FDM methodology. They also exhibit potential significant reductions in terms of cost and time. A wind tunnel model can be designed in order to have a structural support by means of metal rods to be fitted in dedicated slots. In fact, Hildebrand [136] introduced the usage of inner metal rods for enhancing the structural strength and the integration of pressure measurement probes but, when evaluating the quality of the pressure taps, he concluded that they were not properly airtight for undergoing wind tunnel measurements. Additional investigations have been performed during the works of Aghanajafi [137, 138] where a lower grade of accuracy was recognized when compared to traditional models with regard to the surface roughness and the geometrical accuracy. The state of art of the methodology permits the confirmation of the most relevant limitations as well as the most promising qualities and directions of improvement. The current research has the objective to overcome and improve the limitations in order to reach a level of fidelity and quality which guarantees the production of valuable experimental data [120].

The progress of the research is based on the iterative process of fabricating a series of test parts with integrated pressure taps to be empirically evaluated in order to optimize the different parameters that can influence the quality of the final wind tunnel model production. Several properties have to be improved in parallel: the macroscopical and microscopical accuracy, material properties (mainly strength and stiffness), instrumentation procedure and leakage of the pressure taps for steady measurements. At the end of the methodology development a best set of parameters and production procedure is selected. Afterwards, wind tunnel models are produced, tested, measured in a wind tunnel facility and compared to CFD simulation to have an estimation of the data fidelity. After this step, the data are employed for the turbulence modeling conditioning. The applicability of the methodology can be further extended to flank the production and measurement of traditional models gathering additional aerodynamic data for secondary variations at a reduced cost.

Table A.1: Material properties of polyactide (PLA).

Property	**Typical value**
Density [g/cm^3] at 21.5	1.17–1.24
Glass transition temperature [°C]	50–60
Young's modulus [MPa]	1879
Tensile strength [MPa]	28.1
Bending modulus [MPa]	2119
Bending strength [MPa]	48.0

A.2 Methodology Description and Pressure Taps Integration

The FDM is selected for the methodology development as it provides the best balance between quality, flexibility and costs. Compared to SLA or SLS additive manufacturing techniques, FDM offers a prototyping cost of at least one order of magnitude lower. The polyactide (PLA) filament PolyLite$^{\mathrm{TM}}$by Polymaker [139] with a diamater of 1.75 mm is used. PLA offers high reliability during the printing procedure and appropriate material properties (Table A.1).

At the beginning of the methodology development, the target geometry is decided to be a couple of generic delta wings (Sec. 4.1.2) whose data are of interest for their employment into the turbulence model calibration process. The wind tunnel models are half models and this decision offers different advantages. The splitting plane of the model, which corresponds to the root profile of the wing, is planar and it is suitable to be the starting plane of the deposition process. Consequently, the deposition direction is perpendicular to the root profile of the wing and the pressure taps are designed in order to follow this direction starting from the wing root profile. In this way, the connection of the pressure taps to the measurement device is facilitated. Moreover, the connection of the model to the wind tunnel floor can be achieved by means of metal rods forced and glued into dedicated slots integrated in the model during the prototyping procedure. In general, a planar plane of reference simplifies the design of an accessible interface from and to the model, which would be complicated in the case of a full model geometry. However, a full model may be composed of two symmetrical wings which are manufactured as half models and interconnected by means of a central fuselage, designed to enclose their assembling. Another important element to be considered is the size of the model. The FDM device has a limited volume for the deposition and, therefore, a reasonably wind tunnel model needs to be splitted into several parts which are only successively assembled. In this sense, in order to maximize the utilization of the deposition volume, the model size is scaled accordingly to have the minimal number of parts. A possible solution to this problem would be to move to FDM devices with larger deposition volumes. However, only few devices offer large operation volumes for an increase in costs and, more importantly, a reduced printing speed and accuracy of the actuation system. Therefore, the splitting and recombination of the wind tunnel model is a necessary process stage to be addressed at the current state of the methodology.

During the CAD design of the model, the external surfaces are drafted as well as the dedicated slots for the model mounting and the pressure taps geometries. Successively, a "slicer" software is employed for the pre-processing, the model prototyping and preparing the file for being read by the FDM device. The external surfaces are identified as walls, which are distinguished by the inner volume of the prototype. The internal structure is independent from the wall deposition settings. A higher relevance is usually dedicated to the wall settings as they have to provide the highest accuracy and surface quality. With regard to the internal structure, it consists of a filling pattern of the internal volume with a certain infill percentage set by the slicer. Here, the geometrical accuracy and quality are negliged by the standard settings in favour of a faster deposition process. Different parameters are controllable by the user and allow for an empirical evaluation of the effect of the different parameters on the quality of test parts.

However, as a starting point, the traditional deposition settings are at first applied for the production of a test part with integrated pressure taps. A simple cubical specimen is printed with simple pressure taps composed of tubes with a diameter of 0.5 mm which eventually reach the aerodynamic surface perpendicularly. The analysis concentrates on the leakage levels of the pressure taps by means of the injection of pressurized air in the pressure tap while closing the other extremity and immersing the part in water. The outflowing of air bubbles is clearly evincible from different locations. This result confirms, as expected by the state of the art of the application of this technology [136], the pressure tubes are leaking a significant flux of air when printed with the standard deposition parameters. The source of the leakage needs to be identified in order to address any possibility of improvement. Is the leaking of pressurized tubes something inherently inevitable for such FDM technique or is it dependent on the user definition of the deposition process? To answer this question a second test is performed to exclude the first possibility. A straight single tube with one opening is printed, composed only of wall surfaces without any infill structure and it is tested under the same condition as the previous test part. The single tube provides no evincible leakage both under water and by measuring the pressure level. This answers the first main question, suggesting that the air leakage of a prototyped pressure tap is not inherent but consequence of other aspects of the geometrical design and/or deposition process.

A.2.1 Pressure Leakage Measurement

Repeatable measurements of the pressure leakage are established for a suitable investigation of the parameters and design rule dependences. The objective is to formulate a proper quantification of the measured data quality in relation to the pressure tap leakage. The error of a steady surface pressure measurement is therefore estimated based on the leakage levels of a tested pressure tap. The leakage level of a pressure tap is measured with the volume flow rate at a certain imposed pressure. The evaluation of the volume flow rate is performed prior to wind tunnel testing in a controlled environment with the employment of a pressure drop measurement device (Figure A.1). The pressure tap is connected to the measurement device by means of a silicone tube and a pressure level is applied. If leakage occurs, the pressure level measured by the device will drop and the volume flow rate can be evaluated by the pressure drop. As first step, the measurement device plus the connection silicone tube is modeled as a fluid dynamic system with one outflow opening (Figure A.2a). The mass balance equation describes the leaking flow rate for the measurement device.

$$\frac{dm}{dt} = -\dot{m}_{out} \tag{A.1}$$

Consequently, it is assumed that the air behaves as an ideal gas and that the process is isochoric as $V = const$ and isothermal with $T = T_\infty$:

$$\frac{dP}{dt} = -\frac{P_\infty}{V}\dot{V}_{out} \tag{A.2}$$

The ambient pressure P_∞ is known, the system volume V is equal to 100 ml and dp/dt is recorded from the measurement device. At this point, a physical evaluation of the relation between volume flow rate and error in the steady pressure measurement is performed. Considering now the case depicted in Figure A.2, the Bernoulli equation is applied in the y-direction:

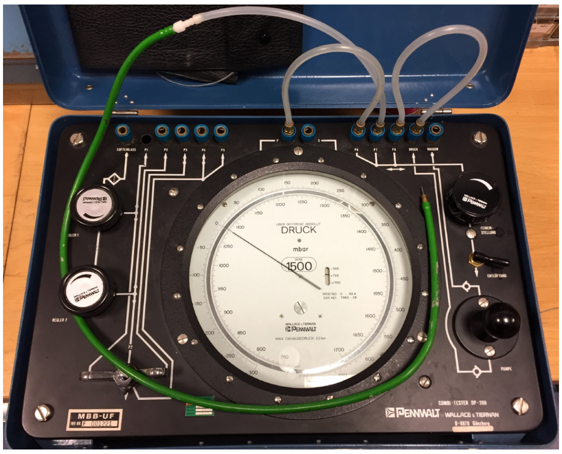

Figure A.1: Pressure drop measurement device in laboratory.

$$P = P' + \frac{1}{2}\rho_\infty v^2 \left(1 + \zeta\frac{l_{tap}}{d_{tap}}\right) \tag{A.3}$$

Where P is the true pressure which is considered constant as it is permanently provided by the flow. P' is the pressure at the measurement device connected at the other part of the pressure tap, assuming properly that no leakage is present in the connection between the wind tunnel model and the device because this is performed by means of silicone tubes. v is the velocity inside the pressure tap which is induced by the leakage flow rate. The tap diameter d_{tap} at the model surface is fixed at 0.5 mm. The flow is assumed as incompressible and the friction factor ζ is defined for laminar flows as

$$\zeta = \frac{64}{Re} = \frac{64\nu}{vd_{tap}} \tag{A.4}$$

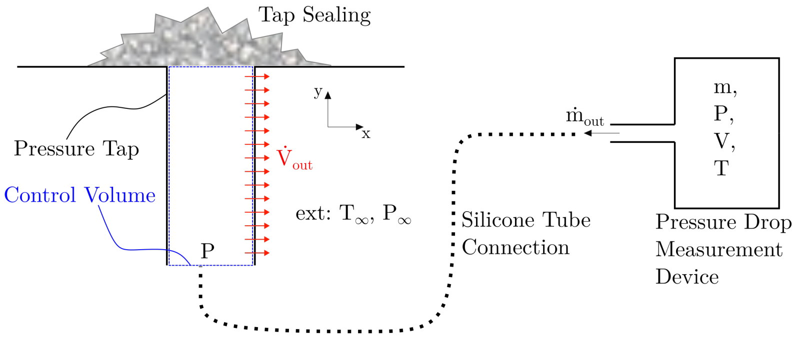

(a) During laboratory test measurement

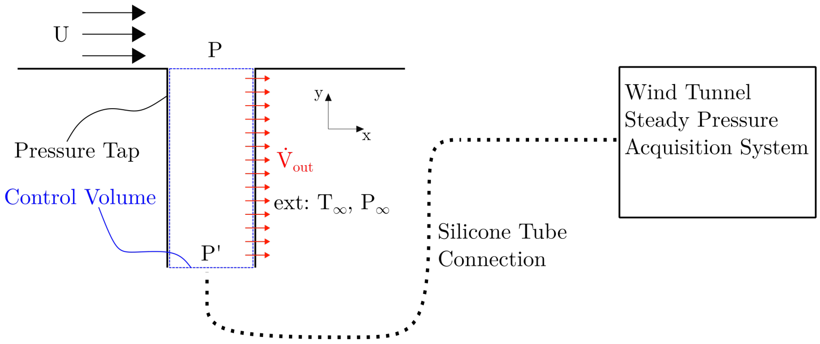

(b) During wind tunnel data acquisition

Figure A.2: Sketch of a leaking pressure tap and the physical interpretation of the system.

The velocity v is correlated to the volume flow rate and the diameter of the pressure tap:

$$v = \frac{4\dot{V}_{out}}{\pi d_{tap}^2} \tag{A.5}$$

And with Eq. A.2:

$$v = -\frac{4}{\pi d_{tap}^2} \frac{\frac{dP}{dt} V}{P_\infty} \propto \frac{dP}{dt} \tag{A.6}$$

The leakage volume flow rate is distributed along the pressure tap and its magnitude may vary in relation with the local geometry. However, since it is not possible to know this distribution a priori, the worst case scenario is considered by concentrating the leakage at the farthest extremity of the pressure tap from the measurement surface. The Bernoulli equation (Eq. A.3) is reformulated to describe the error in terms of C_P due to the measured leakage:

$$C_{p,error} = \frac{2(P - P')}{\rho_\infty U_\infty^2} = \frac{v^2 \left(1 + \zeta \frac{l_{tap}}{d_{tap}}\right)}{U_\infty^2} \tag{A.7}$$

Considering v proportional to the pressure drop (Eq. A.6) and ζ inversely proportional to the velocity v:

$$C_{p,error} \propto \frac{dP}{dt}^2 (1 + \frac{1}{\frac{dP}{dt}}) \tag{A.8}$$

Therefore, a linear dependency between the leakage rate and the measurement error $C_{p,error}$ is assumed as a first estimation.

It is important to notice that this leakage measurement is highly conservative because the assumption are taken under the worst case scenario. Moreover, whereas the tube is only pressurized once and the leakage is measured after closing the tube, during the application of the methodology in a wind tunnel measurement there is not such a static condition but air would continously being embossed into the probe as long as the wind is on. Therefore, the $C_{p,error}$ in a wind tunnel measurement is lower than the values derived from the proposed evaluation of the leakage test.

A.2.2 Deposition Settings Analysis

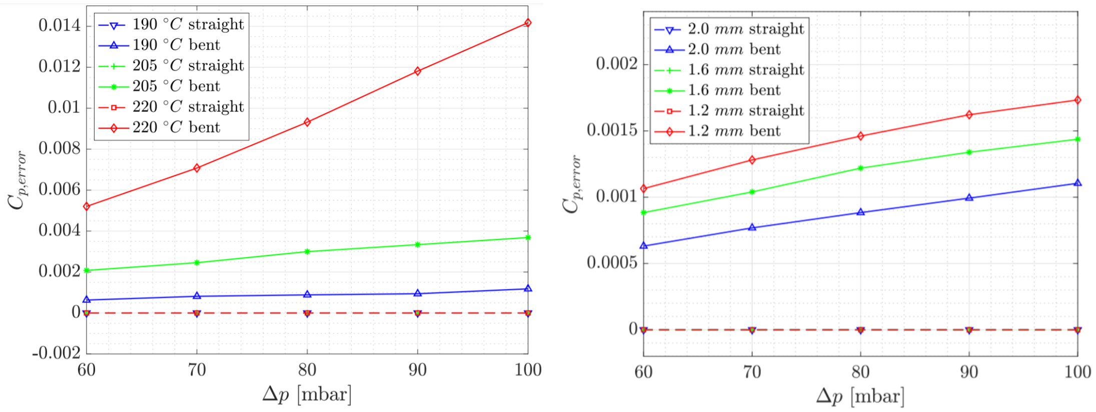

(a) Deposition fusion temperature dependency.

(b) Wall thickness dependency.

Figure A.3: $C_{p,error}$ vs the ΔP for straight and bent tubes in relation to deposition parameters.

A series of specimens are produced where the deposition or geometrical settings are isolated and variated in order to analyze their effect on the leakage level.

The main parameters which influence the leakage values are:

- Temperature: The variation of fusion temperature at the nozzle has shown that a lower temperature results in a lower leakage value (Fig. A.3a). The different

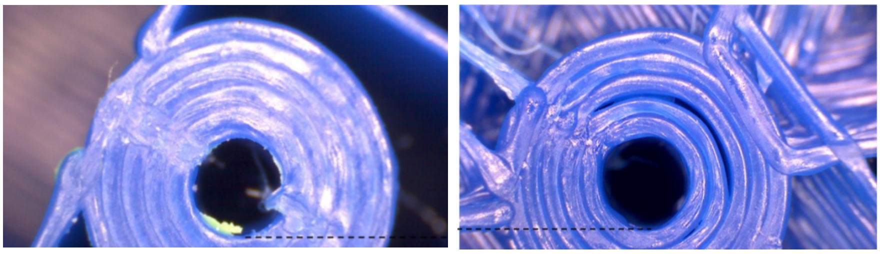

(a) 25 mm/s. **(b)** 50 mm/s.

Figure A.4: Visualization of the better layer-to-layer adhesion and precision with a slower deposition process.

viscosity and the solidification time play a relevant role in the cohesion of the PLA layers.

- Wall thickness: A larger wall thickness corresponds to a lower leakage value (Fig. A.3b). However, an upper limit is present due to the limited space in a wind tunnel model where several probes are present. A value of 2 mm is selected.
- Deposition speed: A slower deposition corresponds to a better cohesion of the plastic layers and, therefore, to a lower leakage value and higher precision (Fig. A.4).
- Retraction setting: The slicer usually avoid to keep the filament retracted in the inner part of the specimen to spare time but this results into material stringing when the nozzle moves. A setting allows to keep this option enabled along the whole deposition process and it allows for a better quality of the produced part.
- Tube geometry and curvature: A straight tube offers the minimum of the leakage values because consecutive layers have the best alignment of the tube walls. As consequence, the smoother the transition of the tube direction from the deposition direction to the surface perpendicular direction is, the lower is the leakage.

At the end of the analysis of the isolated effects a last family of specimen with the best combinations has been produced and the leakage value of the tubes has been measured. The improvement from the standard slicer deposition settings is relevant. The corresponding $C_{p,error}$ is improved from a value of 0.15 to approximately 0.0005, by a factor of 300. This value is significantly lower for the discrepancies encountered from repeated measurements of wind tunnel models which are manufactured in a traditional fashion [119].

A.2.3 Model Quality Evaluation

The delta wing geometries which are produced by means of the developed fused deposition technology have been described in section 4.1.2.

The quality of the prototyped model at the end of the production and preparation process is evaluated. Different characteristics of the final model need to be accomplished in order to reach the target level of fidelity of the experimental data.

- Macroscopic geometric precision: shape and outer surface accuracy.
- Microscopic geometric precision: model surface roughness grade.
- Model structural properties.
- Leakage level of the integrated tubes and steady pressure measurements fidelity.

A.2.3.1 Macroscopic Accuracy

The outer shape accuracy of the manufactured model compared to the CAD geometry is verified by means of a laser scanning process of the resulting wind tunnel model. The laser scanning is performed for the Model53 model after surface finishing before and after the measurement in the wind tunnel. A comparison between the CAD geometry and the scanned surface is shown in Figure A.5. Generally, the geometrical deviation is below 50 μm. Darker regions resulting from the overlapping of the two surfaces are indicated in order to highlight larger deviations. In this region, the mean geometrical deviation corresponds to 0.2 mm which is below the geometrical accuracy of 0.3 mm provided by the laser scanner. The maximal deviation is present in proximity of the trailing edge, which results in an acceptable 0.06° error of the wing twist. Therefore, an appropriate geometrical accuracy of the outer shape is obtained.

A.2.3.2 Stiffness Enhancement

The PLA material stiffness is increased by means of metal inserts which are forced and glued in correspondence of sites produced in the deposition process itself. The inserts increase the stiffness in the spanwise direction of the wing. To analyze the possible stiffness enhancement due to this solution, an experiment is performed by comparing the deformation under a perpendicular force at the extremity of two beams with a quadrilateral section. One beam is full PLA material whereas the other is provided with the insertion of metal rods. The applied weight at the extremity are selected in order to provide a moment of 1.8 Nm which corresponds to the double moment value received by a wing section of the same size under a wind tunnel measurement at $M = 0.15$. The deflection is reduced from 2.7 mm to 0.7 mm, by a factor of 3.8.

A.2.3.3 Microscopic Accuracy

The surface roughness is in general a relevant quantity for any product machined from metal alloys. With regard to wind tunnel models, this feature acquires even further importance because the roughness may have a direct influence on the flow and significantly influence the outcome of the experimental result when used for validation of numerical simulations. The vortex dominated flows of interest of the current research

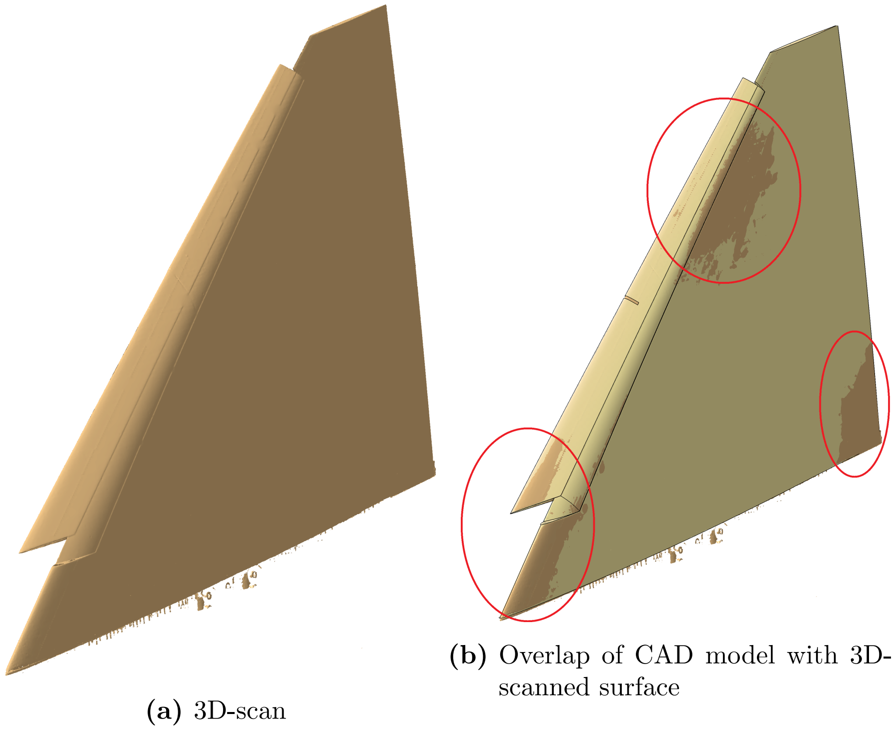
(a) 3D-scan

(b) Overlap of CAD model with 3D-scanned surface

Figure A.5: Comparison between the 3D-scanned data and the CAD geometry.

are concentrated on high Reynolds number flows in a fully turbulent state and, therefore, the influence of the surface roughness is of secondary importance but not negligible. Therefore, the surface roughness of the model is required to be at the lowest possible level and above a certain grade of acceptability, thus in the same order of magnitude as traditional wind tunnel metal models. The FDM technique inherently provide a high level of roughness in the direction of the layer deposition. The roughness is, in this sense, a consequence of the fabrication technique itself and not an inaccuracy of the device, material or deposition software. Moreover, the roughness level is anisotropic and higher when moving perpendicular to the layers. A smaller filament diameter, which correspondes to a smaller layer thickness, would provide a smaller roughness level but longer deposition time. For this reason and the fact that the roughness level would still remain unacceptable for wind tunnel experiments, it is chosen to improve the surface quality during the finishing of the model. This solution offers also the advantage to improve the zones in the proximity of the connection between different parts. A process of finishing is evaluated with the application of a sandpaper cycle over test parts. The surface roughness is measured by means of a portable profilometer which consists of a touching stylus that measures the surface profile by contact along a straight line. The instrument returns values of R_a and R_z, which are then compared in terms of order of magnitude with the state of the art of metal models. Before the sanding finishing, the roughness levels consist of a R_a of 9.3 μm parallel and 2.8 μm perpendicular to deposition direction y. With regard to R_z, the levels are around 28.2 μm and 24.5 μm. The sanding procedure is subdivided into cycles which corresponds to a back-and-forth movement on the surface with a $10N$ applied force. As expected, the roughness of the surface converges with the sanding cycles. A proper value for convergence is established at around 200 cycles. As first result of the finishing procedure, an isotropic roughness is measured along the whole surface. Moreover, the values are significantly reduced to levels of $R_a = 0.45$ μm and $R_z = 6.5$ μm. The values lie now in the same order of magnitude of conventional metal models, larger by a factor of 4. The obtained level is considered appropriate for the experimental investigation of the fully turbulent flow around delta wings.

A.3 Instrumentation and Wind Tunnel Measurement

The Model53 and Model56 have been used for application of the developed turbulence model methodology and their results have been reported in Sections 4.1.2 and 4.4.2. Their dimensions are too large to be produced in a single fused deposition process. The models have been splitted in two portions at around 50% of c_r and fixed together by means of cylindrical plugs and epoxy glue.

Table A.2: Mean absolute and standard deviation values of the C_P difference along repeated measurements for the Model53 and Model56.

C_P **variation**	Model53	Model56
Mean absolute value	0.022	0.00975
Standard deviation	0.07	0.019

The Model53 employ 176 pressure taps over 16 sections whereas the Model56 has a number of 290 points over 21 sections. The larger number of taps for the Model56 was possible thanks to a refinement of the design procedure exploiting the experience gathered with the Model53. At the connection of the pressure probes a metal insert is glued and a silicon tube is used to connect the probe to the acquisition system (Fig. A.6). The pressure measurements are performed by means of three electronic scanning modules (Scanivalve ZOC33 [140]) which provides a measurement range up to 345000 Pa of ΔP with 0.08% precision for values above 17000Pa. A sampling frequency of 200 Hz and an averaging time of 10 s are used. The measurements are performed over a series of angle-of-attack polars and repeated between 15 and 20 times in order to investigate their repeatability accuracy. An appropriate level of repeatability is achieved (Table A.2) for its application to low-speed wind tunnnel measurements and the generation of data of a suitable quality level.

Figure A.6: The lower surface of the Model56 wing showing the silicon tubes of the pressure measurement probes for the connection to the acquisition system.